Photoinduced Formation and Decay of Charge-Separated States in d^6 Metal Complexes

Inauguraldissertation

zur Erlangung der Würde eines Doktors der Philosophie

vorgelegt der Philosophisch-Naturwissenschaftlichen Fakultät

der Universität Basel

von

Martin Kuß-Petermann

aus Hoyerswerda, Deutschland

Basel, 2016

Genehmigt von der Philosophisch-Naturwissenschaftlichen Fakultät auf Antrag von

Fakultätsverantwortlicher/Dissertationsleiter: Prof. Dr. Oliver S. Wenger

Koreferent: Prof. Dr. James K. McCusker

Basel, den 10.11.2015

Prof. Dr. Jörg Schibler

Experiments rarely tell us what we think they're going to tell us. —
That's the dirty secret of science.

Kevin Dunbar

Für meine Eltern

Acknowledgments

I cordially thank **Prof. Dr. Oliver S. Wenger** for accepting me in his group for my diploma thesis and giving me the opportunity to work on this interesting topic as a PhD student. I want to thank him very much for his always open door, for his constant support, and for encouraging me to design research projects independently. I could not have wished for a better supervisor.

Special thanks is given to **Prof. James K. McCusker** for kindly agreeing to be my co-referee.

I want to sincerely thank **Prof. Dr. Thomas R. Ward** for charing my examination.

I kindly acknowledge **Sylvie Mittelheisser** for measuring all my elemental analyses and **Dr. Heinz Nadig** for conducting the high-resolution MS measurements.

Special thanks is given to the whole **Werkstatt-team** for keeping the regular lab-work run as smoothly as possible. To **Markus Hauri** and **Roy Lips** for their support and a steady supply with chemicals. To **Beatrice Erismann** and especially **Brigitte Howald** for the help in organizational and administrative matters.

Thanks to **Dr. Häussinger** and **Dr. John** for solving several NMR problems.

I want to kindly thank **Margherita Orazietti** and **Prof. Dr. Peter Hamm** from the University of Zurich for conducting the transient IR measurements.

I would like to thank all the present and recent members of the **AK Wenger** who made it a pleasure to work in this group.

In particular,

Annabell and **Andrea** for all the helpful discussions and proofreading many parts of this thesis.

Luisa for being such a great lab-mate back in Göttingen and charing the obligate birthday-cake with me.

Julia for her companionship in numerous “Zigi-Pausen” and many an Apéro.

Laura for the "highly professional and always absolutely clean and accurate lab work" we were able to establish in 304 over the past two years.

Jing for conducting my measurements during the time I was not yet in Basel.

Last but not least I want to thank **Jihane**, **Catherine** and **Ann Christin**.

Special thanks to the ***Reisegruppe***, and in particular to **Cindy,** for the great 9 years in Göttingen. We had so much fun, especially in Denmark or at our regular Friday-lunches.

I want to thank all the **GoNo's** for all the matured friendships that developed over the years. It always feels like home when being back adH!

I deeply want to thank **Oliver** for our past years in Basel. His sunny disposition and his patience helped me a lot to stay on track.

Last, but most important I want to thank my parents. **Mum** and **Bernd**; **Papa**, **Petra** and **Martin**. You have supported every decision I made over the past years, especially when I started studying chemistry. Even more so, I thank you all for your encouragement during the time when my motivation was very limited.

Abstract

One of the major challenges mankind faces these days is the growing demand for energy and the associated consequences of combusting fossil fuels. Accordingly, numerous research groups of different scientific backgrounds focus their efforts towards the production of energy and fuels from sunlight and water. For efficient production of so-called solar fuels, a thorough understanding of fundamental characteristics of charge transfer reactions is crucial. In this context, the following thesis will focus on three key aspects of charge separation: (i) the mechanisms of electron transfer reactions that are coupled to concomitant proton transfer, (ii) the kinetics of electron transfer reactions over large distances, and (iii) charge accumulation in a molecular system without the need of sacrificial agents.

In ruthenium(II) and rhenium(I) dyads with an attached phenol which acts as a combined electron and proton donor, the dependence of proton-coupled electron transfer (PCET) reactions on the electron donor-electron acceptor distance was investigated. These measurements yielded the first distance-decay constants (β) for bidirectional concerted PCET reactions. Additionally, a mechanistic change-over was observed for short donor-acceptor distances. When linking the phenol directly to the photosensitizer these dyads exhibit photoacid behavior. In contrast, by introducing one *p*-xylene bridging molecule, proton-coupled electron transfer was operative. In addition to these dyad studies the PCET chemistry of thiophenols was investigated in bimolecular reactions. This study demonstrated that thiophenols, dependent on their substituents, show the whole variety of PCET mechanisms ranging from concerted to stepwise processes. However, in comparison to phenols, the sulfur analogs tend towards a stepwise transfer of the electron and proton, due to easier oxidation combined with a higher acidity.

In a second topic of my thesis, the kinetics of thermal back electron transfer of charge-separated states was investigated in linear triads of variable donor-acceptor distances. These triads are comprised of a ruthenium(II) photosensitizer, a triarylamine (TAA) electron donor, and anthraquinone (AQ) as an electron acceptor. The charge recombination kinetics as a function of spatial separation between donor and acceptor revealed a maximum in rate constants for large distances. This observation was attributed to an increase in the outer-sphere reorganization energy with increasing donor-acceptor distances. According to Marcus theory, this causes a change-over for electron transfer operating in the inverted region for short distances to the normal region at large separations, via an activationless ET for intermediate distances. This is the first unambiguous experimental evidence for rate maxima at large spatial separations, as predicted already 30 years ago by theoretical studies.

With respect to the main objective of light-driven solar fuel production, the accumulation

of multiple charges on a single molecule is pivotal. For the reduction of protons to hydrogen, or the oxidation of water, a single redox equivalent is not sufficient. Therefore, in a third topic of my thesis, the already mentioned donor-photosensitizer-acceptor assembly was extend to a pentad and investigated with respect to its ability to perform photoinduced charge accumulation. Hereby, a central AQ unit served as a potential two-electron acceptor. Upon excitation with light, the formation of twofold reduced anthraquinone was confirmed in transient IR and UV/Vis experiments. Furthermore, in presence of acid the signal of this charge-accumulated state persists even after several hundred microseconds. This is a clear improvement compared to charge-accumulating systems reported in the literature, which either rely on sacrificial agents or do not exhibit sufficiently long lifetimes for the charge-accumulated state.

Contents

Abbreviations

δ	chemical shift
A	acceptor
AQ	anthraquinone
ATP	adenosine triphosphate
bpy	2,2'-bipyridine
BQ	*p*-benzoquinone
Bu	butyl
CPET	concerted proton-coupled electron transfer
CSS1	first charge-separated state
CSS2	second charge-separated state
D	donor
dba	dibenzylideneacetone
DMF	N,N'-dimethylformamide
DMSO	dimethylsulfoxide
e	elementary charge
EPR	electron paramagnetic resonance
ET	electron transfer
Fc	ferrocene
FWHM	full width at half maximum
IR	infrared
M	molar, $mol \cdot L^{-1}$
m/z	mass per charge
MLCT	metal-to-ligand charge transfer
n	normal
NADP	nicotinamide adenine dinucleotide phosphate
NHE	normal hydrogen electrode
NIR	near infrared
NMR	nuclear magnetic resonance
p	para
P	photosensitizer
PT	proton transfer
PCET	proton-coupled electron transfer
PPh_3	triphenylphosphine
ppm	parts per million
SCE	saturated calomel electrode
t	tertiary

TAA	triarylamine
$TBAPF_6$	tetrabutylammonium hexafluorophosphate
THF	tetrahydrofuran
TMS	trimethylsilyl
TMSCl	trimethylsilyl chloride
Tyr_Z	tyrosine Z
UV/Vis	ultraviolet/visible light
XAS	X-ray absorption spectroscopy
xy	*p*-xylene, *p*-xylyl

1. General Introduction

Modern human lifestyle demands for a steady and secure supply of energy for electricity, mobility, manufacturing, and comfort. Until now, the main energy source is still the combustion of fossil fuels, such as coal, oil, or natural gas. Although there is not yet a global shortage of fuels, their supply is finite. Considering the growing demand for energy, not only due to the increasing world population, but also due to the proceeding development of living standards in the so-called newly industrialized countries, new energy sources need to be explored. The main problem with present energy sources, like fossil fuels or nuclear power, is their negative influence on the environment, such as the production of green house gases like CO_2, or the unresolved problems of nuclear waste disposal. As a consequence, over the past decades awareness for the importance of renewable and environmentally friendly energy sources has grown. In this context, using sunlight, as the most abundant source of energy, is logical. The surface of the earth is provided by roughly 120.000 TW of energy from sunlight.[1] In comparison, in 2014 the total energy consumption of mankind was around 16 TW with approximately 15 % of that amount being used for electricity.[2] This comparison visualizes the enormous potential of sunlight as a clean energy source. Already 100 years ago Ciamician declared that sunlight can serve as a nearly infinite source of energy, if converted in an appropriate way.[3] In principle, nature provides us with a blueprint for the conversion of sunlight into useful forms of energy, i.e. photosynthesis. In the photosynthetic process, the energy of light is used to convert the low-energy chemicals H_2O and CO_2 into high-energy carbohydrates. Hereby oxygen is the only waste product. This process involves the splitting of water into protons, electrons, and molecular oxygen. In another reaction step, the released protons and electrons are combined with CO_2 to form carbohydrates. However, in terms of the growing demand for fuels, direct combination of the evolved protons and electrons to hydrogen gas is much more interesting and less difficult to achieve for mankind. Hydrogen gas, in fact, has several advantages compared to fossil fuels. The energy density of hydrogen gas is approximately three times higher than those of carbon-based fuels.[4] Additionally, the only combustion product of H_2 is water. The combination of these two properties makes it a suitable candidate for an environmentally friendly substitute for fossil fuels.

The direct electrochemical splitting of water into oxygen and hydrogen was first observed

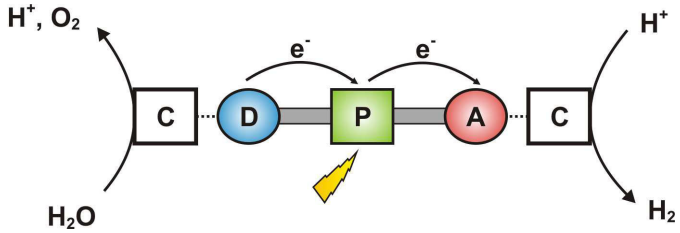

Scheme 1.1 Idealized molecular assembly for the use of solar energy to split water into oxygen and hydrogen. A = electron acceptor, D = electron donor, P = photosensitizer, C = catalyst.

in 1798 by VAN TROOSTWIJK[5, 6] but remained a scientific curiosity throughout the 19th century.[7] By now, electrolysis of water is well explored and extensively used in industrial processes. However, the direct splitting of water by the use of sunlight would not need electricity to proceed. Alas, water does not dissociate into hydrogen and oxygen upon irradiation with visible light, among other reasons due to the lack of significant absorption in this spectral range. Therefore, artificial systems for light absorption and catalytic cleavage need to be employed. For basic research on this topic, often entirely molecular systems are applied due to their well-defined properties. Such an idealized molecular system is depicted in Scheme 1.1. In analogy to photosynthesis, a chromophore (or so-called photosensitizer) needs to absorb as much light energy as possible. This energy is employed to generate a positively charged donor and a negatively charged acceptor. In other words, the light energy is used to promote electron transfer. In addition, these charges need to be spatially separated in order to avoid their direct recombination. Subsequently, the attached catalytic systems would utilize these generated charges to oxidize water and reduce protons to hydrogen.

There are several aspects which are crucial for the design of a system as illustrated in Scheme 1.1 and which are the subject of current research efforts. For example, the optimization of effective light-harvesting assemblies, in order to exploit a larger spectral range of light. Furthermore, efficient catalysts for water oxidation and hydrogen production need to be provided. However, these aspects will not be addressed in particular in this thesis. This work will focus on three general aspects of electron transfer reactions, which are probably the most essential reaction steps in the context of artificial photosynthesis. (1) Kinetic and mechanistic studies of electron transfer reactions which are coupled to proton transfer events. As is obvious from Scheme 1.1, such reactions are an integral part when it comes to hydrogen formation or water oxidation. (2) Kinetic studies on the influence of spatial separation on electron transfer reactions. These investigations are of particular interest with respect to the generation of long-living charge-separated states, which are a prerequisite for efficient catalytic turnover. (3) Attempts towards a molecular system which is capable of performing light-driven charge accumulation. The

formation of hydrogen gas or the oxidation of water require the accumulation of multiple redox equivalents. For hydrogen gas evolution two electrons are needed, and even four positive charges are required for water oxidation. By contrast, the absorption of one photon can usually only generate a single electron-hole pair. In order to overcome this obstacle, multiple charge-separating events within a donor-acceptor system need to occur very rapidly. In addition, such multiply charge-separated states have to be stabilized in order to exhibit significantly long lifetimes for catalytic applications.

The following chapter briefly introduces natural photosynthesis and the oxygen evolving complex (OEC), the reactive center for water oxidation. Subsequently, the fundamental principles of photochemistry and photophysics will be introduced, as well as the general aspects of electron transfer reactions; in particular those being initiated by photon absorption. Additionally, the concept of coupling proton transfer reactions to electron transfer events will be presented. Subsequently, the following chapter will close with a few considerations with respect to charge-accumulation in molecular systems, and some recently reported studies on this topic.

2. Theoretical Background

2.1. Natural photosynthesis

Photosynthesis, as nature's ingenious way to convert solar energy into storable chemical energy, is the fundament for the existence of higher life-forms. It not only uses sunlight to produce essential high-energy chemicals, such as sugars and proteins from low-energy molecules, i.e. water and carbon dioxide, it is also the source of atmospheric oxygen. The process of photosynthesis takes place in the chloroplasts of green plants, cyanobacteria, and algae. It can be divided into two separate parts, the light-dependent reaction and the light-independent fixation of carbon dioxide. The active sites of the light-dependent reaction are located in the thylakoid membrane of the chloroplasts. These reaction centers use the absorbed solar energy to oxidize water and to drive an electron transport chain to finally produce the reducing equivalent NADPH, the biological form of molecular hydrogen. Since the oxidation of water at the oxygen evolving complex (OEC) requires strong oxidants, whereas the reduction of $NADP^+$ to NADPH needs a relatively strong reductant, the light-driven reaction is divided into photosystem I and II (PS I and PS II). Both systems are comprised of a central pair of chlorophyll molecules (P680 for PS II, P700 for PS I) that are surrounded by several well organized chromophores in order to harvest as much light as possible and transfer its energy to the reaction center. The so-called Z-scheme, shown in Scheme 2.1, gives a schematic overview about the spatial separation and the energy levels in PS I and PS II.[8] In photosystem II, absorption of light leads to the formation of a singlet-excited *P680 chlorophyll molecule which can transfer an electron very rapidly to pheophytin (pheo) to form an initial charge-separated state $P680^+/pheo^-$ within a few picoseconds.[9] Subsequently, $pheo^-$ reduces the tightly bound plastoquinone (PQ) Q_A within a few hundred picoseconds.[9] This ion radical pair $P680^+/Q_A^-$ exhibits recombination with a lifetime of approximately 200 μs.[10] The highly oxidizing $P680^+$ (E^0 = +1.26 V vs. NHE) is re-reduced by the nearby tyrosine Tyr_Z. This electron transfer is accompanied by the transfer of the phenolic proton to histidine His_{190} on the nanosecond to microsecond time domain.[11, 12] The formed tyrosyl radical is a sufficiently strong oxidant to promote electron abstraction from the OEC. On the reductive side of the charge separation cascade, the initially reduced Q_A transfers its electron to plastoquinone (PQ)

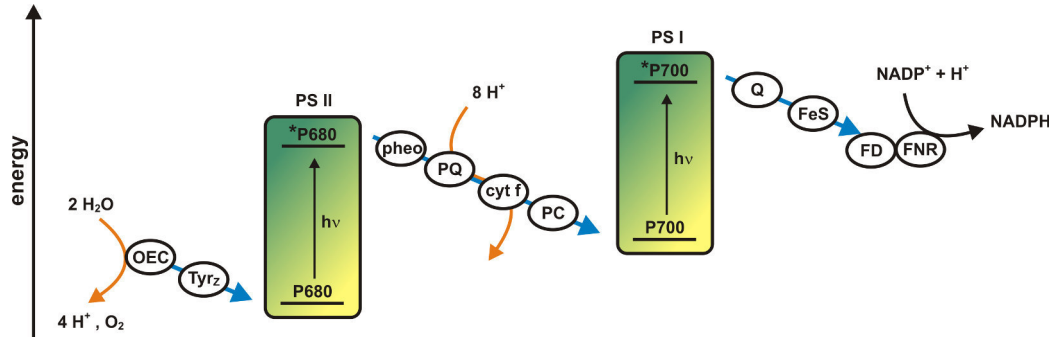

Scheme 2.1 Simplified Z-scheme of the light-dependent reactions in PS I and PS II.

Q_B. The overall distance for charge transfer in PS II is about 50 Å from the OEC to Q_B, with a recombination time in the millisecond time domain. This lifetime exceeds the time which is necessary for the charge accumulation steps to occur on the OEC.[13] After a second reduction of Q_B, coupled to its protonation, the formed hydroplastoquinone H_2Q_B diffuses away into the membrane matrix, transferring its reducing equivalents via cytochrome *f* and plastocyanine (PC) to photosystem I. A proton gradient between the stroma and lumen site of the membrane is established along this electron transfer pathway, which is further used to generate ATP. In PS I a second electron transfer cascade is initiated. With its primary objective, the reduction of $NADP^+$ to NADPH, the excited *P700 in PS I is a very strong reductant. It transfers the electron which comes from PS II further to phylloquinone (Q) and subsequently to ferredoxin (FD) via several iron-sulfur complexes (FeS). This ferredoxin binds to a ferredoxin-NADP-reductase (FNR), promoting the formation of NADPH as the final electron acceptor of the light-dependent reaction.

The molecular structure of the photosystem II is shown in Figure 2.1.[14] It depicts the electron transfer pathway from the OEC to plastoquinone Q_B. The structure of the OEC was found to be a rather unique pentanuclear $CaMn_4$-cluster. Over the last years, the structural elucidation of the cluster earned a lot of attention. Recently, the crystal structure of the OEC was reported with a resolution of 1.9 Å (Figure 2.1).[15] The OEC reveals a rather complex structure, comprised of a cubane-like $CaMn_3O_4$ unit which is linked to a fourth manganese atom by an oxo-bridge. This cluster is well encapsulated by the surrounding protein matrix isolating it from the thylakoid lumen. This ensures a slow and step wise oxidation of the OEC and prevents the conversion into the reduced resting state prior to the release of oxygen and complete oxidation of water.

The mechanism of water oxidation in the OEC, first postulated by Kok in 1970, involves four electron transfer steps to the nearby tyrosyl radical which is formed by photoinduced oxidation from $P680^+$. Furthermore, four protons are liberated during the process of charge accumulation. Several research groups attempted to elucidate the exact mechanis-

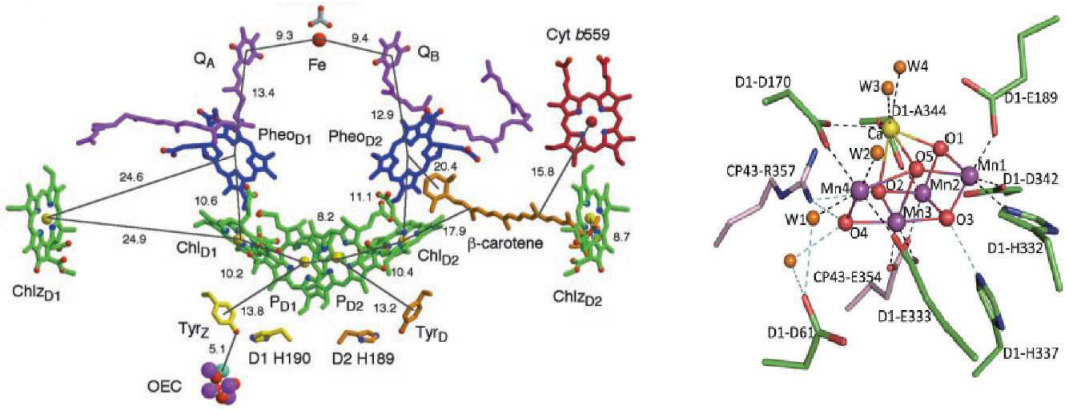

Figure 2.1 Left: Molecular structure of the reaction center in PS II.[14] The surrounding protein matrix was omitted for clarity. The distances between the redox centers are given in Å. Right: Crystal structure of the OEC at a resolution of 1.9 Å with its ligand environment.[15] Reproduced with permissions from[14, 15] © American Association for the Advancement of Science and Nature Publishing Group.

tic sequence being operative in the water oxidizing complex. The catalytic cycle, proposed by Kok, involves four oxidized states and the initial ground state (so called S-states), but does not include any specific information about proton transfer reactions. A more sophisticated mechanism, based on time-resolved EPR and XAS studies, was proposed by Haumann and is illustrated in Scheme 2.2.[16] After the absorption of the first photon, the dark-stable resting state S_1 state undergoes Mn-oxidation to the S_2 state without release of a proton. The $S_2 \rightarrow S_3$ transition, occurring after a second photon absorption, is a proton-coupled electron transfer process. However, its precise mechanism is not certain. The third photon initiates the cascade of transitions which ultimately leads to the formation of molecular oxygen. The starting point is the formation of the S_4-state by release of a proton. This S_4-state reduces the nearby tyrosyl radical of Tyr_Z, forming the S_4'-state, with a time constant of approximately one millisecond. This seems to be the rate-limiting step in the overall process of water oxidation. Subsequently, rapid release of O_2 and formation of the S_0-state occurs. After absorption of the fourth photon, the catalytic cycle is closed. The $S_0 \rightarrow S_1$ step involves a simultaneous oxidation and deprotonation of the complex leading to the formation of the dark-stable resting state. The proposed basic sequence of four electron and four proton removal steps (Scheme 2.2) is certain. However, several aspects are still speculative and require further experimental support. Especially the distinct determination of energetic parameters, such as redox potentials and pK_A values, and their combination with computational methods seem to be of major importance in order to clarify the complex mechanisms occurring in the OEC.

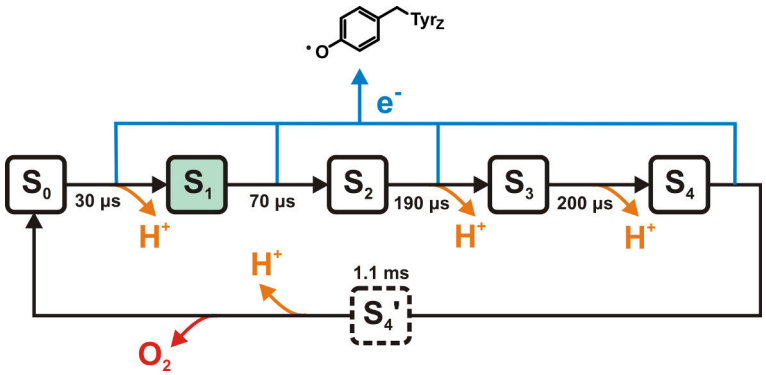

Scheme 2.2 S-state cycle according to HAUMANN, illustrating the sequence of electron and proton transfers necessary for water oxidation in the OEC. The dark-stable resting state S_1 is was highlighted. The times correspond to the individual time constants for the transitions.[16]

2.2. The excited state

In the following section, the relevant basics of photophysics and photochemistry necessary to understand the topics of this thesis will be introduced. Hereby, the general concept of electronic absorption and deactivation of the excited state will be explained for a low-spin d^6 metal center.

In order to understand the concept of absorption and emission of light by matter, their energetic states need to be considered. In principle, the absorption of light, i.e. a photon with a discrete energy, can be described as the transition of an occupied state of the absorbing particle to a state higher in energy. This event only occurs when the energy of the photon matches the energetic difference between these two states. This results in the situation where in different regions of the electromagnetic continuum, different kinds of transitions are observed. For example, the excitation of rotational states usually requires microwave radiation, whereas vibrational transitions are observed in the infrared part of the spectrum. However, the photoinduced reactions described in this thesis rely on electronic transitions, which require the absorption of photons in the visible range of the electromagnetic spectrum. For the transition between electronic states, not only the energy difference of the states, i.e. the frequency of the photon necessary for excitation, need to be considered. There are also certain selection rules, based on quantum-mechanical considerations, that determine the probability of such a transition. In general, an electronic transition is allowed if the overall spin of this system is conserved and the parity of the orbital changes. Such transitions, for example metal-to-ligand charge transfer (MLCT) transitions, result in rather intense bands in the UV/Vis absorption spectra. In contrast, spin-forbidden transitions from a singlet to a triplet state, for example, are muss less

probable, resulting in very weak absorption features.[17]

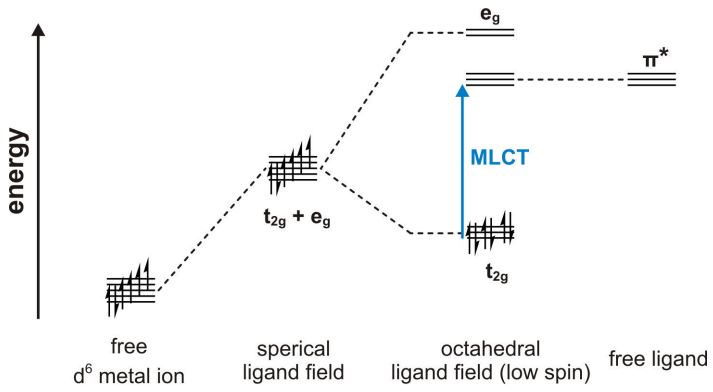

Scheme 2.3 Simplified energy diagram for complexes of d^6 transition metals in their low-spin configuration.

Metal-to-ligand charge transfer transitions are of particular interest for this thesis, due to fact that the resulting state is the starting point of all photoinduced reactions described in the following chapters. A simplified energy diagram for d^6 transition metals, i.e. Ru^{II}, Re^{I}, or Os^{II}, in their low-spin configuration is shown in Scheme 2.3. Starting at the hypothetical point of a free metal ion, the energy levels of the relevant d-orbitals are degenerate and will only increase in energy when applying a spherical ligand field. An octahedral ligand field, as it is present in the metal complexes in this thesis, causes a splitting of the energy levels of the d-orbitals in a t_{2g} and an e_g set of orbitals. In case of d^6 low-spin metal centers, the t_{2g} orbitals will be fully occupied, whereas the e_g orbitals are empty. Transition of an electron from the t_{2g} to the e_g orbital is parity-forbidden. By coordination of the metal center with ligands which bear unoccupied orbitals low in energy (for example π^*-orbitals), the lowest excited state is no longer a forbidden d-d transition, but an allowed MLCT transition. The situation of unoccupied ligand orbitals being lower in energy than the e_g orbitals, i.e. a strong ligand field splitting, is typical for late transition metals.

The Jablonski diagram in Scheme 2.4 shows the possible transitions in a metal complex with respect to an MLCT excitation. Absorption of a photon results in the transition from the ground state (^{1}GS) to a singlet excited state. Depending on the energy of the photon, this singlet excited state can be ligand centered (^{1}LC) or a metal-to-ligand charge transfer (^{1}MLCT). This thermally excited singlet state undergoes very fast vibrational relaxation, by so-called radiationless internal conversion (IC, $> 10^{11}$ s^{-1}) to the vibrational ground state of the lowest singlet state, in this case ^{1}MLCT. For the ruthenium and rhenium complexes used in this thesis the actual observed, luminescent, lowest-lying excited state is the ^{3}MLCT state, which is accessible via intersystem crossing (ISC) from the ^{1}MLCT-state. This transition from a singlet to a triplet state (10^6 - 10^{11} s^{-1}) has to compete

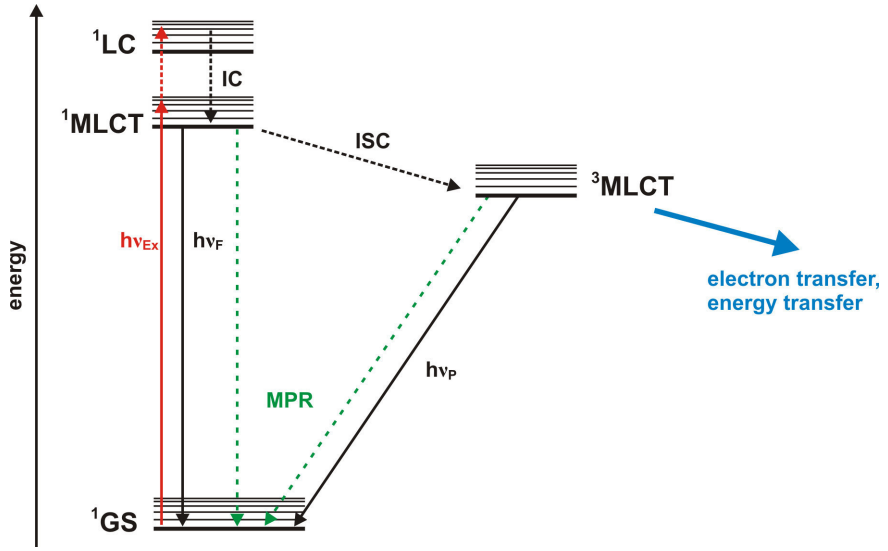

Scheme 2.4 Simplified JABLONSKI diagram.

with other possible deactivation processes of the ^{1}MLCT: (1) release of the excited state energy by emission of a photon, so called fluorescence ($h\upsilon_F$), and (2) radiationless decay to the ground state by multi phonon relaxation (MPR). However, the metal complexes of heavy transition metals such as rhenium and ruthenium, show a high tendency for the population of triplet states due to their strong spin-orbit coupling. Radiative decay from a triplet state, so-called phosphorescence ($h\upsilon_P$), is spin-forbidden and usually occurs on much longer time scales than fluorescence from a singlet state. The comparably long lifetime of this ^{3}MLCT allows for electron or energy transfer reactions to compete with the already mentioned deactivation pathways ($h\upsilon_P$ and MPR).

Especially electron transfer originating from the ^{3}MLCT-state is of importance in this thesis. The lifetime of this excited state is 0.62 µs for $Ru(bpy)_3^{2+}$ (bpy = 2,2'-bipyridine) in deoxygenated water with an emission quantum yield of $\Phi = 0.042$.[18] The LATIMER diagram presented in Scheme 2.5, shows the ground state and excited state redox potentials of $Ru(bpy)_3^{2+}$.[19] After excitation of $Ru(bpy)_3^{2+}$ to its ^{1}MLCT state a fast ISC results in the triplet state.[20] Hereby, it becomes a much stronger oxidant as well as a stronger reductant compared to its ground state. This observation can easily be understood on the basis of the excited state being comprised of a reduced ligand and an oxidized metal center. With a suitable electron acceptor in near proximity, the excited photosensitizer can transfer an electron to the acceptor, which is referred to as the so-called oxidative quenching of the excited state. The analogue procedure of electron transfer from a donor to the photosensitizer is called reductive quenching. Alternatively, the excited state can decay via energy transfer to a triplet state of a suitable quencher or via multiphonon relaxation.

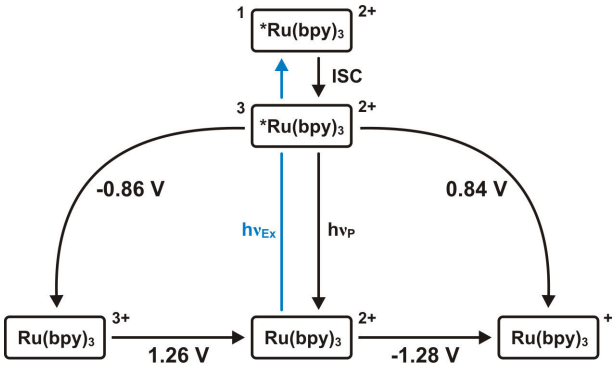

Scheme 2.5 LATIMER diagram of $Ru(bpy)_3^{2+}$. Potentials are in given for aqueous solution in Volts versus NHE.[19]

2.3. Electron transfer reactions

Electron transfer (ET) reactions can occur via two fundamentally different mechanisms: (1) an outer-sphere or (2) an inner-sphere mechanism. The outer-sphere mechanism requires the formation of an encounter complex in order to establish electronic interactions between the two redox centers. In contrast, in the inner-sphere mechanism the redox centers are linked to one another with an enhanced electronic communication between the donor and the acceptor. The rate constants for electron transfer via an inner-sphere mechanism are usually much faster. However, the theory on electron transfer rates, established by RUDOLPH A. MARCUS was initially based on outer-sphere, self-exchange reactions.[21–24] This approach with a mathematical description of electron transfer rates is based on the theory of the transition state established by HENRY EYRING in 1935.[25] In such outer-sphere self-exchange reactions, no bonds are formed or broken. However, the redox centers have to adapt bond lengths and angles to the new charge distribution. Furthermore, the solvent shell which surrounds the molecules needs to rearrange. This necessity for reorganization determines the activation barrier for these self-exchange reactions, and in consequence, their rate constants. The classical MARCUS theory was extended to inner-sphere electron transfer reactions by NOEL S. HUSH. For inner-sphere reactions the electron transfer occurs through a bond between the two redox centers which is established as a result from the formation of an encounter complex. In addition to the considerations of the reorganization made for the outer-sphere mechanism, the strength of electronic communication between the donor and the acceptor needs to be taken into account. This semi-classical theory for electron transfer reactions, so called MARCUS-HUSH theory, is expressed in equation 2.1. It demonstrates that the rate constant for electron transfer, k_{ET}, is mainly dependent on three parameters: (1) the reaction free energy, ΔG^0, (2) the reorganization energy, λ, and (3) the electronic coupling between

the redox centers, H_{AD}.

$$k_{ET} = \frac{2\pi}{h} \cdot H_{AD}^2 \cdot \sqrt{\frac{\pi}{\lambda k_B T}} \cdot e^{\left[-\frac{(\lambda+\Delta G^0)^2}{4\lambda k_B T}\right]} \tag{2.1}$$

Harmonic potential energy wells for an exergonic ($\Delta G^0 < 0$) electron transfer reaction are illustrated in Scheme 2.6. For a non-adiabatic reaction, i.e. weak electronic coupling (H_{AD}), the reactant and product parabola remain separate (blue trace). In this case the electron has to overcome the activation barrier ($\Delta G^{\ddagger}$) for its transfer from the reactant state (D-A) to the product state (D^+-A^-). From Scheme 2.6 the reorganization energy of the system, λ, can be interpreted as the energy difference between the reactant and product potential well for the geometrical configuration of the reactant state. For an adiabatic electron transfer, the electronic coupling between the two states is large, and the two parabola can no longer be treated separately. In fact, the activation barrier, derived from the intersection of the two isolated parabola, is no longer applicable. For this case of an adiabatic electron transfer, the semi-classical Marcus-Hush theory (equation 2.1) is no longer appropriate. The systems in this thesis usually undergo non-adiabatic electron transfer. In the following sections, the parameters determining the rate constants of non-adiabatic electron transfer reactions will be discussed in more detail.

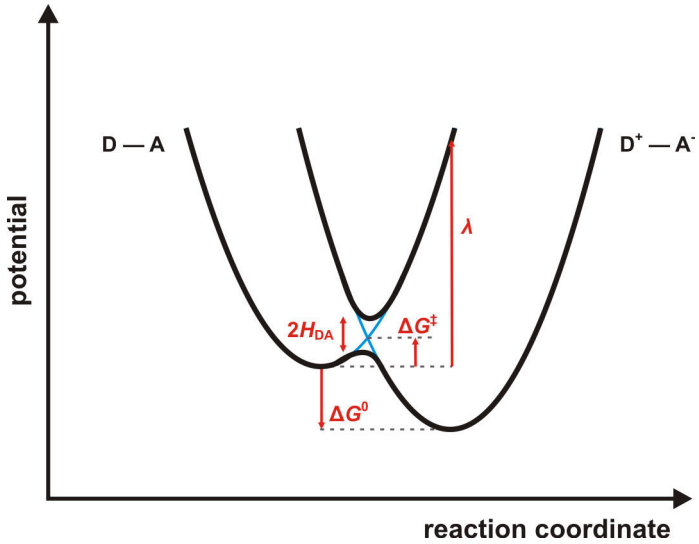

Scheme 2.6 Potential energy wells for an exergonic electron transfer in a D-A system. The blue lines represents the non-adiabatic case, whereas the black parabola depicts adiabatic electron transfer.

Reaction free energy

The energy difference between the reactant and the product state of an electron transfer reaction is the reaction free energy, ΔG^0, or driving force. In Scheme 2.6, an increase in

driving force would lead to a vertical shift of the D^+-A^- state, in consequence, leading to a decreased activation barrier. To obtain a mathematical expression for the relation between $\Delta G^{\ddagger}$ and ΔG^0, as shown in equation 2.2, the reorganization energy of the system needs to be considered as well. The quadratic nature of the expression for the activation energy $\Delta G^{\ddagger}$ causes general implications for electron transfer rates. When assuming a constant reorganization energy, an increase in driving force leads to a decrease in activation energy. In combination with equation 2.1 this results in faster electron transfer rates. This holds true until the reaction free energy equals the reorganization energy ($-\Delta G^0 = \lambda$). In this situation, the electron transfer is activationless ($\Delta G^{\ddagger} = 0$) and the rate constant reaches its maximum. However, a further increase in driving force results in an increase of the activation energy, causing a decrease in electron transfer rate constants. This phenomenon is illustrated in Scheme 2.7. It depicts that an increase in driving force is associated with an increased rate constant in the normal region ($-\Delta G^0 < \lambda$). For the inverted region ($-\Delta G^0 > \lambda$) the opposite holds true. The potential wells shown in Scheme 2.7 visualize this effect.

$$\Delta G^{\ddagger} = \frac{(\Delta G^0 + \lambda)^2}{4\lambda} \tag{2.2}$$

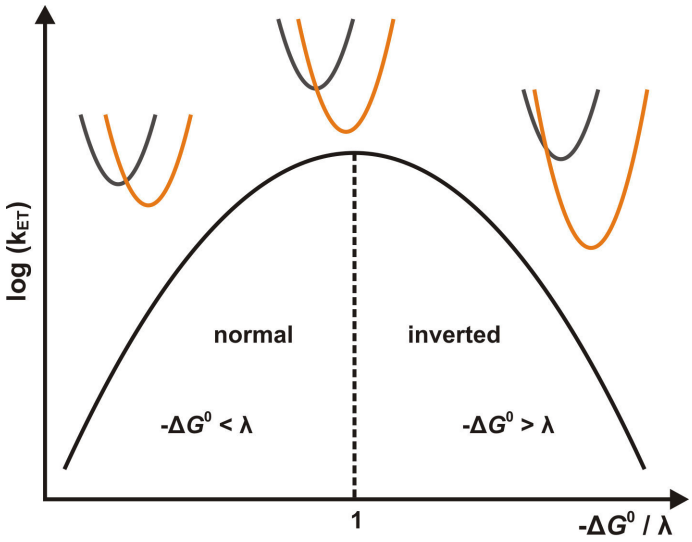

Scheme 2.7 Simplified dependence of the rate constant for electron transfer, k_{ET}, on the driving force, ΔG^0, illustrating the different regions according to the MARCUS theory.

This counter-intuitive phenomenon of an inverted region for electron transfer rates was experimentally confirmed in the 1980s by MILLER and CLOSS,[26–29] more than 20 years after MARCUS had postulated his theory. They studied the intramolecular electron transfer from a biphenyl anion to various acceptors via a rigid bridge, ensuring fixed distances. At large driving forces, a drop in the rate constants was detected and unambiguously assigned to the inverted region of the MARCUS theory.

Reorganization energy

For an electron transfer event to occur, the reactants need to adapt the nuclear geometry of the products, as illustrated in Scheme 2.6. In this context, the reorganization energy, λ, is comprised of an inner and outer-sphere contribution. The inner-sphere reorganization energy, λ_{in}, corresponds to the adjustment of bond lengths and angles and can be calculated by equation 2.3. Hereby, k_{i} are the individual force constants of the normal mode vibrations, and Δq_{i} represents the changes in nuclear configuration of these normal vibrational modes.

$$\lambda_{in} = \tfrac{1}{2} \sum (k_i \cdot \Delta q_i^2) \tag{2.3}$$

$$\lambda_{out} = \tfrac{\Delta e^2}{4\pi\epsilon_0} \cdot \left(\tfrac{1}{2r_A} + \tfrac{1}{2r_D} - \tfrac{1}{R_{DA}} \right) \cdot \left(\tfrac{1}{D_{op}} - \tfrac{1}{D_s} \right) \tag{2.4}$$

In addition to the inner-sphere reorganization, the solvent shell needs to rearrange due to changes in charge distribution. This outer-sphere reorganization energy, λ_{out}, is dependent on the amount of charge, Δe, being transferred (see equation 2.4). Furthermore, the size of the participating redox centers needs to be considered. In the most simple model, the molecules are treated as spherical particles. For small radii of the donor (r_{D}) and the acceptor (r_{A}) the reorganization of the solvent shell is large. For bigger redox centers, the changes in polarization of the solvent upon electron transfer is much weaker. Moreover, the outer-sphere reorganization energy is dependent on the polarity of the solvent, as represented by the optical (D_{op}) and static dielectric constant ($D_{\mathrm{s}} = n^2$, n is the refractive index), and the spatial separation between donor and acceptor (R_{DA}).

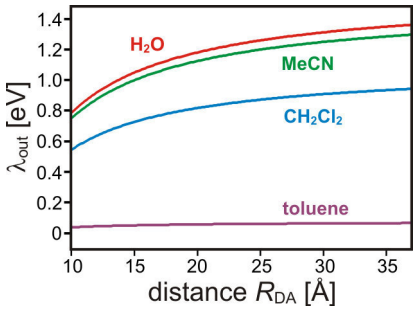

Figure 2.2 Calculated outer-sphere reorganization energies for electron transfer as a function of spatial separation for different solvents according to equation 2.4. The donor and acceptor radii were set to 5 Å.

Figure 2.2 depicts the dependence of λ_{out} as a function of donor-acceptor distance for different solvents, using equation 2.4. Clearly observable from Figure 2.2, the outer-sphere reorganization energy is higher for polar solvents, such as water (red trace) or acetonitrile

(green trace), due to their higher affinity to react to changes in charge distribution. For very apolar solvents such as toluene (purple trace), the reorganization energy is almost neglectable, due to the absence of a significant dipole moment. Furthermore, Figure 2.2 illustrates that the outer-sphere reorganization energy is dependent on the spatial separation between the redox centers. An increase in the donor-acceptor distances results in increasing values for λ_{out}. Hereby, the outer reorganization energy is limited to a saturation value for large separations.

Electronic coupling

The third major contribution to the rate constant as described in equation 2.1 is the electronic coupling between donor and acceptor, i.e. the probability to change to the D^+-A^- state when reaching the crossing point of the two parabola (see Scheme 2.6). In principle, the electronic coupling can be described as the orbital overlap of the donor and the acceptor. This overlap is at its maximum when both reactants are separated only by their Van-der-Waals radius ($H_{AD} = H_{AD,(0)}$). As already mentioned above, for systems with very strong electronic coupling (adiabatic case), a distinct assignment of the electron to the reactant or product state is no longer possible, i.e. the charge is delocalized. A classical example for this situation is the Creutz-Taube ion, a dinuclear ruthenium complex with mixed valences.[30]

$$H_{AD}^2 = H_{AD,(0)}^2 \cdot e^{[-\beta(R_{DA}-\sigma)]} \tag{2.5}$$

For non-adiabatic electron transfer reactions, the electronic coupling between the two reactants is described by equation 2.5. Here, σ is the sum of the hard-sphere radii of the reactants, and β is the distance-decay constant. Equation 2.5 captures the exponential decay of the electronic coupling with increasing D-A distance. Sufficient electronic coupling for large donor-acceptor distances can be achieved by the superexchange mechanism where the intervening medium mediates electronic coupling. Consequently, the distance-decay constant β, a system-specific factor, takes into account the properties of the medium for electron tunneling.

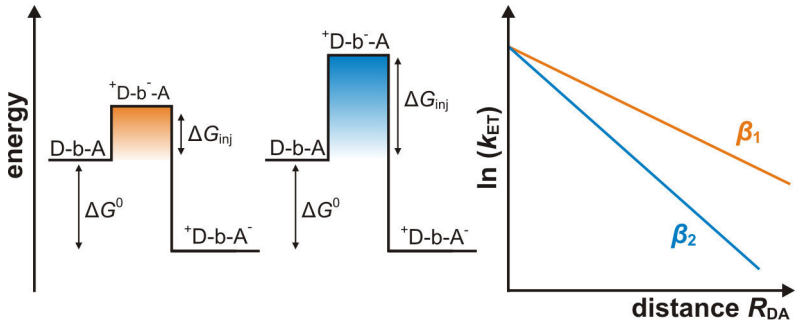

Scheme 2.8 Left: Energy diagram for electron tunneling along bridges with different injection free energies, ΔG_{inj}. Right: The corresponding rate constants for electron transfer as a function of spatial separation. The slopes correspond to the different distance-decay constants β.

In Scheme 2.8 the energy diagram for electron tunneling along two different bridges is shown. In principle, the barrier height for tunneling events corresponds to the injection free energy depicted in Scheme 2.8. This injection free energy, ΔG_{inj}, can be extracted from the reduction potential (or oxidation potential for hole tunneling) of the bridging moiety.[31] The corresponding distance-dependences of electron transfer rate constants with identical reaction free energies but different properties of the bridge are shown in the right part of Scheme 2.8. The slope of the plot of $\ln(k_{\mathrm{ET}})$ as a function of the donor-acceptor distance yields the distance decay constant β. Evidently, for large injection free energies, ΔG_{inj}, the rate constants drop more steeply. Typical values for β are on the order of 0.02 - 0.04 $\mathrm{Å}^{-1}$ for semiconductors, 1.1 $\mathrm{Å}^{-1}$ for proteins, and 1.6 $\mathrm{Å}^{-1}$ for water.[32]

2.4. Proton-coupled electron transfer

Chemical and biological electron transfer processes are often coupled to proton transfer, photosynthesis being an extraordinary relevant example.[11, 33–37] The advantage of the concept of proton-coupled electron transfer (PCET) stems from the fact that charged products of electron transfer events can be stabilized upon uptake or release of a proton, respectively. Additionally, even molecules with very high redox potentials may participate in electron transfer reactions as a consequence of additional driving force gained from the transfer of protons. PCET reactions can occur either bidirectionally, with the electron and proton being transferred into different directions, or in an unidirectional fashion. For the latter, hydrogen atom transfer (HAT) is a special case, where both electron and proton are transferred from a shared orbital to the same accepting orbital. Aside from the question of the electron and proton transfer direction, there are three mechanistically different underlying PCET reactions, as illustrated in Scheme 2.9.

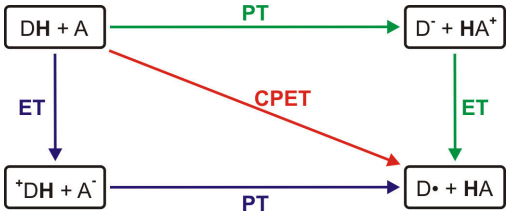

Scheme 2.9 Possible mechanistic pathways for PCET reactions.

Electron and proton transfer can occur either stepwise, or as concerted PCET in a single reaction step, so-called concerted proton-electron transfer (CPET), avoiding charged and highly energetic intermediates (red pathway in Scheme 2.9). The stepwise mechanisms can either occur via initial electron transfer, so called ET-PT (blue pathway in Scheme 2.9), or can be initiated by a proton transfer event, PT-ET (green pathway). For the assignment of a certain mechanism to a particular donor-acceptor system, H/D kinetic isotope effects (KIE) are often considered. Significant KIE values are indicative of the proton transfer step being rate-determining. This is the case for reactions with PT-ET mechanisms, as well as for CPET reactions. However, the absence of a significant H/D kinetic isotope effect can not rule out a CPET mechanism. Even inverse KIEs, with the deuterated analogue exhibiting higher rate constants, have been reported for concerted PCET reactions.[38, 39] In addition to H/D kinetic isotope effects, the determination of a mechanistic pathway can occur on the basis of considering thermodynamic parameters, such as reaction free energies and activation barriers for the individual reaction steps.

With respect to biochemical processes, PCET reactions which occur during photosynthesis are of particular interest for many research groups. In this thesis, the molecular systems designed to investigate certain aspects of PCET reactions were inspired by the $^{+}$P680-Tyr$_{Z}$-His$_{190}$ reaction triple. The underlying PCET chemistry in this natural reaction is most likely a concerted mechanism of electron transfer to the oxidized $^{+}$P680 with the concomitant release of the phenolic proton to the nearby His$_{190}$.[11] Molecular models of this reaction triple have been used to explore properties having an impact on the kinetics of PCET reactions, and in particular on CPET. In this context, the nature of the proton accepting site has been investigated thoroughly. Hereby, the rate constants for PCET were investigated with respect to different proton accepting sites and pH values,[40, 41] proton transfer distances,[42–44] or buffer concentrations.[45] However, the electron transfer distance-dependence for bidirectional concerted proton and electron transfer (CPET) has not yet been explored. Although well understood for pure electron transfer, PCET reactions do not necessarily need to behave the same way. The investigation of this aspect of PCET will be the main subject in Chapter 3 of this thesis.

2.5. Charge accumulation

The aim of many recent studies in photochemistry is the storage of solar energy in chemical bonds, producing so-called solar fuels. Generally, this requires multiple electron transfer events, as demonstrated for water oxidation, hydrogen formation, and CO_2 reduction (Equation 2.6). Especially hydrogen production is of particular interest with respect to a growing demand for energy worldwide. It can be stored, used to run machinery, and its only combustion product is water. In an ideal case, the protons and electrons which are needed for the formation of hydrogen gas, are directly delivered by the oxidation of one of the most abundant raw materials on earth, water.

$$\begin{aligned}
2\,H^+ + 2e^- &\rightarrow H_2 \\
2\,H_2O &\rightarrow 4\,H^+ + 4\,e^- + O_2 \\
CO_2 + 2\,e^- + 2\,H^+ &\rightarrow HCOOH \\
CO_2 + 4\,e^- + 4\,H^+ &\rightarrow HCHO + H_2O \\
CO_2 + 6\,e^- + 6\,H^+ &\rightarrow CH_3OH + H_2O \\
CO_2 + 8\,e^- + 8\,H^+ &\rightarrow CH_4 + 2\,H_2O
\end{aligned} \tag{2.6}$$

One of the first catalytic systems for light-driven water splitting into H_2 and O_2 was reported by Grätzel almost 40 years ago.[46] In this heterogeneous approach, a $Ru(bpy)_3{}^{2+}$ photosensitizer is oxidized by methylviologen (MV^{2+}) upon visible light irradiation. On the reductive site of this catalytic cycle, the photo-generated MV^+ transfers its excess electron to colloidal platinum, which acts as a potent catalyst for hydrogen formation. On the other side, $Ru(bpy)_3{}^{3+}$ oxidizes RuO_2 particles, which were employed as the water oxidation catalyst. The overall catalytic cycle is shown in Scheme 2.10. The quantum efficiency is limited in this system, due to bimolecular charge recombination processes. Nevertheless, it proves the feasibility of artificial photosynthesis.

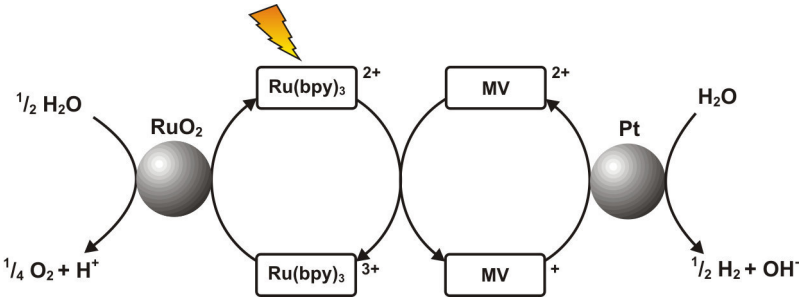

Scheme 2.10 Heterogeneous catalytic system for the light-driven water splitting into H_2 and O_2, developed by Grätzel.[46]

More recently, the research focus turned towards the fundamental investigation of charge accumulation, as the core piece of the conversion of light to chemical energy. In this

context, donor-acceptor assemblies are widely used, since their properties can be adjusted and usually their reaction kinetics can be readily determined. Furthermore, by linking the photosensitizer directly to the charge accumulating site, usually higher quantum efficiencies compared to bimolecular systems can be reached. In the following section selected charge accumulating systems will be introduced.

MacDonnell and coworkers reported on binuclear complexes based on $Ru(phen)_3^{2+}$ (phen = 1,10-phenanthroline) bridged by a tetraazatetrapyridopentacene (tatpp) ligand (Figure 2.3).[47–49] After excitation of the complex with visible light to the ^{3}MLCT state, the central bridging ligand gets reduced. In presence of triethanolamine as sacrificial agent, the oxidized metal center gets re-reduced with subsequent excitation leading to charge accumulation on the tatpp ligand. With additional acid present in solution, visible light irradiation leads to proton-coupled multiple-electron transfer. Hereby, the central ligand accepts two electrons and two protons, which corresponds formally to the storage of H_2.

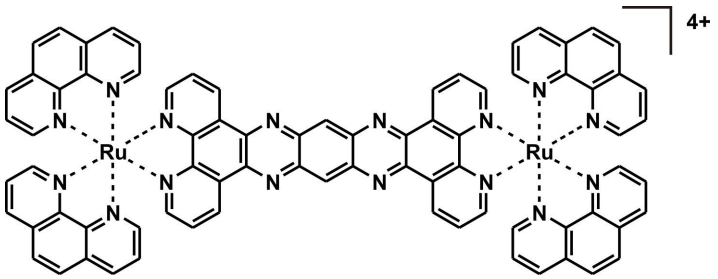

Figure 2.3 Dinuclear ruthenium(II) complex with a bridging tetraazatetrapyridopentacene (tatpp) ligand, capable to perform light-induced charge accumulation in the presence of sacrificial donors. Additional acid results in transfer of two electrons and two protons, formally H_2, to the central ligand.[47–49]

Recently, Hammarström and Odobel reported on a ruthenium(II) dyad bearing an oligotriarylamine (OTA) as a potent multi-electron donor.[50, 51] This dyad was attached to a TiO_2 nanoparticle (see Figure 2.4) and resembles constructs which are widely used in the field of dye-sensitized solar cells. Upon excitation with two laser pulses at 480 nm delayed by 1 µs, twofold oxidized oligotriarylamine was unambiguously observed by means of transient absorption spectroscopy. The same observation was made when excitation occurred with a single 10 ns laser pulse of high intensity. Charge injection into the TiO_2 nanoparticle is extremely fast, producing the first and second charge separated states. In contrast, reverse electron transfer is comparably slow, leading to the situation that absorption of two photons results in charge accumulation with almost quantitative efficiency. Noteworthy, the spectral features of OTA^{2+} were observed up to delay times of at least 100 µs, which is comparable to the timescale of turnover rates in enzymatic

systems, e.g. water oxidation in PS II.

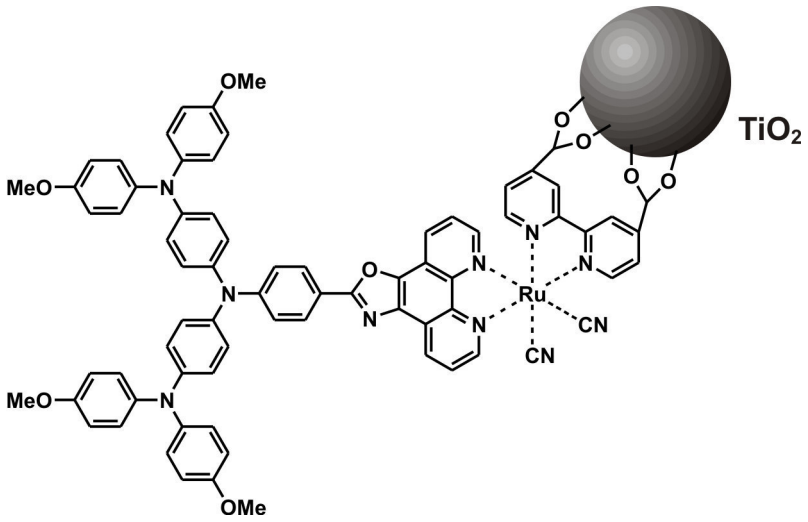

Figure 2.4 Ruthenium(II)-oligotriarylamine dyad attached to a TiO_2 nanoparticle for photoinduced charge accumulation.[50, 51]

Early approaches on light-driven charge accumulation were based on entirely molecular systems and did not even rely on any sacrificial agents. In 1992 Wasielewski and coworkers reported on accumulation of two electrons on a perylenebis(dicarboximide) (PBDCI), which is attached to two porphyrin photosensitizers, as shown in Figure 2.5.[52] Intensity-dependent excitation experiments revealed the formation of $PBDCI^{2-}$ at high pulse energies. In a similar approach, with zinc porphyrins and a central tetracyanoanthraquinodimethane (TCAQ), reported by Imahori and Sakata, twofold reduction of the central electron accepting site was observed as well.[53] Although both systems do not need any sacrificial agents to perform charge accumulation, they lack of long-living photoproducts. Thermal back electron transfer in these charge-accumulated states was found to occur within a few nanoseconds.

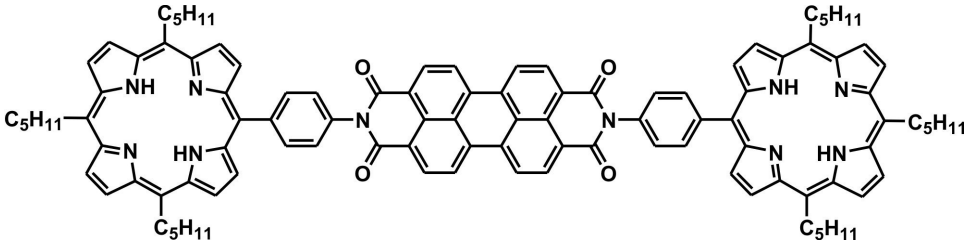

Figure 2.5 Porphyrin-based donor-acceptor-donor triad for photoinduced charge-accumulation at the central perylenebis(dicarboximide) without using sacrificial agents.[52]

The abovementioned examples show that charge accumulating systems driven by light either involve nanoparticels, sacrificial agents, or short lifetimes of the charge-separated

states. A purely molecular system that does not rely on sacrificial agents and exhibits long lifetimes for the charge accumulated state has not yet been reported. In such a system, new unproductive deactivation processes need to be considered that might hamper charge accumulation. The generic energy diagram for an exemplary donor-photosensitizer-acceptor assembly (D-P-A) in Scheme 2.11 illustrates that after formation of the first charge-separated state and subsequent absorption of a second photon, several deactivation pathways are possible. In fact, the excited photosensitizer is both a strong oxidant and reductant, which might result in the re-oxidation of A^-, or re-reduction of D^+, respectively. Additionally, the twofold reduced acceptor can easily undergo charge recombination with the oxidized photosensitizer to the first charge-separated state (D^+-P^+-A^{2-} $\rightarrow$ D^+-P-A^-). Of course, the same holds true for a twofold oxidized donor and a reduced photosensitizer, respectively (D^{2+}-P^--A^- $\rightarrow$ D^+-P-A^-). Not illustrated in Scheme 2.11 is the additional possibility of energy transfer from the excited photosensitizer P* to the neighboring oxidized donor or reduced acceptor. The electron donating and accepting sites, in singly charge-separated states, are usually organic molecules or metal complexes in their doublet states. Triplet-doublet energy transfer has been observed in other systems and therefore needs to be considered as a possible deactivation process.[54–56]

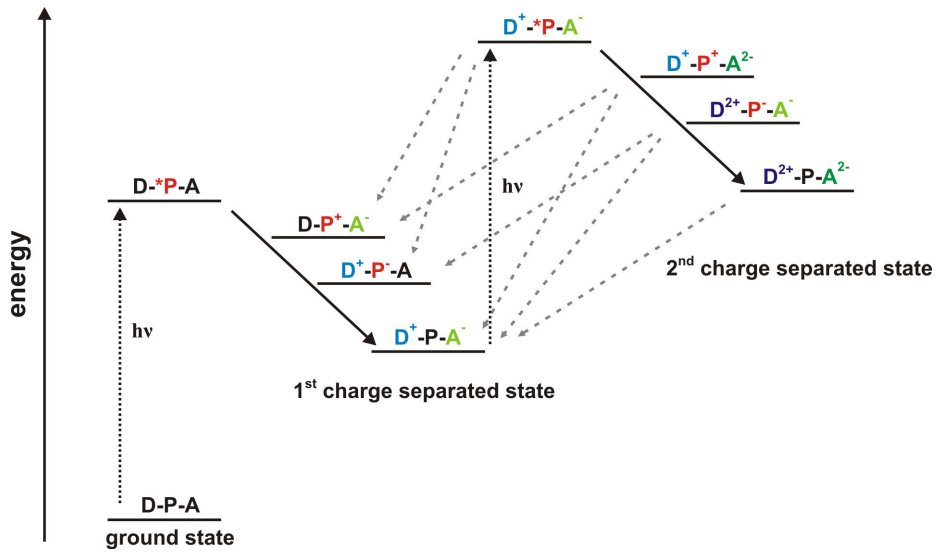

Scheme 2.11 Energy diagram for a donor-photosensitizer-acceptor assembly (D-P-A) undergoing charge accumulation. Unproductive recombination processes are marked by dashed gray arrows.

In addition to the competing unproductive reaction pathways, the accumulation of charge on a small molecule causes electrostatic repulsion. The second oxidation of the donor or reduction of the acceptor, is significantly more difficult than the first and requires a higher potentials. In contrast, the redox potential of the excited photosensitizer does not change. As a consequence, the redox potentials of the corresponding singly and multiply

charged species need to be in a narrow potential range in order to perform a second charge separation. However, these electrostatic repulsions can be compensated be coupling charge accumulation with proton transfer reactions, as seen in the OEC of photosystem II, and as demonstrated in Chapter 5 of this thesis.

3. Studies of Proton-Coupled Electron Transfer

Proton-coupled electron transfer (PCET) is an elementary reaction in many chemical and biological processes. For example, it is of key importance for water oxidation or carbon dioxide reduction as noted in the introductory chapter of this thesis. Consequently, understanding PCET at the most fundamental level is desirable.[33, 36, 57, 58] As already mentioned in Chapter 2, the studies concerning proton-coupled electron transfer in this thesis do mainly focus on the mechanisms and kinetics of PCET reactions as a function of electron transfer distance. In this context, the following papers were published during these PhD studies.

- Kuss-Petermann, M.; Wolf, H.; Stalke, D.; Wenger, O. S. "Influence of Donor-Acceptor Distance Variation on Photoinduced Electron and Proton Transfer in Rhenium(I)-Phenol Dyads". *J. Am. Chem. Soc.* **2012**, *134*, 12844.
- Kuss-Petermann, M.; Wenger, O. S. "Photoacid Behavior versus Proton-Coupled Electron Transfer in Phenol–$Ru(bpy)_3^{2+}$ Dyads". *J. Phys. Chem. A* **2013**, *117*, 5726.
- Chen, J.; Kuss-Petermann, M.; Wenger, O. S. "Distance Dependence of Bidirectional Concerted Proton–Electron Transfer in Phenol-Ru(2,2'-bipyridine)$_3^{2+}$ Dyads". *Chem. Eur. J.* **2014**, *20*, 4098.
- Chen, J.; Kuss-Petermann, M.; Wenger, O. S. "Dependence of Reaction Rates for Bidirectional PCET on the Electron Donor–Electron Acceptor Distance in Phenol–Ru(2,2′-Bipyridine)$_3^{2+}$ Dyads". *J. Phys. Chem. B* **2014**, *119*, 2263.

In analogy to the $^{+}$P680-Tyr$_Z$-His$_{190}$ reaction triple, two series of molecular dyads of variable donor-acceptor distance were synthesized and investigated with respect to the photoinduced PCET reactivity. These dyads are shown in Figure 3.1 and are comprised of a photosensitizer, either $[Ru(bpy)_3]^{2+}$ or $[Re(phen)(CO)_3(py)]^{+}$ (phen = 1,10-phenanthroline, py = pyridine), that is covalently linked to a phenol via varying numbers of *p*-xylene bridging units (n = 0 - 3).

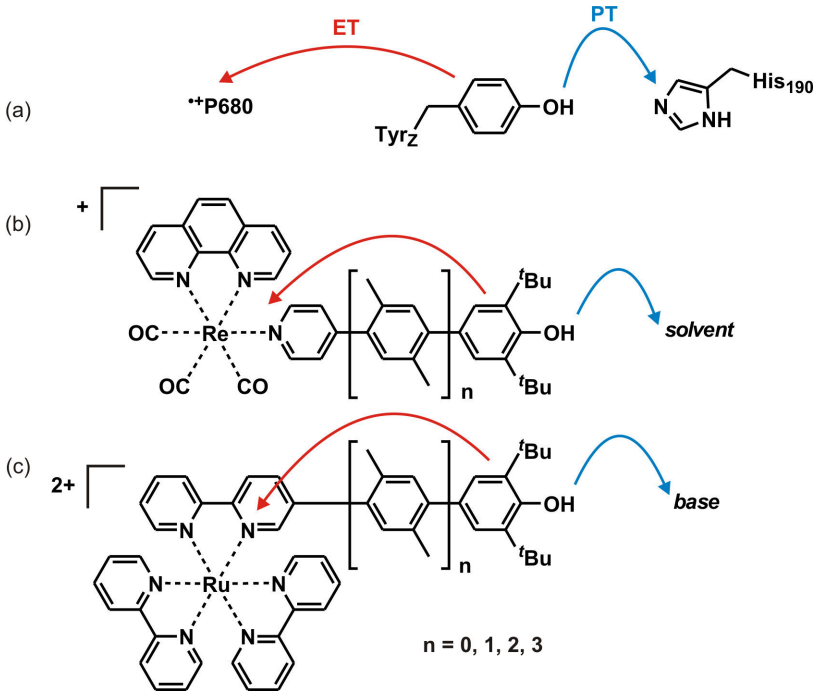

Figure 3.1 (a) $^{+}$P680-Tyr$_Z$-His$_{190}$ reaction triple from photosystem II. (b) Rhenium(I)-phenol and (c) ruthenium(II)-phenol dyads which were investigated in this work with respect to their PCET reactivity as a function of electron transfer distance.

The studies revealed a mechanistic changeover as a function of donor-acceptor distances. When the phenol donor is linked directly to the photosensitizer (n = 0), no PCET reaction was observed. In fact, these dyads showed photoacid behavior, i.e. release of the phenolic proton is directly coupled to recombination of the excited state of photosensitizer to the ground state. In contrast, when increasing the spatial separation (n $\geq$ 1), proton-coupled electron transfer reactivity was observed instead of photoacid behavior. In acetonitrile/water 1:1 (v:v) mixture the rhenium(I)-phenol dyads with n $\geq$ 1 exhibit a step-wise PCET mechanism involving electron transfer from the phenol to the excited metal center, followed by release of the phenolic proton to the solvent. However, the PCET mechanism that is operative in the ruthenium(II)-phenol dyads (n $\geq$ 1) in dichloromethane with additional pyridine as the proton accepting site, was found to be CPET. The initially formed phenoxyl radical subsequently undergoes very fast back electron transfer and was therefore spectroscopically not observed. The observation of concerted proton-coupled electron transfer in the ruthenium dyads allowed to investigate the kinetics of CPET as a function of electron transfer distance for the first time. Based on transient absorption experiments conducted with the ruthenium(II)-phenol dyads (n = 1 - 3) in acetonitrile in the presence of pyrrolidine, a distance-decay constant of $\beta = 0.67 \pm 0.23$ Å^{-1} was determined. In addition, experiments were conducted with methylviologen (MV^{2+}) as an external electron acceptor. Under these experimental conditions the ruthenium(II) trans-

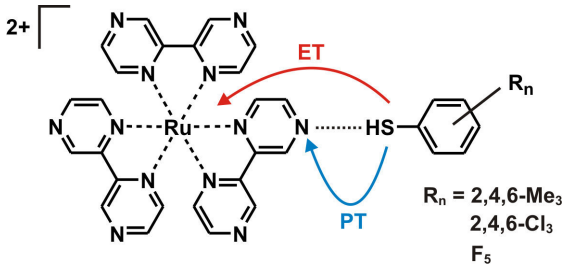

Figure 3.2 Thiophenol/Ru(bpz)$_3^{2+}$ (bzp = 2,2'-bipyrazine) reaction couples for mechanistic PCET studies.

fers an electron to MV^{2+} upon excitation, yielding a strongly oxidizing ruthenium(III) species. This photo-generated Ru(bpy)$_3^{3+}$ in return was reduced by the attached phenol with concerted release of the phenolic proton to imidazole, which was added as a proton acceptor. From this study a distance-decay constant of $\beta = 0.87 \pm 0.09$ Å^{-1}was extracted. Both obtained values are very similar to previously reported β values of 0.77 Å^{-1} and 0.52 Å^{-1} for pure electron transfer along *p*-xylene bridges.[59, 60] These observations point towards a dominant influence of the distance dependence of the electron transfer step on the overall electronic matrix coupling element for bidirectional CPET.

In a separate project the PCET reactivity of thiophenols was investigated. The PCET processes associated with phenol oxidation has been the subject of numerous studies over the past years.[61–66] In contrast, similarly detailed mechanistic investigations of thiophenols are relatively rare, although thiols and thiyl radicals are known to play an important role in biochemical processes.[67, 68] In this study three different thiophenols, ranging from electron-rich 2,4,6-trimethylthiophenol via moderately electron deficient 2,4,6-trichlorothiophenol to electron-poor pentafluorothiophenol, were investigated with respect to their PCET reactivity with ^{3}MLCT-excited Ru(bpz)$_3^{2+}$ (bpz = 2,2'-bipyrazine). The latter served as a combined electron and proton acceptor (see Figure 3.2). The results were published during these PhD studies.

- Kuss-Petermann, M.; Wenger, O. S. "Mechanistic Diversity in Proton-Coupled Electron Transfer between Thiophenols and Photoexcited [Ru(2,2´-Bipyrazine)$_3$]$^{2+}$". *J. Phys. Chem. Lett.* **2013**, *4*, 2535.

It was demonstrated that dependent on the nature of the substituents on the thiophenol, all three possible mechanisms of PCET (see Scheme 2.9) can be observed. For the electron-rich 2,4,6-trimethylthiophenol stepwise PCET involving oxidation followed by proton transfer to the reduced photosensitizer was observed. In contrast, the electron-poor, but acidic, pentafluorothiophenol reacts via proton transfer to the excited Ru(bpz)$_3^{2+}$ with subsequent rapid oxidation of the formed thiolate. Furthermore, the investigations strongly suggest that the moderately electron deficient 2,4,6-trichlorothiophenol is oxidized in concert with proton transfer. Accordingly, the full spectrum of possible PCET

mechanisms was observed for these compounds. Generally, the S-H bond dissociation free energy (BDFE) of thiophenols is significantly smaller than the O-H BDFE of regular phenols. In principle, a smaller DBFE results in a higher tendency towards a CPET mechanism. However, thiophenols are usually oxidized more easily. In combination with their higher acidity, the stepwise PCET mechanisms (ET-PT and PT-ET) become more probable. These opposing trends results in the full spectrum of possible PCET mechanisms being observed in this study.

Author contributions

M.K.-P. carried out molecular design, synthesis, data analysis and contributed equally to the system designs and the preparation of the manuscripts. He also conducted the measurements for *J. Am. Chem. Soc.* **2012**, *134*, 12844, *J. Phys. Chem. A* **2013**, *117*, 5726, *J. Phys. Chem. Lett.* **2013**, *4*, 2535.

H.W. and D.S. provided the crystal structure in .*J. Am. Chem. Soc.* **2012**, *134*, 12844.

J.C. conducted measurements, carried out data analysis and contributed equally to the preparation of the manuscripts for *Chem. Eur. J.* **2014**, *20*, 4098, *J. Phys. Chem. B* **2014**, *119*, 2263.

O.W. contributed equally to the systems designs, data analysis and interpretation and the preparation of the manuscripts.

It has to be noted that the synthesis of the dyads and preliminary measurements on the rhenium(I)-phenol dyads (relevant for: *J. Am. Chem. Soc.* **2012**, *134*, 12844 *J. Phys. Chem. A* **2013**, *117*, 5726, *Chem. Eur. J.* **2014**, *20*, 4098, *J. Phys. Chem. B* **2014**, *119*, 2263) has already been conducted by M.K.-P in his diploma thesis.[69]

JACS
JOURNAL OF THE AMERICAN CHEMICAL SOCIETY
Article
pubs.acs.org/JACS

Influence of Donor–Acceptor Distance Variation on Photoinduced Electron and Proton Transfer in Rhenium(I)–Phenol Dyads

Martin Kuss-Petermann, Hilke Wolf, Dietmar Stalke, and Oliver S. Wenger*

Institut für Anorganische Chemie, Georg-August-Universität Göttingen, Tammannstrasse 4, D-37077 Göttingen, Germany

Supporting Information

ABSTRACT: A homologous series of four molecules in which a phenol unit is linked covalently to a rhenium(I) tricarbonyl diimine photooxidant via a variable number of *p*-xylene spacers (n = 0–3) was synthesized and investigated. The species with a single *p*-xylene spacer was structurally characterized to get some benchmark distances. Photoexcitation of the metal complex in the shortest dyad (n = 0) triggers release of the phenolic proton to the acetonitrile/water solvent mixture; a H/D kinetic isotope effect (KIE) of 2.0 ± 0.4 is associated with this process. Thus, the shortest dyad basically acts like a photoacid. The next two longer dyads (n = 1, 2) exhibit intramolecular photoinduced phenol-to-rhenium electron transfer in the rate-determining excited-state deactivation step, and there is no significant KIE in this case. For the dyad with n = 1, transient absorption spectroscopy provided evidence for release of the phenolic proton to the solvent upon oxidation of the phenol by intramolecular photoinduced electron transfer. Subsequent thermal charge recombination is associated with a H/D KIE of 3.6 ± 0.4 and therefore is likely to involve proton motion in the rate-determining reaction step. Thus, some of the longer dyads (n = 1, 2) exhibit photoinduced proton-coupled electron transfer (PCET), albeit in a stepwise (electron transfer followed by proton transfer) rather than concerted manner. Our study demonstrates that electronically strongly coupled donor–acceptor systems may exhibit significantly different photoinduced PCET chemistry than electronically weakly coupled donor–bridge–acceptor molecules.

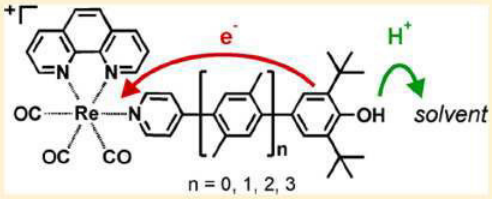

■ INTRODUCTION

Proton-coupled electron transfer (PCET) is an important elementary step in many biochemical processes, photosynthesis being a particularly relevant example.[1−8] If we are to emulate natural photosynthesis in artificial systems, a thorough understanding of all factors governing PCET rates and efficiencies appears indispensable. Although fundamental aspects of PCET chemistry can be investigated directly on suitable enzymes, the use of chemically simpler artificial molecular models is very popular.[9] Phenols are attractive in this context because their hydroxylic proton becomes highly acidic upon oxidation,[10,11] allowing these molecules to act as combined electron/proton donors.[12−14] Certain phenol systems can be viewed as models for the Tyr_Z/His-190 PCET interface in photosystem II (Scheme 1a):[13,15−29] light absorption by chlorophyll leads to the formation of a highly oxidizing porphyrin molecule ($P_{680}^{\bullet+}$) that is reduced by Tyr_Z, and presumably this is coupled to transfer of the phenolic proton to the nearby His-190 base.[6,30] A central question of many fundamental PCET investigations is whether the overall reaction is a concerted process or proceeds by individual electron- and proton-transfer steps. Many phenol-containing systems react via concerted proton–electron transfer (CPET),[13,15−29] but stepwise mechanisms in which initial electron transfer is followed by proton transfer (ETPT) have also been reported.[31−33] Some aspects regarding the PCET chemistry of phenols have received particular attention in recent years, such as the influence of solvent pH on driving forces and rates, the importance of buffer ions as proton acceptors, and the special role played by water as a medium in which PCET takes place.[34−39]

It is not uncommon for the participating electron to be transferred over a significantly longer distance than the proton

Scheme 1. (a) PCET between the $Tyrosine_Z$, $Histidine_{190}$, and Chlorophyll P_{680} Components of Photosystem II; (b) Rhenium(I) Tricarbonyl Photosensitizers with Appended 2,6-Di-*tert*-butylphenol Units Investigated in This Work (n = 0–3)

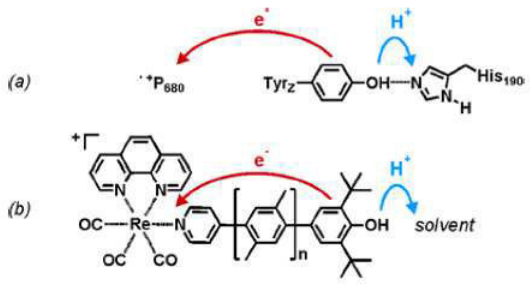

Received: June 1, 2012
Published: July 18, 2012

dx.doi.org/10.1021/ja3053046 | J. Am. Chem. Soc. 2012, 134, 12844−12854

during the course of a PCET reaction. There are systems in which the CPET mechanism is dominant even though electron donor and electron acceptor are separated by more than 6 Å. However, while the distance dependence of pure electron transfer has long been studied,[40,41] the distance dependence of PCET is yet poorly explored and has only recently come into the focus of attention.[42−45] PCET has in fact four relevant distances, namely, the electron- and proton-transfer distances and the separations between the proton and the electron in the donor and the acceptor. Here we focus on the influence of the distance between the proton- and electron-accepting units in bidirectional (multisite) PCET with the rigid rodlike molecules shown in Scheme 1b. 2,6-Di-*tert*-butylphenol (PhOH) serves as a combined electron−proton donor, a tricarbonyl(phenanthroline)(pyridine)rhenium(I) complex (Re) is the photooxidant, and a solvent molecule in the immediate neighborhood of the phenol acts as the proton acceptor. The distance between the two redox partners was varied from 7.9 to 20.8 Å through the introduction of one, two, or three *p*-xylene (xy) units, leading to a simultaneous increase in the distance between the electron-accepting center and the proton-accepting site. These molecules can be viewed as functional models for the Tyr_Z/His-190/P_{680} reaction triple of photosystem II.

■ RESULTS AND DISCUSSION

Synthesis and X-ray Crystal Structure. The synthesis of the molecules from Scheme 1b was performed in a modular fashion as described previously by us for analogous rhenium/ruthenium−(oligo-*p*-xylene)−phenothiazine systems.[46−50] Detailed synthetic protocols and molecule characterization data are given in the Supporting Information. The result of an X-ray crystal structure analysis of Re−xy_1−PhOH is shown in Figure 1.

Figure 1. Crystallographic structure of the Re−xy_1−PhOH cation. Anisotropic displacement parameters are drawn at the 50% probability level. Hydrogen atoms, anions, and cocrystallized solvent molecules have been omitted.

Re−xy_1−PhOH crystallizes in the monoclinic space group *C*2/*c* with a single molecule in the asymmetric unit containing the Re−xy_1−PhOH unit and the triflate counterion. Additionally, a dichloromethane and a disordered diethyl ether solvent molecule are present in the asymmetric unit. As shown in Figure 1, the Re atom is coordinated by three carbonyl, one pyridine, and one phenanthroline ligand to form an almost perfect octahedral coordination polyhedron. While the equatorial positions are occupied by two carbonyls and the phenanthroline ligands, the perfect square is only slightly distorted, with the N3−Re−N2 angle being the smallest at 75.94° and the N2−Re−C40 angle being the largest at 97.26° (Table 1). At one of the axial positions is a carbonyl group,

Table 1. Selected Bond Lengths and Angles

bond	bond length (Å)	angle unit	bond angle (deg)
Re1−N1	2.205(2)	N2−Re1−N3	75.94(9)
Re1−N2	2.181(3)	C42−Re1−C40	91.86(14)
Re1−N3	2.175(3)	N2−Re1−C40	97.26(12)
Re1−C40	1.920(4)	N3−Re1−C42	94.98(12)
Re1−C41	1.928(3)	C41−Re1−N1	92.25(11)
Re1−C42	1.912(3)		

while the other vertex is formed by the pyridine−xy_1−PhOH entity. The C41−Re−N1 unit forms an almost perfectly linear arrangement, with an angle of 177.72°. Regarding the Re−N bonds, one finds the axial Re−N bond to be slightly elongated compared with the equatorial ones (2.205 Å vs 2.175/2.181 Å, respectively). Thus, the bond lengths vary within the expected range. The three Re−CO bonds are almost all of the same length, showing no elongation in the axial position.

The most important piece of information that can be extracted from this structure is that the distance between the center of the phenol and the rhenium atom is 12.2 Å, corresponding to the center-to-center electron-transfer distance in this compound. One further extracts a length of 4.3 Å for a xylene repeating unit, and we thus conclude that the electron donor−acceptor distances (R_{DA}) in Re−xy_0−PhOH, Re−xy_2−PhOH, and Re−xy_3−PhOH are 7.9, 16.5, and 20.8 Å, respectively. In the structure of Re−xy_1−PhOH, the dihedral angle between the phenol and xylene planes (57°) and that between the xylene and pyridine planes (41°) are in the typical range for oligo-*p*-phenylene systems.[51−54] However, while the magnitude of these torsion angles has an important influence on the electronic coupling between the donor and acceptor,[55−57] little can be learned from the solid-state structure regarding the situation in solution.

Optical Absorption and Emission. Figure 2a shows the UV−vis spectra of the four molecules from Scheme 1b (solid lines) in acetonitrile solution. The purple dashed line is the spectrum of the trifluoromethanesulfonate salt of $[Re(phen)(CO)_3(py)]^+$ (phen = 1,10-phenanthroline; py = pyridine), which was used as a reference complex (hereafter called "Re-ref") incapable of exhibiting any PCET, proton transfer, or intramolecular electron transfer reactivity. All five absorption spectra show a prominent absorption maximum at 275 nm due to a phenanthroline-localized $\pi-\pi^*$ transition.[58,59] In the spectrum of Re−xy_0−PhOH there is a band maximum at 323 nm due to a transition with phenol-to-pyridine charge transfer (CT) character.[60] The intensity of this band decreases rapidly with increasing donor−acceptor distance, already being noticeable merely as a shoulder in the spectrum of Re−xy_1−PhOH. This is an important observation because it demonstrates how rapidly the electronic communication between PhOH and Re decreases as a function of distance; on the other hand, this observation is not much of a surprise, given the known exponential distance dependence of superexchange interactions and the fact that a *p*-xylene spacer has a length of ~4.3 Å.[41,61,62]

Bridge lengthening was further observed to lead to increasing extinction at wavelengths shorter than 350 nm, which can be explained by increasing π conjugation between mutually connected phenol, *p*-xylene, and pyridine units. As is commonly the case for rhenium(I) tricarbonyl diimines, metal-to-ligand charge transfer (MLCT) absorptions occur at ~380 nm.[58]

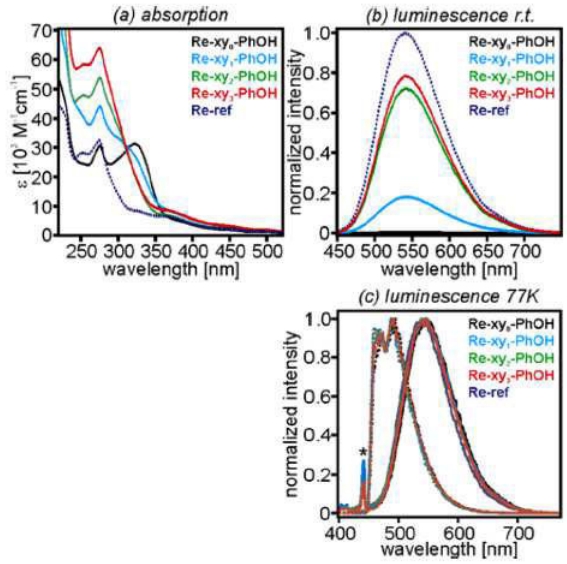

Figure 2. (a) Optical absorption spectra of the four molecules from Scheme 1b and a reference complex in acetonitrile solution. (b) Normalized luminescence spectra of the same compounds in 1:1 (v/v) acetonitrile/water at 25 °C. Excitation occurred at 410 nm. It should be noted that the emission spectrum of Re−xy_0−PhOH almost coincides with the *x* axis. (c) Normalized luminescence spectra of the same compounds in MTHF at room temperature (solid lines) and at 77 K (dashed lines). Excitation occurred at 410 nm. The asterisk in (c) denotes Raman scattering peaks.

Figure 2b shows that the lowest-lying ^{3}MLCT states are emissive in all five compounds in 1:1 (v/v) acetonitrile/water solution, albeit with significantly different luminescence quantum yields. Following excitation at 410 nm with corrections for differences in absorbance between individual solutions at this wavelength, the strongest emission was observed for the reference complex, while the luminescence of the Re−xy_n−PhOH molecules became weaker with decreasing donor−acceptor distance (decreasing *n*). For *n* = 0, the emission spectrum almost coincided with the *x* axis. We note that in the protic CH_3CN/H_2O mixture considered here, the luminescence lifetime of Re−xy_0−PhOH is much shorter than that of Re-ref (40 vs 1270 ns; see below), so the intensity and lifetime decreases go hand in hand when CH_3CN is mixed with H_2O. The observation of increasing luminescence quenching with decreasing *n* signals the presence of a nonradiative excited-state deactivation process that is dependent on the phenol−rhenium distance. Emission quenching by triplet−triplet energy transfer can be ruled out on thermodynamic grounds: the $[Re(phen)(CO)_3(py)]^+$ complex has a triplet energy (E_T) of ~2.75 eV,[63] while (unsubstituted) phenol has E_T = 3.55 eV[64] and the *p*-xylene units can be expected to have even higher triplet energies.[65] Consequently, the emission quenching observed in Figure 2b is most likely due to either photoinduced electron transfer, proton transfer, or a combination of the two (PCET).

Given the observation of strong rhenium(I)−phenol coupling in Re−xy_0−PhOH, we performed low-temperature emission experiments in order to test whether the emissive excited state is indeed the same in all four dyads. Figure 2c shows the results from experiments in which 10^{-5} M solutions of the dyads in 2-methyltetrahydrofuran (MTHF) were excited at 390 nm at room temperature (solid lines) and at 77 K as frozen solutions (dashed lines). The four emission spectra were normalized arbitrarily to an intensity of 1.0 at the emission band maximum for better direct comparison. This procedure made it obvious that the four emission bands are virtually identical, and one may conclude that the emissive excited state is the same in all four dyads, at least at 77 K. However, the relative energies of excited states of rhenium(I) tricarbonyl diimines can change in going from fluid solutions to rigid glasses,[58] so we cannot know for sure whether at 298 K the conclusion from above still holds true. On the other hand, there was no evidence for a rigidochromic effect in our systems. The observation of vibrational fine structure in 77 K emission spectra is common for rhenium(I) tricarbonyl diimines and signals the participation of intraligand ($\pi-\pi^*$) states in the low-temperature luminescence.[58,59]

Cyclic Voltammetry. The electrochemical potentials of the redox-active phenol and rhenium(I) units in the four dyads from Scheme 1b were determined using cyclic voltammetry. The actual voltammograms are shown in the Supporting Information; here we merely report the redox potentials as determined in dry acetonitrile solution in the presence of 0.1 M tetrabutylammonium hexafluorophosphate ($TBAPF_6$) as the electrolyte (Table 2).

The first thing we note is that the phenol oxidations are irreversible, as frequently observed for phenols.[10] In this situation, we estimated the half-wave potential from the inflection point occurring in the rise of the respective redox wave when sweeping from low to high potential. There appeared to be no dependence of the redox potentials determined in this manner on the potential sweep rate, at least not in the range between 10 and 300 mV/s.

Table 2. Center-to-Center Electron Donor−Acceptor Distances (R_{DA}), Electrochemical Potentials, and Driving Forces for Photoinduced Electron Transfer (ΔG_{ET}) in the Four Dyads from Scheme 1b

		electrochemical potentials (V vs Fc^+/Fc)[a]			
dyad	R_{DA} (Å)	$E(PhOH/PhOH^+)$	$E(PhO^-/PhO^\bullet)$	$E(Re^I/Re^0)$	ΔG_{ET} (eV)
Re−xy_0−PhOH	7.9	1.20	−0.28	−1.57	+0.00
Re−xy_1−PhOH	12.2	1.01	−0.59	−1.54	−0.20
Re−xy_2−PhOH	16.5	0.98	−0.64	−1.54	−0.22
Re−xy_3−PhOH	20.9	0.99	−0.63	−1.54	−0.21

[a] $E(PhOH/PhOH^+)$ is the electrochemical potential for oxidation of the phenol component in the dyads, $E(PhO^-/PhO^\bullet)$ is the potential for oxidation of the deprotonated form of the phenol, and $E(Re^I/Re^0)$ is the electrochemical potential for reduction of the rhenium(I) unit in the four dyads. The electrochemical potentials were measured in dry acetonitrile solution containing 0.1 M $TBAPF_6$. See the Supporting Information for the voltammograms.

The shortest member (Re–xy_0–PhOH) stands out from the dyad series in that it exhibits a phenol oxidation potential that is markedly different from those of the three longer congeners (Re–xy_{1-3}–PhOH). Oxidation of the 2,6-di-*tert*-butylphenol unit in Re–xy_0–PhOH occurs at a potential of 1.2 V vs Fc^+/Fc, while in the Re–xy_{1-3}–PhOH dyads, potentials of only ~1.0 V vs Fc^+/Fc are necessary (Figure S1 in the Supporting Information). This is yet another manifestation of the stronger interaction of the phenol with its neighboring molecular units in Re–xy_0–PhOH compared with the longer dyads (in addition to the observation of phenol-to-pyridine CT absorption bands in Re–xy_0–PhOH,[60] as described above). We initially presumed that because of the proximity of the cationic rhenium(I) complex, the phenol unit in Re–xy_0–PhOH is oxidized less readily than in the longer congeners, where the electrostatic influence from the metal site is expected to be weaker. However, cyclic voltammetry of the free pyridine–xy_n–PhOH ligands (Figure S3 in the Supporting Information) revealed that this is not primarily an electrostatic effect, as the observed difference of ~0.2 V between the phenol oxidation potentials of the free ligands was similar to that between Re–xy_0–PhOH and Re–xy_{1-3}–PhOH. It appears plausible that the true physical origin of this 0.2 V potential shift is a strong electronic interaction between phenol and pyridine when these two units are coupled directly to one another. The reason for this may be the electron-withdrawing character of pyridine.

Upon deprotonation of the phenol units by the addition of sodium methoxide, the resulting phenolate moieties are oxidized at −0.28 V vs Fc^+/Fc in Re–xy_0–PhO^- and at about −0.6 V vs Fc^+/Fc in Re–xy_{1-3}–PhO^-, again showing a substantial difference between the shortest member and the longer members of the series (Table 2, fourth column). An analogous observation was made for the free ligands (Figure S4 in the Supporting Information). For the shortest deprotonated ligand, one may draw two resonance structures (Scheme 2),

Scheme 2. Two Resonance Structures of the Phenolate–Pyridine Ligand in Deprotonated Re–xy_0–PhOH

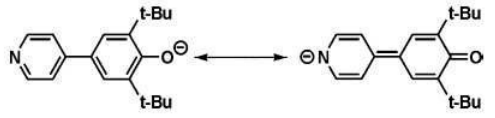

which may help provide an understanding of why this molecular unit is oxidized less readily than the *p*-xylene-bridged congeners: negative charge can simply be delocalized toward the metal center. We note that this interpretation is in line with the assignment of the 323 nm absorption band in the UV–vis spectrum of Re–xy_0–PhOH (Figure 1a) to a phenol-to-pyridine CT transition (see above).[60]

Addition of sodium methoxide to solutions of rhenium(I) tricarbonyl diimine complexes is of some concern because the presence of coordinating CH_3O^- may lead to ligand substitution reactions, particularly at the axial position where the pyridine is located.[66] However, on the basis of the observation of clear differences between the cyclic voltammograms of the shortest member of the series and the longer congeners not only for the dyads but also for the corresponding free ligands (Figures S2 and S4, respectively, in the Supporting Information), we conclude that substitution of the pyridine ligand did not occur to an extent significant for electrochemical investigations.

In the Re–xy_{0-3}–PhOH dyads, the Re moiety is reduced at potentials between −1.54 and −1.57 V vs Fc^+/Fc (Table 2, fifth column), in line with literature values for reduction of rhenium(I) tricarbonyl diimines.[58]

On the basis of the phenol oxidation potentials (E_{ox}) and rhenium(I) reduction potentials (E_{red}) from Table 1, one can use eq 1 to estimate ΔG_{ET}, the driving force for photoinduced electron transfer from the phenol to the ^{3}MLCT-excited rhenium complex:[67]

$$\Delta G_{ET} = e(E_{ox} - E_{red}) - E_{00} + \frac{e^2}{4\pi\varepsilon_0 r}\left(\frac{1}{\varepsilon_s} - \frac{1}{\varepsilon_{ref}}\right) \quad (1)$$

In eq 1, E_{00} is the energy of the photoactive ^{3}MLCT state of the rhenium complex (2.75 eV),[63] ε_0 is the vacuum permittivity, r is the average radius of the two involved redox partners (assumed to be 4.5 Å), ε_s the dielectric constant of the solvent in which the electrochemical potentials were determined (for acetonitrile, ε_s = 35.94), and ε_r is the dielectric constant of the solvent used for the spectroscopic measurements [for 1:1 (v/v) acetonitrile/water, ε_r = 55.7].[68] This analysis leads to the conclusion that electron transfer from the phenol unit to the photoexcited rhenium(I) moiety is expected to be slightly exergonic in the Re–xy_{1-3}–PhOH dyads (Table 2, last column) but should have essentially no driving force in Re–xy_0–PhOH. We note that driving force estimates based on eq 1 are accurate to 0.1 eV at best, particularly in view of the fact that some of the redox waves are irreversible (see above).

Phenol Deprotonation. The pK_a value of the phenol in Re–xy_0–PhOH in 1:1 (v/v) CH_3CN/H_2O was determined via UV–vis titration, monitoring the absorption change at 431 nm upon addition of aqueous sodium hydroxide solution (Figure 3a). The midpoint of the titration was found to occur at a pH

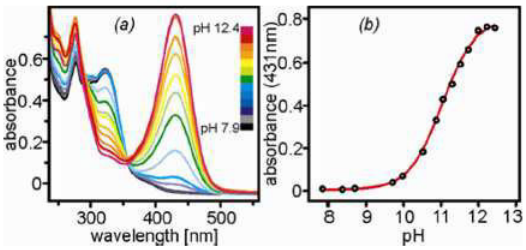

Figure 3. (a) Absorption spectra of Re–xy_0–PhOH in 1:1 (v/v) acetonitrile/water at different pH values. (b) Titration curve obtained by monitoring the absorbance change at 431 nm.

meter reading of 11.0 (Figure 3b), corresponding to an effective pK_a value of 11.3 in 1:1 (v/v) acetonitrile/water.[69] Substantially less prominent spectral changes were observed upon deprotonation of the longer congeners because the phenol–pyridine coupling is weaker in Re–xy_{1-3}–PhOH than in Re–xy_0–PhOH (titration data not shown). For the Re–xy_2–PhOH dyad, we found a pK_a value of 11.4 [effective pK_a in 1:1 (v/v) CH_3CN/H_2O]. Acetonitrile/water mixtures had to be used for these experiments because the triflate salts of our complexes are insoluble in pure water and because the acetonitrile/water mixture was also employed for (time-resolved) luminescence and transient absorption spectroscopy (see below).

Time-Resolved Emission. Table 3 reports the luminescence lifetimes of the Re–xy_n–PhOH dyads and the reference complex in four different solvents (or solvent mixtures). In

Table 3. Luminescence Lifetimes (τ) and Effective H/D Kinetic Isotope Effects (KIE_{eff}) for the Four Dyads from Scheme 1b and the $[Re(phen)(CO)_3(py)]^+$ Reference Complex in Various Solvents under Deoxygenated Conditions[a]

	τ (ns)				
	CH_2Cl_2	CH_3CN	CH_3CN/H_2O	CH_3CN/D_2O	KIE_{eff}
Re-ref	1220	1239	1270	1588	
$Re-xy_0-PhOH$	1141	986	40	95	2.0 ± 0.4
$Re-xy_1-PhOH$	970	582	144	194	1.1 ± 0.2
$Re-xy_2-PhOH$	902	1041	928	1254	
$Re-xy_3-PhOH$	1136	1151	1005	1378	

[a]Excitation occurred at 410 nm with 8 ns laser pulses, and detection was at 550 nm. See the text for definition of KIE_{eff}.

deoxygenated dichloromethane (second column), the lifetimes of the dyads do not differ significantly from that of the reference complex. In deoxygenated acetonitrile (third column), the lifetime of $Re-xy_1-PhOH$ is markedly shorter than those of all the other systems, indicating that an additional nonradiative excited-state deactivation mechanism becomes competitive with ^{3}MLCT deactivation processes that are inherent to the $[Re(phen)(CO)_3(py)]^+$ complex. Triplet–triplet energy transfer has already been ruled out as a possible quenching source (see above), but photoinduced electron transfer is a viable possibility, particularly upon consideration of the ΔG_{ET} values in Table 2: ΔG_{ET} is negative for $Re-xy_{1-3}-PhOH$, but rate constants for electron tunneling (which we expect to be the relevant mechanism for CT in the specific cases of our molecules) decrease exponentially with increasing distance,[61,62,70] which may explain the absence of significant quenching for the $Re-xy_n-PhOH$ dyads with $n = 2$ and $n = 3$ in CH_3CN. For the system with $n = 0$, there is no driving-force for photoinduced electron transfer ($\Delta G_{ET} = 0$ eV) which may account for the absence of luminescence lifetime quenching in this dyad in pure CH_3CN. The transient absorption data presented below provide more direct evidence for photoinduced electron transfer in the $Re-xy_1-PhOH$ dyad.

In a 1:1 (v/v) mixture of acetonitrile and water (Table 3, fourth column), we observed significant lifetime shortening for the $Re-xy_n-PhOH$ dyads with $n = 0-2$, and only the longest member of the series appeared to exhibit emission that was essentially unquenched with respect to the reference complex. Thus, water is an essential ingredient for inducing substantial excited-state quenching in the $Re-xy_n-PhOH$ dyads. Interestingly, somewhat longer lifetimes were measured when water was replaced by heavy water (fifth column); Figure 4 shows a direct comparison of luminescence lifetimes (τ) measured in CH_3CN/H_2O (faster decays of a given color) and CH_3CN/D_2O (slower decays of a given color). The largest H/D kinetic isotope effect (KIE) was detected for $Re-xy_0-PhOH$ ($\tau_H/\tau_D = 2.4$) and the smallest for Re-ref ($\tau_H/\tau_D = 1.3$). The observation of a KIE for the reference complex most likely reflects the fact that multiphonon relaxation of the ^{3}MLCT excited state is less effective in the deuterated solvent, and this can be expected to occur in all three dyads. Thus, we find it useful to define an effective KIE (KIE_{eff}) in which this solvent effect on multiphonon relaxation has been factored out; KIE_{eff} therefore

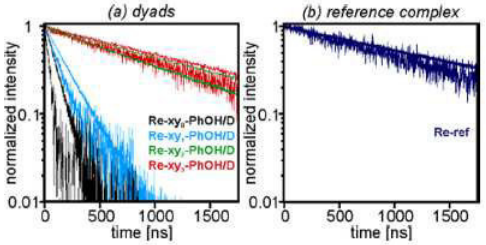

Figure 4. (a) Decays of the luminescence signals of the $Re-xy_n-PhOH$ molecules in deoxygenated 1:1 (v/v) CH_3CN/H_2O (faster decays of a given color) and CH_3CN/D_2O (slower decays of a given color) after pulsed excitation at 410 nm (pulse width ~8 ns); intensities have been arbitrarily normalized to a value of 1 at $t = 0$. (b) Luminescence decay of the reference complex under identical conditions.

reflects the true H/D KIE of the photochemistry occurring from ^{3}MLCT-excited rhenium(I). The resulting effective KIEs are reported in the last column of Table 3, and we note that only for the $Re-xy_0-PhOH$ dyad does KIE_{eff} differ significantly from 1.0. The KIE_{eff} value obtained for the shortest dyad (2.0 ± 0.4) suggests that the rate-determining excited-state deactivation process involves proton motion, while in the longer dyads, most likely only electron motion involved. Since the luminescence quenching was rather weak in $Re-xy_2-PhOH$ and $Re-xy_3-PhOH$, we have refrained from reporting KIEs for these two dyads (also see the comments below).

Equation 2 is commonly used to estimate rate constants for excited-state quenching (k_Q) from luminescence lifetimes:

$$k_Q = \tau^{-1} - \tau_{ref}^{-1} \quad (2)$$

where τ is the luminescence lifetime of the species of interest (here $Re-xy_n-PhOH$) and τ_{ref} is the luminescence lifetime of the reference species (Re-ref in the present case). Rate constants determined in this manner for CH_3CN/H_2O and CH_3CN/D_2O solutions of the $Re-xy_n-PhOH$ molecules are displayed as functions of the donor–acceptor distance R_{DA} in the semilogarithmic plot of Figure 5. Data measured using CH_3CN/H_2O and CH_3CN/D_2O are shown in red and green, respectively. The heights of the vertical lines represent the error bars associated with the individual k_Q values and are based on the experience that each of the luminescence lifetimes could be determined with an experimental accuracy of ±10%. The error

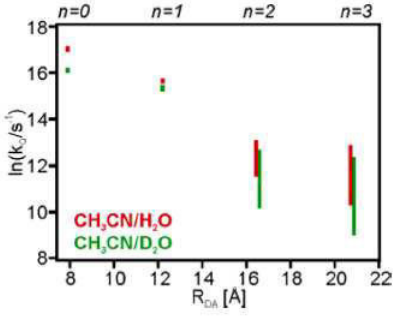

Figure 5. Semilogarthmic representation of the excited-state quenching rate constant k_Q as a function of the phenol–rhenium center-to-center distance R_{DA} in the four $Re-xy_n-PhOH$ molecules in CH_3CN/H_2O (red) and CH_3CN/D_2O (green).

bars increase rapidly with increasing R_{DA} and get very large for Re−xy_2−PhOH and Re−xy_3−PhOH because the luminescence lifetimes of these two dyads approach that of the reference complex (Table 3).

Despite the large error bars, it is possible to discern a nearly exponential distance dependence of k_Q, as would be expected for intramolecular electron or hole tunneling across the *p*-xylene spacers. In view of the observation of KIE_{eff} values that differ significantly between Re−xy_0−PhOH and its longer congeners and upon consideration of the changeover in excited-state quenching mechanism that is most likely associated with this difference in KIE_{eff} (see above), it appears reasonable to extract a distance decay constant (the so-called β value) for k_Q from the data for Re−xy_n−PhOH with $n = 1-3$ and to exclude the dyad with $n = 0$ from this analysis; the transient absorption data shown below strongly support this procedure. From a linear regression fit to the CH_3CN/H_2O data in Figure 5, we thus found $\beta = 0.45 \pm 0.18$ Å^{-1}, while the CH_3CN/D_2O data yielded $\beta = 0.39 \pm 0.18$ Å^{-1}. These distance decay constants are in line with those found for analogous oligo-*p*-xylene and oligo-*p*-phenylene systems,[55,71] but it is to be noted that β is not a bridge-specific parameter but rather a function of the entire donor−bridge−acceptor construct.[61,62,72]

Transient Absorption Spectroscopy. Figure 6a shows transient absorption data obtained after excitation of the two shortest dyads and the reference complex in deoxygenated 1:1 (v/v) CH_3CN/H_2O solutions at 355 nm with laser pulses having a width of ~8 ns. The spectra were recorded by time averaging over the first 200 ns after the laser pulse. The reference complex exhibits a transient absorption spectrum that is typical for ^{3}MLCT-excited rhenium(I) tricarbonyl diimines (green trace): there is a bleach of the $\pi-\pi^*$ absorption of neutral phen at 275 nm along with a positive transient absorption signal at 300 nm characteristic of the reduced phen ligand.[73]. The signals decay with lifetimes of 1217 and 1324 ns, respectively, both in line with the luminescence lifetime measured for this compound under identical conditions (Table 3, fourth column).

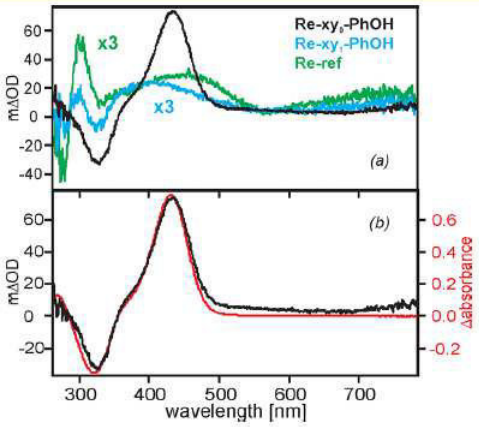

Figure 6. (a) Transient absorption spectra of Re−xy_n−PhOH ($n = 0$, 1) and Re-ref in deoxygenated 1:1 (v/v) acetonitrile/water. Excitation occurred at 355 nm with laser pulses having a width of ~8 ns. Detection was in a time window of 200 ns after the laser pulse. (b) Superposition of the experimental transient absorption spectrum of Re−xy_0−PhOH (black trace) and a derived spectrum (red trace) obtained from subtraction of the absorption spectrum of Re−xy_0−PhOH at pH 7.9 (black trace in Figure 3a) from the absorption spectrum of Re−xy_0−PhOH at pH 12.4 (red trace in Figure 3a).

The transient absorption spectrum of the Re−xy_1−PhOH dyad (blue trace) looks qualitatively similar to that of the reference complex, suggesting at first glance that one primarily observes the spectral signature of the ^{3}MLCT excited state in this case. A subtle but important difference relative to the spectrum of Re-ref (purple trace) is the occurrence of a relatively weak bleach at 325 nm, the wavelength at which the ground-state absorption spectrum of Re−xy_1−PhOH exhibits a shoulder that we attributed above to an electronic transition with phenol-to-pyridine CT character (Figure 2a). This particular bleach is diagnostic of the one-electron-reduced rhenium complex, and this fact will be important below in the discussion of the reaction kinetics of the Re−xy_1−PhOH dyad. Here we focus primarily on the transient absorption spectrum measured for the Re−xy_0−PhOH molecule (black trace in Figure 6a).

The transient absorption spectrum of the shortest dyad (black traces in Figure 6a,b) differs very significantly from those of the Re−xy_1−PhOH dyad and the reference complex. At comparable excitation pulse energies and dyad concentrations, not only are the observed changes in optical density (ΔOD) substantially higher (suggesting longer-lived photoproducts), but there are also significant spectral differences: the bleach at 275 nm and the positive signal at 300 nm (usually indicative of $phen^-$) are absent, but there is now a new bleach at 330 nm and a new absorption with a peak at 435 nm. The red trace in Figure 6b was obtained by subtracting the Re−xy_0−PhOH absorption spectrum at pH 7.9 (black trace in Figure 3a) from the respective absorption spectrum at pH 12.4 (red trace in Figure 3a). The superposition of this derived spectrum and the experimental transient absorption spectrum in Figure 6b demonstrates quite convincingly that photoexcitation of Re−xy_0−PhOH induces phenol deprotonation. In other words, the Re−xy_0−PhOH dyad acts as a photoacid. This finding is in line with the absence of luminescence lifetime quenching in this dyad in CH_2Cl_2 and pure CH_3CN (Table 3, second and third columns), where no protonatable reaction partners are available. In contrast, in acetonitrile/water mixtures, protonation of OH^- or H_2O species may occur, and excited-state quenching is comparatively rapid (Table 3, fourth and fifth columns). Furthermore, this finding is in line with the occurrence of a significant KIE for excited-state quenching in Re−xy_0−PhOH ($KIE_{eff} = 2.0 \pm 0.4$; Table 3). Excited-state deactivation by proton transfer also makes sense in view of the fact that there is essentially no driving force for photoinduced electron transfer in this particular dyad (Table 2, last column).

Charge Transfer Kinetics in Re−xy_1−PhOH. In a prior section, we interpreted excited-state quenching in the three longer dyads (Re−xy_{1-3}−PhOH) in terms of photoinduced electron transfer because there is significant exergonicity associated with this process (contrary to Re−xy_0−PhOH) and because there is no significant H/D KIE in the luminescence quenching data (Table 3); moreover, triplet−triplet energy transfer quenching is thermodynamically unlikely. Unfortunately, the transient absorption spectrum of Re−xy_1−PhOH in Figure 6a (light-blue trace) failed to provide completely unambiguous evidence for oxidation products. Phenol radical cations and phenoxyl radicals have well-defined absorptions in the 350−500 nm spectral range,[74,75] but we were unable to detect any of these species unambiguously by transient absorption spectroscopy because in the same spectral

range there appear to be absorptions from the reduced rhenium moiety. The spectral signature of the reduced rhenium complex in turn is somewhat difficult to distinguish from the spectrum of ^{3}MLCT-excited rhenium because the dominant features are a bleach at 275 nm and a positive signal at 300 nm due to transient reduction of the phen ligand,[73,88] but this is the case not only for the one-electron-reduced form of the complex but also for its ^{3}MLCT-excited form. As mentioned above, the most diagnostic feature of the one-electron-reduced rhenium complex in Re–xy$_1$–PhOH is the weak bleach observed at 325 nm (blue trace in Figure 6a). This bleach cannot be observed for ^{3}MLCT-excited [Re(phen)(CO)$_3$(py)]$^+$.

Figure 7 shows the temporal evolution of the diagnostic bleach at 325 nm for Re–xy$_1$–PhOH in 1:1 (v/v) CH_3CN/H_2O (black trace) and 1:1 (v/v) CH_3CN/D_2O (red trace) after excitation at 355 nm with laser pulses of ~8 ns duration. The two transients are noticeably different, both in the formation part of the bleach and in regard to the bleach recovery at times longer than 100–250 ns.

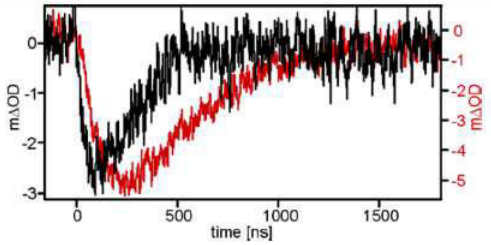

Figure 7. Temporal evolution of the transient absorption signals of Re–xy$_1$–PhOH at 325 nm in deoxygenated 1:1 (v/v) CH_3CN/H_2O (black trace) and 1:1 (v/v) CH_3CN/D_2O (red trace) after pulsed excitation at 355 nm. The pulse width was ~8 ns.

We analyzed the two transients in Figure 7 using a kinetic model for an A → B → C reaction sequence. In this model, A is the initial photoexcited state, B is the charge-separated state with reduced rhenium, and C is the final (ground) state (Scheme 3a). From a fit to the black transient in Figure 7 we obtained time constants of 148 and 85 ns (Table 4). It appears tempting and most straightforward to associate the faster component (85 ns) to the buildup of state B (the A → B step), while the slower time constant (148 ns) would be attributed to the disappearance of state B (the B → C step). However, in A → B → C reaction sequences, the rise time for the population of state B need not necessarily correspond to the kinetics of the A → B reaction step but may instead reflect the kinetics of the B → C step.[54,76,77] There is evidence for exactly this scenario in the case of the Re–xy$_1$–PhOH dyad in CH_3CN/H_2O solution because the slower time constant (148 ns) in fact closely approaches the ^{3}MLCT lifetime extracted from luminescence measurements (144 ns; Table 3). In the luminescence experiments, we monitored the disappearance of state A (the A → B step), and hence it appears plausible to conclude that the 148 ns component in the transient absorption data is in fact due to the A → B step. In this picture, the 85 ns time constant is then due to the B → C step.

From a similar analysis of the red transient in Figure 7 (i.e., the data obtained for the same dyad in CH_3CN/D_2O), we obtained time constants of 169 and 313 ns (Table 4). The ^{3}MLCT lifetime extracted from luminescence measurements in this case was 194 ns (Table 3), so it appears plausible to assign the 169 ns time constant observed in transient absorption spectroscopy to the A → B step, while the 313 ns time constant then logically would be due to the B → C reaction step. In view of the fact that we have two complementary sets of data (time-resolved luminescence and transient absorption), these assignments appear plausible.[78]

In the framework of our kinetic model, the B → C reaction step is associated with a sizable H/D KIE of 3.7 ± 0.5 (i.e., the ratio of 313 and 85 ns), which cannot be reconciled with simple electron transfer. Indeed, this H/D KIE strongly suggests that there is proton movement in the B → C reaction step. This appears peculiar at first glance, but we think there is a very plausible explanation for this observation (Scheme 3b): once intramolecular phenol-to-rhenium(I) electron transfer has occurred, the oxidized phenol radical cation is a highly acidic species; in the case of tyrosine, the pK_a of the phenolic proton drops from a value of ~9 in the charge-neutral form to a value of around −2 in the oxidized species.[17,33,79] It therefore appears plausible to assume that when water is present (pK_a for H_3O^+ = −1.7), the oxidized phenol releases a proton, forming a neutral phenoxyl radical. This hypothesis is illustrated by Scheme 3b, which gives a more accurate description of the photoinduced chemistry in Re–xy$_1$–PhOH than Scheme 3a: after the rate-determining initial electron transfer step forming "state B$_1$" (with oxidized but still protonated phenol), there is rapid proton release to H_2O, thereby forming "state B$_2$" (with reduced rhenium, neutral phenoxyl radical, and protonated water); however, in time-resolved luminescence and transient absorption, we monitor only the A → B$_1$ step, but re-establishment of the original rhenium(I) dyad (state C) via intramolecular electron transfer must be coupled to reprotonation of the phenol moiety. This may explain the occurrence of the significant KIE in the B$_2$ → C step (observable in transient absorption spectroscopy).[80]

Charge Transfer Kinetics in Re–xy$_0$–PhOH. We now turn our attention back to the transient absorption data obtained from the Re–xy$_0$–PhOH dyad. On the basis of the data in Figure 6b, we concluded above that this molecule acts

Scheme 3. Reaction Sequence Models for Re–xy$_1$–PhOH

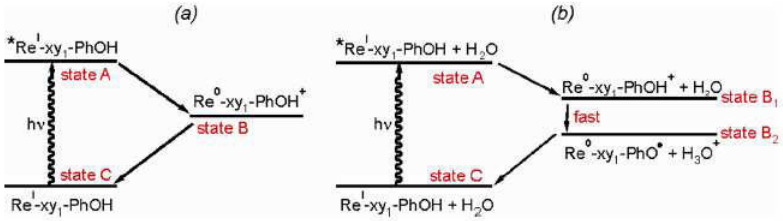

dx.doi.org/10.1021/ja3053046 | J. Am. Chem. Soc. 2012, 134, 12844–12854

Table 4. Transient Absorption Lifetimes and H/D Kinetic Isotope Effects for Excited-State Quenching and Charge Recombination in Re–xy$_0$–PhOH and Re–xy$_1$–PhOH in Deoxygenated 1:1 (v/v) CH_3CN/H_2O and CH_3CN/D_2O[a]

	excited-state quenching			thermal charge recombination		
	τ_H (ns)	τ_D (ns)	KIE_{eff}	τ_H (ns)	τ_D (ns)	KIE
Re–xy$_0$–PhOH	43[b]/41[c]/36[d]	95[b]/86[c]/76[d]	1.8 ± 0.3[b,c,d]	13200[c]/14000[d]	47200[c]/49200[d]	3.6 ± 0.5[c]/3.5 ± 0.5[d]
Re–xy$_1$–PhOH	148[c]	169[c]	1.0 ± 0.3[c]	85[c]	313[c]	3.7 ± 0.5[c]

[a]Excitation occurred at 355 nm with 8 ns laser pulses. τ_H = lifetime in CH_3CN/H_2O; τ_D = lifetime in CH_3CN/D_2O. [b]Detected at 275 nm. [c]Detected at 325 or 330 nm. [d]Detected at 435 nm.

essentially as a photoacid, but we have not yet presented and discussed the reaction kinetics of this dyad.

Figure 8a shows the temporal evolution of the phenol-based transient absorption signals of Re–xy$_0$–PhOH at 435 nm (upper half) and 330 nm (lower half). The black traces were measured in deoxygenated 1:1 (v/v) CH_3CN/H_2O and the red traces in deoxygenated 1:1 (v/v) CH_3CN/D_2O. It is obvious from these data that there is a significant H/D KIE. The specific rise times of these signals are on the order of 40 ns for protonated samples (Table 4, second column) and on the order of 80 ns for deuterated samples (Table 4, third column), yielding a KIE of 1.8 ± 0.3. These transient absorption data are fully consistent with the findings from time-resolved luminescence spectroscopy (Table 3).

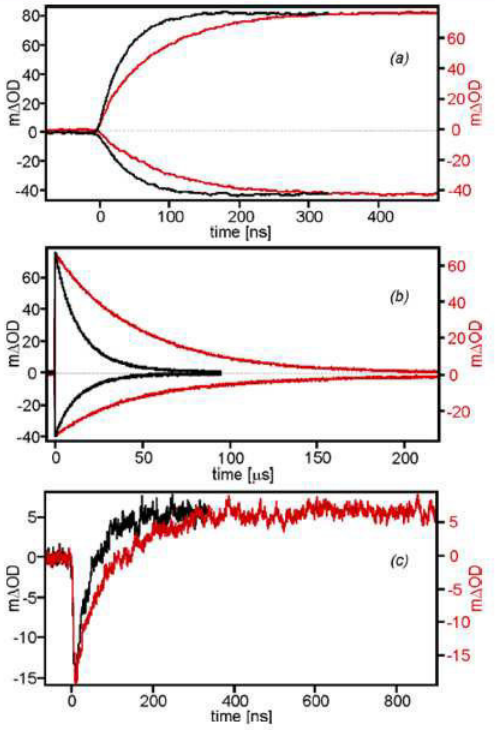

Figure 8. Temporal evolution of the transient absorption signals of Re–xy$_0$–PhOH in deoxygenated 1:1 (v/v) CH_3CN/H_2O (black traces) and 1:1 (v/v) CH_3CN/D_2O (red traces) at various detection wavelengths: (a, b) 435 nm (upper traces) and 330 nm (lower traces); (c) 275 nm. The different time scales in (a) and (b) should be noted. Excitation occurred with 8 ns laser pulses at 355 nm in all cases.

Figure 8c shows the temporal evolution of the transient absorption signal of Re–xy$_0$–PhOH at 275 nm (the bleach of neutral phen). The black traces were measured in 1:1 (v/v) CH_3CN/H_2O and the red traces in 1:1 (v/v) CH_3CN/D_2O. The time constants for the recovery of these bleaches are 43 and 95 ns for the protonated and deuterated species, respectively (Table 4), giving a H/D KIE similar to that found above from the time-resolved luminescence experiments (Table 3). This finding is consistent with release of the phenolic proton by the photoexcited Re–xy$_0$–PhOH to the bulk solvent coupled with simultaneous relaxation to the electronic ground state.

Figure 8b shows the decays of the transient absorption signals of Re–xy$_0$–PhOH at 435 nm (upper half) and 330 nm (lower half). The decays are remarkably slow and occur with time constants of 14.0 and 13.2 μs, respectively, in CH_3CN/H_2O, and 49.2 and 47.2 μs, respectively, in CH_3CN/D_2O. Thus, as in the case of the longer Re–xy$_1$–PhOH dyad, the rate-determining step leading the photoproducts back to the initially present species is associated with a significant H/D KIE. In the specific case of the Re–xy$_0$–PhOH dyad, we found KIEs of 3.5 ± 0.5 (435 nm) and 3.6 ± 0.5 (330 nm), while for Re–xy$_1$–PhOH, we found a KIE of 3.7 ± 0.5 (Table 4, last column).

The observation of photoproducts with microsecond lifetimes after photoexcitation of Re–xy$_0$–PhOH is interesting, particularly in view of the fact that the Re–xy$_1$–PhOH photoproducts exhibit lifetimes on the order of only ~100 ns (Table 3). We think this discrepancy mainly stems from the fact that the photoproducts are different in these two dyads: the shorter molecule reacts to give a Re(I)–xy$_0$–PhO$^-$ species with a phenolate anion (at least formally; see the comments below), while the longer congener gives a Re(0)–xy$_1$–PhO$^\bullet$ species with a phenoxyl radical (the B_2 state in Scheme 3b). The driving forces and reorganization energies for re-establishing the initial Re(I)–xy$_0$–PhOH and Re(I)–xy$_1$–PhOH species would be expected to be significantly different, and this could easily be manifested in substantially different reaction kinetics. In addition, we note that for the Re(I)–xy$_0$–PhO$^-$ species, the resonance structure on the right-hand side of Scheme 2 is presumably more important. Furthermore, it appears plausible to state that this resonance structure would be less easily reprotonated at the oxygen atom than the phenolate structure on the left-hand side of Scheme 2.

Transient absorption experiments with the longer Re–xy$_2$–PhOH and Re–xy$_3$–PhOH dyads were largely inconclusive because the photoinduced chemistry in these systems is too slow with respect to the inherent ^{3}MLCT lifetime of the rhenium(I) photosensitizer. Hence, the time-resolved absorption studies were limited to the two shortest dyads.

Possible Reasons for Different Photoreactivities of Re–xy$_0$–PhOH and Re–xy$_1$–PhOH. In the Cyclic Voltammetry section, we noted that the phenol oxidations and some of the rhenium (or more precisely the phenanthroline-based) reductions in our dyads are irreversible in cyclic voltammetry. Thus, there is significant uncertainty in the redox potential

values reported in Table 2. Nevertheless, it seems clear that the Re–xy_0–PhOH molecule stands out from the dyad series in that it has a phenol oxidation potential which is ~0.2 V more positive than in the longer dyads. Use of eq 1 has led us to the conclusion that photoinduced electron transfer from the phenol units to photoexcited rhenium(I) complexes should be slightly exergonic in the Re–xy_{1-3}–PhOH dyads ($\Delta G_{ET} \approx -0.2$ eV; Table 2, last column), whereas we expect essentially no driving force in Re–xy_0–PhOH. We think that this is one of the key reasons for the different photoreactivities of the Re–xy_0–PhOH and Re–xy_1–PhOH dyads. Another important reason may be the possible resonance stabilization of the phenolate anion in Re–xy_0–PhOH; the fact that the phenolate–pyridine unit may adopt a stable quinonoid structure (right half of Scheme 2)[81] may potentially provide a significant driving force for phototriggered proton release. Scheme 4 illustrates the situation in Re–xy_0–PhOH. Initial photoexcitation populates mainly the emissive ^{3}MLCT state, which is energetically below the phenol → pyridine CT state. Upon deprotonation (possibly involving the phenol → pyridine CT state itself), the phenol → pyridine CT state is energetically stabilized because it is now a *phenolate* → pyridine CT state. This leads to emission quenching and provides the driving force for the transfer of electron density from the phenolate unit toward the metal center.

Scheme 4. Energy-Level Scheme Showing the Most Relevant Excited States of Re–xy_0–PhOH (a) before and (b) after Deprotonation

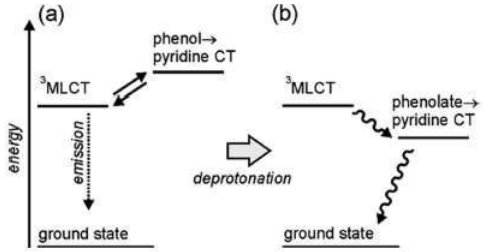

In the Re–xy_1–PhOH dyad, we expect the phenomenon of different resonance structures to play a much less important role because the phenol and pyridine units are electronically decoupled from each other by an intervening *p*-xylene spacer.

■ SUMMARY AND CONCLUSIONS

The initial aim of this work was to explore how variation of the distance between the electron-accepting and electron/proton-donating sites affects the rates and mechanism of bidirectional (multisite) PCET in rhenium–(oligo-*p*-xylene)–phenol molecules. We anticipated that all four dyads shown in Scheme 1b would exhibit photoinduced PCET chemistry in acetonitrile/water mixtures and wondered how the PCET rates and mechanisms would change with increasing phenol–rhenium distance. Interestingly, we found that the Re–xy_0–PhOH dyad acts as a photoacid, while the Re–xy_1–PhOH molecule exhibits photoinduced PCET chemistry involving a stepwise ETPT reaction sequence. However, to some extent, the term "photoacid" does not sufficiently accurately describe the photoinduced chemistry of the Re–xy_0–PhOH dyad because the deprotonated phenol–pyridine ligand has two resonance structures (Scheme 2). When considering the quinonoid structure at the right in Scheme 2, one may note that electron transfer from the phenolate moiety to the pyridine moiety has taken place; with some caution, one may therefore consider the overall photoreaction of Re–xy_0–PhOH in acetonitrile/water as a variant of PCET. At any rate, it is clear from our transient absorption studies that the rate-determining steps in the photoinduced reactions of the donor–acceptor molecule Re–xy_0–PhOH and the donor–bridge–acceptor compound Re–xy_1–PhOH are different: proton motion is involved in the case of the shortest dyad (KIE = 1.8 ± 0.3), while in Re–xy_1–PhOH there is no significant KIE for the photoinduced forward reaction (as determined by the combination of time-resolved emission and transient absorption studies). In contrast, the thermal backward reaction of Re–xy_1–PhOH (like that of Re–xy_0–PhOH) exhibits a H/D KIE of >3, indicating that proton motion is important in the rate-determining step leading back to the initially present species. Thus, our study provides significant new insight into photoinduced PCET chemistry, particularly with respect to the influence of the donor–acceptor distance on the overall reaction and the importance of strong electronic coupling between the donor and acceptor units.

■ EXPERIMENTAL SECTION

Synthesis, Electrochemistry, and Optical Spectroscopy. Detailed synthetic protocols and characterization data for the four dyads from Scheme 1b are given in the Supporting Information. Thin-layer chromatography was performed using Polygram SIL G/UV254 plates from Machery-Nagel, and for column chromatography, Silica Gel 60 from the same company was employed. Reaction products were characterized by ^{1}H spectroscopy on a Bruker Avance DRX 300 spectrometer, by electrospray ionization mass spectrometry using a Bruker APEX IV (FTICR-MS) instrument, and by elemental analysis (conducted by Susanne Petrich at the Institute for Inorganic Chemistry, Göttingen). Optical absorption spectroscopy was performed using Cary 50 and Cary 300 spectrophotometers from Varian, and steady-state luminescence spectra were measured on a Fluorolog-3 instrument (FL322) from HORIBA Jobin Yvon. For time-resolved luminescence and transient absorption spectroscopy, an LP920-KS instrument from Edinburgh Instruments, equipped with a Hamamatsu photomultiplier and an iCCD camera from Andor, was used. The excitation source was a Quantel Brilliant b laser equipped with an optical parametric oscillator from Opotek. A VersaSTAT 3-200 potentiostat from Princeton Applied Research was used for cyclic voltammetry. A glassy carbon electrode served as the working electrode, and two silver wires were used as counter and quasi-reference electrodes. Ferrocene was used as an internal reference. Prior to voltage scans at rates of 100 mV/s, nitrogen gas was bubbled through the dried solvent. The supporting electrolyte was a 0.1 M solution of $TBAPF_6$.

Crystal Structure Determination. The single crystal was mounted in inert oil under cryogenic conditions employing the X-Temp2 device.[82−84] The X-ray data set was collected at 100(2) K on an INCOATEC microfocus source[85] with mirror-monochromatized Mo Kα radiation (λ = 0.71073 Å) and equipped with a Bruker Smart Apex II detector and integrated with SAINT, and an empirical absorption correction with SADABS was applied.[86] The structure was solved with direct methods (SHELXS in SHELXTL, version 2008/3) and refined by full-matrix least-squares methods against F^2 (SHELXS in SHELXTL, version 2008/3).[87] All non-hydrogen atoms were refined with anisotropic displacement parameters. The hydrogen atoms were refined isotropically on calculated positions using a riding model with their U_{iso} values constrained to equal to 1.5 times the U_{eq} of their pivot atoms for terminal sp^3 carbon atoms and 1.2U_{eq} for all other carbon atoms. An exception was the O1 bonded H100, whose position was taken from the residual density map and refined freely.

In the crystal structure of Re–xy_1–PhOH, the diethyl ether solvent molecule was disordered at two positions. The molecule was set on a

special position, thus revealing a total of four positions. Disordered moieties were refined using bond length and displacement parameter restraints. Crystallographic data (excluding structure factors) for the structures reported in this paper have been deposited with the Cambridge Crystallographic Data Centre (CCDC) as supplementary publication no. 838939. Copies of the data can be obtained free of charge upon application to the CCDC, 12 Union Road, Cambridge CB2 1EZ, U.K. [fax, (internat.) +44(1223)336-033; e-mail, deposit@ccdc.cam.ac.uk].

■ ASSOCIATED CONTENT

Supporting Information

Detailed synthetic protocols and characterization data, additional electrochemical data, and crystallographic data for Re–xy_1–PhOH (CIF). This material is available free of charge via the Internet at http://pubs.acs.org.

■ AUTHOR INFORMATION

Corresponding Author

oliver.wenger@chemie.uni-goettingen.de

Notes

The authors declare no competing financial interest.

■ ACKNOWLEDGMENTS

This work was supported by the Deutsche Forschungsgemeinschaft (DFG) through IRTG 1422. The MWK Niedersachsen and the DFG (INST186/872-1) are thanked for funding the transient absorption setup. We kindly acknowledge funding from the DNRF-funded Centre of Materials Crystallography and the doctoral programme Catalysis for Sustainable Synthesis, provided by the Land Niedersachsen.

■ REFERENCES

(1) Mayer, J. M. *Annu. Rev. Phys. Chem.* **2004**, *55*, 363–390.
(2) Huynh, M. H. V.; Meyer, T. J. *Chem. Rev.* **2007**, *107*, 5004–5064.
(3) Reece, S. Y.; Nocera, D. G. *Annu. Rev. Biochem.* **2009**, *78*, 673–699.
(4) Magnuson, A.; Anderlund, M.; Johansson, O.; Lindblad, P.; Lomoth, R.; Polivka, T.; Ott, S.; Stensjö, K.; Styring, S.; Sundström, V.; Hammarström, L. *Acc. Chem. Res.* **2009**, *42*, 1899–1909.
(5) Hammes-Schiffer, S. *Acc. Chem. Res.* **2009**, *42*, 1881–1889.
(6) Dempsey, J. L.; Winkler, J. R.; Gray, H. B. *Chem. Rev.* **2010**, *110*, 7024–7039.
(7) Costentin, C.; Robert, M.; Savéant, J.-M. *Acc. Chem. Res.* **2010**, *43*, 1019–1029.
(8) Gagliardi, C. J.; Westlake, B. C.; Kent, C. A.; Paul, J. J.; Papanikolas, J. M.; Meyer, T. J. *Coord. Chem. Rev.* **2010**, *254*, 2459–2471.
(9) Cukier, R. I.; Nocera, D. G. *Annu. Rev. Phys. Chem.* **1998**, *49*, 337–369.
(10) Bordwell, F. G.; Cheng, J. P. *J. Am. Chem. Soc.* **1991**, *113*, 1736–1743.
(11) Warren, J. J.; Tronic, T. A.; Mayer, J. M. *Chem. Rev.* **2010**, *110*, 6961–7001.
(12) Biczok, L.; Gupta, N.; Linschitz, H. *J. Am. Chem. Soc.* **1997**, *119*, 12601–12609.
(13) Concepcion, J. J.; Brennaman, M. K.; Deyton, J. R.; Lebedeva, N. V.; Forbes, M. D. E.; Papanikolas, J. M.; Meyer, T. J. *J. Am. Chem. Soc.* **2007**, *129*, 6968–6969.
(14) Bronner, C.; Wenger, O. S. *J. Phys. Chem. Lett.* **2012**, *3*, 70–74.
(15) Mayer, J. M.; Rhile, I. J.; Larsen, F. B.; Mader, E. A.; Markle, T. F.; DiPasquale, A. G. *Photosynth. Res.* **2006**, *87*, 3–20.
(16) Lachaud, T.; Quaranta, A.; Pellegrin, Y.; Dorlet, P.; Charlot, M. F.; Un, S.; Leibl, W.; Aukauloo, A. *Angew. Chem., Int. Ed.* **2005**, *44*, 1536–1540.
(17) Magnuson, A.; Berglund, H.; Korall, P.; Hammarström, L.; Åkermark, B.; Styring, S.; Sun, L. C. *J. Am. Chem. Soc.* **1997**, *119*, 10720–10725.
(18) Sun, L. C.; Burkitt, M.; Tamm, M.; Raymond, M. K.; Abrahamsson, M.; LeGourriérec, D.; Frapart, Y.; Magnuson, A.; Kenéz, P. H.; Brandt, P.; Tran, A.; Hammarström, L.; Styring, S.; Åkermark, B. *J. Am. Chem. Soc.* **1999**, *121*, 6834–6842.
(19) Johansson, O.; Wolpher, H.; Borgström, M.; Hammarström, L.; Bergquist, J.; Sun, L. C.; Åkermark, B. *Chem. Commun.* **2004**, 194–195.
(20) Maki, T.; Araki, Y.; Ishida, Y.; Onomura, O.; Matsumura, Y. *J. Am. Chem. Soc.* **2001**, *123*, 3371–3372.
(21) Benisvy, L.; Bittl, R.; Bothe, E.; Garner, C. D.; McMaster, J.; Ross, S.; Teutloff, C.; Neese, F. *Angew. Chem., Int. Ed.* **2005**, *44*, 5314–5317.
(22) Rhile, I. J.; Markle, T. F.; Nagao, H.; DiPasquale, A. G.; Lam, O. P.; Lockwood, M. A.; Rotter, K.; Mayer, J. M. *J. Am. Chem. Soc.* **2006**, *128*, 6075–6088.
(23) Quaranta, A.; Lachaud, F.; Herrero, C.; Guillot, R.; Charlot, M. F.; Leibl, W.; Aukauloo, A. *Chem.—Eur. J.* **2007**, *13*, 8201–8211.
(24) Markle, T. F.; Rhile, I. J.; DiPasquale, A. G.; Mayer, J. M. *Proc. Natl. Acad. Sci. U.S.A.* **2008**, *105*, 8185–8190.
(25) Markle, T. F.; Mayer, J. M. *Angew. Chem., Int. Ed.* **2008**, *47*, 738–740.
(26) Moore, G. F.; Hambourger, M.; Gervaldo, M.; Poluektov, O. G.; Rajh, T.; Gust, D.; Moore, T. A.; Moore, A. L. *J. Am. Chem. Soc.* **2008**, *130*, 10466–10467.
(27) Rhile, I. J.; Mayer, J. M. *J. Am. Chem. Soc.* **2004**, *126*, 12718–12719.
(28) Costentin, C.; Robert, M.; Savéant, J.-M. *J. Am. Chem. Soc.* **2006**, *128*, 4552–4553.
(29) Reece, S. Y.; Nocera, D. G. *J. Am. Chem. Soc.* **2005**, *127*, 9448–9458.
(30) Bertini, I.; Gray, H. B.; Stiefel, E. I.; Valentine, J. S. *Biological Inorganic Chemistry*; University Science Books: Sausalito, CA, 2007.
(31) Sjödin, M.; Irebo, T.; Utas, J. E.; Lind, J.; Merenyi, G.; Åkermark, B.; Hammarström, L. *J. Am. Chem. Soc.* **2006**, *128*, 13076–13083.
(32) Sjödin, M.; Ghanem, R.; Polivka, T.; Pan, J.; Styring, S.; Sun, L. C.; Sundström, V.; Hammarström, L. *Phys. Chem. Chem. Phys.* **2004**, *6*, 4851–4858.
(33) Sjödin, M.; Styring, S.; Wolpher, H.; Xu, Y. H.; Sun, L. C.; Hammarström, L. *J. Am. Chem. Soc.* **2005**, *127*, 3855–3863.
(34) Irebo, T.; Johansson, O.; Hammarström, L. *J. Am. Chem. Soc.* **2008**, *130*, 9194–9195.
(35) Irebo, T.; Reece, S. Y.; Sjödin, M.; Nocera, D. G.; Hammarström, L. *J. Am. Chem. Soc.* **2007**, *129*, 15462–15464.
(36) Bonin, J.; Costentin, C.; Louault, C.; Robert, M.; Savéant, J.-M. *J. Am. Chem. Soc.* **2011**, *133*, 6668–6674.
(37) Bonin, J.; Costentin, C.; Louault, C.; Robert, M.; Routier, M.; Savéant, J.-M. *Proc. Natl. Acad. Sci. U.S.A.* **2010**, *107*, 3367–3372.
(38) Costentin, C.; Robert, M.; Savéant, J.-M. *J. Am. Chem. Soc.* **2007**, *129*, 5870–5879.
(39) Hankache, J.; Hanss, D.; Wenger, O. S. *J. Phys. Chem. A* **2012**, *116*, 3347–3358.
(40) Oevering, H.; Paddon-Row, M. N.; Heppener, M.; Oliver, A. M.; Cotsaris, E.; Verhoeven, J. W.; Hush, N. S. *J. Am. Chem. Soc.* **1987**, *109*, 3258–3269.
(41) Gray, H. B.; Winkler, J. R. *Proc. Natl. Acad. Sci. U.S.A.* **2005**, *102*, 3534–3539.
(42) Manner, V. W.; DiPasquale, A. G.; Mayer, J. M. *J. Am. Chem. Soc.* **2008**, *130*, 7210–7211.
(43) Manner, V. W.; Mayer, J. M. *J. Am. Chem. Soc.* **2009**, *131*, 9874–9875.
(44) Markle, T. F.; Rhile, I. J.; Mayer, J. M. *J. Am. Chem. Soc.* **2011**, *133*, 17341–17352.
(45) Zhang, M.-T.; Irebo, T.; Johansson, O.; Hammarström, L. *J. Am. Chem. Soc.* **2011**, *133*, 13224–13227.
(46) Walther, M. E.; Wenger, O. S. *Dalton Trans.* **2008**, 6311–6318.

(47) Hanss, D.; Walther, M. E.; Wenger, O. S. *Coord. Chem. Rev.* **2010**, *254*, 2584−2592.
(48) Hanss, D.; Wenger, O. S. *Inorg. Chem.* **2008**, *47*, 9081−9084.
(49) Hanss, D.; Wenger, O. S. *Inorg. Chem.* **2009**, *48*, 671−680.
(50) Walther, M. E.; Wenger, O. S. *ChemPhysChem* **2009**, *10*, 1203−1206.
(51) Bouzakraoui, S.; Bouzzine, S. M.; Bouachrine, M.; Hamidi, M. *J. Mol. Struct.* **2005**, *725*, 39−44.
(52) Lukeš, V.; Aquino, A. J. A.; Lischka, H.; Kauffmann, H. F. *J. Phys. Chem. B* **2007**, *111*, 7954−7962.
(53) Grave, C.; Risko, C.; Shaporenko, A.; Wang, Y. L.; Nuckolls, C.; Ratner, M. A.; Rampi, M. A.; Zharnikov, M. *Adv. Funct. Mater.* **2007**, *17*, 3816−3828.
(54) Hanss, D.; Wenger, O. S. *Eur. J. Inorg. Chem.* **2009**, 3778−3790.
(55) Weiss, E. A.; Ahrens, M. J.; Sinks, L. E.; Gusev, A. V.; Ratner, M. A.; Wasielewski, M. R. *J. Am. Chem. Soc.* **2004**, *126*, 5577−5584.
(56) Weiss, E. A.; Tauber, M. J.; Kelley, R. F.; Ahrens, M. J.; Ratner, M. A.; Wasielewski, M. R. *J. Am. Chem. Soc.* **2005**, *127*, 11842−11850.
(57) Hanss, D.; Walther, M. E.; Wenger, O. S. *Coord. Chem. Rev.* **2010**, *254*, 2584−2592.
(58) Sacksteder, L.; Zipp, A. P.; Brown, E. A.; Streich, J.; Demas, J. N.; DeGraff, B. A. *Inorg. Chem.* **1990**, *29*, 4335−4340.
(59) Wallace, L.; Rillema, D. P. *Inorg. Chem.* **1993**, *32*, 3836−3843.
(60) Cargill Thompson, A. M. W.; Smailes, M. C. C.; Jeffery, J. C.; Ward, M. D. *J. Chem. Soc., Dalton Trans.* **1997**, 737−743.
(61) Wenger, O. S. *Acc. Chem. Res.* **2011**, *44*, 25−35.
(62) Albinsson, B.; Eng, M. P.; Pettersson, K.; Winters, M. U. *Phys. Chem. Chem. Phys.* **2007**, *9*, 5847−5864.
(63) Connick, W. B.; Di Bilio, A. J.; Hill, M. G.; Winkler, J. R.; Gray, H. B. *Inorg. Chim. Acta* **1995**, *240*, 169−173.
(64) Das, P. K.; Encinas, M. V.; Scaiano, J. C. *J. Am. Chem. Soc.* **1981**, *103*, 4154−4162.
(65) Lafolet, F.; Welter, S.; Popovic, Z.; De Cola, L. *J. Mater. Chem.* **2005**, *15*, 2820−2828.
(66) Hevia, E.; Perez, J.; Riera, L.; Riera, V.; del Rio, I.; Garcia-Granda, S.; Miguel, D. *Chem.—Eur. J.* **2002**, *8*, 4510−4521.
(67) Weller, A. *Z. Phys. Chem.* **1982**, *133*, 93−98.
(68) Gagliardi, L. G.; Castells, C. B.; Rafols, C.; Roses, M.; Bosch, E. *J. Chem. Eng. Data* **2007**, *52*, 1103−1107.
(69) Gagliardi, L. G.; Castells, C. B.; Rafols, C.; Roses, M.; Bosch, E. *Anal. Chem.* **2007**, *79*, 3180−3187.
(70) McConnell, H. M. *J. Chem. Phys.* **1961**, *35*, 508−515.
(71) Wenger, O. S. *Chem. Soc. Rev.* **2011**, *40*, 3538−3550.
(72) Eng, M. P.; Albinsson, B. *Angew. Chem., Int. Ed.* **2006**, *45*, 5626−5629.
(73) Chen, P. Y.; Westmoreland, T. D.; Danielson, E.; Schanze, K. S.; Anthon, D.; Neveux, P. E.; Meyer, T. J. *Inorg. Chem.* **1987**, *26*, 1116−1126.
(74) Das, P. K.; Encinas, M. V.; Steenken, S.; Scaiano, J. C. *J. Am. Chem. Soc.* **1981**, *103*, 4162−4166.
(75) Gadosy, T. A.; Shukla, D.; Johnston, L. J. *J. Phys. Chem. A* **1999**, *103*, 8834−8839.
(76) Atkins, P. W.; de Paula, J. *Physical Chemistry*, 8th ed.; Oxford University Press: Oxford, U.K., 2006.
(77) Borgström, M.; Johansson, O.; Lomoth, R.; Baudin, H. B.; Wallin, S.; Sun, L. C.; Åkermark, B.; Hammarström, L. *Inorg. Chem.* **2003**, *42*, 5173−5184.
(78) Transient IR spectroscopy might be able to provide additional insight, but this experimental method is not readily available.
(79) Sjödin, M.; Styring, S.; Åkermark, B.; Sun, L. C.; Hammarström, L. *J. Am. Chem. Soc.* **2000**, *122*, 3932−3936.
(80) Our transient absorption experiments monitor the reappearance of state C.
(81) Alternatively, the relevant structure might be called a pyridone-like structure.
(82) Kottke, T.; Stalke, D. *J. Appl. Crystallogr.* **1993**, *26*, 615−619.
(83) Kottke, T.; Lagow, R. J.; Stalke, D. *J. Appl. Crystallogr.* **1996**, *29*, 465−468.
(84) Stalke, D. *Chem. Soc. Rev.* **1998**, *27*, 171−178.
(85) Schulz, T.; Meindl, K.; Leusser, D.; Stern, D.; Graf, J.; Michaelsen, C.; Ruf, M.; Sheldrick, G. M.; Stalke, D. *J. Appl. Crystallogr.* **2009**, *42*, 885−891.
(86) Sheldrick, G. M. *SADABS 2008/2*; University of Göttingen: Göttingen, Germany, 2008.
(87) Sheldrick, G. M. *Acta Crystallogr., Sect. A.* **2008**, *64*, 112−122.
(88) Záliš, S.; Cosani, C.; Cannizzo, A.; Chergui, M.; Hartl, F.; Vlček, A., Jr. *Inorg. Chim. Acta* **2011**, *374*, 578−585.

THE JOURNAL OF PHYSICAL CHEMISTRY A

Article

pubs.acs.org/JPCA

Photoacid Behavior versus Proton-Coupled Electron Transfer in Phenol−Ru(bpy)$_3^{2+}$ Dyads

Martin Kuss-Petermann[†] and Oliver S. Wenger*[,‡]

[†]Institut für Anorganische Chemie, Georg-August-Universität Göttingen, Tammannstraße 4, D-37077 Göttingen, Germany

[‡]Departement für Chemie, Universität Basel, Spitalstrasse 51, CH-4056 Basel, Switzerland

Supporting Information

ABSTRACT: Two dyads composed of a Ru(bpy)$_3^{2+}$ (bpy = 2,2′-bipyridine) photosensitizer and a covalently attached phenol were synthesized and investigated. In the shorter dyad (Ru−PhOH) the ruthenium complex and the phenol are attached directly to each other whereas in the longer dyad there is a *p*-xylene (xy) spacer in between (Ru−xy−PhOH). Electrochemical investigations indicate that intramolecular electron transfer (ET) from phenol to the photoexcited metal complex is endergonic by more than 0.3 eV in both dyads, explaining the absence of any ^{3}MLCT (metal-to-ligand charge transfer) excited-state quenching by the phenols in pure CH_3CN and CH_2Cl_2. When pyridine is added to a CH_2Cl_2 solution, significant excited-state quenching can be observed for both dyads, but the bimolecular quenching rate constants differ by 2 orders of magnitude between Ru−PhOH and Ru−xy−PhOH. Transient absorption spectroscopy shows that in the presence of pyridine both dyads react to photoproducts containing Ru(II) and phenolate. The activation energies associated with the photoreactions in the two dyads differ by 1 order of magnitude, and this might suggest that the formation of identical photoproducts proceeds through fundamentally different reaction pathways in Ru−PhOH and Ru−xy−PhOH. For Ru−PhOH direct proton release from the photoexcited dyad is a plausible reaction pathway. For Ru−xy−PhOH a sequence of a photoinduced proton-coupled electron transfer (PCET) followed by an intramolecular (thermal) electron transfer in the reverse direction is a plausible reaction pathway; this two-step process involves a reaction intermediate containing Ru(I) and phenoxyl radical that reacts very rapidly to Ru(II) and phenolate. Thermal back-reactions to restore the initial starting materials occur on a 30−50 μs time scale in both dyads; i.e., due to proton release the photoproducts are very long-lived. These back-reactions exhibit inverse H/D kinetic isotope effects of 0.7 ± 0.1 (Ru−PhOH) and 0.6 ± 0.1 (Ru−xy−PhOH) at room temperature.

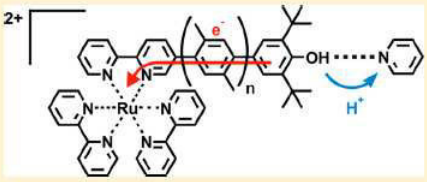

INTRODUCTION

Proton-coupled electron transfer (PCET) is an elementary reaction in many enzymes, and it is of key importance, for example, for water oxidation or carbon dioxide reduction; hence, it seems desirable to understand PCET at the most fundamental level.[1,2] Phenols are well suited PCET reactants for mechanistic studies because the acidity of their OH group and their oxidation potential are strongly interrelated.[3,4] There have been numerous studies of PCET with phenols, focusing on various aspects such as the driving-force dependence of reaction rates and mechanisms,[5−8] the importance of hydrogen-bonding,[9−21] proton transfer distance,[22,23] and pH of the surrounding medium.[15,24−27] The importance of the separation between the redox-active and the acidic/basic reaction sites has also been studied in suitable models.[28,29] However, the influence of the electron donor−acceptor distance on PCET rates and mechanisms is yet poorly explored,[30,31] unlike the distance dependence of "simple" (i.e., not proton-coupled) electron transfer.[32−37]

PCET reactivity in model systems can be induced chemically,[5,14,23] electrochemically,[8,38,39] or photochemically.[15,17,21,40−44] Our group recently reported on photo-triggered bimolecular PCET between phenols and Ru(2,2′-bipyrazine)$_3^{2+}$ or rhenium(I) tricarbonyl complexes.[45−47] Building on this work we investigated the influence of electron donor−acceptor distance on the PCET chemistry of covalent rhenium(I)−phenol dyads in CH_3CN/H_2O mixtures.[30] In this paper we report on analogous Ru(bpy)$_3^{2+}$−phenol dyads (bpy = 2,2′-bipyridine) and their photochemistry in CH_2Cl_2/pyridine solution. Our system may be regarded as a functional model for the P680/TyrZ/His-190 reaction triple of photosystem II (Scheme 1).[48] The phenol plays the role of the combined electron/proton donor (TyrZ), the photoexcited Ru(bpy)$_3^{2+}$ mimicks the function of P680, and the pyridine acts as a base like His-190. Though similar functional models have been reported previously,[21,25,44,49−53] the influence of the distance between the phenolic electron donor and the electron acceptor on the overall PCET chemistry is yet little explored. In one of our dyads the phenol is attached directly to the Ru(bpy)$_3^{2+}$ complex (Ru−PhOH), whereas in the other there is a *p*-xylene (xy) spacer in between (Ru−xy−PhOH).

Received: March 14, 2013
Revised: May 27, 2013
Published: July 8, 2013

dx.doi.org/10.1021/jp402567m | J. Phys. Chem. A 2013, 117, 5726−5733

Scheme 1. (a) P680/TyrZ/His-190 Bidirectional PCET Reaction Triple of Photosystem II and (b) Functional Model Compounds Investigated in This Work (n = 0, 1)

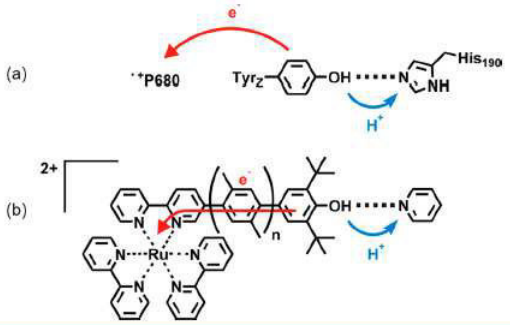

RESULTS AND DISCUSSION

UV–Vis Spectroscopy and Cyclic Voltammetry. Figure 1 shows the UV–vis absorption spectrum of Ru–PhOH and Ru–xy–PhOH at 3 × 10^{-5} M concentration in CH_2Cl_2 at 295 K. For both compounds the usual absorptions of the $Ru(bpy)_3^{2+}$ complex, namely an MLCT (metal-to-ligand charge transfer) band centered around 450 nm and a bpy-localized $\pi-\pi^*$ transition near 300 nm are observed. The shorter dyad exhibits an additional band near 380 nm, which had been observed previously in a closely related rhenium(I) complex with a pendant phenol.[30]

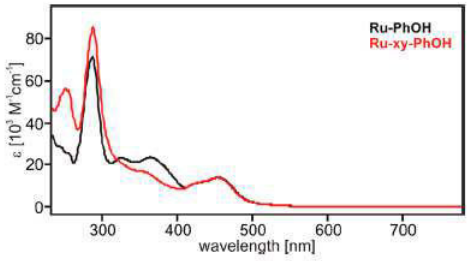

Figure 1. UV–vis absorption spectra of the two dyads in CH_2Cl_2 at 295 K.

The reduction potentials of the individual electrochemically active components of Ru–PhOH and Ru–xy–PhOH were extracted from the data in Figure 2. The cyclic voltammograms were recorded in deoxygenated and freshly distilled CH_2Cl_2 (black traces) in the presence of 0.1 M $TBAPF_6$ (TBA = tetra-*n*-butylammonium). Ferrocene (Fc) was added for internal voltage calibration, manifesting in the reversible waves at 0.0 V. Near 1.0 V vs Fc^+/Fc one detects two oxidation processes in both dyads: One of them is reversible and is attributed to the $Ru(bpy)_3^{3+}/Ru(bpy)_3^{2+}$ couple. The other is irreversible and is assigned to the $PhOH^+/PhOH$ couple. The values in Table 1 are half-wave potentials; for the irreversible phenol oxidation processes we used the inflection point in the rising part of the observable wave as an approximate value; we did not detect any significant voltage scan rate dependence for any of these potentials. As seen from Table 1, the $Ru(bpy)_3^{2+}$ oxidation potentials are very close to 1.0 V vs Fc^+/Fc, whereas phenol oxidation occurs near 0.9 V vs Fc^+/Fc, both in line with literature values.[3,4,54] The irreversibility of the phenol oxidation is commonly attributed to proton loss to bulk solution.[3,4,9–11]

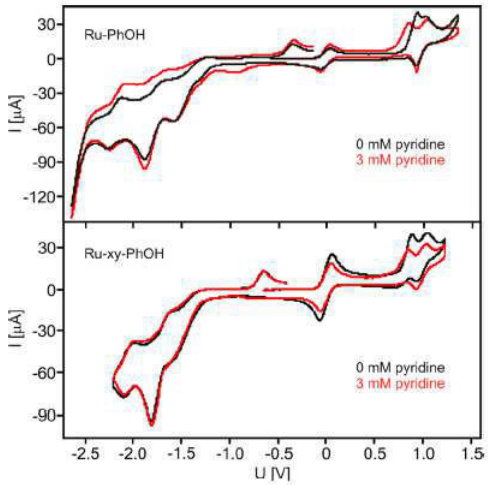

Figure 2. Cyclic voltammograms of Ru–PhOH (upper half) and Ru–xy–PhOH (lower half) in pure CH_2Cl_2 (black traces) and in CH_2Cl_2 with 3 mM pyridine (red traces). The supporting electrolyte was 0.1 M $TBAPF_6$, and the voltage scan rate was 100 mV/s.

Table 1. Reduction Potentials of the Individual Electrochemically Active Components of the Two Dyads in CH_2Cl_2[a]

	E(bpy/bpy$^-$)	E(PhO$^•$/PhO$^-$)	E(PhOH$^+$/PhOH)	E(Ru^{III}/Ru^{II})	ΔG_{ET}^0
Ru–PhOH	−1.77	−0.40	0.89	0.99	0.34 eV
Ru–xy–PhOH	−1.72	−0.70	0.83	1.00	0.30 eV

[a]All potentials are reported in V vs Fc^+/Fc. The data were extracted from the voltammograms in Figure 2. The supporting electrolyte was 0.1 M $TBAPF_6$.

On the reductive side of the voltage sweeps we detect prominent waves that can be attributed to reduction of the bpy ligands with up to three electrons.[54] The subsequent oxidative sweep between −2.5 V vs Fc^+/Fc and 0 V vs Fc^+/Fc reveals an irreversible oxidation at −0.40 V vs Fc^+/Fc for Ru–PhOH and at −0.70 V vs Fc^+/Fc for Ru–xy–PhOH. The respective waves only appear after an initial oxidative sweep to potentials more positive than 0.8 V vs Fc^+/Fc, and consequently, we attribute these waves to oxidation of phenolate to phenoxyl radical. The phenolate is generated in the course of phenol oxidation as mentioned above.

Interestingly, the potential for the $PhOH^+/PhOH$ couple is nearly the same in Ru–PhOH and Ru–xy–PhOH (0.89/0.83 V vs Fc^+/Fc) whereas phenolate oxidation is easier by 300 mV in the longer dyad. This likely reflects the resonance stabilization of the phenolate in deprotonated Ru–PhOH through delocalization of the negative charge from the O-atom toward the N-atom of bpy (Scheme 2).[55] In principle, one can draw an analogous resonance structure for the bpy–xy–PhOH ligand of the longer dyad but in that system electronic coupling

Scheme 2. Two Resonance Structures of the Deprotonated bpy–PhOH Ligand in the Ru–PhOH Dyad

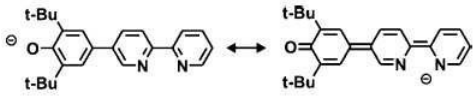

dx.doi.org/10.1021/jp402567m | J. Phys. Chem. A 2013, 117, 5726–5733

between bpy and PhOH is weaker, and the respective resonance stabilization is probably less important.

The red traces in Figure 2 are the voltammograms of analogous CH_2Cl_2 solutions containing 3 mM pyridine. One detects a small shift of the phenol oxidation potentials to less positive values compared to pure CH_2Cl_2. For Ru−PhOH the $PhOH^+$/PhOH couple shifts from 0.89 to 0.80 V vs Fc^+/Fc, for Ru−xy−PhOH it shifts from 0.83 to 0.80 V vs Fc^+/Fc. Because of the small magnitude of this shift it is difficult to extract a clear correlation between phenol oxidation potential and pyridine concentration (Figure S1 of the Supporting Information). All other redox potentials stay essentially unchanged upon pyridine addition.

Luminescence and Transient Absorption Spectroscopy. In pure deoxygenated CH_2Cl_2 solution the ^{3}MLCT excited state of the $Ru(bpy)_3^{2+}$ unit in Ru−PhOH and Ru−xy−PhOH is essentially unquenched, the emission intensities and lifetimes are similar to those of free $Ru(bpy)_3^{2+}$ under identical conditions. By transient absorption spectroscopy one detects the spectral signature of the ^{3}MLCT state of $Ru(bpy)_3^{2+}$ (black traces in Figure 3a,b): A bleach near 450 nm, a positive ΔOD

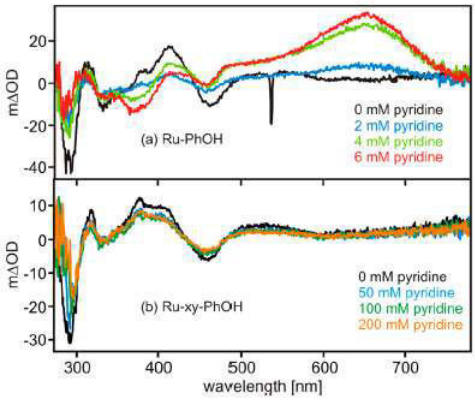

Figure 3. Transient absorption spectra of Ru−PhOH (a) and Ru−xy−PhOH (b) in deoxygenated CH_2Cl_2 in the presence of variable concentrations of pyridine (color code in inset). The concentration of the dyads was 10^{-5} M in all cases. Excitation occurred with laser pulses of 10 ns width at 532 nm. The spectra are time-averaged over a period of 200 ns starting immediately after the pulse.

signal around 315 nm, and another bleach near 300 nm.[56] Additionally, the spectral signature of the reduced bpy−phenol ligands can be observed as a positive signal around 400 nm ("reduced" when the MLCT state is considered to be composed of an oxidized metal center and a reduced ligand). These spectra were recorded by time-averaging over 200 ns after excitation with laser pulses of ~10 ns duration at 532 nm. Evidently, electron transfer (ET) from phenol to the photoexcited metal complex is not kinetically competitive with inherent ^{3}MLCT deactivation processes under these experimental conditions. The electrochemical data from the previous section are helpful to understand why: Using eq 1 and $E_{ox} = E(PhOH^+/PhOH)$, $E_{red} = E(bpy/bpy^-)$, E_{00} = 2.12 eV, and R_{DA} = 7.9 Å for Ru−PhOH/12.2 Å for Ru−xy−PhOH,[30] we arrive at the conclusion that in CH_2Cl_2 the reaction free energy (ΔG_{ET}^0) associated with electron transfer from phenol to photoexcited $Ru(bpy)_3^{2+}$ is +0.34 eV for Ru−PhOH and +0.30 eV for Ru−xy−PhOH (last column of Table 1).[57] Given the significantly endergonic nature of intramolecular photoinduced electron transfer, its kinetic inefficiency is not surprising.

$$\Delta G_{ET}^0 = e\cdot(E_{ox} - E_{red}) - E_{00} - e^2/(4\cdot\pi\cdot\varepsilon_0\cdot\varepsilon_s\cdot R_{DA}) \quad (1)$$

When pyridine is added to the CH_2Cl_2 solutions, ^{3}MLCT excited-state quenching is observed in both dyads, manifesting in luminescence intensity decreases and lifetime shortenings (Figure S2 and Figure S3, Supporting Information), as well as in the appearance of new signals in the transient absorption spectra: In the Ru−PhOH dyad pyridine addition leads to the emergence of a broad transient absorption signal in the 480−740 nm spectral range (colored traces in Figure 3a), which is obviously due to the formation of a photoproduct. In the Ru−xy−PhOH dyad, the photoproducts form much more slowly than in Ru−PhOH (see below), and therefore, when time-averaging transient absorption spectra over the first 200 ns after the excitation pulses, we mostly observe the spectroscopic signature of the ^{3}MLCT excited state in this case (Figure 3b). Consequently, for identification of the photoproducts it is useful to consider transient absorption spectra that have been recorded with sufficiently long time delays after excitation (using solutions with sufficiently high pyridine concentrations). Such spectra are shown as black traces in Figure 4a (Ru−PhOH, time delay: 2 μs) and in Figure 4c (Ru−xy−PhOH, time delay: 4 μs); the long delays are possible because the photoproducts have lifetimes >30 μs (see below). The red trace in Figure 4a is a derived spectrum obtained from subtraction of the blue trace in Figure 4b (UV−vis spectrum of Ru−PhOH in

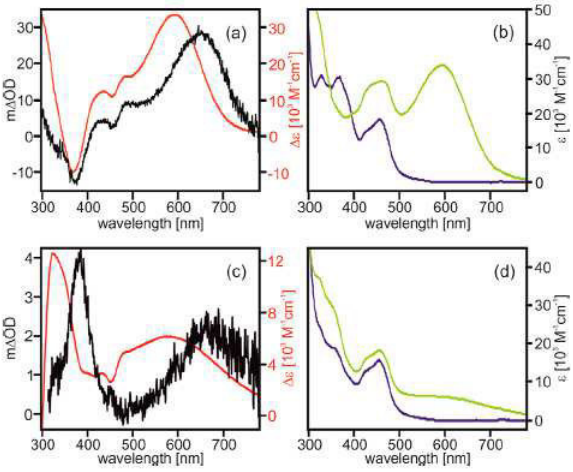

Figure 4. (a) Black trace: transient absorption spectrum measured from Ru−PhOH in CH_2Cl_2 with 6 mM pyridine after excitation at 532 nm with ~10 ns laser pulses. Detection occurred by time-averaging over a 200 ns period starting 2 μs after pulsed excitation. Red trace: spectrum obtained from subtraction of the blue trace in (b) from the green trace in (b). (b) Blue trace: UV−vis spectrum of Ru−PhOH in CH_2Cl_2. Green trace: UV−vis spectrum of Ru−PhO^- in CH_2Cl_2 (deprotonation by using excess TBAOH). (c) Black trace: transient absorption spectrum measured from Ru−xy−PhOH in CH_2Cl_2 with 200 mM pyridine after excitation at 532 nm with ~10 ns laser pulses. Detection occurred by time-averaging over a 200 ns period starting 4 μs after pulsed excitation. Red trace: spectrum obtained from subtraction of the blue trace in (d) from the green trace in (d). (d) Blue trace: UV−vis spectrum of Ru−xy−PhOH in CH_2Cl_2. Green trace: UV−vis spectrum of Ru−xy−PhO^- in CH_2Cl_2 (deprotonation by using excess TBAOH).

dx.doi.org/10.1021/jp402567m | J. Phys. Chem. A 2013, 117, 5726−5733

CH_2Cl_2) from the green trace in Figure 4b (UV−vis spectrum of Ru−PhO^- in CH_2Cl_2; measured after addition of excess TBAOH). There is significant resemblance between the derived (red) and measured (black) spectrum in Figure 4a, suggesting that the observed photoproduct is in fact the ground state of the short dyad in its deprotonated form (Ru−PhO^-) with ruthenium in its +II oxidation state. For the longer dyad, we perform a completely analogous analysis: The red trace in Figure 4c is a derived spectrum that is obtained when the blue trace in Figure 4d (spectrum of Ru−xy−PhOH in CH_2Cl_2) is subtracted from the green trace in Figure 4d (spectrum of Ru−xy−PhO^-). As for the shorter dyad, there is significant resemblance between experimental (black) and derived (red) spectra in Figure 4c, suggesting that Ru−xy−PhO^- with ruthenium in its +II oxidation state and phenolate are the photoproducts in the longer dyad, too. There are non-negligible red shifts of some of the experimental band maxima with respect to the calculated maxima in Figure 4a,c, which may have to do with the fact that the experimental transient absorption data were measured in the presence of pyridine whereas the derived spectra rely on data recorded in the absence of pyridine. Be that as it may, the similarity of experimental and derived spectra is undeniable. Notably, none of the experimental transient absorption spectra can be reconciled with a Ru(I) photoproduct (for simplicity, we use the notation "Ru(I)" to describe a one-electron reduced complex even though the additional electron is ligand-based) because for this species one would expect intense absorptions at ∼380 nm and at ∼510 nm combined with a bleach at ∼450 nm.[58−60] However, the latter two features are absent, and consequently one must observe a Ru(II) species here.

There are two possible reaction pathways leading to Ru(II)/phenolate photoproducts: (i) simple photoacid behavior and (ii) a photoinduced PCET reaction in which the phenolic proton is released to the pyridine base and an electron is transferred from the phenol to the excited $Ru(bpy)_3^{2+}$ complex, followed by rapid (thermal) back-electron transfer from the reduced ruthenium complex to the phenoxyl radical. Such a thermal back-electron transfer is thermodynamically possible because the $Ru(bpy)_3^{2+}$ unit is reduced at substantially more negative potential than the phenoxyl radical; the relevant redox potentials are listed in Table 1. Based on these values, the driving-force for the thermal back-electron transfer after initial PCET is ca. −1.37 eV for Ru(I)−$PhO^•$ and ca. −1.02 eV for Ru(I)−xy−$PhO^•$. Consequently, if such intermediates are formed, they potentially react very rapidly to Ru(II)−PhO^- and Ru(II)−xy−PhO^-, particularly in view of the high driving-forces and the comparatively short donor−acceptor distances.

For the short Ru−PhOH dyad simple photoacid behavior is a very plausible photochemical reaction pathway for the following reason: Initial MLCT excitation occurs at least partially toward one of the unsubstituted bpy ancillary ligands, and the formal Ru(III) center then increases the acidity of the pendant phenol group. Electrostatically driven changes in acidity and basicity are a common phenomenon for metal complexes with deprotonatable/protonatable ligands,[5,55,61−63] also for their excited states.[42,64−67] In the longer Ru−xy−PhOH dyad, such electrostatic effects are expected to play a smaller role, and the reaction pathway involving PCET followed by Ru(I)-to-phenoxyl electron transfer seems therefore more likely, but we are unable to observe Ru(I) or phenoxyl intermediates. However, we will show below that the activation energies associated with the photoreactions in the Ru−PhOH and Ru−xy−PhOH dyads differ by an order of magnitude which supports the hypothesis that the two dyads react through different pathways to the Ru(II)/phenolate photoproducts. On the basis of this hypothesis, we first focus on a kinetic analysis of the photoreactions in Ru−PhOH and Ru−xy−PhOH.

Parts a and b of Figure 5 show the temporal evolution of the transient absorption signal at 655 nm as a function of time for Ru−PhOH (a) and Ru-PhOD (b). (Deuteration of the complexes occurred by repeated dissolution in CH_3CN/D_2O mixture and drying in vacuo.) Analysis of these two sets of data (Figure 5c) yields Stern−Volmer constants of $K_{SV,H}$ = 1921 ±

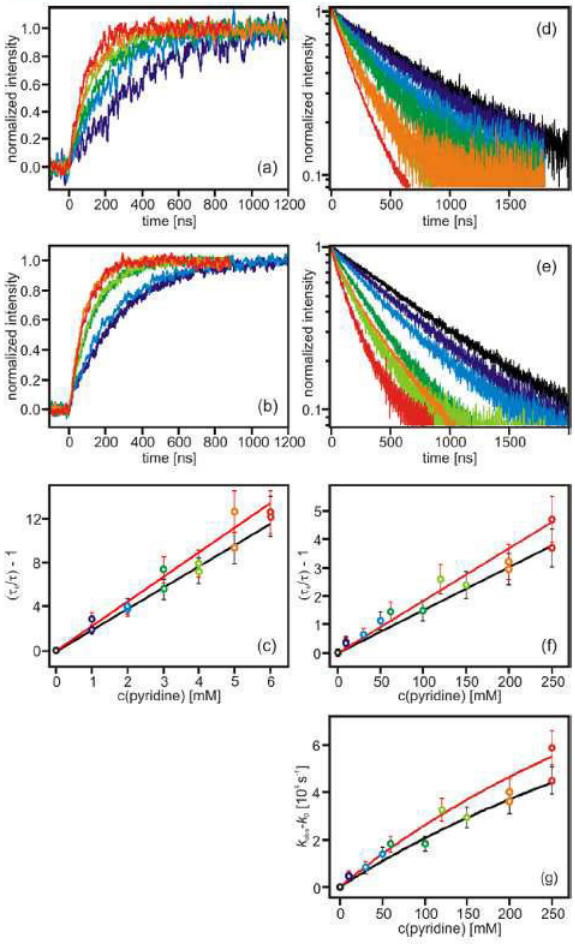

Figure 5. Rise of the transient absorption signal of Ru−PhOH (a) and Ru−PhOD (b) at 655 nm in the presence of pyridine concentrations ranging from 1 to 6 mM. (c) Stern−Volmer plots based on the data from (a) and (b). The linear regression fits were forced to have intercepts of 0; their slopes correspond to the $K_{SV,H}$ and $K_{SV,D}$ values in Table 2. Luminescence decays in Ru−xy−PhOH (d) and Ru−xy−PhOD (e) at 600 nm in the presence of pyridine concentrations ranging from 0 to 250 mM. (f) Stern−Volmer plots based on the data from (d) and (e). The linear regression fits were forced to have intercepts of 0; their slopes correspond to the $K_{SV,H}$ and $K_{SV,D}$ values in Table 2. (g) Plots of excited-state decay rate constants versus pyridine concentration for Ru−xy−PhOH and Ru−xy−PhOD with fits of eq 2 to the experimental data as described in the text. The black lines in (c), (f), (g) are for the proteo-analogs, the red lines are for the deuterated species.

dx.doi.org/10.1021/jp402567m | J. Phys. Chem. A 2013, 117, 5726−5733

Table 2. Kinetic Parameters for the Two Dyads and Excited-State Quenching by Pyridine

		τ_0 (ns)[a]	$K_{SV,X}$ (M^{-1})[b]	k_X (M^{-1} s^{-1})[c]	KIE = k_H/k_D
Ru−PhOX	X = H	1168	1921 ± 37	(1.7 ± 0.2) × 10^9	0.8 ± 0.2
	X = D		2224 ± 98	(2.0 ± 0.2) × 10^9	
Ru−xy−PhOX	X = H	818	15.1 ± 0.5	(1.9 ± 0.2) × 10^7	0.8 ± 0.2
	X = D		18.4 ± 0.8	(2.3 ± 0.3) × 10^7	

[a]^{3}MLCT lifetime in deoxygenated CH_2Cl_2 at 293 K. [b]Stern−Volmer constants corresponding to the slopes of linear regression fits to the data in Figure 5c,f (forced to have intercepts of 0). [c]Rate constants for bimolecular excited-state quenching were calculated using the relation $k_X = K_{SV,X}/\tau_0$.

37 M^{-1} and $K_{SV,D}$ = 2224 ± 98 M^{-1} for Ru−PhOH and Ru−PhOD, respectively (Table 2). Using a lifetime of 1168 ns for the $Ru(bpy)_3^{2+}$ unit of this dyad in pure CH_2Cl_2, one obtains rate constants for bimolecular excited-state quenching of k_H = (1.7 ± 0.2)·10^9 M^{-1} s^{-1} and k_D = (2.0 ± 0.2)·10^9 M^{-1} s^{-1} (Table 2).

In the Ru−xy−PhOH dyad excited-state quenching following pyridine addition is markedly less efficient than in Ru−PhOH, and we have found it most convenient to perform a Stern−Volmer analysis based on the luminescence lifetime data presented in Figure 5d,e. The emission decays were measured at 600 nm after ~10 ns pulsed excitation at 532 nm, using normal Ru−xy−PhOH (d) and its deuterated analogue (e). The Stern−Volmer plot in Figure 5f yields $K_{SV,H}$ = 15.1 ± 0.5 M^{-1} and $K_{SV,D}$ = 18.4 ± 0.8 M^{-1} (Table 2).

The ^{3}MLCT lifetime of Ru−xy−PhOH in the absence of pyridine is 818 ns, and this leads to k_H = (1.9 ± 0.2) × 10^7 M^{-1} s^{-1} and k_D = (2.3 ± 0.3) × 10^7 M^{-1} s^{-1}, which is roughly a factor of 100 lower than what has been determined for the shorter dyad (Table 2). We note that all experimental emission decays of Ru−xy−PhOH exhibited both a fast and a slow decay component (the deviation from single exponential decay behavior is readily visible in Figure 5d,e). We attribute the slow decay component to impurities of $Ru(bpy)_3^{2+}$, the luminescence of which is essentially unaffected by pyridine addition (at least in the concentration range used here). In our biexponential fits we fixed the slow component to 786 ns, which is what we have measured for the luminescence lifetime of $Ru(bpy)_3^{2+}$ in deoxygenated CH_2Cl_2 at room temperature. The fast decay components arise due excited-state quenching by a photochemical reaction. As discussed above, our hypothesis is that Ru−xy−PhOH reacts through a sequence of PCET and ET reactions. The initial PCET process forming Ru(I) and phenoxyl intermediates is considered rate-determining, the ensuing Ru(I)-to-phenoxyl radical is likely to be very rapid for reasons mentioned above.

A key problem with the foregoing Stern−Volmer analysis is that it does not take into account the hydrogen-bonding equilibrium between the phenol and pyridine in CH_2Cl_2. We address this shortcoming for the Ru−xy−PhOH dyad with Figure 5g, which shows a plot of $k_{obs} - k_0$ versus the pyridine concentration and make a fit to the experimental data with eq 2;[40] k_{obs} is the inverse of τ at a given pyridine concentration, k_0 is the excited-state decay rate constant in the absence of pyridine. [B] is the pyridine concentration, and K_A is the association constant for the formation of hydrogen-bonded phenol−pyridine adducts. k_{PCET} is the rate constant for intramolecular phenol-to-ruthenium electron transfer occurring in concert with release of the phenolic proton to the hydrogen-bonded pyridine.

$$k_{obs} - k_0 = k_{PCET}\cdot(K_A\cdot[B])/(1 + K_A\cdot[B]) \quad (2)$$

This is a simplified version of an equation used recently in a very similar context;[21] the simple form of eq 2 is due to the absence of significant direct excited-state quenching by pyridine and the fact that intramolecular electron transfer is negligible in the absence of pyridine. We have attempted to determine the association constants in an independent manner, using a luminescence-intensity based method described previously.[43] This analysis (Figure S3, Supporting Information) yields K_A = 1695 ± 172 M^{-1} for Ru−PhOH and 14.2 ± 1.3 M^{-1} for Ru−xy−PhOH. It is impossible to reconcile these K_A values with fits of eq 2 to the experimental data in Figure 5g using k_{PCET} as a sole fit parameter; K_A values on the order of 10 M^{-1} or greater will lead to significant curvature in the calculated plots of $k_{obs} - k_0$. What is more, the K_A value of 1695 ± 172 M^{-1} seems far too large in comparison to other phenol−pyridine adducts in solvents of comparable polarity.[40,68] We therefore decided to let both k_{PCET} and K_A vary freely in our fits to the data in Figure 5g, but this procedure naturally leads to large error bars. We find k_{PCET} = (1.8 ± 1.0) × 10^7 s^{-1}/K_A = 1.2 ± 0.8 M^{-1} for Ru−xy−PhOH and k_{PCET} = (2.1 ± 1.4) × 10^7 s^{-1}/K_A = 1.4 ± 1.2 M^{-1} for Ru−xy−PhOD. Evidently, we can only make order-of-magnitude estimates for k_{PCET} and K_A using this method.

H/D Kinetic Isotope Effects and Activation Energies. In room temperature solution essentially no H/D kinetic isotope effects (KIEs) are observed in the data from Figure 5 even though proton motion is likely to be involved in the deactivation processes of both dyads (Table 2): In both cases we find k_H/k_D = 0.8 ± 0.2. However, in the course of determining the activation energies for the photoreactions of the two dyads we found that the shorter one exhibits a temperature dependent H/D KIE because for Ru−PhOD the activation energy is 3 times larger than for Ru−PhOH.

The Arrhenius plot in Figure 6a shows the rates for formation of Ru(II)-PhO^- after photoexcitation of Ru−PhOH

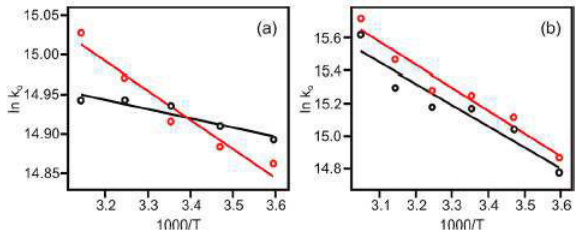

Figure 6. Arrhenius plots based on the rate constants for formation of the photoproducts obtained after pulsed excitation of (a) Ru−PhOH/D in CH_2Cl_2 with 2 mM pyridine (experimental observable: luminescence decay detected at 600 nm) and (b) Ru−xy−PhOH/D in CH_2Cl_2 with 200 mM pyridine (experimental observable: luminescence decay detected at 600 nm): black circles, normal samples; red circles, deuterated samples. The solid lines are linear regression fits from the slopes of which the activation energies (E_A) in Table 3 were calculated.

dx.doi.org/10.1021/jp402567m | J. Phys. Chem. A 2013, 117, 5726−5733

(black circles) and Ru−PhOD (red circles) in 1,2-dichloroethane in the presence of 2 mM pyridine; the individual data points were obtained from emission decay measurements (Figure S4, Supporting Information), and the lifetimes extracted from these data are in good agreement with the risetimes observed for the transient absorption signal at 655 nm (data not shown). Linear regression yields an activation energy (E_A) of 0.010 ± 0.002 eV for Ru−PhOH, whereas E_A = 0.032 ± 0.004 eV for Ru−PhOD (Table 3).

Table 3. Activation Energies (E_A) for the Photoreactions of the Two Dyads

	E_A (X = H) (eV)	E_A (X = D) (eV)
Ru−PhOX	0.010 ± 0.002	0.032 ± 0.004
Ru−xy−PhOX	0.112 ± 0.017	0.121 ± 0.014

For the Ru−xy−PhOH dyad (Figure 6b) we determine activation energies, which are much more similar for proteo- and deuterio-analogues: Using emission lifetimes as an experimental observable and a pyridine concentration of 200 mM in 1,2-dichloroethane (Figure S4, Supporting Information), we determine E_A = 0.112 ± 0.017 eV for Ru−xy−PhOH and E_A = 0.121 ± 0.014 eV for Ru−xy−PhOD (Table 3). The factor of 10 increase of E_A between Ru−xy−PhOH and Ru−PhOH supports the hypothesis that the two dyads react via different pathways to the Ru(II)/phenolate photoproducts. The factor of 3 increase of E_A between Ru−PhOH and Ru−PhOD possibly reflects the lower zero-point energy of the O−D vibration with respect to the O−H vibration. The association constant for formation of hydrogen-bonded phenol−pyridine adducts is temperature-dependent; however, we expect that this hydrogen-bonding equilibrium is similarly influenced by temperature in all dyads considered here.

Thermal Backward Reactions with Inverse H/D Kinetic Isotope Effects. The transient absorption intensities at 655 nm in the shorter dyad and at 395 nm in the longer dyad exhibit single exponential decays which, in the 2−200 mM pyridine concentration range, are essentially independent of the exact amount of pyridine present. Under these conditions the concentration of pyridinium ions seems to determine the rate for reaction of the deprotonated phenols back to their initial forms. The pyridinium concentration in turn is limited by the number of dyads that have undergone photochemical reaction, and this concentration is always lower than 10^{-5} M. In deoxygenated CH_2Cl_2 in the presence of pyridine, the average decay time of the transient absorption signal at 655 nm (Figure 4a) is 50.9 μs when Ru−PhOH is used and 34.2 μs when Ru−PhOD is used (Table 4). Representative decay curves

Table 4. Time Constants and Kinetic Isotope Effects for Thermal Back-Reaction

	τ_{BR} (X = H) (μs)	τ_{BR} (X = D) (μs)	KIE
Ru−PhOX	50.9	34.2	0.7 ± 0.1
Ru−xy−PhOX	31.9	19.1	0.6 ± 0.1

(obtained at a pyridine concentration of 3 mM) are shown in Figure S5a of the Supporting Information. In deoxygenated CH_2Cl_2 in the presence of up to 200 mM pyridine the transient absorption intensity at 395 nm (Figure 4c) has an average lifetime of 31.9 μs when Ru−xy−PhOH is used and an average lifetime of 19.1 μs when Ru−xy−PhOD is used (Table 4). Representative decay curves for the longer dyad are shown in Figure S5b (Supporting Information). The occurrence of inverse H/D kinetic isotope effects of 0.7 ± 0.1 for Ru−PhOH and 0.6 ± 0.1 for Ru−xy−PhOH is rather unusual, but at present the origin of this phenomenon is not clear.

In a previously investigated rhenium(I)−phenol dyad (Re−PhOH) we had also observed a phenolate species as a major photoproduct (in CH_3CN/H_2O), whereas for a rhenium(I)−xylene−phenol dyad (Re−xy−PhOH) the spectroscopic data were consistent with a PCET reaction leading to a reduced rhenium complex and a phenoxyl radical.[30] Interestingly, the PCET phenoxyl radical photoproduct is much shorter-lived (85 ns) than the phenolate photoproducts observed for Ru−PhOH (50.9 μs), Ru−xy−PhOH (31.9 μs), and Re−xy−PhOH (14 μs). It thus seems that phenolate protonation in these dyads occurs significantly more slowly than the (thermal) PCET reaction leading to disappearance of the phenoxyl radical in Re−xy−PhOH.

■ SUMMARY AND CONCLUSION

In pure CH_2Cl_2 neither of the two dyads exhibits any photochemistry, neither electron transfer nor proton transfer nor PCET. When pyridine is present, selective excitation of their $Ru(bpy)_3^{2+}$ moieties leads to photoproducts containing Ru(II) in the ground state and a phenolate moiety. In principle, phenol deprotonation can occur via two different reaction mechanisms: (i) direct proton release from the excited dyad or (ii) initial rate-determining PCET forming Ru(I) and phenoxyl intermediates followed by rapid (because highly exergonic) phenoxyl-to-Ru(I) electron transfer. Photoacid behavior seems plausible for Ru−PhOH because of the short ruthenium−phenol distance but is less likely in the longer Ru−xy−PhOH dyad. The observation of activation energies that differ by an order of magnitude for the photochemical reactions of Ru−PhOH and Ru−xy−PhOH supports the hypothesis that the two dyads react through different reaction pathways.

The present study illustrates one of the key difficulties that can be associated with the observation of intramolecular photoinduced PCET: Initial excited-state PCET can be followed by rapid (thermal) electron transfer in the reverse direction, thereby impeding the observation of PCET photoproducts. In practice, it then becomes challenging to distinguish such a reaction sequence from simple photoacid behavior.

■ EXPERIMENTAL SECTION

UV−vis spectra were recorded on a Cary 300 instrument from Varian, and steady-state luminescence was measured on a Fluorolog-3 instrument from Horiba Jobin-Yvon using a TBC-07C photomultiplier from Hamamatsu. Transient absorption and time-resolved emission were measured on the LP920-KS flash photolysis system from Edinburgh Instruments employing an iCCD camera from Andor and an R928 photomultiplier for detection. The laser excitation source was a frequency-doubled Quantel Brilliant b laser. Temperature control in the activation energy experiments occurred with a TC-125 instrument from Quantum Northwest. For cyclic voltammetry a Versastat3-200 potentiostat from Princeton Applied Research was employed, using a Pt disk working electrode and two silver wires as quasi-reference and counter-electrodes. Synthetic protocols and product characterization data are given in the Supporting Information. For product characterization we used the NMR, mass spectrometry, and elemental analysis equipment described

dx.doi.org/10.1021/jp402567m | J. Phys. Chem. A 2013, 117, 5726−5733

previously.[30,54] Errors reported for rate constants and KIEs are standard deviations, as obtained from corresponding fits and based on the experience that our kinetic measurements are accurate to ±10%.

■ ASSOCIATED CONTENT

Supporting Information

Detailed synthetic protocols and product characterization data and additional electrochemical, luminescence, and transient absorption data. This material is available free of charge via the Internet at http://pubs.acs.org.

■ AUTHOR INFORMATION

Corresponding Author

*E-mail: oliver.wenger@unibas.ch.

Notes

The authors declare no competing financial interest.

■ ACKNOWLEDGMENTS

Funding from the Deutsche Forschungsgemeinschaft (DFG) through IRTG-1422 is gratefully acknowledged.

■ REFERENCES

(1) Meyer, T. J.; Huynh, M. H. V.; Thorp, H. H. The Possible Role of Proton-Coupled Electron Transfer (PCET) in Water Oxidation by Photosystem II. *Angew. Chem., Int. Ed.* **2007**, *46*, 5284−5304.

(2) Meyer, T. J. Chemical Approaches to Artificial Photosynthesis. *Acc. Chem. Res.* **1989**, *22*, 163−170.

(3) Bordwell, F. G.; Cheng, J. P. Substituent Effects on the Stabilities of Phenoxyl Radicals and the Acidities of Phenoxyl Radical Cations. *J. Am. Chem. Soc.* **1991**, *113*, 1736−1743.

(4) Warren, J. J.; Tronic, T. A.; Mayer, J. M. Thermochemistry of Proton-Coupled Electron Transfer Reagents and its Implications. *Chem. Rev.* **2010**, *110*, 6961−7001.

(5) Mayer, J. M. Proton-Coupled Electron Transfer: A Reaction Chemist's View. *Annu. Rev. Phys. Chem.* **2004**, *55*, 363−390.

(6) Roth, J. P.; Yoder, J. C.; Won, T. J.; Mayer, J. M. Application of the Marcus Cross Relation to Hydrogen Atom Transfer Reactions. *Science* **2001**, *294*, 2524−2526.

(7) Reece, S. Y.; Nocera, D. G. Proton-Coupled Electron Transfer in Biology: Results from Synergistic Studies in Natural and Model Systems. *Annu. Rev. Biochem.* **2009**, *78*, 673−699.

(8) Costentin, C.; Robert, M.; Savéant, J.-M. Concerted Proton-Electron Transfers: Electrochemical and Related Approaches. *Acc. Chem. Res.* **2010**, *43*, 1019−1029.

(9) Maki, T.; Araki, Y.; Ishida, Y.; Onomura, O.; Matsumura, Y. Construction of Persistent Phenoxyl Radical with Intramolecular Hydrogen Bonding. *J. Am. Chem. Soc.* **2001**, *123*, 3371−3372.

(10) Markle, T. F.; Mayer, J. M. Concerted Proton-Electron Transfer in Pyridylphenols: The Importance of the Hydrogen Bond. *Angew. Chem., Int. Ed.* **2008**, *47*, 738−740.

(11) Rhile, I. J.; Markle, T. F.; Nagao, H.; DiPasquale, A. G.; Lam, O. P.; Lockwood, M. A.; Rotter, K.; Mayer, J. M. Concerted Proton-Electron Transfer in the Oxidation of Hydrogen-Bonded Phenols. *J. Am. Chem. Soc.* **2006**, *128*, 6075−6088.

(12) Rhile, I. J.; Mayer, J. M. One-Electron Oxidation of a Hydrogen-Bonded Phenol Occurs by Concerted Proton-Coupled Electron Transfer. *J. Am. Chem. Soc.* **2004**, *126*, 12718−12719.

(13) Markle, T. F.; Tenderholt, A. L.; Mayer, J. M. Probing Quantum and Dynamic Effects in Concerted Proton-Electron Transfer Reactions of Phenol-Base Compounds. *J. Phys. Chem. B* **2012**, *116*, 571−584.

(14) Markle, T. F.; Rhile, I. J.; DiPasquale, A. G.; Mayer, J. M. Probing Concerted Proton-Electron Transfer in Phenol-Imidazoles. *Proc. Natl. Acad. Sci. U. S. A.* **2008**, *105*, 8185−8190.

(15) Irebo, T.; Johansson, O.; Hammarström, L. The Rate Ladder of Proton-Coupled Tyrosine Oxidation in Water: A Systematic Dependence on Hydrogen Bonds and Protonation State. *J. Am. Chem. Soc.* **2008**, *130*, 9194−9195.

(16) Sjödin, M.; Irebo, T.; Utas, J. E.; Lind, J.; Merenyi, G.; Åkermark, B.; Hammarström, L. Kinetic Effects of Hydrogen Bonds on Proton-Coupled Electron Transfer from Phenols. *J. Am. Chem. Soc.* **2006**, *128*, 13076−13083.

(17) Schrauben, J. N.; Cattaneo, M.; Day, T. C.; Tenderholt, A. L.; Mayer, J. M. Mutiple-Site Concerted Proton-Electron Transfer Reactions of Hydrogen-Bonded Phenols are Nonadiabatic and Well Described by Semiclassical Marcus Theory. *J. Am. Chem. Soc.* **2012**, *134*, 16635−16645.

(18) Costentin, C.; Robert, M.; Savéant, J. M.; Tard, C. Inserting a Hydrogen-Bond Relay between Proton Exchanging Sites in Proton-Coupled Electron Transfers. *Angew. Chem., Int. Ed.* **2010**, *49*, 3803−3806.

(19) Costentin, C.; Robert, M.; Savéant, J. M.; Tard, C. H-Bond Relays in Proton-Coupled Electron Transfers. Oxidation of a Phenol Concerted with Proton Transport to a Distal base Through an OH Relay. *Phys. Chem. Chem. Phys.* **2011**, *13*, 5353−5358.

(20) Benisvy, L.; Bittl, R.; Bothe, E.; Garner, C. D.; McMaster, J.; Ross, S.; Teutloff, C.; Neese, F. Phenoxyl Radicals Hydrogen-Bonded to Imidazolium: Analogues of Tyrosyl D of Photosystem II: High-Field EPR and DFT Studies. *Angew. Chem., Int. Ed.* **2005**, *44*, 5314−5317.

(21) Pizano, A. A.; Yang, J. L.; Nocera, D. G. Photochemical Tyrosine Oxidation with a Hydrogen-Bonded Proton Acceptor by Bidirectional Proton-Coupled Electron Transfer. *Chem. Sci.* **2012**, *3*, 2457−2461.

(22) Zhang, M.-T.; Irebo, T.; Johansson, O.; Hammarström, L. Proton-Coupled Electron Transfer from Tyrosine: A Strong Rate Dependence on Intramolecular Proton Transfer Distance. *J. Am. Chem. Soc.* **2011**, *133*, 13224−13227.

(23) Markle, T. F.; Rhile, I. J.; Mayer, J. M. Kinetic Effects of Increased Proton Transfer Distance on Proton-Coupled Oxidations of Phenol-Amines. *J. Am. Chem. Soc.* **2011**, *133*, 17341−17352.

(24) Irebo, T.; Reece, S. Y.; Sjödin, M.; Nocera, D. G.; Hammarström, L. Proton-Coupled Electron Transfer of Tyrosine Oxidation: Buffer Dependence and Parallel Mechanisms. *J. Am. Chem. Soc.* **2007**, *129*, 15462−15464.

(25) Irebo, T.; Zhang, M.-T.; Markle, T. F.; Scott, A. M.; Hammarström, L. Spanning Four Mechanistic Regions of Intramolecular Proton-Coupled Electron Transfer in a $Ru(bpy)_3^{2+}$-Tyrosine Complex. *J. Am. Chem. Soc.* **2012**, *134*, 16247−16254.

(26) Costentin, C.; Robert, M.; Savéant, J. M. Concerted Proton-Electron Transfer Reactions in Water. Are the Driving Force and Rate Constant Depending on pH When Water Acts as Proton Donor or Acceptor? *J. Am. Chem. Soc.* **2007**, *129*, 5870−5879.

(27) Bonin, J.; Costentin, C.; Louault, C.; Robert, M.; Savéant, J. M. Water (in Water) as an Intrinsically Efficient Proton Acceptor in Concerted Proton Electron Transfers. *J. Am. Chem. Soc.* **2011**, *133*, 6668−6674.

(28) Manner, V. W.; DiPasquale, A. G.; Mayer, J. M. Facile Concerted Proton-Electron Transfers in a Ruthenium Terpyridine-4′-carboxylate Complex with a Long Distance between the Redox and Basic Sites. *J. Am. Chem. Soc.* **2008**, *130*, 7210−7211.

(29) Manner, V. W.; Mayer, J. M. Concerted Proton-Electron Transfer in a Ruthenium Terpyridyl-Benzoate System with a Large Separation between the Redox and Basic Sites. *J. Am. Chem. Soc.* **2009**, *131*, 9874−9875.

(30) Kuss-Petermann, M.; Wolf, H.; Stalke, D.; Wenger, O. S. Influence of Donor-Acceptor Distance Variation on Photoinduced Electron and Proton Transfer in Rhenium(I)-Phenol Dyads. *J. Am. Chem. Soc.* **2012**, *134*, 12844−12854.

(31) Warren, J. J.; Menzeleev, A. R.; Kretchmer, J. S.; Miller, T. F.; Gray, H. B.; Mayer, J. M. Long-Range Proton-Coupled Electron-Transfer Reactions of Bis(imidazole) Iron Tetraphenylporphyrins Linked to Benzoates. *J. Phys. Chem. Lett.* **2013**, *4*, 519−523.

(32) Edwards, P. P.; Gray, H. B.; Lodge, M. T. J.; Williams, R. J. P. Electron Transfer and Electronic Conduction through an Intervening Medium. *Angew. Chem., Int. Ed.* **2008**, *47*, 6758−6765.
(33) Gray, H. B.; Winkler, J. R. Long-Range Electron Transfer. *Proc. Natl. Acad. Sci. U. S. A.* **2005**, *102*, 3534−3539.
(34) Eng, M. P.; Albinsson, B. Non-Exponential Distance Dependence of Bridge-Mediated Electronic Coupling. *Angew. Chem., Int. Ed.* **2006**, *45*, 5626−5629.
(35) Weiss, E. A.; Ahrens, M. J.; Sinks, L. E.; Gusev, A. V.; Ratner, M. A.; Wasielewski, M. R. Making a Molecular Wire: Charge and Spin Transport through Para-Phenylene Oligomers. *J. Am. Chem. Soc.* **2004**, *126*, 5577−5584.
(36) Wenger, O. S. How Donor-Bridge-Acceptor Energetics Influence Electron Tunneling Dynamics and their Distance Dependences. *Acc. Chem. Res.* **2011**, *44*, 25−35.
(37) Indelli, M. T.; Chiorboli, C.; Flamigni, L.; De Cola, L.; Scandola, F. Photoinduced Electron Transfer across Oligo-*p*-Phenylene Bridges. Distance and Conformational Effects in Ru(II)-Rh(III) Dyads. *Inorg. Chem.* **2007**, *46*, 5630−5641.
(38) Costentin, C.; Robert, M.; Savéant, J. M. Electrochemical and Homogeneous Proton-Coupled Electron Transfers: Concerted Pathways in the One-Electron Oxidation of a Phenol Coupled with an Intramolecular Amine-Driven Proton Transfer. *J. Am. Chem. Soc.* **2006**, *128*, 4552−4553.
(39) Costentin, C.; Robert, M.; Savéant, J. M. Concerted Proton-Electron Transfers in the Oxidation of Phenols. *Phys. Chem. Chem. Phys.* **2010**, *12*, 11179−11190.
(40) Biczok, L.; Gupta, N.; Linschitz, H. Coupled Electron-Proton Transfer in Interactions of Triplet C-60 with Hydrogen-Bonded Phenols: Effects of Solvation, Deuteration, and Redox Potentials. *J. Am. Chem. Soc.* **1997**, *119*, 12601−12609.
(41) Gagliardi, C. J.; Westlake, B. C.; Kent, C. A.; Paul, J. J.; Papanikolas, J. M.; Meyer, T. J. Integrating Proton Coupled Electron Transfer (PCET) and Excited States. *Coord. Chem. Rev.* **2010**, *254*, 2459−2471.
(42) Wenger, O. S. Proton-Coupled Electron Transfer Originating from Excited States of Luminescent Transition-Metal Complexes. *Chem.—Eur. J.* **2011**, *17*, 11692−11702.
(43) Concepcion, J. J.; Brennaman, M. K.; Deyton, J. R.; Lebedeva, N. V.; Forbes, M. D. E.; Papanikolas, J. M.; Meyer, T. J. Excited-State Quenching by Proton-Coupled Electron Transfer. *J. Am. Chem. Soc.* **2007**, *129*, 6968−6969.
(44) Moore, G. F.; Hambourger, M.; Gervaldo, M.; Poluektov, O. G.; Rajh, T.; Gust, D.; Moore, T. A.; Moore, A. L. A Bioinspired Construct that Mimics the Proton Coupled Electron Transfer between $P680^{\bullet+}$ and the Tyr_z-His_{190} pair of Photosystem II. *J. Am. Chem. Soc.* **2008**, *130*, 10466−10467.
(45) Bronner, C.; Wenger, O. S. Proton-Coupled Electron Transfer between 4-Cyanophenol and Photoexcited Rhenium(I) Complexes with Different Protonatable Sites. *Inorg. Chem.* **2012**, *51*, 8275−8283.
(46) Bronner, C.; Wenger, O. S. Kinetic Isotope Effects in Reductive Excited-State Quenching of $Ru(2,2'\text{-bipyrazine})_3^{2+}$ by Phenols. *J. Phys. Chem. Lett.* **2012**, *3*, 70−74.
(47) Wenger, O. S. Proton-Coupled Electron Transfer with Photoexcited Metal Complexes. *Acc. Chem. Res.* **2013**, DOI: 10.1021/ar300289x.
(48) Renger, G.; Renger, T. Photosystem II: The Machinery of Photosynthetic Water Splitting. *Photosynth. Res.* **2008**, *98*, 53−80.
(49) Magnuson, A.; Berglund, H.; Korall, P.; Hammarström, L.; Åkermark, B.; Styring, S.; Sun, L. C. Mimicking Electron Transfer Reactions in Photosystem II: Synthesis and Photochemical Characterization of a Ruthenium(II) tris(bipyridyl) Complex with a Covalently linked Tyrosine. *J. Am. Chem. Soc.* **1997**, *119*, 10720−10725.
(50) Lachaud, T.; Quaranta, A.; Pellegrin, Y.; Dorlet, P.; Charlot, M. F.; Un, S.; Leibl, W.; Aukauloo, A. A Biomimetic Model of the Electron Transfer between P-680 and the Tyr_Z-His_{190} pair of PSII. *Angew. Chem., Int. Ed.* **2005**, *44*, 1536−1540.
(51) Sun, L. C.; Burkitt, M.; Tamm, M.; Raymond, M. K.; Abrahamsson, M.; LeGourriérec, D.; Frapart, Y.; Magnuson, A.; Kenéz, P. H.; Brandt, P.; Tran, A.; Hammarström, L.; Styring, S.; Åkermark, B. Hydrogen-Bond Promoted Intramolecular Electron Transfer to Photogenerated Ru(III): A Functional Mimic of Tyrosine(Z) and Histidine 190 in Photosystem II. *J. Am. Chem. Soc.* **1999**, *121*, 6834−6842.
(52) Sjödin, M.; Styring, S.; Åkermark, B.; Sun, L. C.; Hammarström, L. Proton-Coupled Electron Transfer from Tyrosine in a Tyrosine-Ruthenium-Tris-Bipyridine Complex: Comparison with Tyrosine(z) Oxidation in Photosystem II. *J. Am. Chem. Soc.* **2000**, *122*, 3932−3936.
(53) Johansson, O.; Wolpher, H.; Borgström, M.; Hammarström, L.; Bergquist, J.; Sun, L. C.; Åkermark, B. Intramolecular Charge Separation in a Hydrogen Bonded Tyrosine-Ruthenium(II)-Naphthalene Diimide Triad. *Chem. Commun.* **2004**, 194−195.
(54) Hankache, J.; Niemi, M.; Lemmetyinen, H.; Wenger, O. S. Photoinduced Electron Transfer in Linear Triarylamine-Photosensitizer-Anthraquinone Triads with Ruthenium(II), Osmium(II), and Iridium(III). *Inorg. Chem.* **2012**, *51*, 6333−6344.
(55) Cargill Thompson, A. M. W.; Smailes, M. C. C.; Jeffery, J. C.; Ward, M. D. Ruthenium Tris-(bipyridyl) Complexes with Pendant Protonatable and Deprotonatable Moieties: pH Sensitivity of Electronic Spectral and Luminescence Properties. *J. Chem. Soc., Dalton Trans.* **1997**, 737−743.
(56) Milder, S. J.; Gold, J. S.; Kliger, D. S. Temperature-Dependence of the Excited-State Absorption of $Ru(bpy)_3^{2+}$. *J. Phys. Chem.* **1986**, *90*, 548−550.
(57) Weller, A. Photoinduced Electron-Transfer in Solution - Exciplex and Radical Ion-Pair Formation Free Enthalpies and their Solvent Dependence. *Z. Phys. Chem.* **1982**, *133*, 93−98.
(58) Heath, G. A.; Yellowlees, L. J.; Braterman, P. S. Spectro-Electrochemical Studies on Tris-Bipyridyl Ruthenium Complexes - UV, Visible, and Near-Infrared Spectra of the Series $Ru(bipyridyl)_3^{2+/1+/0/1-}$. *J. Chem. Soc., Chem. Commun.* **1981**, 287−289.
(59) Lomoth, R.; Haupl, T.; Johansson, O.; Hammarström, L. Redox-Switchable Direction of Photoinduced Electron Transfer in an $Ru(bpy)_3^{2+}$-Viologen Dyad. *Chem.—Eur. J.* **2002**, *8*, 102−110.
(60) Hanss, D.; Wenger, O. S. Conformational Effects on Long-Range Electron Transfer: Comparison of Oligo-*p*-Phenylene and Oligo-*p*-Xylene Bridges. *Eur. J. Inorg. Chem.* **2009**, 3778−3790.
(61) Carina, R. F.; Verzegnassi, L.; Bernardinelli, G.; Williams, A. F. Modulation of Iron Reduction Potential by Deprotonation at a Remote Site. *Chem. Commun.* **1998**, 2681−2682.
(62) Jones, H.; Newell, M.; Metcalfe, C.; Spey, S. E.; Adams, H.; Thomas, J. A. Deprotonation of a Ruthenium(II) Complex Incorporating a Bipyrazole Ligand Leading to Optical and Electrochemical Switching. *Inorg. Chem. Commun.* **2001**, *4*, 475−477.
(63) Klein, S.; Dougherty, W. G.; Kassel, W. S.; Dudley, T. J.; Paul, J. J. Structural, Electronic, and Acid/Base Properties of $Ru(bpy)_2(bpy(OH)_2)^{2+}$ (bpy=2,2′-Bipyridine, bpy(OH)$_2$=4,4′-Dihydroxy-2,2′-bipyridine. *Inorg. Chem.* **2011**, *50*, 2754−2763.
(64) Vos, J. G. Excited-State Acid-Base Properties of Inorganic Compounds. *Polyhedron* **1992**, *11*, 2285−2299.
(65) Sun, H.; Hoffman, M. Z. Protonation of the Excited-States of Ruthenium(II) Complexes Containing 2,2′-Bipyridine, 2,2′-Bipyrazine, and 2,2′-Bipyrimidine Ligands in Aqueous Solution. *J. Phys. Chem.* **1993**, *97*, 5014−5018.
(66) Giordano, P. J.; Bock, C. R.; Wrighton, M. S.; Interrante, L. V.; Williams, R. F. X. Excited-State Proton-Transfer of a Metal-Complex - Determination of Acid Dissociation-Constant for a Metal-to-Ligand Charge-Transfer State of a Ruthenium(II) Complex. *J. Am. Chem. Soc.* **1977**, *99*, 3187−3189.
(67) Bare, W. D.; Mack, N. H.; Demas, J. N.; DeGraff, B. A. pH-Dependent Photophysical Behavior of Rhenium Complexes Containing Hydroxypyridine Ligands. *Appl. Spectrosc.* **2004**, *58*, 1093−1100.
(68) Biczók, L.; Linschitz, H. Concerted Electron and Proton Movement in Quenching of Triplet C-60 and Tetracene Fluorescence by Hydrogen-Bonded Phenol-Base Pairs. *J. Phys. Chem.* **1995**, *99*, 1843−1845.

ChemPubSoc Europe

DOI: 10.1002/chem.201304256

CHEMISTRY A European Journal Full Paper

Proton-Coupled Electron Transfer

Distance Dependence of Bidirectional Concerted Proton–Electron Transfer in Phenol-Ru(2,2′-bipyridine)$_3^{2+}$ Dyads

Jing Chen, Martin Kuss-Petermann, and Oliver S. Wenger*[a]

Abstract: Proton-coupled electron transfer (PCET) was investigated in three covalent donor–bridge–acceptor molecules with different bridge lengths. Upon photoexcitation of their Ru(bpy)$_3^{2+}$ (bpy = 2,2′-bipyridine) photosensitizer in acetonitrile, intramolecular long-range electron transfer from a phenolic unit to Ru(bpy)$_3^{2+}$ occurs in concert with release of the phenolic proton to pyrrolidine base. The kinetics of this bidirectional concerted proton–electron transfer (CPET) reaction were studied as a function of phenol–Ru(bpy)$_3^{2+}$ distance by increasing the number of bridging *p*-xylene units. A distance decay constant (β) of 0.67 ± 0.23 Å^{-1} was determined. The distance dependence of the rates for CPET is thus not significantly steeper than that for ordinary (i.e., not proton coupled) electron transfer across the same bridges, despite the concerted motion of oppositely charged particles into different directions. Long-range bidirectional CPET is an important reaction in many proteins and plays a key role in photosynthesis; our results are relevant in the context of photoinduced separation of protons and electrons as a means of light-to-chemical energy conversion. This is the first determination of β for a bidirectional CPET reaction.

Introduction

The distance dependence of "simple" electron transfer has been thoroughly explored in proteins,[1] DNA,[2,3] self-assembled monolayers,[4] and donor–bridge–acceptor molecules.[5,6] An important open question is how the distance between an electron donor and an electron acceptor affects the rates of proton-coupled electron transfer (PCET) reactions, particularly when electron and proton transfer occur in concerted fashion and when the electron and the proton are transferred into different directions. Long-range PCET reactions of this type are biologically relevant, for instance in photosystem II, in ribonucleotide reductase, and in DNA.[7–9] We are unaware of prior investigations of the distance dependence of bidirectional concerted proton-electron transfer (CPET) reactions.

The rate constant for a PCET reaction can be expressed in a similar way as the rate constant for "simple" electron transfer, that is, in analogy to what is commonly known as the Marcus equation.[10] In Equation (1), $H_{AB,PCET}$ is the electronic coupling between the PCET reactant and product states, λ_{PCET} is the reorganization energy associated with the overall PCET process, and ΔG^0_{PCET} is the reaction free energy.[11] The interplay between these three factors governs the PCET rate constant (k_{PCET}).

In many cases of "simple" electron transfer the distance dependence of reaction rates is dominated by the electronic coupling term (H_{AB}),[1,5] but in other cases changes in reorganization energy (λ) or reaction free energy (ΔG^0) with increasing donor–acceptor distance are more important.[12,13] It is not a priori clear which one of the three factors ($H_{AB,PCET}$, λ_{PCET}, ΔG^0_{PCET}) will dominate the distance dependence of a bidirectional CPET reaction. On the one hand, increasing the electron donor/electron acceptor distance is expected to have a significant influence on $H_{AB,PCET}$.[11] On the other hand, it is known that bidirectional CPET reactions can be associated with significantly larger reorganization energies (λ_{PCET}) than "simple" electron-transfer reactions,[14] and significant changes in λ_{PCET} with distance could strongly influence CPET rates.

$$k_{PCET} = \frac{2\pi}{\hbar} H^2_{AB,PCET} \frac{1}{\sqrt{4\pi\lambda_{PCET}RT}} \exp\left[-\frac{(\Delta G^0_{PCET} + \lambda_{PCET})^2}{4\lambda_{PCET}RT}\right] \quad (1)$$

In the work presented herein we aimed to explore these basic aspects by using the phenol–Ru(bpy)$_3^{2+}$ (bpy = 2,2′-bipyridine) dyads shown in Scheme 1. They are comprised of a phenolic

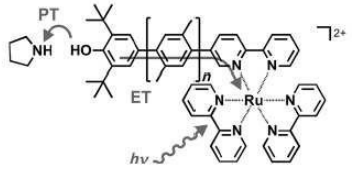

Scheme 1. Molecular structures of the PhOH-xy$_n$-Ru^{2+} molecules (n = 1–3) investigated in this work and illustration of their light-induced bidirectional CPET reaction involving pyrrolidine. ET = electron transfer, PT = proton transfer.

[a] Dr. J. Chen,[+] M. Kuss-Petermann,[+] Prof. Dr. O. S. Wenger
Department of Chemistry, University of Basel
St. Johanns-Ring 19, 4056 Basel (Switzerland)
Fax: (+41) 61-267-09-76
E-mail: oliver.wenger@unibas.ch

[+] These authors contributed equally to this work.

Supporting information for this article is available on the WWW under http://dx.doi.org/10.1002/chem.201304256.

ChemPubSoc Europe

CHEMISTRY A European Journal Full Paper

unit acting as a combined electron–proton donor, *p*-xylene bridges of variable length, and a ruthenium photosensitizer as an electron acceptor. The proton acceptor is a base (pyrrolidine) which is added separately to the solution. Phenols have received much attention for mechanistic PCET studies,[15–17] and there have been several investigations of donor–bridge–acceptor molecules incorporating phenols.[18–24] Long-range PCET reactions have received increasing attention recently,[24–28] but to our knowledge the dependence of the rates for bidirectional CPET on the electron donor/electron acceptor distance has never been investigated before. Given the biological relevance of this reaction type a systematic investigation of the model compounds from Scheme 1 seemed to be a worthy research endeavor.

Results and Discussion

Basic photochemistry and electrochemistry of the dyads

In pure acetonitrile photoexcitation of the three dyads from Scheme 1 leads to ^{3}MLCT emission of the $Ru(bpy)_3^{2+}$ moieties, but there is no photochemistry. In absence of any base the ^{3}MLCT excited state lifetimes of the dyads are within experimental accuracy the same as for isolated $Ru(bpy)_3^{2+}$. Although a significantly better oxidant in the ^{3}MLCT state than in the electronic ground state, $Ru(bpy)_3^{2+}$ is obviously not strongly oxidizing enough to convert the phenols to phenoxyl radical cations ($PhOH^+$). This finding can be understood on the basis of the electrochemical data in Table 1 which were extracted from cyclic voltammetry measurements (Figure S1 in the Supporting Information). Reduction of $Ru(bpy)_3^{2+}$ is ligand based and occurs at approximately −1.7 V vs. Fc^+/Fc in CH_3CN in all cases considered here. Oxidation of phenol (PhOH) to phenoxyl radical cation ($PhOH^+$) occurs at approximately 0.9 V vs. Fc^+/Fc in the three dyads. Given a ^{3}MLCT energy (ΔE_{MLCT}) of 2.1 eV,[29] one estimates a free energy of $\Delta G^0_{ET1} = -e\times[E(bpy/bpy^-) - E(PhOH^+/PhOH)] - \Delta E_{MLCT} \approx +0.5$ eV for photoinduced electron transfer.[30] Such driving-force estimates are usually accurate to ±0.1 eV. In the present case it seems safe to conclude that "simple" electron transfer from phenol to photoexcited $Ru(bpy)_3^{2+}$ in pure CH_3CN does not occur at measurable rates because it is too endergonic. Pyrrolidine does not deprotonate our charge-neutral phenols to a significant extent (see pK_a values below).

Table 1. Electrochemical potentials (in [V] vs. Fc^+/Fc in CH_3CN with 0.1 M Bu_4NPF_6) of the individual redox-active moieties of the dyads and some reference molecules.

Molecule	$Ru^{II/II}$	bpy/bpy^-	$PhOH^+$/PhOH	$PhO^\cdot/PhO^-$
PhOH-xy_1-Ru^{2+}	0.90	−1.73	0.88	−0.54
PhOH-xy_2-Ru^{2+}	0.90	−1.72	0.90	−0.58
PhOH-xy_3-Ru^{2+}	0.90	−1.72	0.86	−0.58
$Ru(bpy)_3^{2+}$	0.90	−1.73		
2,4,6-tBu$_2$PhOH			1.18[a]	−0.70[a]

These data were extracted from the cyclic voltammograms shown in Figure S1 in the Supporting Information. [a] From Ref. [15].

The situation changes completely when base is present because the neutral phenoxyl radical ($PhO^\cdot$) instead of phenoxyl radical cation ($PhOH^+$) can be formed upon photoexcitation of the $Ru(bpy)_3^{2+}$ photosensitizers. In other words, phenol oxidation becomes thermodynamically possible when combined with proton release (see below for driving-force estimates). In acetonitrile solution, addition of 4-aminopyridine quenches the ^{3}MLCT excited state of the PhOH-xy_1-Ru^{2+} dyad but has no effect on the longer congeners. The stronger base pyrrolidine leads to a photoreaction in all three dyads. We have therefore chosen pyrrolidine as a base for our PCET investigations. Importantly, up to concentrations of 1 M in CH_3CN pyrrolidine does not have any noticeable influence on the ^{3}MLCT decay of the $Ru(bpy)_3^{2+}$ reference complex (Figure S2 in the Supporting Information).

Photochemistry in presence of pyrrolidine

Transient absorption spectra of the three dyads in aerated CH_3CN obtained in presence of excess pyrrolidine are shown in Figure 1a (solid black lines). These spectra were measured after selective excitation of the $Ru(bpy)_3^{2+}$ moieties at 532 nm. The dyad concentrations were always 2×10^{-5} M, but with increasing bridge length increasing pyrrolidine concentrations were necessary in order to induce efficient photochemistry. For PhOH-xy_1-Ru^{2+} a pyrrolidine concentration of 25 mM was sufficient whereas for PhOH-xy_2-Ru^{2+} and PhOH-xy_3-Ru^{2+} concentrations of 96 mM and 3 M, respectively, were employed.

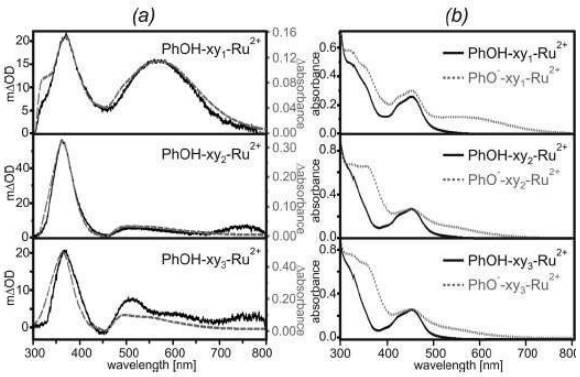

Figure 1. a) Solid black lines: Transient absorption spectra measured after excitation of the three dyads in aerated CH_3CN (2×10^{-5} M) in presence of pyrrolidine at 532 nm. Detection occurred by time averaging over a period of 200 ns starting immediately after excitation with pulses of ca. 10 ns duration. The pyrrolidine concentrations were: 25 mM (PhOH-xy_1-Ru^{2+}), 96 mM (PhOH-xy_2-Ru^{2+}), and 3 M (PhOH-xy_3-Ru^{2+}). Dashed grey traces: Difference spectra obtained by subtraction of the solid black traces in Figure 1b from the dotted grey traces in Figure 1b. b) Solid black traces: UV/Vis absorption of the dyads in pure CH_3CN. Dotted grey traces: UV/Vis spectra of the deprotonated dyads in CH_3CN.

ChemPubSoc Europe

CHEMISTRY A European Journal Full Paper

Under these conditions, conversion to the photoproducts was essentially complete after the 10 ns duration of the laser excitation pulses in all three cases. Measurement of the transient absorption data in Figure 1a occurred by time integration over a period of 200 ns. The three resulting spectra are relatively similar to each other and feature a prominent band near 365 nm in addition to weaker bands at longer wavelengths. The shape of the transient absorption spectra can be understood readily on the basis of the UV/Vis data shown in Figure 1b. The solid black traces in Figure 1b are the absorption spectra of the PhOH-xy$_n$-Ru^{2+} dyads in pure CH_3CN, whereas the dotted grey traces are the absorption spectra of their deprotonated forms (PhO$^-$-xy$_n$-Ru^{2+}). Deprotonation occurred by addition of excess tetrabutylammonium hydroxide to the CH_3CN solutions. When subtracting the solid black traces from the dotted grey traces in Figure 1b, one obtains the difference spectra shown as dashed grey traces in Figure 1a. The similarity between these derived difference spectra and the experimental transient absorption spectra (solid black lines in Figure 1a) is evident, and we conclude that the photoproducts which are detected on the nanosecond timescale are comprised of the deprotonated phenols and Ru(bpy)$_3^{2+}$ in the electronic ground state. It is as if the three dyads from Scheme 1 merely acted as photoacids.

Excitation at 532 nm occurs selectively into the Ru(bpy)$_3^{2+}$ moieties. The phenols have insignificant extinction at this wavelength, and it is not obvious why the phenolic units should become more acidic upon excitation of the Ru(bpy)$_3^{2+}$ moieties which are more than 12 Å away. However, the apparent photoacid behavior can be explained by a reaction sequence of concerted proton–electron transfer (CPET) followed by "simple" electron transfer (back-ET) in the reverse direction (Scheme 2).[31] In order to understand this reaction sequence it

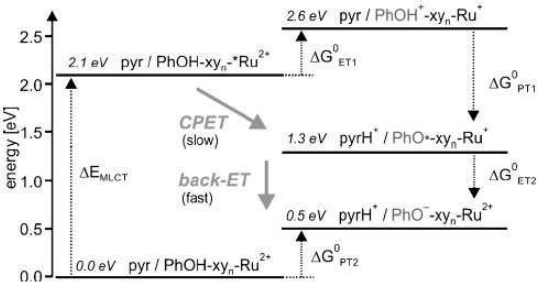

Scheme 2. Energy-level diagram established on the basis of the electrochemical potentials in Table 1 and the acidity constants in Table 2 (see the Supporting Information for details).

is necessary to work out the thermodynamics of the different photochemical reaction pathways for the PhOH-xy$_n$-Ru^{2+} dyads in presence of pyrrolidine (pyr).

The starting point in the energy-level diagram of Scheme 2 is the ^{3}MLCT state 2.1 eV above the ground state.[29] As discussed above, "simple" photoinduced electron transfer to produce phenoxyl radical cations and reduced ruthenium complex (pyr/PhOH$^+$-xy$_n$-Ru$^+$ state at 2.6 eV) is endergonic by 0.5 eV. The absence of any photochemical reaction in pure CH_3CN without base strongly suggests that the pyr/PhOH$^+$-xy$_n$-Ru$^+$ photoproduct is never formed, not even as a short-lived intermediate when base is present. However, on the basis of Equation (2) photoinduced CPET producing protonated pyrrolidine (pyrH$^+$), phenoxyl radical (PhO$^\bullet$), and reduced ruthenium complex (Ru$^+$) is estimated to be exergonic by approximately 0.8 eV.

$$\Delta G^0_{PT1} = 0.059\ \text{eV} \times [pK_a(\text{PhOH}^+) - pK_a(\text{pyrH}^+)] \quad (2)$$

Specifically, Equation (2) is used to estimate the free energy associated with protonation of pyrrolidine by phenoxyl radical cation.[32] The pK_a of PhOH$^+$ in CH_3CN is −3 and the pK_a of the conjugate acid of pyrrolidine (pyrH$^+$) in CH_3CN is 19.56 (Table 2),[15,33] resulting in $\Delta G^0_{PT1} \approx -1.3$ eV. Consequently, the

Table 2. Acidity constants in CH_3CN.

Acid	pK_a
pyrH$^+$	19.56[a]
PhOH	28[b]
PhOH$^+$	−3[b]

[a] From Ref. [33]. [b] Values for 2,4,6-tBu$_3$PhOH from Ref. [15].

pyrH$^+$/PhO$^\bullet$-xy$_n$-Ru$^+$ state must be approximately 1.3 eV below the pyr/PhOH$^+$-xy$_n$-Ru$^+$ state, that is, at 2.6 eV − 1.3 eV = 1.3 eV. This is 0.8 eV below the initially populated ^{3}MLCT state. Thus, the CPET reaction in which phenol oxidation by photoexcited Ru(bpy)$_3^{2+}$ occurs in concert with release of the phenolic proton to pyrrolidine (arrow marked with "CPET" in Scheme 2) has $\Delta G^0_{CPET} = -0.8$ eV. It seems reasonable to conclude that this is indeed the first reaction step occurring after photoexcitation.

The pyrH$^+$/PhO$^\bullet$-xy$_n$-Ru$^+$ photoproduct at 1.3 eV is composed of a strongly reducing ruthenium complex (Ru(bpy)$_3^+$) connected to a relatively good electron acceptor (PhO$^\bullet$). Using Equation (3), one can estimate the reaction free energy associated with intramolecular electron transfer from Ru(bpy)$_3^+$ to PhO$^\bullet$.

$$\Delta G^0_{ET2} = -e \times [E(\text{PhO}^\bullet/\text{PhO}^-) - E(\text{bpy/bpy}^-)] \quad (3)$$

With the electrochemical potentials in Table 1, Equation (3) yields $\Delta G^0_{ET2} \approx -1.1$ eV. In other words, after initial CPET thermal electron transfer from Ru(bpy)$_3^+$ to PhO$^\bullet$ is exergonic by 1.1 eV. This second reaction step (downward arrow in Scheme 2 labeled "back-ET") leads to the photoproducts which are detected by transient absorption spectroscopy in Figure 1a, that is, to Ru(bpy)$_3^{2+}$ in the ground state and phenolate. Using the thermodynamic cycle described above, one arrives at the conclusion that the pyrH$^+$/PhO$^-$-xy$_n$-Ru^{2+} state is

ChemPubSoc Europe
CHEMISTRY A European Journal Full Paper

approximately 0.2 eV above the ground state. Alternatively, using the pK_a values of phenol (28)[15] and the conjugate acid of pyrrolidine (19.56)[33] in CH_3CN one arrives at the conclusion that the respective state is 0.5 eV above the ground state (ΔG^0_{PT2}). The deviation between the two energy estimates for the same state (0.2 eV vs. 0.5 eV) simply reflects the approximate character of these thermodynamic considerations and the uncertainty in the electrochemical potentials and acidity constants.

The conclusion from this section is that the apparent photoacid behavior of the three dyads in presence of pyrrolidine is due to a sequence of two consecutive reaction steps: Photoinduced CPET followed by electron transfer in the reverse direction (two thick grey arrows in Scheme 2).[31] The $pyrH^+/PhO^{\bullet}$-xy_n-Ru^+ intermediate (at 1.3 eV) produced after initial CPET escapes detection because it decays more rapidly than it is formed.[34] In other words, CPET is the rate-determining step leading to the observable $pyrH^+/PhO^-$-xy_n-Ru^{2+} photoproducts. This view is consistent with previously reported rates exceeding $10^9\ s^{-1}$ for "simple" electron transfer over three adjacent *p*-phenylene units as well as with the relative sluggishness of CPET reactions in related phenol-$Ru(bpy)_3^{3+}$ and phenol–rhenium(I) systems.[14,23,24,35–38] Some of the H/D kinetic isotope effects reported below provide additional support for the conclusion that CPET is rate-determining.

Kinetics of the photoreaction in presence of pyrrolidine

In order for the photoinduced CPET reaction to occur, pyrrolidine must be in immediate proximity to the phenolic units because the proton cannot tunnel very far.[39] It is therefore reasonable to expect CPET to occur predominantly from the hydrogen-bonded encounter adducts on the right-hand side of the chemical equilibrium in Equation (4), in analogy to prior studies of PCET with hydrogen-bonded phenols.[22,31,39–46]

$$pyr + PhOH\text{-}xy_n\text{-}Ru^{2+} \rightleftharpoons pyr\cdots PhOH\text{-}xy_n\text{-}Ru^{2+} \quad (4)$$

Any analysis of the CPET kinetics must take this equilibrium into account. The CPET kinetics of the three dyads can be measured by monitoring the transient absorption signal at 450 nm as a function of time after excitation at 532 nm with laser pulses of 10 ns width. Exemplary bleach recoveries for the PhOH-xy_1-Ru^{2+} dyad are shown in Figure 2, all others are reported in Figure S3 in the Supporting Information. Immediately after the laser pulses one detects a bleach at 450 nm due to the disappearance of the ^{1}MLCT absorption as a consequence of $Ru(bpy)_3^{2+}$ excitation.[47] In absence of pyrrolidine the bleach recovery time is about 200 ns in aerated CH_3CN for all three dyads, corresponding to relaxation of the ^{3}MLCT state to the ground state like in free $Ru(bpy)_3^{2+}$. In presence of pyrrolidine the bleach recovery becomes significantly more rapid (Figure 2, Figure S3 in the Supporting Information) due to the sequence of photoreactions (CPET, back-ET) discussed in the previous paragraph. Since the CPET step is rate determining,

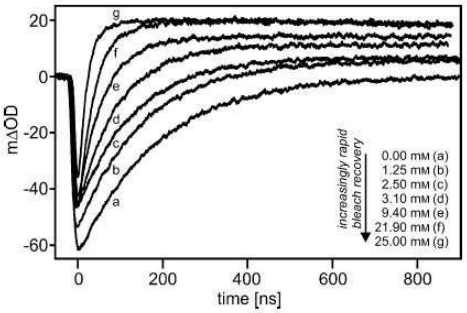

Figure 2. Temporal evolution of the transient absorption signal of PhOH-xy_1-Ru^{2+} (2×10^{-5} M) in aerated CH_3CN at 450 nm after excitation at 532 nm with pulses of ca. 10 ns duration. Pyrrolidine concentrations are given in the inset.

these bleach recovery times essentially reflect the kinetics of the CPET reaction.

The observed rate constants (k_{obs}, extracted from single exponential fits to the data in Figure 2 and Figure S3 in the Supporting Information) are plotted as a function of pyrrolidine concentration in Figure 3. Squares, circles, and triangles are used to visually set apart data for dyads with 1, 2, and 3 *p*-xylene spacers; open symbols represent data for ordinary dyads, filled symbols represent data obtained for their deuterated analogs in presence of deuterated pyrrolidine. In this context "deuterated" means replacement of the phenolic proton

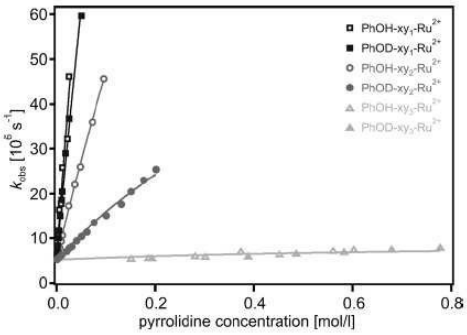

Figure 3. Experimentally observable ^{3}MLCT-depopulation rate constants (k_{obs}) as a function of pyrrolidine concentration for the three dyads and their deuterated analogues. The actual experimental data are shown in Figure 2 and Figure S3 in the Supporting Information. The solid lines are fits to the experimental data with Equation (5) as described in the text. Results from these fits are reported in Table 3.

by a deuteron and replacement of the easily exchangeable N–H proton of pyrrolidine by a deuteron. The most important observation is that upon bridge lengthening increasing pyrrolidine concentrations are necessary to induce similar reaction kinetics. This is a manifestation of the fact that the CPET reaction rate decreases with increasing bridge length.

The experimentally determined bleach recovery rate constants (k_{obs}) are principally a function of the intrinsic ^{3}MLCT ex-

ChemPubSoc Europe

CHEMISTRY A European Journal Full Paper

cited-state decay rate constant (k_0) and the rate constant for CPET (k_{CPET}). Equation (5) further contains a rate constant for "simple" electron transfer (k_{ET}) and a k_Q[base] term describing direct ^{3}MLCT excited-state quenching by the base.[22,40,41]

$$k_{obs} = k_0 + k_{ET} + k_Q[\text{base}] + k_{CPET}\frac{K_A[\text{base}]}{1 + K_A[\text{base}]} \quad (5)$$

As discussed above, in absence of pyrrolidine the ^{3}MLCT lifetime of the three dyads in aerated CH_3CN is within experimental accuracy the same as that of isolated $Ru(bpy)_3^{2+}$ hence we conclude that k_{ET} is negligible compared to k_0. Addition of up to 1 M pyrrolidine to a 2×10^{-5} M solution of $Ru(bpy)_3^{2+}$ in aerated CH_3CN has no influence on the ^{3}MLCT emission and its lifetime (Figure S2 in the Supporting Information). From this we conclude that $k_Q \leq 10^5\,M^{-1}s^{-1}$. Fits with Equation (5) to the experimental data in Figure 3 are therefore possible with only two adjustable parameters: The CPET rate constant (k_{CPET}) and the association constant (K_A) describing the chemical equilibrium in Equation (4). We attempted to determine K_A independently on the basis of steady-state luminescence data as described previously (Figure S4 and S5 in the Supporting Information) but have not been able to extract meaningful K_A values from this procedure (see the Supporting Information).[48]

Two-parameter fits to single sets of data from Figure 3 turned out to be not meaningful,[49] and therefore we decided to fit all six data sets globally with the restriction to one common K_A value for all six cases. In other words, we assume that the equilibrium in Equation (4) is affected neither by the number of *p*-xylene spacers nor by deuteration. Our fits employed $k_0 = 5.2\times10^6\,s^{-1}$, $k_{ET} = 0\,s^{-1}$, and $k_Q = 10^5\,M^{-1}s^{-1}$ as non-adjustable parameters and produced the k_{CPET} values reported in the third column of Table 3 and $K_A = 1.4\pm0.2\,M^{-1}$. The fits are shown as solid lines in Figure 3. The quality of these fits supports the CPET hypothesis based on the chemical equilibrium in Equation (4) and speaks against any stepwise proton transfer, electron transfer mechanisms.

A value of $1.4\pm0.2\,M^{-1}$ for K_A is in line with previously reported equilibrium constants of hydrogen-bonded phenols in benzonitrile.[40,41] The H/D kinetic isotope effect (KIE) of 3.91 ± 0.95 (ratio between k_{CPET} of PhOH-xy_2-Ru^{2+} and PhOD-xy_2-Ru^{2+}) found for the dyad with two *p*-xylene bridging units is significant and supports the hypothesis of a rate-determining CPET step. The two other dyads exhibit smaller KIEs (1.26 ± 0.40, xy_1 system) and (0.95 ± 0.44, xy_3 system), but the absence of a significant KIE is not an argument against CPET.[50] Trends in the magnitudes of KIEs associated with PCETs are generally difficult to rationalize because the KIE depends on many different parameters.[11]

Table 3. CPET rate constants (k_{CPET}) as a function of phenol–ruthenium (center-to-center) distance (R_{DA}).

Molecule	R_{DA} [Å]	k_{CPET} [s^{-1}]
PhOH-xy_1-Ru^{2+}	12.2	$(1.07\pm0.14)\times10^9$
PhOD-xy_1-Ru^{2+}	12.2	$(0.85\pm0.12)\times10^9$
PhOH-xy_2-Ru^{2+}	16.5	$(3.35\pm0.41)\times10^8$
PhOD-xy_2-Ru^{2+}	16.5	$(0.86\pm0.10)\times10^8$
PhOH-xy_3-Ru^{2+}	20.8	$(3.41\pm1.22)\times10^6$
PhOD-xy_3-Ru^{2+}	20.8	$(3.58\pm1.14)\times10^6$

The distance dependence of the CPET rate constants is shown in Figure 4 in semilogarithmic representation; R_{DA} corresponds to center-to-center distances between the phenol and $Ru(bpy)_3^{2+}$ moieties as obtained by molecular modeling. Linear

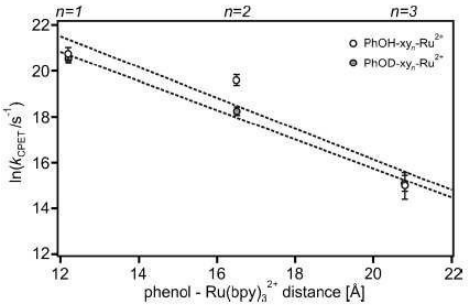

Figure 4. Distance dependence of k_{CPET}. The solid lines are linear regression fits yielding the β-values reported in the text.

regression fits to the data in Figure 4 yields distance decay constants (β) of 0.67 ± 0.23 Å^{-1} and 0.64 ± 0.06 Å^{-1} for the PhOH-xy_n-Ru^{2+} and PhOD-xy_n-Ru^{2+} series, respectively. These β values are much in line with those extracted for "simple" (i.e., not proton-coupled) electron tunneling across oligo-*p*-xylene spacers (0.77 Å^{-1}, 0.52 Å^{-1})[51,52] and oligo-*p*-phenylene bridges.[35,36,53,54] Extrapolation of these exponential fits to van der Waals contact distance between phenol and $Ru(bpy)_3^{2+}$ reactants ($R_{DA} = 4$ Å) yields $k_{CPET} = 4.5\times10^{11}\,s^{-1}$ for ordinary phenol and $k_{CPET} = 1.8\times10^{11}\,s^{-1}$ for deuterated phenol. These rates compare favorably to those of "simple" electron transfer between reactants in van der Waals contact.[1,10]

Conclusion

The distance dependence of the rates for bidirectional CPET in the systems investigated here does not deviate drastically from that of ordinary (i.e., not proton-coupled) electron transfer. The dominant contribution to this distance dependence likely comes from $H_{AB,PCET}$ [Eq. (1)], which can be described as a product of electronic coupling matrix elements for the electron transfer ($H_{AB,ET}$) and proton transfer components ($H_{AB,PT}$) of the overall CPET reaction.[11,39] Increasing the electron transfer distance decreases $H_{AB,ET}$ whereas $H_{AB,PT}$ remains constant. From this perspective the observed similarity between the distance dependences of bidirectional CPET ($\beta = 0.67\pm0.23$ Å^{-1}) and ordinary electron transfer ($\beta = 0.52$–0.77 Å^{-1})[51,52,55] across the same type of bridges is readily understandable. Changes in reorganization energy (λ_{PCET}, [Eq. (1)]) with increasing electron donor/electron acceptor distance appear to be relatively minor. It is possible that reorganization energy effects are re-

ChemPubSoc Europe

CHEMISTRY A European Journal Full Paper

sponsible for the deviation from the exponential distance dependence of CPET rates observed here.[12]

Since this is the first determination of β for a bidirectional CPET reaction it is delicate to make a general statement, but it seems that the dependence of rates for bidirectional CPET on electron donor/electron acceptor distance is not steeper than that of ordinary electron transfer rates, despite the concerted motion of oppositely charged particles into different directions. This finding is of key importance when attempting to perform light-driven separation of electrons and protons in order to build up charge gradients across natural or artificial membranes, similar to what occurs in photosystem II. We find that a long electron transfer distance (up to ca. 20 Å) is no obstacle to bidirectional CPET.

Experimental Section

^{1}H NMR spectra were measured on a 400 MHz Bruker Avance instrument. The ^{1}H spectra were referenced relative to tetramethylsilane by using the solvent signals as internal standards. High-resolution mass spectra were recorded on a Finnigan MAT8200 mass spectrometer. Elemental analysis was performed using a Vario EL III CHNS analyzer from Elementar. For cyclic voltammetry a Versastat3-200 potentiostat from Princeton Applied Research was used, and a glassy carbon disk served as a working electrode. A silver wire was used as a counter-electrode, and a second silver wire was employed as a quasi-reference electrode. Proper referencing of the potentials occurred through addition of small amounts of ferrocene and by recording of the ferrocenium/ferrocene redox wave. Voltage sweeps were performed with rates of 100 mV s^{-1}. Optical absorption spectra were recorded on a Shimadzu UV-1800 instrument. Steady-state luminescence was measured on a Fluorolog322 instrument from Horiba Jobin–Yvon. Transient absorption was performed with an LP920-KS spectrometer from Edinburgh Instruments, equipped with an R928 photomultiplier and an iCCD camera from Andor. The frequency-doubled output from a Quantel Brilliant b laser was used as an excitation source. The duration of the laser excitation pulses was approximately 10 ns. Transient absorption spectra were generally recorded by time-averaging the signal over a detection period of 200 ns. Quartz cuvettes from Starna were employed for all optical spectroscopic experiments. For H/D kinetic isotope effect studies, the deuterated dyads were dissolved in pure CH_3CN and deuterated pyrrolidine was added. Synthetic protocols and product characterization data are given in the Supporting Information.

Acknowledgements

This work was supported by the Swiss National Science Foundation (grant number 200021 146231/1) and by the Deutsche Forschungsgemeinschaft (IRTG-1422).

Keywords: electron transfer · hydrogen bonds · molecular wires · photochemistry · time-resolved spectroscopy

[1] H. B. Gray, J. R. Winkler, *Proc. Natl. Acad. Sci. USA* **2005**, *102*, 3534.
[2] B. Giese, *Annu. Rev. Biochem.* **2002**, *71*, 51.
[3] J. C. Genereux, J. K. Barton, *Chem. Rev.* **2010**, *110*, 1642.
[4] H. J. Yoon, N. D. Shapiro, K. M. Park, M. M. Thuo, S. Soh, G. M. Whitesides, *Angew. Chem. Int. Ed.* **2012**, *51*, 4658.
[5] V. Balzani, *Electron transfer in chemistry*, Wiley-VCH, Weinheim, **2001**.
[6] P. P. Edwards, H. B. Gray, M. T. J. Lodge, R. J. P. Williams, *Angew. Chem.* **2008**, *120*, 6860; *Angew. Chem. Int. Ed.* **2008**, *47*, 6758.
[7] B. A. Barry, G. T. Babcock, *Proc. Natl. Acad. Sci. USA* **1987**, *84*, 7099.
[8] E. C. Minnihan, D. G. Nocera, J. Stubbe, *Acc. Chem. Res.* **2013**, *46*, 2524.
[9] A. Kumar, M. D. Sevilla, *Chem. Rev.* **2010**, *110*, 7002.
[10] R. A. Marcus, N. Sutin, *Biochim. Biophys. Acta Rev. Bioenerg.* **1985**, *811*, 265.
[11] S. Hammes-Schiffer, A. A. Stuchebrukhov, *Chem. Rev.* **2010**, *110*, 6939.
[12] B. S. Brunschwig, S. Ehrenson, N. Sutin, *J. Am. Chem. Soc.* **1984**, *106*, 6858.
[13] S. S. Isied, A. Vassilian, J. F. Wishart, C. Creutz, H. A. Schwarz, N. Sutin, *J. Am. Chem. Soc.* **1988**, *110*, 635.
[14] M. Sjödin, S. Styring, B. Åkermark, L. C. Sun, L. Hammarström, *J. Am. Chem. Soc.* **2000**, *122*, 3932.
[15] J. J. Warren, T. A. Tronic, J. M. Mayer, *Chem. Rev.* **2010**, *110*, 6961.
[16] D. R. Weinberg, C. J. Gagliardi, J. F. Hull, C. F. Murphy, C. A. Kent, B. C. Westlake, A. Paul, D. H. Ess, D. G. McCafferty, T. J. Meyer, *Chem. Rev.* **2012**, *112*, 4016.
[17] C. Costentin, M. Robert, J.-M. Savéant, *Acc. Chem. Res.* **2010**, *43*, 1019.
[18] T. Irebo, M.-T. Zhang, T. F. Markle, A. M. Scott, L. Hammarström, *J. Am. Chem. Soc.* **2012**, *134*, 16247.
[19] M. Sjödin, T. Irebo, J. E. Utas, J. Lind, G. Merenyi, B. Åkermark, L. Hammarström, *J. Am. Chem. Soc.* **2006**, *128*, 13076.
[20] L. C. Sun, M. Burkitt, M. Tamm, M. K. Raymond, M. Abrahamsson, D. Le-Gourriérec, Y. Frapart, A. Magnuson, P. H. Kenéz, P. Brandt, A. Tran, L. Hammarström, S. Styring, B. Åkermark, *J. Am. Chem. Soc.* **1999**, *121*, 6834.
[21] T. Lachaud, A. Quaranta, Y. Pellegrin, P. Dorlet, M. F. Charlot, S. Un, W. Leibl, A. Aukauloo, *Angew. Chem.* **2005**, *117*, 1560; *Angew. Chem. Int. Ed.* **2005**, *44*, 1536.
[22] A. A. Pizano, J. L. Yang, D. G. Nocera, *Chem. Sci.* **2012**, *3*, 2457.
[23] T. Irebo, S. Y. Reece, M. Sjödin, D. G. Nocera, L. Hammarström, *J. Am. Chem. Soc.* **2007**, *129*, 15462.
[24] M. Kuss-Petermann, H. Wolf, D. Stalke, O. S. Wenger, *J. Am. Chem. Soc.* **2012**, *134*, 12844.
[25] O. S. Wenger, *Acc. Chem. Res.* **2013**, *46*, 1517.
[26] V. W. Manner, A. G. DiPasquale, J. M. Mayer, *J. Am. Chem. Soc.* **2008**, *130*, 7210.
[27] V. W. Manner, J. M. Mayer, *J. Am. Chem. Soc.* **2009**, *131*, 9874.
[28] J. J. Warren, A. R. Menzeleev, J. S. Kretchmer, T. F. Miller, H. B. Gray, J. M. Mayer, *J. Phys. Chem. Lett.* **2013**, *4*, 519.
[29] D. M. Roundhill, *Photochemistry and Photophysics of Metal Complexes*, Plenum Press, New York, **1994**.
[30] A. Weller, *Z. Phys. Chem. (Muenchen Ger.)* **1982**, *133*, 93.
[31] M. Kuss-Petermann, O. S. Wenger, *J. Phys. Chem. A* **2013**, *117*, 5726.
[32] J. M. Mayer, *Annu. Rev. Phys. Chem.* **2004**, *55*, 363.
[33] I. Kaljurand, A. Kütt, L. Soovali, T. Rodima, V. Maemets, I. Leito, I. A. Koppel, *J. Org. Chem.* **2005**, *70*, 1019.
[34] Note that this is not a matter of temporal resolution of the used equipment. It is easily possible to decelerate the overall reaction to rates well below 10^8 s^{-1} by using lower pyrrolidine concentrations. The intermediate remains undetectable under such conditions.
[35] O. S. Wenger, *Chem. Soc. Rev.* **2011**, *40*, 3538.
[36] E. A. Weiss, M. J. Ahrens, L. E. Sinks, A. V. Gusev, M. A. Ratner, M. R. Wasielewski, *J. Am. Chem. Soc.* **2004**, *126*, 5577.
[37] T. Irebo, O. Johansson, L. Hammarström, *J. Am. Chem. Soc.* **2008**, *130*, 9194.
[38] A. Magnuson, H. Berglund, P. Korall, L. Hammarström, B. Åkermark, S. Styring, L. C. Sun, *J. Am. Chem. Soc.* **1997**, *119*, 10720.
[39] M.-T. Zhang, T. Irebo, O. Johansson, L. Hammarström, *J. Am. Chem. Soc.* **2011**, *133*, 13224.
[40] L. Biczók, N. Gupta, H. Linschitz, *J. Am. Chem. Soc.* **1997**, *119*, 12601.
[41] L. Biczok, H. Linschitz, *J. Phys. Chem.* **1995**, *99*, 1843.
[42] I. J. Rhile, T. F. Markle, H. Nagao, A. G. DiPasquale, O. P. Lam, M. A. Lockwood, K. Rotter, J. M. Mayer, *J. Am. Chem. Soc.* **2006**, *128*, 6075.
[43] I. J. Rhile, J. M. Mayer, *J. Am. Chem. Soc.* **2004**, *126*, 12718.
[44] J. N. Schrauben, M. Cattaneo, T. C. Day, A. L. Tenderholt, J. M. Mayer, *J. Am. Chem. Soc.* **2012**, *134*, 16635.
[45] C. Costentin, M. Robert, J. M. Savéant, C. Tard, *Angew. Chem.* **2010**, *122*, 3891; *Angew. Chem. Int. Ed.* **2010**, *49*, 3803.

ChemPubSoc Europe

CHEMISTRY A European Journal Full Paper

[46] W. Herzog, C. Bronner, S. Löffler, B. C. He, D. Kratzert, D. Stalke, A. Hauser, O. S. Wenger, *ChemPhysChem* **2013**, *14*, 1168.
[47] P. Müller, K. Brettel, *Photochem. Photobiol. Sci.* **2012**, *11*, 632.
[48] J. J. Concepcion, M. K. Brennaman, J. R. Deyton, N. V. Lebedeva, M. D. E. Forbes, J. M. Papanikolas, T. J. Meyer, *J. Am. Chem. Soc.* **2007**, *129*, 6968.
[49] Error bars associated with such fits are unreasonably large.
[50] T. F. Markle, I. J. Rhile, J. M. Mayer, *J. Am. Chem. Soc.* **2011**, *133*, 17341.
[51] D. Hanss, O. S. Wenger, *Inorg. Chem.* **2008**, *47*, 9081.
[52] D. Hanss, O. S. Wenger, *Inorg. Chem.* **2009**, *48*, 671.
[53] M. T. Indelli, C. Chiorboli, L. Flamigni, L. De Cola, F. Scandola, *Inorg. Chem.* **2007**, *46*, 5630.
[54] B. Albinsson, M. P. Eng, K. Pettersson, M. U. Winters, *Phys. Chem. Chem. Phys.* **2007**, *9*, 5847.
[55] O. S. Wenger, *Acc. Chem. Res.* **2011**, *44*, 25.

Received: October 31, 2013
Published online on February 26, 2014

Please note: Minor changes have been made to this manuscript since its publication in *Chemistry—A European Journal* Early View. The Editor.

THE JOURNAL OF PHYSICAL CHEMISTRY B

Article

pubs.acs.org/JPCB

Dependence of Reaction Rates for Bidirectional PCET on the Electron Donor−Electron Acceptor Distance in Phenol−Ru(2,2′-Bipyridine)$_3^{2+}$ Dyads

Jing Chen,[†] Martin Kuss-Petermann,[†] and Oliver S. Wenger*

Department of Chemistry, University of Basel, St. Johanns-Ring 19, CH-4056 Basel, Switzerland

Supporting Information

ABSTRACT: A homologous series of three donor−bridge−acceptor molecules in which a phenolic unit is attached covalently to a Ru(bpy)$_3^{2+}$ (bpy =2,2′-bipyridine) complex via rigid rod-like *p*-xylene spacers was investigated. Photoexcitation at 532 nm in the presence of a large excess of methyl viologen leads to rapid (<10 ns) formation of Ru(bpy)$_3^{3+}$. When imidazole base is present in CH_3CN solution, intramolecular electron transfer from the phenol to Ru(bpy)$_3^{3+}$ occurs, and this is coupled to proton transfer from the phenol to imidazole. All mechanistic possibilities for this proton-coupled electron transfer (PCET) process are considered, and based on a combination of kinetic and thermodynamic data, one arrives at the conclusion that electron and proton release by the phenol occur in concert. By varying the number of *p*-xylene bridging units, it then becomes possible to investigate the dependence of the reaction rates for concerted proton−electron transfer (CPET) on the phenol−Ru(bpy)$_3^{3+}$ distance. A distance decay constant of 0.87 ± 0.09 Å^{-1} is obtained. This is one of the largest β values reported for electron transfer across oligo-*p*-phenylene-based molecular bridges, but it is still relatively close to what was determined for "simple" (i. e., not proton-coupled) electron transfer across oligo-*p*-xylenes. Bidirectional CPET plays a key role in photosystem II. Understanding the distance dependence of such reactions is of interest, for example, in the context of separating protons and electrons across artificial membranes in order to build up charge gradients for light-to-chemical energy conversion.

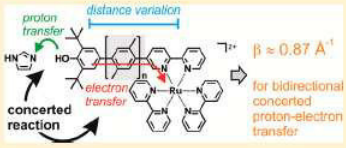

INTRODUCTION

The dependence of electron-transfer rates (k_{ET}) on the distance between an electron donor and an electron acceptor has been investigated for several decades, and many aspects of long-range electron transfer are now relatively well understood.[1] In the tunneling regime, k_{ET} exhibits an exponential dependence on the donor−acceptor distance, characterized by a distance decay constant (β) that is strongly dependent on the intervening medium separating the donor from the acceptor.[2] For proton-coupled electron transfer (PCET), the dependence of reaction rates on the distance between individual reactants is much less well explored. Over the past few years, the influence of the proton-transfer distance on PCET rates has received significant attention, and in one experimental study, it has been possible to determine a β value for the involved proton-transfer event.[3,4] The dependence of PCET rates on the electron donor−electron acceptor distance is beginning to be explored by several research groups, but until now, there exist only a handful of studies on this specific subject.[3,5,6]

PCET can either occur via individual electron-transfer and proton-transfer steps (in whichever sequence) or in concerted fashion.[7,8] Concerted proton−electron transfer (CPET) is energy-conservative in the sense that high-energy intermediates are avoided, making this mechanism particularly interesting.[9,10] Irrespective of the mechanism, PCET can be either unidirectional or bidirectional, meaning that either the electron and proton are transferred from one reactant to another, similar to hydrogen-atom transfer (HAT) reactions, or the electron and the proton can be taken up by separate oxidants and bases. The dependence of rates for unidirectional CPET on the electron donor−electron acceptor distance has recently been explored for the first time by Mayer and Gray.[3] We have recently reported the first experimental study of rates for bidirectional CPET as a function of the electron donor−electron acceptor distance.[5] Here, we provide a significantly more detailed report of the influence of the electron donor−electron acceptor distance on the rates for bidirectional CPET.

Our study is based on the three donor−bridge−acceptor molecules shown in Scheme 1. They are comprised of a phenolic unit that acts as a combined electron and proton donor, a variable number (1−3) of rigid rod-like *p*-xylene spacers, and a Ru(bpy)$_3^{2+}$ (bpy =2,2′-bipyridine) complex playing the role of a photosensitizer. Excess methyl viologen was used for the photogeneration of Ru(bpy)$_3^{3+}$ in order to trigger the PCET reaction in CH_3CN. PCET can only occur in the presence of base, for example, with imidazole. From the sketch in Scheme 1, the bidirectional nature of the overall PCET process is evident. Variation of the number of *p*-xylene spacers permits phenol−ruthenium (center-to-center) distance

Special Issue: Photoinduced Proton Transfer in Chemistry and Biology Symposium

Received: June 18, 2014
Revised: July 20, 2014
Published: July 31, 2014

Scheme 1. Molecular Structures of the Three PhOH-xy$_n$-Ru^{2+} Dyads Investigated in This Work[a]

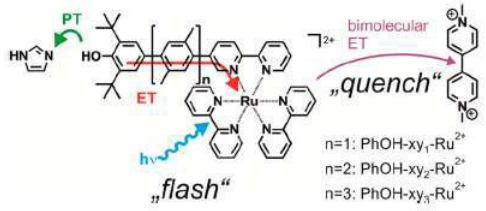

[a]Photoexcitation in the presence of methyl viologen and imidazole induces intramolecular electron transfer (ET) occurring in concert with intermolecular proton transfer (PT).

variation between 12.2 and 20.8 Å. Related tyrosine−ruthenium and tyrosine−rhenium dyads have been investigated by several other research groups,[11−25] but to our knowledge, the dependence of PCET rates on the tyrosine−metal distance has never been explored.

In this paper, we will thoroughly consider all mechanistic possibilities for phototriggered PCET in the reaction systems from Scheme 1. We will show that CPET is indeed the most plausible reaction mechanism, and we will determine a distance decay constant for bidirectional CPET across *p*-xylene spacers and compare it to β values obtained in prior studies of "simple" (i. e., not proton-coupled) electron transfer across comparable molecular bridges. We will close with a few general thoughts and conclusions regarding the dependence of CPET rates on electron donor−electron acceptor distances.

■ RESULTS

Cyclic voltammograms of the three donor−bridge−acceptor molecules from Scheme 1 and the Ru(bpy)$_3^{2+}$ reference complex measured in dry CH_3CN are shown in Figure 1.

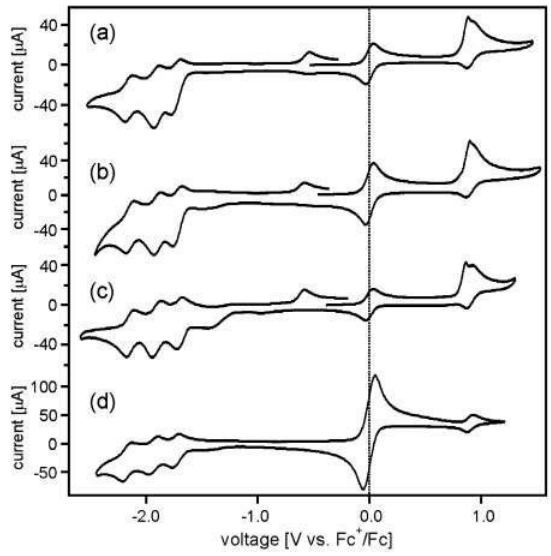

Figure 1. Cyclic voltammograms of (a) PhOH-xy$_1$-Ru^{2+}, (b) PhOH-xy$_2$-Ru^{2+}, (c) PhOH-xy$_3$-Ru^{2+}, and (d) Ru(bpy)$_3^{2+}$ in CH_3CN with 0.1 M $TBAPF_6$. The voltage sweep rate was 0.1 V/s; the reversible wave at 0.0 V is due to ferrocene, which was added in small quantities for voltage calibration.

The reversible waves at 0.0 V are due to ferrocene, which was added in small amounts for internal voltage calibration. All voltammograms were recorded in the presence of 0.1 M $TBAPF_6$ at scan rates of 100 mV/s. In the potential range considered here, most of the detectable waves are due to the Ru(bpy)$_3^{2+}$ complex.

Specifically, oxidation of Ru(II) to Ru(III) occurs at about 0.9 V versus Fc$^+$/Fc (Figure 1d), whereas one-electron reduction of the three bpy ligands takes places at potentials between −1.7 and −2.2 V versus Fc$^+$/Fc, as commonly observed.[26] Careful inspection of the dyad voltammograms (Figure 1a−c) reveals an additional oxidation wave near 0.9 V versus Fc$^+$/Fc next to the ruthenium oxidation wave; this is particularly evident in Figure 1c, but the additional wave is also present in Figure 1a,b. This additional wave is attributed to phenol oxidation, which is irreversible,[27,28] presumably due to proton loss.[29] The three dyads further exhibit an additional wave near −0.6 V versus Fc$^+$/Fc, which only appears after an initial oxidative sweep to potentials above 0.9 V versus Fc$^+$/Fc. We attribute this wave to oxidation of phenolate (PhO^-) to phenoxyl radical ($PhO^\bullet$).[30] Table 1 lists the pertinent reduction potentials extracted from Figure 1 along with two relevant potentials of the 2,4,6-tri-*tert*-butylphenol (2,4,6-^{t}Bu$_3$PhOH) reference molecule taken from the literature.[28] In Table 1, only the first reduction potentials for the Ru(bpy)$_3^{2+}$ complexes are listed, and these potentials are labeled with $E^0(Ru^{2+}/Ru^+)$ for simplicity even though this reduction is ligand-centered.

The solid black lines in Figure 2 are the optical absorption spectra of the three dyads from Scheme 1 in CH_3CN. They are dominated by the ^{1}MLCT absorption band of the Ru(bpy)$_3^{2+}$ moiety at 450 nm and a bpy-centered $\pi-\pi^*$ transition at around 290 nm. The dyad spectra differ rather little from the spectrum of free Ru(bpy)$_3^{2+}$. Addition of excess TBAOH (tetra-*n*-butylammonium hydroxide) leads to deprotonation of the phenolic units, and the absorption spectra of the resulting phenolate forms of the three dyads are shown as red traces in Figure 2. The phenolate forms exhibit additional absorption bands near 350 nm and at wavelengths longer than 500 nm. The Ru(bpy)$_3^{2+}$-localized MLCT state appears to be no longer the lowest energetic electronically excited state in the deprotonated dyads.

The protonated forms of the three dyads exhibit luminescence from the lowest-lying ^{3}MLCT state upon excitation at 450 nm in CH_3CN (Figure S1, Supporting Information). In the deprotonated forms, the emission is nearly completely quenched, suggesting that the ^{3}MLCT state is indeed no longer the lowest energetic electronically excited state, as suspected based on the absorption spectra. The ^{3}MLCT luminescence lifetime of the protonated forms in aerated CH_3CN is approximately 200 ns (Figure S2, Supporting Information), similar to what is measured for the Ru(bpy)$_3^{2+}$ reference complex under identical conditions. The very weak remaining luminescence of the deprotonated dyads decays with an instrumentally limited lifetime of ~10 ns (Figure S2, Supporting Information).

Imidazole does not react with photoexcited Ru(bpy)$_3^{2+}$ (Figure S3, Supporting Information), but methyl viologen (MV^{2+}) quenches the ^{3}MLCT excited state of the protonated dyads with similar efficiency as it quenches the ^{3}MLCT state of free Ru(bpy)$_3^{2+}$. The black and blue lines in Figure 3 are transient difference spectra measured after excitation of 2 × 10^{-5} M solutions of the three dyads from Scheme 1 in CH_3CN in the presence of 80 mM methyl viologen (MV^{2+})

dx.doi.org/10.1021/jp506087t | J. Phys. Chem. B 2015, 119, 2263−2273

Table 1. Reduction Potentials (in V versus Fc^+/Fc in CH_3CN) for One-Electron Reduction of the Individual Molecular Components[a]

molecule	$E^0(Ru^{3+}/Ru^{2+})$	$E^0(Ru^{2+}/Ru^+)$	$E^0(PhOH^+/PhOH)$	$E^0(PhO^\bullet/PhO^-)$
PhOH-xy_1-Ru^{2+}	0.90	−1.73	0.88	−0.54
PhOH-xy_2-Ru^{2+}	0.90	−1.72	0.90	−0.58
PhOH-xy_3-Ru^{2+}	0.88	−1.72	0.86	−0.58
$Ru(bpy)_3^{2+}$	0.86	−1.72		
2,4,6-^{t}Bu$_3$PhOH			1.18	−0.70

[a]Data extracted from cyclic voltammograms are shown in Figure 1, except those of 2,4,6-^{t}Bu$_3$PhOH, which were taken from the literature.[28] The first reduction of the $Ru(bpy)_3^{2+}$ complex is ligand-based and is only for simplicity labeled with $E^0(Ru^{2+}/Ru^+)$.

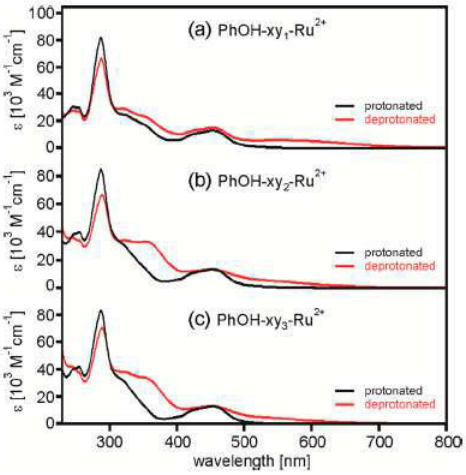

Figure 2. UV−vis absorption spectra of the three dyads (black traces) and their deprotonated phenolate forms (red traces) in CH_3CN. Deprotonation occurred by adding excess TBAOH.

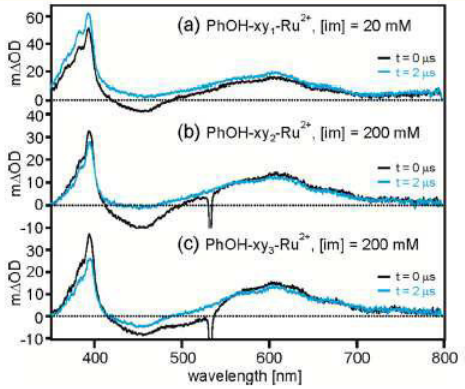

Figure 3. Transient difference spectra for 2×10^{-5} M solutions of the dyads in the presence of 80 mM methyl viologen and 20−200 mM imidazole after excitation at 532 nm with pulses of ∼10 ns duration. The black traces were recorded by time-averaging over the first 200 ns immediately after excitation. The blue traces were measured with a time delay of 2 μs and time-averaging over the subsequent 200 ns.

hexafluorophosphate and in the presence of imidazole (im) base. The imidazole concentration was 20 mM in the case of PhOH-xy_1-Ru^{2+} and 200 mM for the two longer dyads. Laser pulses of ∼10 ns duration at 532 nm were used for excitation, and detection of the spectra occurred by time-integrating the signal on an iCCD camera over a time period of 200 ns.

The black lines in Figure 3 are spectra that were measured in the first 200 ns immediately after the laser pulses, while the blue lines are spectra that were recorded after a time delay of 2 μs. The most prominent features of all six transient absorption spectra are a relatively narrow band at 395 nm and a broader band centered around 605 nm, which are characteristic features of one-electron reduced methyl viologen ($MV^{\bullet+}$).[31] The spectra recorded without time delay (black lines) additionally exhibit a negative signal near 450 nm, which is characteristic for the oxidized ruthenium complex ($Ru(bpy)_3^{3+}$); this spectral feature is often referred to as the MLCT bleach.[15,23,32−34] Thus, photoexcitation of the dyads in the presence of imidazole and methyl viologen induces electron transfer from their ^{3}MLCT-excited $Ru(bpy)_3^{2+}$ moieties to methyl viologen. In the spectra of PhOH-xy_1-Ru^{2+} and PhOH-xy_2-Ru^{2+} recorded with a 2 μs time delay (blue lines), the bleach at 450 nm has disappeared, but the signals at 395 and 605 nm are still present, indicating that $Ru(bpy)_3^{3+}$ disappears more rapidly than $MV^{\bullet+}$.[35]

Figure 4 shows the temporal evolution of the MLCT bleach at 450 nm after excitation of the PhOH-xy_1-Ru^{2+} dyad in

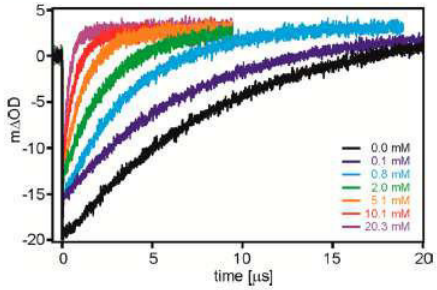

Figure 4. Recovery of the ^{1}MLCT bleach after 532 nm excitation of a 2×10^{-5} M solution of PhOH-xy_1-Ru^{2+} in CH_3CN with 80 mM methyl viologen and various concentrations of imidazole.

aerated CH_3CN in the presence of 80 mM MV^{2+} and increasing concentrations of imidazole. The excitation wavelength was 532 nm, and the pulse width was ∼10 ns. Analogous data sets for the two longer dyads are shown in the Supporting Information (Figure S4). The general observation for all three dyads is that the MLCT bleach recovers more rapidly with increasing imidazole concentration, and in all cases, single-exponential decay curves are measured. However, the longer the *p*-xylene bridge becomes, the more imidazole is required to accelerate the MLCT bleach recovery. For instance, in the PhOH-xy_1-Ru^{2+} dyad, the bleach recovery time (based on a single-exponential fit) is 1.2 μs at an imidazole concentration of 5.1 mM (Figure 4), but for the PhOH-xy_2-Ru^{2+} dyad, an imidazole concentration of 200 mM can only accelerate the MLCT bleach recovery to 1.7 μs (Figure S4c, Supporting Information). In the

PhOH-xy$_3$-Ru^{2+} dyad, addition of imidazole has an even weaker effect (Figure S4e, Supporting Information). In the case of PhOH-xy$_3$-Ru^{2+}, the acceleration of the MLCT bleach recovery induced by imidazole is, within experimental accuracy, the same as that observed for the Ru(bpy)$_3^{2+}$ reference complex (Figure S4g, Supporting Information); an increase in the imidazole concentration from 0 to 200 mM can only induce a change in bleach recovery time from ~40 to ~14 μs for PhOH-xy$_3$-Ru^{2+} and Ru(bpy)$_3^{2+}$. A Stern–Volmer experiment monitoring the MLCT bleach recovery time as a function of imidazole concentration (Figure S6, Supporting Information) shows that Ru(bpy)$_3^{3+}$ (in contrast to photoexcited Ru(bpy)$_3^{2+}$ (Figure S3, Supporting Information)) reacts with imidazole with a rate constant of 5.6×10^5 M^{-1} s^{-1}. While this rate constant can fully account for the acceleration of MLCT bleach recoveries detected for PhOH-xy$_3$-Ru^{2+} in the presence of imidazole, it is clear that the bleach recoveries detected for PhOH-xy$_1$-Ru^{2+} and PhOH-xy$_2$-Ru^{2+} are too fast to be explained by direct interaction of their Ru(bpy)$_3^{3+}$ moieties with imidazole.

When replacing the phenolic protons and the easily exchangeable imidazole N–H protons by deuterons, the MLCT bleach recovery kinetics characterizing the disappearance of Ru(bpy)$_3^{3+}$ in the PhOH-xy$_1$-Ru^{2+} and PhOH-xy$_2$-Ru^{2+} dyads are somewhat changed (Figure S4b/d, Supporting Information). At a given imidazole concentration, the bleach recoveries are slower than those before deuteration. In other words, there is a H/D kinetic isotope effect (KIE; 1.5 ± 0.5 for PhOH-xy$_1$-Ru^{2+}, 2.1 ± 0.6 for PhOH-xy$_2$-Ru^{2+}; see below), indicating that reduction of Ru(bpy)$_3^{3+}$ is coupled to a proton-transfer step.

In Figure 5a, the acceleration of the MLCT bleach recoveries is shown as a function of the imidazole concentration for the shortest dyad (PhOH-xy$_1$-Ru^{2+}, open squares) and its deuterated analogue (PhOD-xy$_1$-Ru^{2+}, filled squares). Specifically, we plot $k_{obs} - k_0$, that is, the difference between the bleach recovery time in the presence of a given concentration of imidazole (k_{obs}) and the inherent bleach recovery measured in pure CH_3CN containing no imidazole (k_0). The H/D KIE mentioned above is readily visible from the data in Figure 5a. In Figure 5b, analogous sets of data for PhOH-xy$_2$-Ru^{2+} (open circles) and PhOD-xy$_2$-Ru^{2+} (filled circles) are shown.

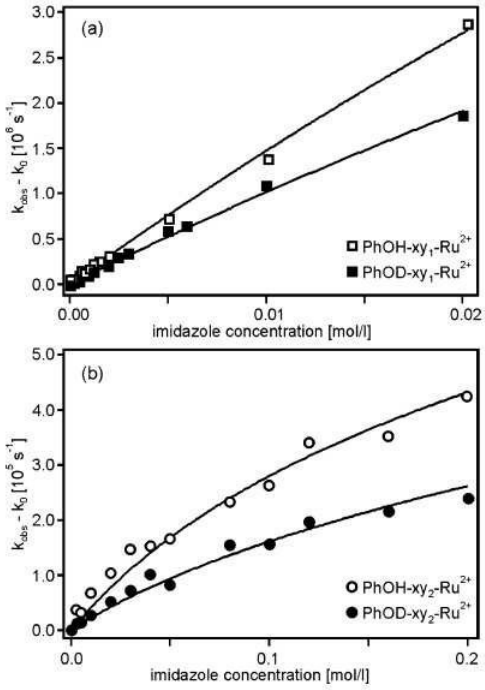

Figure 5. Dependence of the ^{3}MLCT bleach recovery rate of PhOH/D-xy$_1$-Ru^{2+} and PhOH/D-xy$_2$-Ru^{2+} in CH_3CN with 80 mM methyl viologen on the imidazole concentration. k_{obs} is the experimentally observable rate in the presence of imidazole (extracted from the data in Figures 4 and S4, Supporting Information), and k_0 is the experimentally observable rate for a given dyad in the absence of imidazole. The solid lines are fits with eq 4 to the experimental data, yielding the CPET rate constants in Table 3

■ DISCUSSION

Photochemistry in the Presence of MV^{2+} and Imidazole. Up to concentrations of 0.4 M, imidazole has no detectable influence on the ^{3}MLCT emission of Ru(bpy)$_3^{2+}$ (Figure S3, Supporting Information). However, the emissive ^{3}MLCT excited state of Ru(bpy)$_3^{2+}$ in CH_3CN is quenched oxidatively by methyl viologen with a rate constant of 2.4×10^9 M^{-1} s^{-1}.[36] Thus, when 80 mM of MV^{2+} is present, Ru(bpy)$_3^{3+}$ and MV$^{\bullet+}$ can be formed within less than 5 ns. Indeed, the transient absorption spectra in Figure 3 recorded without a time delay (black trace) provide evidence for these two species in the form of a bleach at 450 nm (due to Ru(bpy)$_3^{3+}$)[37] and absorption bands at 395 and 605 nm (due to MV$^{\bullet+}$).[31] Then, 2 μs later, the bleach at 450 nm has essentially disappeared (at least in the PhOH-xy$_1$-Ru^{2+} and PhOH-xy$_2$-Ru^{2+} dyads), but the signals at 395 and 605 nm are still present (blue traces in Figure 3). As noted above, this indicates that Ru(bpy)$_3^{3+}$ disappears more rapidly than MV$^{\bullet+}$.

Ru(bpy)$_3^{3+}$ reacts with imidazole in an undesired side reaction, presumably leading to oxidation of imidazole and formation of Ru(bpy)$_3^{2+}$ (Figure S6, Supporting Information).[38] However, given our experimentally determined rate constant of 5.6×10^5 M^{-1} s^{-1} (Supporting Information), the bimolecular reaction between Ru(bpy)$_3^{3+}$ and imidazole cannot account for a bleach recovery time of ~350 ns in PhOH-xy$_1$-Ru^{2+} in the presence of 20 mM imidazole (Figure 4) or a bleach recovery time of ~1700 ns in PhOH-xy$_2$-Ru^{2+} in the presence of 200 mM imidazole (Figure S4c, Supporting Information). Consequently, yet another reaction must be responsible for the rapid disappearance of Ru(bpy)$_3^{3+}$ in PhOH-xy$_1$-Ru^{2+} and PhOH-xy$_2$-Ru^{2+} in the presence of imidazole. Intramolecular electron transfer from phenol to Ru(bpy)$_3^{3+}$ (coupled to transfer of the phenolic proton to imidazole) is the only plausible option to account for the rapid bleach recovery kinetics. Several prior studies of tyrosine–ruthenium dyads in aqueous solutions using methyl viologen for the photogeneration of Ru(bpy)$_3^{3+}$ have reached the same conclusion; in the presence of base, Ru(bpy)$_3^{3+}$ can oxidize tyrosine (and most other phenols) by intramolecular long-range electron transfer.[11−20,24,39] Similar observations have been made for tyrosine–rhenium and phenol–rhenium systems, for which PCET originates from an electronically excited state.[6,21,22,40] The neutral phenoxyl radicals, which are formed as a result of this photoreaction, usually remain undetected because they absorb around 400 nm with extinction coefficients on the order of 5000 M^{-1} cm^{-1},[41,42] that is, in a spectral range where MV$^{\bullet+}$ has an extinction of approximately 17500 M^{-1} cm^{-1}.[31] From

the spectra in Figure 3, it is equally clear that phenolate photoproducts are not formed; the phenolate forms would lead to new absorption bands around 550 nm with extinction coefficients on the order of 5000 M^{-1} cm^{-1} (red traces in Figure 2), which is of comparable magnitude as the $MV^{\bullet+}$ extinction at 605 nm (~6000 M^{-1} cm^{-1}).[31]

Thus, the sequence of reactions shown in Scheme 2 is likely to occur after photoexcitation of the PhOH-xy_n-Ru^{2+} dyads in the presence of MV^{2+} and imidazole. Following the initial laser flash, photoexcited $Ru(bpy)_3^{2+}$ is quenched oxidatively by methyl viologen. The resulting $Ru(bpy)_3^{3+}$ species then abstracts an electron from phenol, and the phenolic proton is released to imidazole in an overall PCET reaction. The reaction products are phenoxyl radical ($PhO^{\bullet}$), $Ru(bpy)_3^{2+}$, and protonated imidazole (imH^+). We have not been able to determine the oxidation potential of imidazole nor have we found a value for it in the literature, but we suspect that in an undesired side reaction, $Ru(bpy)_3^{3+}$ can oxidize imidazole. For the dyads with n = 1 and 2, the PCET step is more rapid than the undesired side reaction because the electron-transfer distance is short enough, but in the dyad with n = 3, this is not the case anymore. For this reason, the subsequent discussion will focus largely on the PhOH-xy_1-Ru^{2+} and PhOH-xy_2-Ru^{2+} dyads. The flash/quench procedure shown in Scheme 2 has been previously applied many times for studies of electron transfer in proteins,[32,43,44] donor–bridge–acceptor molecules,[33,34,45] and for PCET investigations.[11−20,23]

Aside from the reaction sequence in Scheme 2, another scenario, illustrated by Scheme 3, is in principle conceivable. In a proton-transfer pre-equilibrium, PhO^--xy_n-Ru^{2+} and imH^+ could potentially be formed out of PhOH-xy_n-Ru^{2+} and imidazole. A flash-quench sequence could then lead to PhO^--xy_n-Ru^{3+}, which could react onward to the same photoproduct as above ($PhO^{\bullet}$-xy_n-Ru^{2+}).[46] Alternatively, PhO^--xy_n-$*Ru^{2+}$ could react to $PhO^{\bullet}$-xy_n-Ru^+, followed by reduction of MV^{2+} by $Ru(bpy)_3^+$, leading to the same photoproducts. There are several arguments that speak strongly against the sequences of reactions shown in Scheme 3, and these arguments will be discussed in detail below.

Scheme 2. Sequence of Reactions Occurring after Photoexcitation of the PhOH-xy_n-Ru^{2+} Dyads in CH_3CN in the Presence of Methyl Viologen (MV^{2+}) and Imidazole[a]

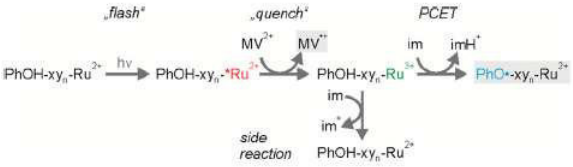

[a]The experimentally observable photoproducts (Figure 3) are marked with a grey shaded background.

Scheme 3. Pre-equilibrium between the Phenol and Phenolate Forms of the PhOH-xy_n-Ru^{2+} Dyads in CH_3CN in the Presence of Imidazole and Subsequent Possible Photoreactions with the Phenolate Forms[a]

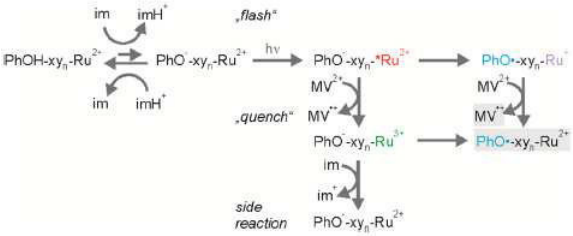

[a]The experimentally observable photoproducts are marked with a grey shaded background.

PCET Mechanisms. Assuming that the reaction sequence shown in Scheme 2 is correct (we will provide strong evidence for this below when we discuss all other possibilities on the basis of an energy level scheme), the starting point for the overall PCET reaction is the mixture comprised of imidazole and PhOH-xy_n-Ru^{3+} (top left corner of Scheme 4). PCET can then occur via three different mechanistic pathways.[7] In principle, there can first be a rate-determining electron-transfer step (top right corner of Scheme 4) that is followed by proton transfer, but the opposite reaction sequence (passing along the bottom left corner of Scheme 4) is also conceivable. The third option is CPET across the diagonal of Scheme 4.

Scheme 4. Three Possible Mechanistic Pathways for PCET in the Reaction System Comprised of Ruthenium-Oxidized Dyads and Imidazole[a]

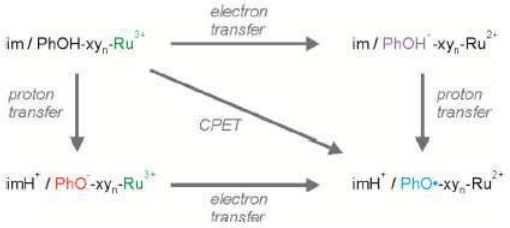

[a]The flash-quench-generated PhOH-xy_n-Ru^{3+} species and neutral imidazole on the top left corner are the starting point for PCET, and the $PhO^{\bullet}$-xy_n-Ru^{2+} dyads and protonated imidazole (imH^+) at the bottom right are the experimentally observable photoproducts. Reaction along the diagonal corresponds to concerted proton-electron transfer. Reactions along the corners are stepwise processes.

This last option is particularly interesting because it avoids the high-energy intermediates resulting from individual electron- and proton-transfer steps. In the following, we will discuss which one of the three mechanistic options is the most probable for our PhOH-xy_n-Ru^{2+} dyads.

The mechanistic discussion can only be made properly when the thermodynamics of the individual reaction steps are known.[7] On the basis of the reduction potentials in Table 1 and the acidity constants in Table 2, it is possible to estimate

Table 2. Acidity Constants of All Relevant Molecular Components in Various Solvents

molecule	pK_a in CH_3CN	pK_a in DMSO	pK_a in H_2O
2,4,6-^{t}Bu$_3$PhOH	29.8[a]	17.8[b]	13[b]
2,4,6-^{t}Bu$_3$PhOH$^+$	−3[b]	−10[b]	−5[b]
imidazole (im)	30.5[a]	18.6[b]	13[c]
imidazolium (imH^+)	18.6[a]	6.4[d]	7[c]

[a]Calculated from the values in DMSO using the relationship $pK_a(CH_3CN) = 12.31 + 0.98 \cdot pK_a(DMSO)$.[47] [b]From ref 28. [c]From ref 48. [d]From ref 49. Note that the imH^+ (and not the im) species is relevant for the CPET reaction considered in this work.

dx.doi.org/10.1021/jp506087t | J. Phys. Chem. B 2015, 119, 2263−2273

Scheme 5. Energy Level Diagram for the Various Possible Photoproducts Resulting from the Reaction Triple Comprised of PhOH-xy$_n$-Ru^{2+}, Methyl Viologen (MV^{2+}), and Imidazole (im)[a]

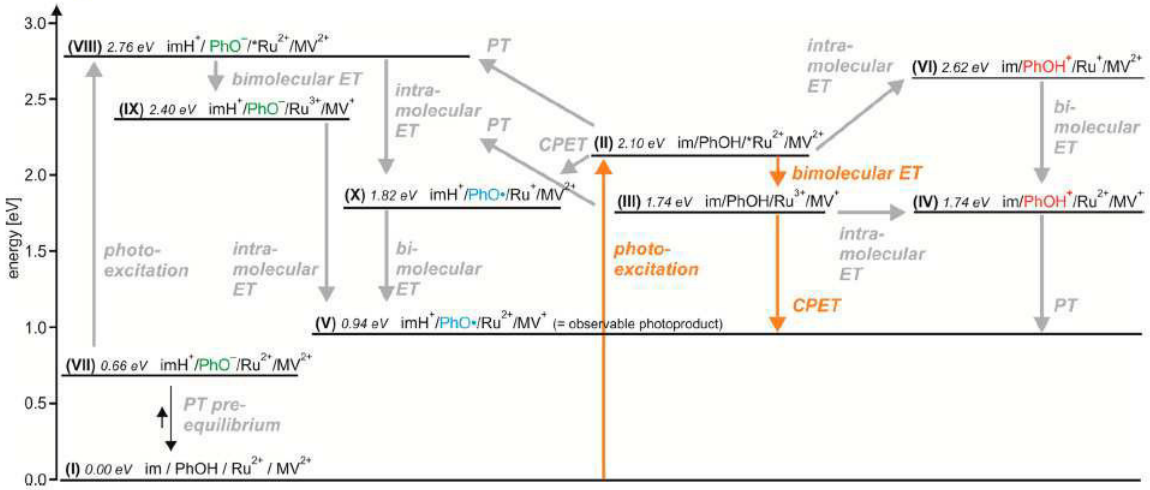

[a]The energies were estimated on the basis of redox potentials and acidity constants as described in the Supporting Information. The orange arrows mark the principal photochemical reaction pathway. ET = electron transfer; PT = proton transfer; CPET = concerted proton−electron transfer.

the energies of all potentially relevant reaction products that can emerge from the reaction triple comprised of PhOH-xy$_n$-Ru^{2+}, imidazole, and methyl viologen (MV^{2+}) in CH_3CN. How exactly this is done is explained in detail in the Supporting Information; Scheme 5 merely summarizes the results. In the following, we report energies with two digits, but we note that our energy estimates are only accurate to ±0.1 eV for electron-transfer steps and to ±0.3 eV for proton-transfer steps.

Following excitation of the Ru(bpy)$_3^{2+}$ moieties in the dyads, one reaches the ^{3}MLCT state at 2.10 eV above the ground state (state II in Scheme 5, orange upward arrow).[36] Bimolecular electron transfer with MV^{2+} then leads to state III (orange downward arrow) at 1.74 eV, comprised of ordinary imidazole, PhOH-xy$_n$-Ru^{3+}, and $MV^{\bullet+}$. From state III, proton transfer from PhOH-xy$_n$-Ru^{3+} to imidazole is endergonic by 0.66 eV (gray upward arrow to state IX). This energy estimate is based on the pK_a values of 2,4,6-^{t}Bu$_3$PhOH (29.8) and imH^+ (18.6) in CH_3CN (Table 2) and eq 1[7]

$$\Delta G_{PT}^{\ 0} = 0.059\ \text{eV}\cdot[pK_a(2,4,6\text{-}^t\text{Bu}_3\text{PhOH}) - pK_a(\text{imH}^+)] \quad (1)$$

If one considers states III and IX to be in chemical equilibrium, the molar ratio between PhO$^-$-xy$_n$-Ru^{3+} (in state IX) and PhOH-xy$_n$-Ru^{3+} (in state III) is 6.9×10^{-12}:1 (see the Supporting Information for details). Even under the assumption that the rate constant for the exergonic proton transfer from imH^+ to PhO$^-$-xy$_n$-Ru^{3+} is 6×10^{12} s^{-1} (i.e., corresponding to the frequency factor of absolute rate theory),[50] the rate constant for the endergonic proton transfer from PhOH-xy$_n$-Ru^{3+} to imidazole is limited to $(6 \times 10^{12}\ s^{-1}) \times (6.9 \times 10^{-12}) = \sim 40\ s^{-1}$. Thus, the expected maximal rate constant for the proton-transfer step from state III to state IX is ~40 s^{-1}, which is far too slow to account for the experimentally observable reaction kinetics. The same line of arguments holds for proton transfer from PhOH-xy$_n$-*Ru^{2+} to imidazole, that is, the reaction of state II to state VIII (gray upward arrow). Moreover, in view of the exergonic bimolecular ET with 80 mM MV^{2+} (conversion of state II to state III with $k = 2.4 \times 10^9$ M^{-1} s^{-1}),[36] the PT step from state II to state VIII is particularly unlikely.

The considerations made above are also relevant regarding the proton-transfer pre-equilibrium discussed in Scheme 3. In Scheme 5, this pre-equilibrium is included on the bottom left, with state VII at 0.66 eV above the ground state. In principle, photoexcitation of the small subset of dyads that are in their phenolate forms could promote them from state VII to state VIII at 2.76 eV (gray upward arrow), from which a sequence of intra- and bimolecular reactions could subsequently lead to the observable photoproducts (state V at 0.94 eV). On the basis of the considerations from above, the formation of the species in state VII (from state I) is not rapid enough to account for the observable reaction kinetics. What is more, the ^{3}MLCT state does not appear to be the lowest electronically excited state in the deprotonated dyads (see above), and consequently, photoexcitation of PhO$^-$-xy$_n$-Ru^{2+} at 532 nm is likely to lead to nonradiative relaxation without inducing any photochemistry at all.

The key conclusion until here is that a sequence of proton transfer followed by electron transfer, either via a PT pre-equilibrium (state VII in Scheme 5) or via rapid PT after initial ^{3}MLCT excitation (reaction from state II to state VIII or from state III to state IX) is very unlikely; the experimentally observable reaction kinetics as a function of imidazole concentration cannot be reconciled with either one of the two proton transfer−electron transfer scenarios (see also the Supporting Information and attempted fits with proton transfer−electron transfer models). Neither one of the reaction sequences shown in Scheme 3 can be a viable reaction pathway.

The logical next question then is whether an electron transfer−proton transfer reaction sequence is possible. According to Scheme 5, two different electron transfer−proton transfer reaction sequences are conceivable. The first one would involve intramolecular electron transfer from phenol to photoexcited Ru(bpy)$_3^{2+}$ as an initial reaction step (state II to state VI in Scheme 5). However, this reaction is endergonic by 0.5 eV; hence, in the presence of 80 mM MV^{2+} and given

Table 3. CPET Rate Constants Extracted from a Global Fit with Equation 4 to the Experimental Data in Figure 5

dyad	$k_{CPET,X=H}$ [s^{-1}]	$k_{CPET,X=D}$ [s^{-1}]	$k_{CPET,X=H}/k_{CPET,X=D}$
PhOX-xy_1-Ru^{2+}	$(2.35 \pm 0.42) \times 10^7$	$(1.62 \pm 0.29) \times 10^7$	1.5 ± 0.5
PhOX-xy_2-Ru^{2+}	$(5.62 \pm 0.67) \times 10^5$	$(2.64 \pm 0.39) \times 10^5$	2.1 ± 0.6

the above-mentioned rate constant for $Ru(bpy)_3^{2+}$ ^{3}MLCT quenching by MV^{2+} (2.4×10^9 M^{-1} s^{-1}),[36] intermolecular electron transfer from photoexcited $Ru(bpy)_3^{2+}$ to MV^{2+} must be the dominant reaction pathway (orange downward arrow from state II to state III). Once the PhOH-xy_n-Ru^{3+} photoproducts are formed, there is essentially no driving force for intramolecular electron transfer from phenol to $Ru(bpy)_3^{3+}$ (horizontal gray arrow from state III to state IV) because the electrochemical potentials for oxidation of phenol and $Ru(bpy)_3^{2+}$ are nearly identical (Table 1). This equiergic electron-transfer step is in competition with the CPET process marked by the orange downward arrow between states III and V, which is exergonic by 0.80 eV. Thus, the concerted release of an electron and a proton from the phenol is a far more plausible reaction pathway than an electron transfer−proton transfer reaction sequence. Furthermore, the experimentally observable H/D KIE (Figure 5) indicates that the rate-determining step involves proton motion, and this is another argument against an electron transfer−proton transfer sequence with a rate-determining electron-transfer process.

In principle, direct photoinduced CPET from state II to state X, involving MLCT-excited $Ru(bpy)_3^{2+}$ (as the case in one of our prior studies)[5] represents yet another mechanistic option. However, at 80 mM methyl viologen concentration, this CPET step is kinetically not competitive with oxidative quenching by MV^{2+} (Figure S6, Supporting Information).

We conclude that after the flash-quench sequence producing $Ru(bpy)_3^{3+}$ and $MV^{\bullet+}$, phenol oxidation by $Ru(bpy)_3^{3+}$ occurs in concert with release of the phenolic O−H proton to imidazole. Thus, the rate-determining reaction step leading to the experimentally observable MLCT bleach recoveries (Figures 4 and S4, Supporting Information) is CPET (orange arrows in Scheme 5, upper line in Scheme 2). CPET has been identified as the prevalent PCET mechanism in many cases of phenol oxidation.[6,11−15,18,19,40,50−64] We note that all thermodynamic considerations made above are based on the phenol oxidation potentials from Figure 1 and Table 1, which were measured in pure CH_3CN with 0.1 M $TBAPF_6$. In the photochemical experiments, however, substantial concentrations of imidazole are present (Figures 4 and 5). The presence of base can lower the phenol oxidation potentials significantly, but this is mostly the result of concerted proton−electron release.[52,53] That state of matters provides further support for our mechanistic assignment of CPET rather than electron transfer−proton transfer.

CPET Kinetics as a Function of Phenol−$Ru(bpy)_3^{2+}$ Distance. Only phenols that are hydrogen-bonded to imidazole are predisposed for CPET. Consequently, any analysis of the experimentally observable bleach recovery kinetics must take the hydrogen-bonding equilibrium between the phenols and imidazole (eq 2) into account.

$$\text{PhOH} + \text{im} \leftrightarrows \text{PhOH}\cdots\text{im} \tag{2}$$

The observable bleach recovery rate constant (k_{obs}) is a function of the CPET rate constant (k_{CPET}) times the fraction of hydrogen-bonded phenol−imidazole adducts (eq 3).[5,21]

$$k_{obs} = k_0 + k_Q\cdot[\text{im}] + \frac{k_{CPET}\cdot[\text{PhOH}\cdots\text{im}]}{c_{PhOH}} \tag{3}$$

In eq 3, k_0 is the inherent ^{3}MLCT bleach recovery rate constant for a given dyad in the absence of imidazole. The $k_Q\cdot[\text{im}]$ term describes the undesired side reaction between $Ru(bpy)_3^{3+}$ and imidazole (Scheme 2), and c_{PhOH} is the phenol concentration. Under the assumption that the concentration of hydrogen-bonded phenol−imidazole pairs is small compared to the actual concentration of free imidazole, the expression for k_{obs} can be reformulated to eq 4 (see the Supporting Information for details)[63,65]

$$k_{obs} - k_0 = k_Q\cdot[\text{im}] + \frac{k_{CPET}\cdot(K_A\cdot[\text{im}])}{(1 + K_A\cdot[\text{im}])} \tag{4}$$

In eq 4, K_A is the association constant for hydrogen-bonded phenol−imidazole, adducts as described by eq 2. The solid lines in Figure 5 are the result of a global two-parameter fit (using K_A and k_{CPET} as adjustable parameters) to the experimental $k_{obs} - k_0$ versus [im] data. k_Q was held at a value of 5.6×10^5 M^{-1} s^{-1} (Figure S5 (Supporting Information); see above). The fit occurred globally to all four sets of data (PhOH/D-xy_1-Ru^{2+}, PhOH/D-xy_2-Ru^{2+}) with one common K_A value. In other words, K_A was assumed to be independent of bridge length and deuteration. Our attempts to determine K_A in an independent manner (e.g., using UV−vis or IR spectroscopy) were unsuccessful. The above-mentioned global fit yields $K_A = 6.6 \pm 1.3$ M^{-1}, in line with previously determined association constants for phenol−pyridine adducts in benzonitrile.[63,65] The k_{CPET} values extracted from the global fit are summarized in Table 3. The most important finding is a decrease of k_{CPET} by roughly 2 orders of magnitude between the shortest dyad and the dyad with two *p*-xylene spacers. From the data points in Figure 5, it is already evident that for a given dyad and imidazole concentration, k_{CPET} is lower for the deuterated phenols than that for the ordinary ones. From the global fit with eq 4, one obtains H/D KIEs of 1.5 ± 0.5 for the shortest dyad and 2.1 ± 0.6 for the dyad with two *p*-xylene spacers (last column of Table 3). The necessity of assuming a common K_A value for all four systems considered here is an unavoidable shortfall in this analysis, but in light of the chemical similarity of all four systems relative to each other (variations only in bridge length and O−H versus O−D functions), it would appear to be a reasonable assumption.

In the tunneling regime, electron-transfer rates (k_{ET}) commonly exhibit an exponential distance dependence that can be described adequately with eq 5, in particular, when the variation of reaction free energy and reorganization energy with increasing distance (d) is small compared to that of the electronic coupling between the donor and the acceptor.[66]

$$k_{ET}(d) = k_{ET}^{(0)}\cdot\exp(-\beta\cdot d) \tag{5}$$

$k_{ET}^{(0)}$ is the electron-transfer rate constant when the donor and the acceptor are in van der Waals contact, and β is the distance decay constant. The latter is usually associated with a certain type of bridge (or intervening medium) separating the donor

dx.doi.org/10.1021/jp506087t | J. Phys. Chem. B 2015, 119, 2263−2273

from the acceptor, but in principle, β is dependent on the entire combination of donor, bridge, and acceptor.[66−68] Assuming that eq 5 can be applied to k_{CPET}, it is possible to extract a β value for bidirectional CPET in our systems. Ideally, β is determined on the basis of a homologous series of variable-length donor−bridge−acceptor molecules, but this is not possible in the present case because CPET is only kinetically competitive with other reactions of $Ru(bpy)_3^{3+}$ in the two shortest dyads. Equation 6 was used to determine the distance decay constant characterizing the decrease of k_{CPET} between PhOH/D-xy_1-Ru^{2+} and PhOH/D-xy_2-Ru^{2+}.

$$\beta = \ln\left(\frac{k_{CPET,xy1}}{k_{CPET,xy2}}\right)(d_{xy2} - d_{xy1}) \quad (6)$$

In eq 6, $k_{CPET,xy1}$ and $k_{CPET,xy2}$ are the CPET rate constants for the PhOH/D-xy_1-Ru^{2+} and PhOH/D-xy_2-Ru^{2+} dyads, respectively (Table 3). d_{xy1} and d_{xy2} are the (center-to-center) phenol−$Ru(bpy)_3^{2+}$ distances in the two systems. The result is a β value of 0.87 ± 0.09 $Å^{-1}$.[69]

Discussion of the Distance Decay Constant. The closest possible comparison of the β value determined for bidirectional CPET in the PhOH-$xy_{1,2}$-Ru^{2+}/imidazole system is to phenothiazine-xylene-$Ru(bpy)_3^{2+}$ molecules, in which a distance decay constant of 0.77 $Å^{-1}$ was found for intramolecular electron transfer.[34,68,70] Investigations of analogous phenothiazine-xylene-rhenium(I) molecules gave β = 0.52 $Å^{-1}$.[34,68,71] Electron transfer across unsubstituted oligo-*p*-phenylene bridges usually occurs with β values around 0.4 $Å^{-1}$ or even lower.[72,73] Our own recent study of bidirectional CPET with PhOH-$xy_{1,2,3}$-Ru^{2+} dyads (involving photoexcited $Ru(bpy)_3^{2+}$ rather than $Ru(bpy)_3^{3+}$ and pyrrolidine instead of imidazole) yielded β = 0.67 ± 0.23 $Å^{-1}$.[5] Thus, for the same set of molecules, thermal CPET initiated from photogenerated $Ru(bpy)_3^{3+}$ is associated with a larger β value than CPET initiated from photoexcited $Ru(bpy)_3^{2+}$. This discrepancy could be simply a manifestation of different (superexchange-mediated) electronic donor−acceptor couplings.[68,74] We have previously observed that electron transfer from a phenothiazine donor across multiple *p*-xylene bridges produces significantly different β values for thermal and excited-state electron transfer; with photogenerated $Ru(bpy)_3^{3+}$ as an electron acceptor, we obtained β = 0.77 $Å^{-1}$, and with a photoexcited $[Re(1,10\text{-phenanthroline})(CO)_3(pyridine)]^+$ complex, we found β = 0.52 $Å^{-1}$.[70,71]

Clearly, the distance decay constant determined herein is one of the largest (possibly the largest) ever reported for an oligo-*p*-phenylene-based donor−bridge−acceptor system. However, the deviation from what has been previously reported for simple (i.e., not proton-coupled) electron transfer in phenothiazine-xylene-$Ru(bpy)_3^{2+}$ dyads (0.77 $Å^{-1}$) is within the margins of typical variations for a given bridge.

■ SUMMARY AND CONCLUSIONS

In the PhOH-xy_n-Ru^{2+}/imidazole/methyl viologen reaction triples with n = 1 and 2, the sequence of photoreactions illustrated by Scheme 2 and the orange arrows in Scheme 5 takes place. The rate-determining step leading to phenol oxidation and $Ru(bpy)_3^{3+}$ re-reduction is CPET. The rate constant for this bidirectional CPET process decreases by roughly 2 orders of magnitude between the n = 1 and 2 systems, translating to a distance decay constant of 0.87 ± 0.09 $Å^{-1}$.

There are now two β values for the electron-transfer distance dependence of bidirectional CPET available in the literature. Both of them (0.87 ± 0.09 and 0.67 ± 0.23 $Å^{-1}$)[5] are clearly at the higher end of the usual range for simple (i.e., not proton-coupled) electron transfer across oligo-*p*-phenylene-based bridges.[73] From these two distance dependence studies of bidirectional CPET, it seems that if an effect of proton motion on the electron-transfer distance dependence is present at all, this effect is relatively small.

Assuming that the distance dependence of the CPET rates is dominated by the distance dependence of the electronic coupling matrix element ($H_{AB,CPET}$) describing the interaction between the potential energy surfaces of starting materials and CPET products, the relative insensitivity of the β value to the concerted proton motion is not particularly surprising. This is because $H_{AB,CPET}$ can be expressed as a product of electronic coupling matrix elements for proton transfer ($H_{AB,PT}$) and for electron transfer ($H_{AB,ET}$).[10] Increasing the electron donor−electron acceptor distance leads to a significant decrease in $H_{AB,ET}$, but $H_{AB,PT}$ is relatively unaffected as the proton donor−proton acceptor distance remains essentially unchanged.

Purely electrostatic effects that, in principle, could lead to a steeper distance dependence of electron transfer when proton motion occurs concertedly into a different direction appear to be of minor importance. This makes sense because $H_{AB,ET}$ is exponentially dependent on the electron donor−electron acceptor distance, but the Coloumb attraction between the electron and proton is inversely proportional to their separation distance.

A key message from this paper is that a long electron-transfer distance is no obstacle to concerted proton motion into a separate direction. On the basis of a β value of 0.87 ± 0.09 $Å^{-1}$ and assuming a reaction rate of 10^{13} s^{-1} for reactants in van der Waals contact, bidirectional CPET involving an electron-transfer step over 20 Å can, in principle, occur on the microsecond time scale; an electron-transfer step over 25 Å would require milliseconds.

■ EXPERIMENTAL SECTION

The synthesis and characterization of the PhOH/D-xy_n-Ru^{2+} molecules from Scheme 1 were reported in a recent paper.[5] UV−vis spectra were measured on a Cary 5000 instrument from Varian, and steady-state luminescence spectroscopy was performed on a Fluorolog3 from Horiba Jobin-Yvon with an R928 photomultiplier. For cyclic voltammetry, we used a Versastat3-200 potentiostat from Princeton Applied Research. A Pt disk working electrode and two silver wires as quasi-reference and counter electrodes were employed. Time-resolved luminescence and transient absorption spectroscopy were performed with an LP920-KS instrument from Edinburgh Instruments and the frequency-doubled output of a Quantel Brilliant b Nd:YAG laser.

■ ASSOCIATED CONTENT

Supporting Information

Additional luminescence and transient absorption data, derivation of the energy level diagram shown in Scheme 5, derivation of reaction rate expressions in the CPET and proton transfer−electron transfer limits, and more detailed discussion of the proton transfer−electron transfer mechanism. This material is available free of charge via the Internet at http://pubs.acs.org.

AUTHOR INFORMATION

Corresponding Author

*E-mail: oliver.wenger@unibas.ch.

Author Contributions

†J.C. and M.K.-P. contributed equally.

Notes

The authors declare no competing financial interest.

ACKNOWLEDGMENTS

Funding from the Swiss National Science Foundation through Grant Number 200021_146231/1 and from the Deutsche Forschungsgemeinschaft through IRTG-1422 is gratefully acknowledged.

REFERENCES

(1) Winkler, J. R.; Gray, H. B. Long-Range Electron Tunneling. *J. Am. Chem. Soc.* **2014**, *136*, 2930−2939.

(2) Edwards, P. P.; Gray, H. B.; Lodge, M. T. J.; Williams, R. J. P. Electron Transfer and Electronic Conduction through an Intervening Medium. *Angew. Chem., Int. Ed.* **2008**, *47*, 6758−6765.

(3) Warren, J. J.; Menzeleev, A. R.; Kretchmer, J. S.; Miller, T. F.; Gray, H. B.; Mayer, J. M. Long-Range Proton-Coupled Electron-Transfer Reactions of Bis(imidazole) Iron Tetraphenylporphyrins Linked to Benzoates. *J. Phys. Chem. Lett.* **2013**, *4*, 519−523.

(4) Markle, T. F.; Rhile, I. J.; Mayer, J. M. Kinetic Effects of Increased Proton Transfer Distance on Proton-Coupled Oxidations of Phenol-Amines. *J. Am. Chem. Soc.* **2011**, *133*, 17341−17352.

(5) Chen, J.; Kuss-Petermann, M.; Wenger, O. S. Distance Dependence of Bidirectional Concerted Proton−Electron Transfer in Phenol-Ru(2,2′-bipyridine)$_3^{2+}$ Dyads. *Chem.—Eur. J.* **2014**, *20*, 4098−4104.

(6) Kuss-Petermann, M.; Wolf, H.; Stalke, D.; Wenger, O. S. Influence of Donor−Acceptor Distance Variation on Photoinduced Electron and Proton Transfer in Rhenium(I)−Phenol Dyads. *J. Am. Chem. Soc.* **2012**, *134*, 12844−12854.

(7) Mayer, J. M. Proton-Coupled Electron Transfer: A Reaction Chemist's View. *Annu. Rev. Phys. Chem.* **2004**, *55*, 363−390.

(8) Weinberg, D. R.; Gagliardi, C. J.; Hull, J. F.; Murphy, C. F.; Kent, C. A.; Westlake, B. C.; Paul, A.; Ess, D. H.; McCafferty, D. G.; Meyer, T. J. Proton-Coupled Electron Transfer. *Chem. Rev.* **2012**, *112*, 4016−4093.

(9) Costentin, C.; Robert, M.; Savéant, J.-M. Concerted Proton−Electron Transfers: Electrochemical and Related Approaches. *Acc. Chem. Res.* **2010**, *43*, 1019−1029.

(10) Hammes-Schiffer, S.; Stuchebrukhov, A. A. Theory of Coupled Electron and Proton Transfer Reactions. *Chem. Rev.* **2010**, *110*, 6939−6960.

(11) Hammarström, L.; Styring, S. Proton-Coupled Electron Transfer of Tyrosines in Photosystem II and Model Systems for Artificial Photosynthesis: The Role of a Redox-Active Link between Catalyst and Photosensitizer. *Energy Environ. Sci.* **2011**, *4*, 2379−2388.

(12) Irebo, T.; Johansson, O.; Hammarström, L. The Rate Ladder of Proton-Coupled Tyrosine Oxidation in Water: A Systematic Dependence on Hydrogen Bonds and Protonation State. *J. Am. Chem. Soc.* **2008**, *130*, 9194−9195.

(13) Irebo, T.; Reece, S. Y.; Sjödin, M.; Nocera, D. G.; Hammarström, L. Proton-Coupled Electron Transfer of Tyrosine Oxidation: Buffer Dependence and Parallel Mechanisms. *J. Am. Chem. Soc.* **2007**, *129*, 15462−15464.

(14) Irebo, T.; Zhang, M.-T.; Markle, T. F.; Scott, A. M.; Hammarström, L. Spanning Four Mechanistic Regions of Intramolecular Proton-Coupled Electron Transfer in a Ru(bpy)$_3^{2+}$−Tyrosine Complex. *J. Am. Chem. Soc.* **2012**, *134*, 16247−16254.

(15) Magnuson, A.; Berglund, H.; Korall, P.; Hammarström, L.; Åkermark, B.; Styring, S.; Sun, L. C. Mimicking Electron Transfer Reactions in Photosystem II: Synthesis and Photochemical Characterization of a Ruthenium(II) Tris(bipyridyl) Complex with a Covalently Linked Tyrosine. *J. Am. Chem. Soc.* **1997**, *119*, 10720−10725.

(16) Sjödin, M.; Styring, S.; Åkermark, B.; Sun, L. C.; Hammarström, L. Proton-Coupled Electron Transfer from Tyrosine in a Tyrosine−Ruthenium−tris-Bipyridine Complex: Comparison with Tyrosine$_Z$ Oxidation in Photosystem II. *J. Am. Chem. Soc.* **2000**, *122*, 3932−3936.

(17) Sjödin, M.; Styring, S.; Wolpher, H.; Xu, Y. H.; Sun, L. C.; Hammarström, L. Switching the Redox Mechanism: Models for Proton-Coupled Electron Transfer from Tyrosine and Tryptophan. *J. Am. Chem. Soc.* **2005**, *127*, 3855−3863.

(18) Sun, L. C.; Burkitt, M.; Tamm, M.; Raymond, M. K.; Abrahamsson, M.; LeGourriérec, D.; Frapart, Y.; Magnuson, A.; Kenéz, P. H.; Brandt, P.; Tran, A.; Hammarström, L.; Styring, S.; Åkermark, B. Hydrogen-Bond Promoted Intramolecular Electron Transfer to Photogenerated Ru(III): A Functional Mimic of Tyrosine(Z) and Histidine 190 in Photosystem II. *J. Am. Chem. Soc.* **1999**, *121*, 6834−6842.

(19) Zhang, M.-T.; Irebo, T.; Johansson, O.; Hammarström, L. Proton-Coupled Electron Transfer from Tyrosine: A Strong Rate Dependence on Intramolecular Proton Transfer Distance. *J. Am. Chem. Soc.* **2011**, *133*, 13224−13227.

(20) Sjödin, M.; Ghanem, R.; Polivka, T.; Pan, J.; Styring, S.; Sun, L. C.; Sundström, V.; Hammarström, L. Tuning Proton Coupled Electron Transfer from Tyrosine: A Competition between Concerted and Step-wise Mechanisms. *Phys. Chem. Chem. Phys.* **2004**, *6*, 4851−4858.

(21) Pizano, A. A.; Yang, J. L.; Nocera, D. G. Photochemical Tyrosine Oxidation with a Hydrogen-Bonded Proton Acceptor by Bidirectional Proton-Coupled Electron Transfer. *Chem. Sci.* **2012**, *3*, 2457−2461.

(22) Reece, S. Y.; Nocera, D. G. Direct Tyrosine Oxidation Using the MLCT Excited States of Rhenium Polypyridyl Complexes. *J. Am. Chem. Soc.* **2005**, *127*, 9448−9458.

(23) Lachaud, T.; Quaranta, A.; Pellegrin, Y.; Dorlet, P.; Charlot, M. F.; Un, S.; Leibl, W.; Aukauloo, A. A Biomimetic Model of the Electron Transfer between P-680 and the Tyr$_Z$-His$_{190}$ Pair of PSII. *Angew. Chem., Int. Ed.* **2005**, *44*, 1536−1540.

(24) Quaranta, A.; Lachaud, F.; Herrero, C.; Guillot, R.; Charlot, M. F.; Leibl, W.; Aukauloo, A. Influence of the Protonic State of an Imidazole-Containing Ligand on the Electrochemical and Photophysical Properties of a Ruthenium(II) Polypyridine-Type Complex. *Chem.—Eur. J.* **2007**, *13*, 8201−8211.

(25) Megiatto, J. D.; Mendez-Hernandez, D. D.; Tejeda-Ferrari, M. E.; Teillout, A. L.; Llansola-Portoles, M. J.; Kodis, G.; Poluektov, O. G.; Rajh, T.; Mujica, V.; Groy, T. L.; Gust, D.; Moore, T. A.; Moore, A. L. A Bioinspired Redox Relay that Mimics Radical Interactions of the Tyr-His Pairs of Photosystem II. *Nat. Chem.* **2014**, *6*, 423−428.

(26) Hankache, J.; Niemi, M.; Lemmetyinen, H.; Wenger, O. S. Photoinduced Electron Transfer in Linear Triarylamine−Photosensitizer−Anthraquinone Triads with Ruthenium(II), Osmium(II), and Iridium(III). *Inorg. Chem.* **2012**, *51*, 6333−6344.

(27) Bordwell, F. G.; Cheng, J. P. Substituent Effects on the Stabilities of Phenoxyl Radicals and the Acidities of Phenoxyl Radical Cations. *J. Am. Chem. Soc.* **1991**, *113*, 1736−1743.

(28) Warren, J. J.; Tronic, T. A.; Mayer, J. M. Thermochemistry of Proton-Coupled Electron Transfer Reagents and Its Implications. *Chem. Rev.* **2010**, *110*, 6961−7001.

(29) Some rapid dimerization of phenoxyl radicals cannot be completely excluded despite the presence of bulky *tert*-butyl groups.

(30) The initial oxidative sweep produces phenoxyl radicals that are reduced to phenolate in the subsequent reductive sweep to potentials below −2.0 V. Re-oxidation of the phenolate to the phenoxyl radical is then detected at −0.6 V.

(31) Braterman, P. S.; Song, J. I. Spectroelectrochemistry of Aromatic Ligands and their Derivatives. 1. Reduction Products of 4,4′-Bipyridine, 2,2′-Bipyridine, 2,2′-Bipyrimidine, and Some Quaternized Derivatives. *J. Org. Chem.* **1991**, *56*, 4678−4682.

(32) Crane, B. R.; Di Bilio, A. J.; Winkler, J. R.; Gray, H. B. Electron Tunneling in Single Crystals of Pseudomonas Aeruginosa Azurins. *J. Am. Chem. Soc.* **2001**, *123*, 11623−11631.
(33) Walther, M. E.; Wenger, O. S. Tuning the Rates of Long-Range Charge Transfer across Phenylene Wires. *ChemPhysChem* **2009**, *10*, 1203−1206.
(34) Hanss, D.; Walther, M. E.; Wenger, O. S. Importance of Covalence, Conformational Effects and Tunneling-Barrier Heights for Long-Range Electron Transfer: Insights from Dyads with Oligo-*p*-phenylene, Oligo-*p*-xylene and Oligo-*p*-dimethoxybenzene Bridges. *Coord. Chem. Rev.* **2010**, *254*, 2584−2592.
(35) In Figure 3a, the intensity of the $MV^{\bullet+}$ signal at 395 nm is somewhat higher in the spectrum measured with a 2 μs delay than that in the spectrum measured without time delay. This is attributed to fluctuations in laser excitation power.
(36) Roundhill, D. M. *Photochemistry and Photophysics of Metal Complexes*; Plenum Press: New York, 1994.
(37) Heath, G. A.; Yellowlees, L. J.; Braterman, P. S. Spectro-Electrochemical Studies on Tris-Bipyridyl Ruthenium Complexes — UV, Visible, and Near-Infrared Spectra of the Series Ru(bipyridyl)$_3^{2+/1+/0/1-}$. *J. Chem. Soc., Chem. Commun.* **1981**, 287−289.
(38) In principle oxidized imidazole and reduced methyl viologen can then react back to the starting materials on a longer time scale, but we did not investigate this.
(39) Mayer, J. M.; Rhile, I. J.; Larsen, F. B.; Mader, E. A.; Markle, T. F.; DiPasquale, A. G. Models for Proton-Coupled Electron Transfer in Photosystem II. *Photosynth. Res.* **2006**, *87*, 3−20.
(40) Bonin, J.; Costentin, C.; Robert, M.; Savéant, J. M. Pyridine as Proton Acceptor in the Concerted Proton Electron Transfer Oxidation of Phenol. *Org. Biomol. Chem.* **2011**, *9*, 4064−4069.
(41) Lind, J.; Shen, X.; Eriksen, T. E.; Merenyi, G. The One-Electron Reduction Potential of 4-Substituted Phenoxyl Radicals in Water. *J. Am. Chem. Soc.* **1990**, *112*, 479−482.
(42) Das, P. K.; Encinas, M. V.; Steenken, S.; Scaiano, J. C. Reaction of *tert*-Butoxy Radicals with Phenols. Comparison with the Reactions of Carbonyl Triplets. *J. Am. Chem. Soc.* **1981**, *103*, 4162−4166.
(43) Bjerrum, M. J.; Casimiro, D. R.; Chang, I.-J.; Di Bilio, A. J.; Gray, H. B.; Hill, M. G.; Langen, R.; Mines, G. A.; Skov, L. K.; Winkler, J. R.; Wuttke, D. S. Electron-Transfer in Ruthenium-Modified Proteins. *J. Bioenerg. Biomembr.* **1995**, *27*, 295−302.
(44) Winkler, J. R.; Gray, H. B. Electron-Transfer in Ruthenium-Modified Proteins. *Chem. Rev.* **1992**, *92*, 369−379.
(45) He, B.; Wenger, O. S. Ruthenium−Phenothiazine Electron Transfer Dyad with a Photoswitchable Dithienylethene Bridge: Flash-Quench Studies with Methyl Viologen. *Inorg. Chem.* **2012**, *51*, 4335−4342.
(46) In principle, PhO^{-}-xy_n-$*Ru^{2+}$ could also react intramolecularly to form $PhO^{\bullet}$-xy_n-Ru^{+}. This species is then more likely to react intramolecularly to give PhO^{-}-xy_n-Ru^{2+} than to react with methyl viologen to the observed photoproducts.
(47) Kütt, A.; Leito, I.; Kaljurand, I.; Soovali, L.; Vlasov, V. M.; Yagupolskii, L. M.; Koppel, I. A. A Comprehensive Self-Consistent Spectrophotometric Acidity Scale of Neutral Bronsted Acids in Acetonitrile. *J. Org. Chem.* **2006**, *71*, 2829−2838.
(48) Bordwell, F. G. Equilibrium Acidities in Dimethyl-Sulfoxide Solution. *Acc. Chem. Res.* **1988**, *21*, 456−463.
(49) Crampton, M. R.; Robotham, I. A. Acidities of Some Substituted Ammonium Ions in Dimethyl Sulfoxide. *J. Chem. Res.* **1997**, 22−23.
(50) Sjödin, M.; Irebo, T.; Utas, J. E.; Lind, J.; Merenyi, G.; Åkermark, B.; Hammarström, L. Kinetic Effects of Hydrogen Bonds on Proton-Coupled Electron Transfer from Phenols. *J. Am. Chem. Soc.* **2006**, *128*, 13076−13083.
(51) Markle, T. F.; Mayer, J. M. Concerted Proton−Electron Transfer in Pyridylphenols: The Importance of the Hydrogen Bond. *Angew. Chem., Int. Ed.* **2008**, *47*, 738−740.
(52) Rhile, I. J.; Markle, T. F.; Nagao, H.; DiPasquale, A. G.; Lam, O. P.; Lockwood, M. A.; Rotter, K.; Mayer, J. M. Concerted Proton−Electron Transfer in the Oxidation of Hydrogen-Bonded Phenols. *J. Am. Chem. Soc.* **2006**, *128*, 6075−6088.
(53) Rhile, I. J.; Mayer, J. M. One-Electron Oxidation of a Hydrogen-Bonded Phenol Occurs by Concerted Proton-Coupled Electron Transfer. *J. Am. Chem. Soc.* **2004**, *126*, 12718−12719.
(54) Schrauben, J. N.; Cattaneo, M.; Day, T. C.; Tenderholt, A. L.; Mayer, J. M. Multiple-Site Concerted Proton−Electron Transfer Reactions of Hydrogen-Bonded Phenols Are Nonadiabatic and Well Described by Semiclassical Marcus Theory. *J. Am. Chem. Soc.* **2012**, *134*, 16635−16645.
(55) Markle, T. F.; Rhile, I. J.; DiPasquale, A. G.; Mayer, J. M. Probing Concerted Proton−Electron Transfer in Phenol-Imidazoles. *Proc. Natl. Acad. Sci. U.S.A.* **2008**, *105*, 8185−8190.
(56) Bonin, J.; Costentin, C.; Louault, C.; Robert, M.; Savéant, J. M. Water (in Water) as an Intrinsically Efficient Proton Acceptor in Concerted Proton Electron Transfers. *J. Am. Chem. Soc.* **2011**, *133*, 6668−6674.
(57) Costentin, C.; Robert, M.; Savéant, J. M. Electrochemical and Homogeneous Proton-Coupled Electron Transfers: Concerted Pathways in the One-Electron Oxidation of a Phenol Coupled with an Intramolecular Amine-Driven Proton Transfer. *J. Am. Chem. Soc.* **2006**, *128*, 4552−4553.
(58) Costentin, C.; Robert, M.; Savéant, J. M. Concerted Proton−Electron Transfer Reactions in Water. Are the Driving Force and Rate Constant Depending on pH When Water Acts as Proton Donor or Acceptor? *J. Am. Chem. Soc.* **2007**, *129*, 5870−5879.
(59) Costentin, C.; Robert, M.; Savéant, J. M. Concerted Proton−Electron Transfers in the Oxidation of Phenols. *Phys. Chem. Chem. Phys.* **2010**, *12*, 11179−11190.
(60) Bonin, J.; Costentin, C.; Louault, C.; Robert, M.; Routier, M.; Savéant, J. M. Intrinsic Reactivity and Driving Force Dependence in Concerted Proton−Electron Transfers to Water Illustrated by Phenol Oxidation. *Proc. Natl. Acad. Sci. U.S.A.* **2010**, *107*, 3367−3372.
(61) Bronner, C.; Wenger, O. S. Kinetic Isotope Effects in Reductive Excited-State Quenching of Ru(2,2′-bipyrazine)$_3^{2+}$ by Phenols. *J. Phys. Chem. Lett.* **2012**, *3*, 70−74.
(62) Bronner, C.; Wenger, O. S. Proton-Coupled Electron Transfer between 4-Cyanophenol and Photoexcited Rhenium(I) Complexes with Different Protonatable Sites. *Inorg. Chem.* **2012**, *51*, 8275−8283.
(63) Biczok, L.; Gupta, N.; Linschitz, H. Coupled Electron−Proton Transfer in Interactions of Triplet C-60 with Hydrogen-Bonded Phenols: Effects of Solvation, Deuteration, and Redox Potentials. *J. Am. Chem. Soc.* **1997**, *119*, 12601−12609.
(64) Cape, J. L.; Bowman, M. K.; Kramer, D. M. Reaction Intermediates of Quinol Oxidation in a Photoactivatable System that Mimics Electron Transfer in the Cytochrome bc_1 Complex. *J. Am. Chem. Soc.* **2005**, *127*, 4208−4215.
(65) Biczók, L.; Linschitz, H. Concerted Electron and Proton Movement in Quenching of Triplet C-60 and Tetracene Fluorescence by Hydrogen-Bonded Phenol-Base Pairs. *J. Phys. Chem.* **1995**, *99*, 1843−1845.
(66) Gray, H. B.; Winkler, J. R. Long-Range Electron Transfer. *Proc. Natl. Acad. Sci. U.S.A.* **2005**, *102*, 3534−3539.
(67) Albinsson, B.; Eng, M. P.; Pettersson, K.; Winters, M. U. Electron and Energy Transfer in Donor−Acceptor Systems with Conjugated Molecular Bridges. *Phys. Chem. Chem. Phys.* **2007**, *9*, 5847−5864.
(68) Wenger, O. S. How Donor−Bridge−Acceptor Energetics Influence Electron Tunneling Dynamics and Their Distance Dependences. *Acc. Chem. Res.* **2011**, *44*, 25−35.
(69) The error here reflects the uncertainty in the k_{CPET} values from Table 3.
(70) Hanss, D.; Wenger, O. S. Tunneling Barrier Effects on Photoinduced Charge Transfer through Covalent Rigid Rod-Like Bridges. *Inorg. Chem.* **2009**, *48*, 671−680.
(71) Hanss, D.; Wenger, O. S. Electron Tunneling through Oligo-*p*-xylene Bridges. *Inorg. Chem.* **2008**, *47*, 9081−9084.
(72) Weiss, E. A.; Ahrens, M. J.; Sinks, L. E.; Gusev, A. V.; Ratner, M. A.; Wasielewski, M. R. Making a Molecular Wire: Charge and Spin Transport through *para*-Phenylene Oligomers. *J. Am. Chem. Soc.* **2004**, *126*, 5577−5584.

(73) Wenger, O. S. Photoinduced Electron and Energy Transfer in Phenylene Oligomers. *Chem. Soc. Rev.* **2011**, *40*, 3538−3550.
(74) Eng, M. P.; Albinsson, B. Non-Exponential Distance Dependence of Bridge-Mediated Electronic Coupling. *Angew. Chem., Int. Ed.* **2006**, *45*, 5626−5629.

THE JOURNAL OF PHYSICAL CHEMISTRY Letters

Letter

pubs.acs.org/JPCL

Mechanistic Diversity in Proton-Coupled Electron Transfer between Thiophenols and Photoexcited [Ru(2,2′-Bipyrazine)$_3$]$^{2+}$

Martin Kuss-Petermann[†] and Oliver S. Wenger*[,‡]

[†]Institut für Anorganische Chemie, Georg-August-Universität Göttingen, Tammannstrasse 4, D-37077 Göttingen, Germany

[‡]Departement für Chemie, Universität Basel, Spitalstrasse 51, CH-4065 Basel, Switzerland

Supporting Information

ABSTRACT: Proton-coupled electron transfer (PCET) with phenols has been investigated in considerable detail in recent years while at the same time analogous mechanistic studies of PCET with thiophenols have remained scarce. We report on PCET between a series of thiophenols and a photoexcited Ru(II) complex, which acts as a combined electron/proton acceptor. Depending on the exact nature of the thiophenol, PCET occurs through different reaction mechanisms. The results are discussed in the context of recent studies of PCET between phenols and photoexcited d^6 metal complexes.

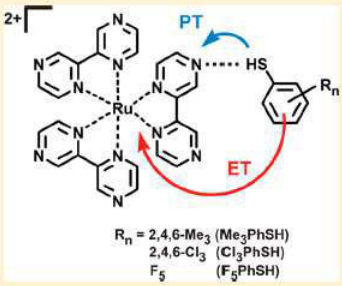

SECTION: Spectroscopy, Photochemistry, and Excited States

Proton-coupled electron transfer (PCET) can generally take place via three different reaction pathways, (i) electron transfer followed by proton transfer (ET−PT), (ii) proton transfer followed by electron transfer (PT−ET), and (iii) concerted proton−electron transfer (CPET).[1−3] Phenol oxidation is a PCET process for which numerous mechanistic studies were performed in recent years,[4−15] but similarly detailed mechanistic investigations of thiophenol oxidation remained comparatively scarce.[16,17] This and the fact that thiyl radicals are known to play an important role in biochemistry provided the motivation for the work presented in this Letter.

The S−H bond dissociation free energies (BDFEs) in thiophenols are significantly lower than the O−H BDFEs in phenols.[18,19] In the case of phenols, the CPET rates increase with decreasing O−H BDFEs;[1,20] hence, the low S−H BDFE of thiophenols could in principle be expected to favor the CPET mechanism. On the other hand, thiophenols are considerably more acidic than phenols,[19,21] and this could make the PT−ET mechanism more favorable.

In our study, we focused on three phenols with different substituents, 2,4,6-trimethylthiophenol (Me_3PhSH), 2,4,6-trichlorothiophenol (Cl_3PhSH), and pentafluorothiophenol (F_5PhSH). Ru(bpz)$_3^{2+}$ (bpz = 2,2′-bipyrazine) served as a reaction partner with which PCET can be phototriggered; the reduction/protonation chemistries of photoexcited Ru(bpz)$_3^{2+}$ are strongly interrelated.[22−27]

Figure 1a shows transient absorption spectra of 10^{-5} M Ru(bpz)$_3^{2+}$ solutions in CH_3CN containing millimolar concentrations of the three different thiophenols; excitation occurred at 532 nm with pulses of ∼10 ns duration. The green trace was obtained when using Me_3PhSH. This spectrum is exemplary for the spectra of the two other thiophenols. The transient difference spectrum measured for the Me_3PhSH/*Ru(bpz)$_3^{2+}$ reaction pair exhibits positive signals at 360 and 490 nm in addition to a bleach centered at around 440 nm. These three spectral features are compatible with the formation of the one-electron reduced and protonated ruthenium complex (=[Ru(bpz)$_2$(bpzH)]$^{2+}$).[22,25] The bleach at 440 nm is rather weak, but this is in line with protonation of a bpz ligand in addition to reduction.[22,25]

Figure 1b shows transient difference spectra that were recorded after photolysis of the disulfides of our thiophenols at 355 nm in CH_3CN; the green trace was obtained for $(Me_3PhS)_2$, that is, the disulfide of Me_3PhSH. UV photolysis of disulfides is known to produce thiyl radicals.[21,28] We observe identical thiyl spectra when using a redox photosensitization method and the thiophenols as starting materials (Figure S1, Supporting Information).[29] The spectra from Figure 1b and Figure S1 (Supporting Information) exhibit a band at 490 nm, in line with previously reported spectra of phenylthiyl radicals.[21,28,30,31] Thus, in Figure 1a, the thiyl radical absorption overlaps with one of the absorption bands of [Ru(bpz)$_2$(bpzH)]$^{2+}$.

For Cl_3PhSH and F_5PhSH, qualitatively similar transient difference spectra as those for Me_3PhSH were measured (blue and red traces in Figure 1a). UV photolysis of $(F_5PhS)_2$ proved to be inefficient (presumably this is due to poor solubility of the disulfide in acetonitrile and the comparatively weak absorption of this compound at 355 nm), and the spectrum of the $F_5PhS^{\bullet}$ radical could not be detected.

Received: June 14, 2013
Accepted: July 18, 2013
Published: July 22, 2013

The Journal of Physical Chemistry Letters Letter

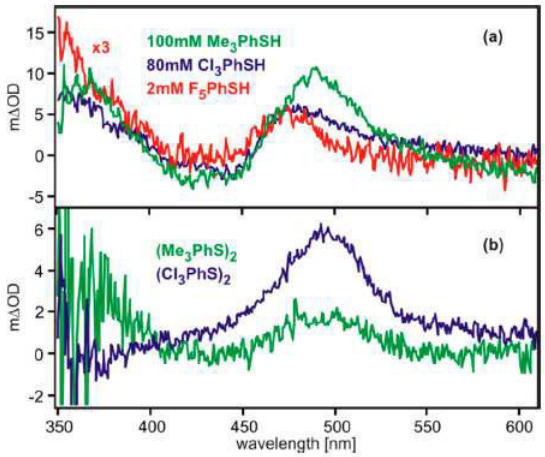

Figure 1. (a) Transient absorption spectra obtained from $Ru(bpz)_3^{2+}$/thiophenol mixtures in deoxygenated CH_3CN at 298 K. Excitation occurred at 532 nm with pulses of ~10 ns width. The $Ru(bpz)_3^{2+}$ concentration was 10^{-5} M, and the thiophenol concentrations ranged from 2 to 100 mM. (b) Transient absorption spectra measured after photolysis of saturated solutions of $(Me_3PhS)_2$ and $(Cl_3PhS)_2$ in CH_3CN at 313 K with 355 nm laser pulses of ~10 ns duration. Detection occurred via integration over a time range of 200 ns in all cases. The data in (a) were recorded with time delays of 2 μs (Me_3PhSH/Cl_3PhSH) and 3 μs (F_5PhSH), respectively. In the case of (b), detection occurred without any time delay.

Figure 2 shows the results of luminescence decay measurements of $Ru(bpz)_3^{2+}$ in the presence of increasing concentrations of the three thiophenols in deoxygenated CH_3CN at 293 K. In the absence of thiophenol, the luminescence lifetime of $Ru(bpz)_3^{2+}$ under these conditions is 788 ns at 600 nm, but in the presence of thiophenols, it can be quenched down to ~10 ns, which corresponds to the temporal resolution of the employed instrument. In the case of trimethylthiophenol, deuteration has no noticeable influence as we observe similar quenching behavior for Me_3PhSH (Figure 2a) and Me_3PhSD (Figure 2b). This manifests in equal slopes for proteo- and deutero-analogues in the corresponding Stern–Volmer plot (Figure 2c).

Time-integrated steady-state luminescence quenching studies were performed in parallel, but these experiments are less insightful because it seems that during photoirradiation of the $Ru(bpz)_3^{2+}$/thiophenol solutions, luminescent impurities are formed. This is particularly detrimental for time-integrated luminescence intensity measurements, but it is less of a problem for the time-resolved data in Figure 2.

For trichlorothiophenol (Figure 2d/e) and pentafluorothiophenol (Figure 2g/h), there are noticeable differences between proteo- and deutero-analogues, that is, non-negligible H/D kinetic isotope effects (KIEs) are detected. From the Stern–Volmer plots in the third row of Figure 2, we determine rate constants for bimolecular excited-state quenching ($k_{Q,H}$) that are on the order of 10^7 M^{-1} s^{-1} for Me_3PhSH (Figure 2c) and Cl_3PhSH (Figure 2f), while for F_5PhSH (Figure 2i), $k_{Q,H}$ is

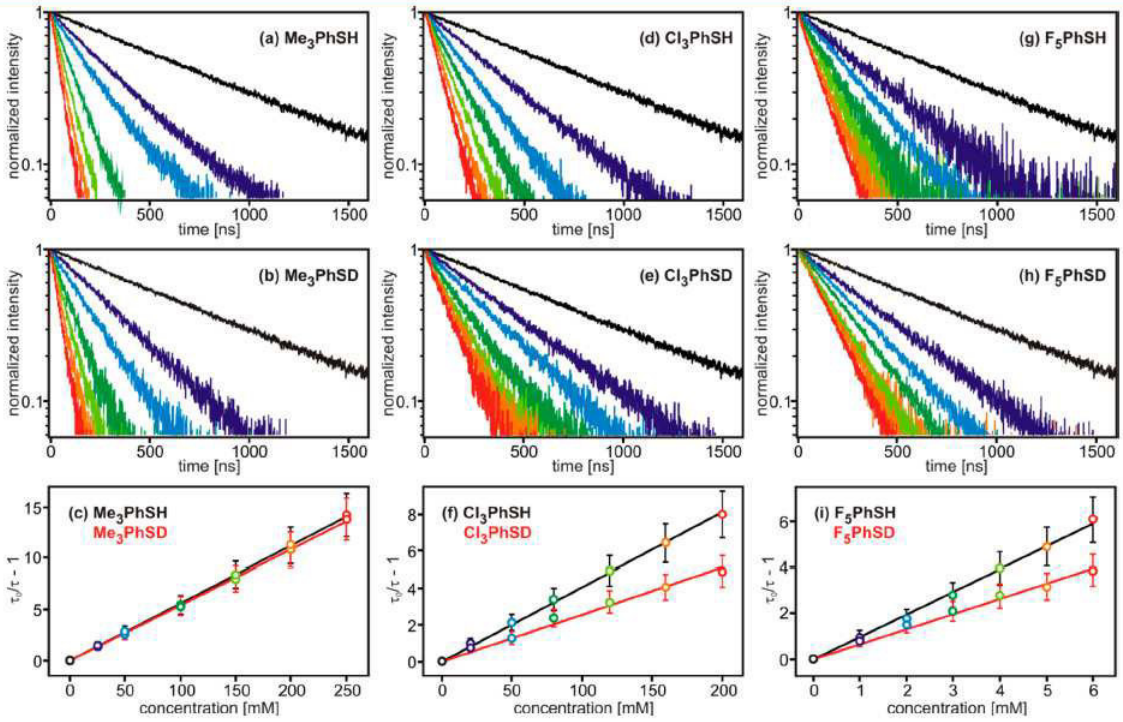

Figure 2. Luminescence decays of $Ru(bpz)_3^{2+}$ in deoxygenated CH_3CN at 293 K detected at 600 nm in the absence (black traces) and presence (colored traces) of various concentrations of thiophenols, (a) Me_3PhSH, (b) Me_3PhSD, (d) Cl_3PhSH, (e) Cl_3PhSD, (g) F_5PhSH, and (h) F_5PhSD. Panels (c), (f), and (i) show Stern–Volmer plots based on the data in (a/b), (d/e), and (g/h). Linear regression fits were forced to have intercepts of 0; from their slopes, the $k_{Q,H}$ and $k_{Q,D}$ values in Table 1 were calculated using τ_0 = 788 ns for the excited-state lifetime of $Ru(bpz)_3^{2+}$. Photoexcitation was at 532 nm with laser pulses of ~10 ns width.

dx.doi.org/10.1021/jz4012349 | J. Phys. Chem. Lett. 2013, 4, 2535–2539

roughly a factor of 20 greater (Table 1; the $k_{Q,D}$ values are the rate constants for the deuterated thiophenols). The H/D KIEs

Table 1. Rate Constants for Bimolecular Excited-State Quenching of $Ru(bpz)_3^{2+}$ with Ordinary ($k_{Q,H}$) and Deuterated ($k_{Q,D}$) Thiophenols As Extracted from the Slopes of the Stern–Volmer Plots in Figure 2[a]

thiophenol	$k_{Q,H}$ [M^{-1} s^{-1}]	$k_{Q,D}$ [M^{-1} s^{-1}]	H/D KIE
Me_3PhSH/D	$(7.1 \pm 0.8) \times 10^7$	$(6.9 \pm 0.7) \times 10^7$	1.0 ± 0.2
Cl_3PhSH/D	$(5.1 \pm 0.6) \times 10^7$	$(3.2 \pm 0.4) \times 10^7$	1.6 ± 0.3
F_5PhSH/D	$(12.5 \pm 1.4) \times 10^8$	$(8.4 \pm 1.0) \times 10^8$	1.5 ± 0.3

[a] $k_{Q,H/D}$ = slopes/τ_0; τ_0 = excited-state lifetime of $Ru(bpz)_3^{2+}$; 788 ns. KIEs correspond to ratios of $k_{Q,H}/k_{Q,D}$.

($=k_{Q,H}/k_{Q,D}$) are 1.0 ± 0.2 for Me_3PhSH/D, 1.6 ± 0.3 for Cl_3PhSH/D, and 1.5 ± 0.3 for F_5PhSH/D. The observation of significant KIEs for trichlorothiophenol and pentafluorothiophenol suggests that the rate-determining step (RDS) of the PCET reaction involves proton motion, and therefore, PT–ET and CPET mechanisms appear plausible for these two thiophenols.

The absence of a significant KIE for trimethylthiophenol suggests that the RDS involves no proton motion, and therefore, an ET–PT mechanism appears plausible in this case. The absence of a significant KIE need not necessarily exclude PT–ET or CPET mechanisms, but thermodynamic considerations support the interpretation of the PCET reaction between trimethylthiophenol and $Ru(bpz)_3^{2+}$ in terms of an ET–PT mechanism; Me_3PhSH is oxidized at 0.95 V versus Fc^+/Fc in CH_3CN (Table 2 and Figure S2, Supporting

Table 2. Oxidation (E_{ox}) and Reduction (E_{red}) Potentials[a] and Acidity Constants (in H_2O) for the Thiophenols and $Ru(bpz)_3^{2+}$[b]

compound	E_{ox}	E_{red}	pK_a
Me_3PhSH	0.95		6.8[f]
Cl_3PhSH	1.7		4.8[g]
F_5PhSH	>2.0		2.7[h]
$Ru(bpz)_3^{2+}$	1.6[c]	−1.1	
$*Ru(bpz)_3^{2+}$		0.92[d]	
$[Ru(bpz)_2(bpzH)]^{2+}$			7.1[i]
$*[Ru(bpz)_2(bpzH)]^{3+}$		1.06[e]	2.3[j]
$[Ru(bpz)_2(bpzH)]^{3+}$			−2.2[k]

[a] In V versus Fc^+/Fc in CH_3CN; converted from other reference electrodes when necessary[35]. [b] The asterisks denote photoexcited species. [c] From ref 25. [d] From ref 32. [e] From ref 26. [f] From ref 36. [g] From ref 37. [h] From ref 38. [i] From refs 25 and 34. [j] From ref 23. [k] From ref 39.

Information), whereas photoexcited $Ru(bpz)_3^{2+}$ is reduced at 0.92 V versus Fc^+/Fc in CH_3CN.[32] Consequently, ET from Me_3PhSH to $*Ru(bpz)_3^{2+}$ has $\Delta G_{ET}^0 \approx 0$ eV, and this is compatible with a $k_{Q,H}$ value on the order of 10^7 M^{-1} s^{-1}.[33] After initial ET, the ensuing PT from Me_3PhSH^+ to $Ru(bpz)_3^+$ is expected to be highly exergonic (the pK_a of thiol radical cations is <0 in H_2O;[18,19] the pK_a of the conjugate acid of $Ru(bpz)_3^+$ is 7.1 in H_2O).[25,34] For these reasons, it seems plausible that the $Me_3PhS^\bullet$ radical and $[Ru(bpz)_2(bpzH)]^{2+}$ are formed in an ET–PT sequence.

For trichlorothiophenol and pentafluorothiophenol, an ET–PT sequence is less probable not only because there are non-negligible KIEs but also for thermodynamic reasons; Cl_3PhSH is oxidized at 1.7 V versus Fc^+/Fc in CH_3CN, while F_5PhSH is oxidized at >2 V versus Fc^+/Fc in CH_3CN (Figure S2, Supporting Information and Table 2). Consequently, $\Delta G_{ET}^0 \approx +0.8$ eV for Cl_3PhSH and $\Delta G_{ET}^0 > 1.1$ eV for F_5PhSH. Excited-state deactivation rate constants on the order of 10^7–10^9 M^{-1} s^{-1} (Table 1) cannot be reconciled with such strongly endergonic ET steps. Therefore, PCET with Cl_3PhSH and F_5PhSH is likely to either involve PT–ET, CPET, or a combination of these two mechanisms. The thermodynamics of the initial PT step of PT–ET sequences can only be crudely estimated because the pK_a values of the relevant thiophenols and the conjugate acid of the photoexcited ruthenium complex, $*[Ru(bpz)_2(bpzH)]^{3+}$, are known only for aqueous solution but not for CH_3CN. In H_2O, the pK_a of Cl_3PhSH is 4.8, whereas the pK_a of F_5PhSH is 2.7 (Table 2).[37,38] The conjugate acid of the excited complex, $*[Ru(bpz)_2(bpzH)]^{3+}$, has a pK_a value of 2.3 under identical conditions (Table 2).[23] Consequently, in aqueous solution, the initial PT step has $\Delta G_{PT}^0 \approx 0$ eV in the case of F_5PhSH and $\Delta G_{PT}^0 \approx 0.059$ eV·(4.8 − 2.3) ≈ +0.15 eV in the case of Cl_3PhSH, but in CH_3CN, the relevant pK_a values are expected to be significantly different, and therefore, our ΔG_{PT}^0 estimates are likely to be associated with errors of ±0.5 eV.[32] On this basis, we cannot exclude PT–ET as a viable reaction mechanism for the $F_5PhSH/*Ru(bpz)_3^{2+}$ and $Cl_3PhSH/*Ru(bpz)_3^{2+}$ reaction pairs; in principle, it is conceivable that the decrease in reaction rates from $(1.25 \pm 0.14) \times 10^9$ M^{-1} s^{-1} (for F_5PhSH) to $(5.1 \pm 0.6) \times 10^7$ M^{-1} s^{-1} (for Cl_3PhSH) is caused by an increase of ΔG_{PT}^0 to more positive values. The thermodynamics of the ET steps ensuing initial PT can be estimated with greater accuracy; the Cl_3PhS^- and F_5PhS^- thiolate anions are both oxidized at ∼−0.1 V versus Fc^+/Fc in CH_3CN (Figure S2 and Table S1, Supporting Information), whereas the protonated and excited ruthenium complex is reduced at 1.06 V versus Fc^+/Fc in CH_3CN (Table 2).[26,35] Consequently, ET from the thiolates to $*[Ru(bpz)_2(bpzH)]^{3+}$ would be exergonic by ∼1.2 eV in both cases.

In an attempt to determine the activation energies for the photoinduced PCET reactions in the three thiophenol/$*Ru(bpz)_3^{2+}$ couples, the temperature dependence of the luminescence decays at a given thiophenol concentration was measured in the 5–55 °C range (Figure S3, Supporting Information). An Arrhenius plot of the respective data for $Me_3PhSH/*Ru(bpz)_3^{2+}$ yields an activation energy (E_A) of 0.17 ± 0.03 eV (Figure S3a, Supporting Information). For the $Cl_3PhSH/*Ru(bpz)_3^{2+}$ and $F_5PhSH/*Ru(bpz)_3^{2+}$ reaction pairs, the Arrhenius plots yield apparent negative E_A values (Figure S3b/c, Supporting Information), indicating that the RDS of the PCET reactions in these two cases is in fact activationless. For the $F_5PhSH/*Ru(bpz)_3^{2+}$ couple, activationless PT followed by ET is in line with a $k_{Q,H}$ value near the diffusion limit (∼10^9 M^{-1} s^{-1}). However, for the $Cl_3PhSH/*Ru(bpz)_3^{2+}$ couple, we find $E_A = 0$ as well, yet the photoreaction is clearly not diffusion-controlled (Table 1). This might be an indication that the CPET mechanism plays a significant role for this reaction couple.[40]

For a series of six phenols that react with photoexcited $Ru(bpz)_3^{2+}$ in CH_3CN via PCET, we previously found a linear correlation between $\ln(k_{Q,H})$ and the O–H BDFEs (black circles in Figure 3; BDFEs in DMSO).[20,32] This correlation is in line with a CPET mechanism for all six phenols.[41,42] Experimental S–H BDFE values for Me_3PhSH, Cl_3PhSH, and F_5PhSH are not available; there exist only computed bond

dx.doi.org/10.1021/jz4012349 | J. Phys. Chem. Lett. 2013, 4, 2535–2539

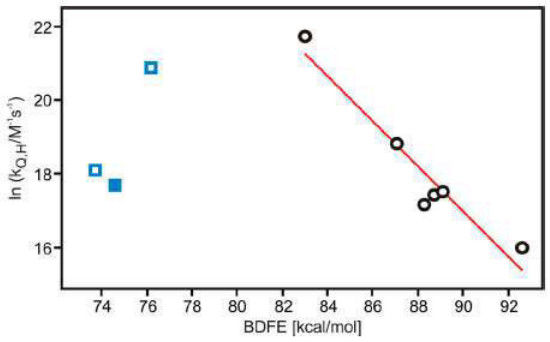

Figure 3. Plot of $\ln(k_{Q,H})$ versus O−H/S−H BDFEs in phenols (black circles) and thiophenols (blue squares; the blue filled square marks Cl_3PhSH). The phenol data are from refs 20 and 32, and the BDFEs (in DMSO) were calculated from BDEs (of comparable thiophenols in DMSO), as described in the Supporting Information.[19] BDEs (in DMSO) for comparable thiophenols were taken from ref 18. The PCET reaction partner was photoexcited $Ru(bpz)_3^{2+}$ in all cases.

dissociation enthalpies (BDEs).[37,43,44] In lack of better alternatives, we use the experimental S−H BDEs (in DMSO) of 4-methylthiophenol (78.3 kcal/mol), 4-chlorothiophenol (79.2 kcal/mol), and 3-trifluoromethylthiophenol (80.8 kcal/mol) as input values for the estimation of BDFEs (in DMSO) for Me_3PhSH, Cl_3PhSH, and F_5PhSH as described in the Supporting Information.[18,19] This somewhat crude approximation procedure yields the BDFE values used for the three thiophenols in Figure 3 (blue squares). None of the thiophenol data points fall onto the correlation found between $\ln(k_{Q,H})$ and O−H BDFEs for the phenols.

Me_3PhSH and F_5PhSH (open blue squares) are not expected to follow this correlation because they react predominantly through stepwise mechanisms, but CPET is a possibility for Cl_3PhSH. However, in order for the $k_{Q,H}$ value of Cl_3PhSH (filled blue square) to match the correlation observed for CPET with phenols, our S−H BDFE estimate would have to be in error by roughly 14 kcal/mol, which we consider unlikely. This finding can be interpreted in two ways; (i) it can be used as an argument against CPET for Cl_3PhSH, or (ii) phenols and thiophenols represent sufficiently dissimilar sets of reactants that are not expected to fall onto the same $\ln(k_{Q,H})$ versus BDFE correlation.[41,45] It is known that bond strengths are not the only determinants of hydrogen atom transfer (HAT) reactivity (this is particularly obvious when comparing the rates for hydrogen atom abstraction from C−H and O−H bonds).[45] Interpretation (ii) does make some sense even though one might expect S−H and O−H bonds to be more similar to each other than C−H and O−H bonds.[46]

An important difference between phenoxyl and phenylthiyl radicals is certainly the extent of delocalization of the unpaired electron into the π-system. Delocalization is significant in the phenoxyl radicals, whereas in the phenylthiyls, the unpaired electron stays much more localized on the sulfur atom.[21,30] In one specific case study, the difference in resonance stabilization between phenoxyl and phenylthiyl radicals has been estimated to ~9 kcal/mol.[21]

In conclusion, we find that PCET in three different thiophenol/$Ru(bpz)_3^{2+}$ couples occurs via at least two different reaction pathways, namely, ET−PT (Me_3PhSH) and PT−ET (F_5PhSH). For Cl_3PhSH, the situation is less clear; some of the evidence suggests that a CPET mechanism is operative, while other evidence is also compatible with PT−ET. Thiol oxidation has long been known to lead to net H loss and the formation of thiyl radicals; our study illustrates the full breadth of mechanistic possibilities that may lead to phenylthiyl radicals.

■ ASSOCIATED CONTENT

Supporting Information

Experimental methods, synthetic protocols, additional transient absorption, electrochemical and temperature-dependent luminescence data, and calculation of BDFEs from BDEs. This material is available free of charge via the Internet at http://pubs.acs.org.

■ AUTHOR INFORMATION

Corresponding Author

*E-mail: oliver.wenger@unibas.ch.

Notes

The authors declare no competing financial interest.

■ ACKNOWLEDGMENTS

This work was supported by the DFG through IRTG-1422 and by the Swiss NSF.

■ REFERENCES

(1) Mayer, J. M. Proton-Coupled Electron Transfer: A Reaction Chemist's View. *Annu. Rev. Phys. Chem.* **2004**, *55*, 363−390.

(2) Weinberg, D. R.; Gagliardi, C. J.; Hull, J. F.; Murphy, C. F.; Kent, C. A.; Westlake, B. C.; Paul, A.; Ess, D. H.; McCafferty, D. G.; Meyer, T. J. Proton-Coupled Electron Transfer. *Chem. Rev.* **2012**, *112*, 4016−4093.

(3) Hammes-Schiffer, S.; Stuchebrukhov, A. A. Theory of Coupled Electron and Proton Transfer Reactions. *Chem. Rev.* **2010**, *110*, 6939−6960.

(4) Biczok, L.; Gupta, N.; Linschitz, H. Coupled Electron−Proton Transfer in Interactions of Triplet C-60 with Hydrogen-Bonded Phenols: Effects of Solvation, Deuteration, and Redox Potentials. *J. Am. Chem. Soc.* **1997**, *119*, 12601−12609.

(5) Schrauben, J. N.; Cattaneo, M.; Day, T. C.; Tenderholt, A. L.; Mayer, J. M. Multiple-Site Concerted Proton−Electron Transfer Reactions of Hydrogen-Bonded Phenols Are Nonadiabatic and Well Described by Semiclassical Marcus Theory. *J. Am. Chem. Soc.* **2012**, *134*, 16635−16645.

(6) Markle, T. F.; Mayer, J. M. Concerted Proton−Electron Transfer in Pyridylphenols: The Importance of the Hydrogen Bond. *Angew. Chem., Int. Ed.* **2008**, *47*, 738−740.

(7) Irebo, T.; Zhang, M.-T.; Markle, T. F.; Scott, A. M.; Hammarström, L. Spanning Four Mechanistic Regions of Intramolecular Proton-Coupled Electron Transfer in a $Ru(bpy)_3^{2+}$−Tyrosine Complex. *J. Am. Chem. Soc.* **2012**, *134*, 16247−16254.

(8) Zhang, M.-T.; Irebo, T.; Johansson, O.; Hammarström, L. Proton-Coupled Electron Transfer from Tyrosine: A Strong Rate Dependence on Intramolecular Proton Transfer Distance. *J. Am. Chem. Soc.* **2011**, *133*, 13224−13227.

(9) Costentin, C.; Robert, M.; Savéant, J. M. Electrochemical and Homogeneous Proton-Coupled Electron Transfers: Concerted Pathways in the One-Electron Oxidation of a Phenol Coupled with an Intramolecular Amine-Driven Proton Transfer. *J. Am. Chem. Soc.* **2006**, *128*, 4552−4553.

(10) Costentin, C.; Robert, M.; Savéant, J. M. Concerted Proton−Electron Transfers in the Oxidation of Phenols. *Phys. Chem. Chem. Phys.* **2010**, *12*, 11179−11190.

(11) Lebedeva, N. V.; Schmidt, R. D.; Concepcion, J. J.; Brennaman, M. K.; Stanton, I. N.; Therien, M. J.; Meyer, T. J.; Forbes, M. D. E. Structural and pH Dependence of Excited State PCET Reactions involving Reductive Quenching of the MLCT Excited State of Ru-

II(bpy)$_2$(bpz)$^{2+}$ by Hydroquinones. *J. Phys. Chem. A* **2011**, *115*, 3346−3356.
(12) Cape, J. L.; Bowman, M. K.; Kramer, D. M. Reaction Intermediates of Quinol Oxidation in a Photoactivatable System that Mimics Electron Transfer in the Cytochrome bc(1) Complex. *J. Am. Chem. Soc.* **2005**, *127*, 4208−4215.
(13) Lachaud, T.; Quaranta, A.; Pellegrin, Y.; Dorlet, P.; Charlot, M. F.; Un, S.; Leibl, W.; Aukauloo, A. A Biomimetic Model of the Electron Transfer between P-680 and the Tyr$_Z$−His$_{190}$ Pair of PSII. *Angew. Chem., Int. Ed.* **2005**, *44*, 1536−1540.
(14) Pizano, A. A.; Yang, J. L.; Nocera, D. G. Photochemical Tyrosine Oxidation with a Hydrogen-Bonded Proton Acceptor by Bidirectional Proton-Coupled Electron Transfer. *Chem. Sci.* **2012**, *3*, 2457−2461.
(15) Kuss-Petermann, M.; Wolf, H.; Stalke, D.; Wenger, O. S. Influence of Donor−Acceptor Distance Variation on Photoinduced Electron and Proton Transfer in Rhenium(I)−Phenol Dyads. *J. Am. Chem. Soc.* **2012**, *134*, 12844−12854.
(16) Alam, M. M.; Sato, M.; Watanabe, A.; Akasaka, T.; Ito, O. Photochemical Reactions between C-60 and Aromatic Thiols, Protonation of C-60 via Photoinduced Electron Transfer. *J. Phys. Chem. A* **1998**, *102*, 7447−7451.
(17) Nauser, T.; Koppenol, W. H.; Schöneich, C. Reversible Hydrogen Transfer Reactions in Thiyl Radicals from Cysteine and Related Molecules: Absolute Kinetics and Equilibrium Constants Determined by Pulse Radiolysis. *J. Phys. Chem. B* **2012**, *116*, 5329−5341.
(18) Bordwell, F. G.; Zhang, X. M.; Satish, A. V.; Cheng, J. P. Assessment of the Importance of Changes in Ground-State Energies on the Bond-Dissociation Enthalpies of the O−H Bonds in Phenols and the S−H Bonds in Thiophenols. *J. Am. Chem. Soc.* **1994**, *116*, 6605−6610.
(19) Warren, J. J.; Tronic, T. A.; Mayer, J. M. Thermochemistry of Proton-Coupled Electron Transfer Reagents and Its Implications. *Chem. Rev.* **2010**, *110*, 6961−7001.
(20) Wenger, O. S. Proton-Coupled Electron Transfer with Photoexcited Metal Complexes. *Acc. Chem. Res.* **2013**, *46*, 1517−1526.
(21) Armstrong, D. A.; Sun, Q.; Tripathi, G. N. R.; Schuler, R. H.; McKinnon, D. Spectra, Ionization-Constants, and Rates of Oxidation of 1,4-Dimercaptobenzene and Properties of the *p*-Mercaptophenythiyl and *p*-Benzodithiyl Anion-Radicals. *J. Phys. Chem.* **1993**, *97*, 5611−5617.
(22) D'Angelantonio, M.; Mulazzani, Q. G.; Venturi, M.; Ciano, M.; Hoffman, M. Z. One-Electron Reduction of Ruthenium(II)−Diimine Complexes — Characterization of Reduced Species Containing 2,2′-Bipyridine, 2,2′-Bipyrimidine, and 2,2′-Bipyrazine in Aqueous Solution. *J. Phys. Chem.* **1991**, *95*, 5121−5129.
(23) Sun, H.; Hoffman, M. Z. Protonation of the Excited-States of Ruthenium(II) Complexes Containing 2,2′-Bipyridine, 2,2′-Bipyrazine, and 2,2′-Bipyrimidine Ligands in Aqueous Solution. *J. Phys. Chem.* **1993**, *97*, 5014−5018.
(24) Venturi, M.; Mulazzani, Q. G.; Ciano, M.; Hoffman, M. Z. Radiolytic and Electrochemical Reduction of Ru(bpz)$_3^{2+}$ in Aqueous Solution — Stability, Redox, and Acid−Base Properties of Ru(bpz)$_3^{+}$. *Inorg. Chem.* **1986**, *25*, 4493−4498.
(25) Anderson, P. A.; Anderson, R. F.; Furue, M.; Junk, P. C.; Keene, F. R.; Patterson, B. T.; Yeomans, B. D. Protonation Studies of Reduced Ruthenium(II) Complexes with Polypyridyl Ligands. *Inorg. Chem.* **2000**, *39*, 2721−2728.
(26) Haga, M. A.; Dodsworth, E. S.; Eryavec, G.; Seymour, P.; Lever, A. B. P. Luminescence Quenching of the Tris(2,2′-Bipyrazine)-ruthenium(II) Cation and Its Monoprotonated Complex. *Inorg. Chem.* **1985**, *24*, 1901−1906.
(27) Wenger, O. S. Proton-Coupled Electron Transfer Originating from Excited States of Luminescent Transition-Metal Complexes. *Chem.—Eur. J* **2011**, *17*, 11692−11702.
(28) Ito, O.; Matsuda, M. Kinetic-Study for Spin-Trapping Reactions of Thiyl Radicals with Nitroso-Compounds. *J. Am. Chem. Soc.* **1983**, *105*, 1937−1940.
(29) Gadosy, T. A.; Shukla, D.; Johnston, L. J. Generation, Characterization, and Deprotonation of Phenol Radical Cations. *J. Phys. Chem. A* **1999**, *103*, 8834−8839.
(30) Armstrong, D. A.; Sun, Q.; Schuler, R. H. Reduction Potentials and Kinetics of Electron Transfer Reactions of Phenylthiyl Radicals: Comparisons with Phenoxyl Radicals. *J. Phys. Chem.* **1996**, *100*, 9892−9899.
(31) Bonifacic, M.; Weiss, J.; Chaudhri, S. A.; Asmus, K. D. Oxidation of Thiols by Radical Cations of Organic Sulfides. *J. Phys. Chem.* **1985**, *89*, 3910−3914.
(32) Bronner, C.; Wenger, O. S. Kinetic Isotope Effects in Reductive Excited-State Quenching of Ru(2,2′-bipyrazine)$_3^{2+}$ by Phenols. *J. Phys. Chem. Lett.* **2012**, *3*, 70−74.
(33) Roundhill, D. M., *Photochemistry and Photophysics of Metal Complexes*; Plenum Press: New York, 1994.
(34) Casalboni, F.; Mulazzani, Q. G.; Clark, C. D.; Hoffman, M. Z.; Orizondo, P. L.; Perkovic, M. W.; Rillema, D. P. Acid−Base and Electrochemical Properties of the MLCT Excited States and One-Electron-Reduced Forms of Ruthenium(II) Complexes Containing 2-(2′-Pyridyl)pyrimidine and 2,2′-Bipyridine in Aqueous Solution. *Inorg. Chem.* **1997**, *36*, 2252−2257.
(35) Pavlishchuk, V. V.; Addison, A. W. Conversion Constants for Redox Potentials Measured Versus Different Reference Electrodes in Acetonitrile Solutions at 25 Degrees C. *Inorg. Chim. Acta* **2000**, *298*, 97−102.
(36) Bordwell, F. G.; Hughes, D. L. Thiol Acidities and Thiolate Reactivities Toward Butyl Chloride in Dimethylsulfoxide Solution — The Question of Curvature in Brönsted Plots. *J. Org. Chem.* **1982**, *47*, 3224−3232.
(37) Altarawneh, M.; Dar, T.; Dlugogorski, B. Z. Thermochemical Parameters and pK_a Values for Chlorinated Congeners of Thiophenol. *J. Chem. Eng. Data* **2012**, *57*, 1834−1842.
(38) Jencks, W. P.; Salvesen, K. Equilibrium Deuterium Isotope Effects on Ionization of Thiol Acids. *J. Am. Chem. Soc.* **1971**, *93*, 4433−4436.
(39) Rugge, A.; Clark, C. D.; Hoffman, M. Z.; Rillema, D. P. Protonation of the Ground States of Ruthenium(II) Photosensitizers. *Inorg. Chim. Acta* **1998**, *279*, 200−205.
(40) For a PT−ET mechanism, one might expect the activationless reaction of trichlorophenol to be essentially diffusion-controlled, in analogy to what is observed for pentafluorothiophenol.
(41) Evans, M. G.; Polanyi, M. Inertia and Driving Force of Chemical Reactions. *Trans. Faraday Soc.* **1938**, *34*, 0011−0023.
(42) Matsuo, T.; Mayer, J. M. Oxidations of NADH Analogues by *cis*-Ru-IV(bpy)$_2$(py)(O)$^{2+}$ Occur by Hydrogen-Atom Transfer Rather Than by Hydride Transfer. *Inorg. Chem.* **2005**, *44*, 2150−2158.
(43) Nam, P. C.; Nguyen, M. T.; Chandra, A. K. Theoretical Study of the Substituent Effects on the S−H Bond Dissociation Energy and Ionization Energy of 3-Pyridinethiol: Prediction of Novel Antioxidant. *J. Phys. Chem. A* **2006**, *110*, 10904−10911.
(44) Heidbrink, J. L.; Ramirez-Arizmendi, L. E.; Thoen, K. K.; Guler, L.; Kenttamaa, H. I. Polar Effects Control Hydrogen-Abstraction Reactions of Charged, Substituted Phenyl Radicals. *J. Phys. Chem. A* **2001**, *105*, 7875−7884.
(45) Mayer, J. M. Understanding Hydrogen Atom Transfer: From Bond Strengths to Marcus Theory. *Acc. Chem. Res.* **2011**, *44*, 36−46.
(46) Mayer, J. M.; Hrovat, D. A.; Thomas, J. L.; Borden, W. T. Proton-Coupled Electron Transfer versus Hydrogen Atom Transfer in Benzyl/Toluene, Methoxyl/Methanol, and Phenoxyl/Phenol Self-Exchange Reactions. *J. Am. Chem. Soc.* **2002**, *124*, 11142−11147.

4. Electron Transfer Rate Maxima at Large Donor-Acceptor Distances

Electron transfer (ET) reactions play a very important role in many biological processes.[70] For example, electron transfer is the key reaction step in photosynthesis and the terminal point of cellular respiration, as discussed in Chapter 2 of this thesis.[11, 71] In the 1950s and 1960s Rudolph A. Marcus developed his theory on electron transfer, for which he was awarded the Nobel Prize in chemistry in 1992. The Marcus-theory describes the rates for electron transfer as a function of several parameters such as the reaction free energy, the reorganization energy, the spatial separation between donor and acceptor, or the solvent properties. There are several implications arising from the equation postulated by Marcus. A rather unusual one is that with an increase in the reaction free energy for electron transfer its rate constant only increases to a certain maximum value. A further increase of the driving force leads to a decrease of the rate constants. The system is then operative in the so called Marcus-inverted region. This counter-intuitive postulation was first confirmed experimentally by Closs and Miller in the1980s and is well established nowadays.[26–29]

Another unusual but less well known prediction of the Marcus equation is that a system operating in the inverted region (large reaction free energy) should exhibit a unique distance-dependency as demonstrated in Figure 4.1. It depicts the calculated rate con-

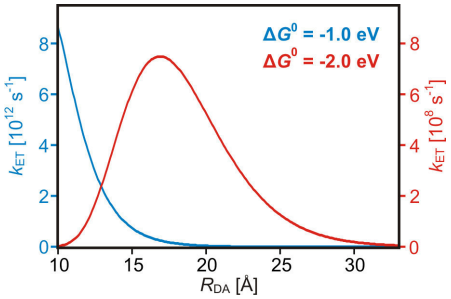

Figure 4.1 Calculated rate constants for electron transfer in acetonitrile as a function of donor-acceptor separation for ΔG^0 = -1.0 eV (blue trace) and -2.0 eV (red trace) using equations 2.1 and 2.4. The following parameters were applied: $r_A = r_D = 5$ Å, $H_{DA,(0)} = 200$ cm^{-1}, and $\beta = 0.5$ Å^{-1}.

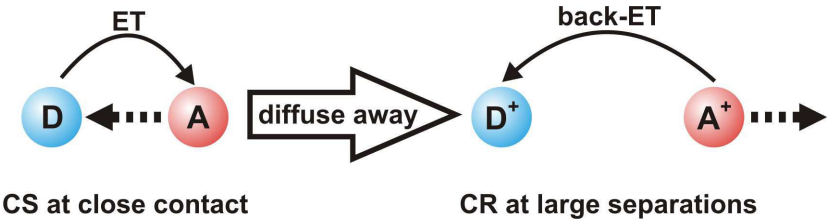

Scheme 4.1 Schematic bimolecular reaction. For small reaction free energies the charge separation (CS) takes place at close contact. Thermal charge recombination (CR) associated with large driving forces (MARCUS inverted region) is accelerated at larger distances.

stants according to equation 2.1 and 2.4, for electron transfer in acetonitrile for driving forces of -1.0 eV and -2.0 eV as a function of donor-acceptor distance (assuming $r_A = r_D = 5$ Å, $H_{DA,(0)} = 200$ cm^{-1}, and $\beta = 0.5$ Å^{-1}). In contrast to electron transfer rates in the normal region (blue trace in Figure 4.1), decaying exponentially with increasing donor-acceptor-distance as discussed in Chapter 2 of this thesis, the rates for electron transfer in the inverted region were predicted to exhibit a maximum rate constant which is not at "close contact" (red trace in Figure 4.1). In other words, rate constants for electron transfer operating in the inverted region should increase to a maximum value upon increasing the distance between donor and acceptor. A further increase of spatial separation should then result in an exponential decay of the rate constants similar to what is observed in the normal region of the MARCUS theory. This phenomenon has been investigated theoretically by SUTIN in 1984 but has not yet been confirmed experimentally.[72–74] Examples for increasing rate constants with increasing donor-acceptor distances are scarce[75, 76] and a defined rate maximum for large distances compatible with the theoretical prediction has not been reported yet. In bimolecular ET reactions where charge recombination is expected to occur in the inverted region, this phenomenon plays an important role. It is assumed to be one of the reasons why charge recombination for bimolecular ET reactions is often faster than expected.[77]

Scheme 4.1 illustrates that if charge separation is to take place in the normal region of the MARCUS theory, the reactants have to be very close for efficient electron transfer. After ET took place the reactants diffuse away from each other. This increased donor-acceptor distance in return should increase the reaction rate for the back electron transfer when it is operative in the inverted region for short distances. Unfortunately, this effect is a substantial drawback for systems where electron transfer is part of a catalytic process and long-lived charge-separated states are required.

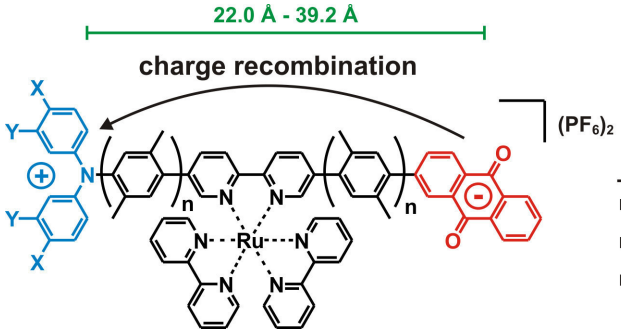

	X=OMe, Y=H	X,Y=OMe	X=Me, Y=H
n=1	anisyl-xy$_1$	veratryl-xy$_1$	tolyl-xy$_1$
n=2	anisyl-xy$_2$	veratryl-xy$_2$	tolyl-xy$_2$
n=3	anisyl-xy$_3$	veratryl-xy$_3$	tolyl-xy$_3$

Scheme 4.2 Linear triads investigated with respect to their charge recombination kinetics.

This chapter will focus on the first systematic investigation of this unusual phenomenon. Three series of rigid rod-like donor-acceptor triads as shown in Scheme 4.2 were synthesized and studied. A detailed description of the synthesis of these molecules is given in the experimental section in Chapter 7. The forward electron transfer (charge separation) has already been studied in detail for anisyl-xy$_1$ in acetonitrile solution and will not be discussed further in this chapter.[78–81] The linear triads investigated in this work are comprised of a central Ru(bpy)$_3^{2+}$ (bpy = 2,2'-bipyridine) photosensitizer moiety as well as a terminal anthraquinone acting as electron acceptor. A triarylamine (TAA) acts as electron donor. In order to vary the reaction free energy of charge recombination, the triarylamines were substituted with different electron donating groups ranging from very electron rich (veratryl), via moderately electron rich (anisyl) to relatively electron poor (tolyl). The distance between donor and acceptor was adjusted by introducing one, two or three *p*-xylene spacer groups between the photosensitizer and the donor and acceptor sites, respectively. This resulted in donor-acceptor distances ranging from 22.0 Å to 39.2 Å according to molecular modeling. The triad design has several advantages that were crucial for this investigation. The rigid rod-like shape of the triad ensures that kinetics of electron transfer can be measured at defined and fixed distances. The use of *p*-xylene as bridging units prevents that the linear bridge becomes redox active itself. This is due to a reduced π-conjugation as a consequence of relatively large equilibrium torsion angles between adjacent bridge units. In oligo-*p*-phenylene systems bridge elongation leads to enhanced π-conjugation. As a result, the mechanism for electron transfer can change from a coherent tunneling process to an incoherent hopping mechanism.[75]

4.1. Optical absorption

The absorption spectra of 20 µM solutions of the triads and [Ru(bpy)$_3$](PF$_6$)$_2$ as a reference compound in a 1:1 (v:v) mixture of acetonitrile and water are shown in Figure 4.2. All complexes show a prominent absorption band around 450 nm which can be assigned to

a metal-to-ligand charge transfer (MLCT) as well as an absorption around 290 nm arising from a $\pi \rightarrow \pi^*$ transitions centered on the bipyridine ligands. Additionally, the triads exhibit a broad absorption band between 300 nm and 400 nm that can be attributed to transitions centered on anthraquinone and triarylamine. Interestingly, for the three shortest triads, these absorption features are less intense. Furthermore, an increased absorbance in the MLCT-region of the spectra was detected for these triads. This is an indication for enhanced electronic communication between the metal center and the pendant donor and acceptor moieties. Another conclusion drawn from the absorption spectra of the triads is that with increasing amount of *p*-xylene spacers there is no significantly enhanced π-conjugation on the bridge. Increasing π-conjugation would manifest in a red shift of the absorption band around 350 nm. Therefore, redox-active behavior of the bridging units upon elongation seems unlikely, and a coherent tunneling mechanism can be expected for all compounds.

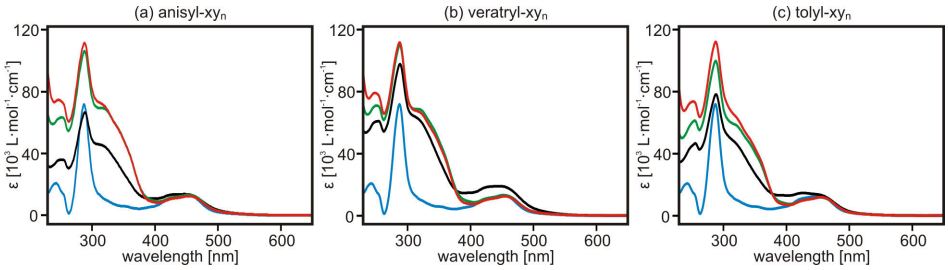

Figure 4.2 UV-Vis absorption spectra of 20 µM solutions of (a) anisyl-xy$_n$, (b) veratryl-xy$_n$ and (c) tolyl-xy$_n$ and $[Ru(bpy)_3](PF_6)_2$ (blue traces) with n = 1 (black traces), n = 2 (green traces) and n = 3 (red traces) in acetonitrile/water 1:1 (v:v).

4.2. Electrochemistry and reaction free energies

In order to estimate the reaction free energies for the individual charge separation steps and especially for the charge recombination, the reduction potentials of the relevant moieties were determined by cyclic voltammetry. The measurements were performed in deoxygenated acetonitrile/water 1:1 (v:v) mixtures containing 1 mM compound and 0.1 M KCl as supporting electrolyte. The measured voltammograms are shown in Figure 4.3 and the extracted potentials are summarized in Table 4.1.

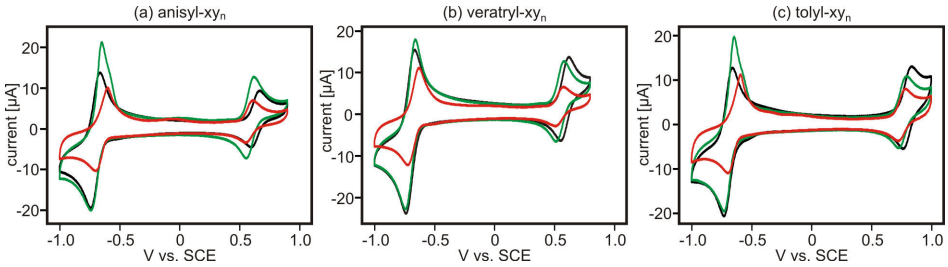

Figure 4.3 Cyclic voltammograms of (a) anisyl-xy$_n$, (b) veratryl-xy$_n$ and (c) tolyl-xy$_n$ with n = 1 (black traces), n = 2 (green traces) and n = 3 (red traces) in acetonitrile/water 1:1 (v:v) with 0.1 M KCl as supporting electrolyte and a scan rate of 0.1 V/s. The triad concentrations were 1 mM for n = 1, 2 and 0.5 mM for n = 3.

Table 4.1 Reduction potentials (in Volts vs. SCE) of the triads in acetonitrile/water 1:1 (v:v) and their reaction free energies for charge recombination ΔG_{CR}.

triad	$E(TAA^{+/0})$	$E(AQ^{0/-})$	R_{DA} [Å]	ΔG_{CR} [eV][a]
anisyl-xy$_1$	0.63	-0.70	22.0	-1.34
anisyl-xy$_2$	0.59	-0.70	30.6	-1.30
anisyl-xy$_3$	0.58	-0.65	39.2	-1.24
veratryl-xy$_1$	0.59	-0.70	22.0	-1.30
veratryl-xy$_2$	0.55	-0.70	30.6	-1.26
veratryl-xy$_3$	0.54	-0.68	39.2	-1.23
tolyl-xy$_1$	0.80	-0.70	22.0	-1.51
tolyl-xy$_2$	0.76	-0.69	30.6	-1.46
tolyl-xy$_3$	0.75	-0.65	39.2	-1.41

[a] calculated using equation 4.1.

The voltammograms in Figure 4.3 show the oxidation of the triarylamines between +0.54 V and +0.80 V as well as the first reduction of the anthraquinone moiety at approximately -0.7 V. An extension of the scanning range to observe the oxidation and reduction waves of the photosensitizer was not possible due to occurrence of water oxidation and reduction, respectively. It has to be noted that with increasing distance between the donor and acceptor moiety both potentials show a small shift towards easier oxidation (TAA) or reduction (AQ), respectively. Despite working in aqueous solutions, protonation of anthraquinone upon single reduction can be excluded, since the reduction waves are fully reversible. Protonation would lead to an irreversible wave caused by a second electron uptake of AQ (the pK_A value of the singly reduced form of anthraquinone was found to be 5.3 in aqueous solution containing 3 M isopropanol[82]). In comparison to non-aqueous solutions, the reduction of AQ in acetonitrile/water is shifted by at least 150 mV to less negative potentials. This well-known effect originates from strong hydrogen bonds formed upon reduction of anthraquinone.[83]

With the reduction potentials listed in Table 4.1 and the donor-acceptor distance R_{DA} at hand, it is possible to estimate the reaction free energy for charge recombination (ΔG_{CR}) using equation 4.1 established by WELLER.[84] In this equation, ε_0 is the vacuum permittivity and ε_s the dielectric constant of the solvent (for acetonitrile/water 1:1, $\varepsilon_s = 55.7$[85]). The calculated driving forces are summarized in the last column of Table 4.1. The reaction free energies for charge recombination of the anisyl-xy$_n$ triads are on the order of -1.3 eV, whereas those for the veratryl-xy$_n$ triads are approximately 40 meV less exergonic, and those for tolyl-xy$_n$ are more exergonic by about 160 meV. In addition, all three series of triads show a decrease of driving force upon increasing donor-acceptor distance from n = 1 to n = 3. This decrease in ΔG_{CR} is a result of the shift in reduction potentials (see above) and amounts to approximately 0.1 eV.

$$\Delta G_{CR} = e \cdot (E_{red} - E_{ox}) - \frac{e^2}{4\pi\varepsilon_0\varepsilon_S R_{DA}} \tag{4.1}$$

To allow estimations about the reaction free energies relevant for the charge separation, the literature values of the reduction potentials of Ru(bpy)$_3^{2+}$ in water [$E(Ru^{3+/2+})$ = +1.02 V vs SCE, $E(Ru^{2+/+})$ = -1.52 V vs SCE] and the energy of the lowest excited state (E_{00} = 2.12 eV) have to be considered.[86] Combining these values with the experimentally obtained values for the donor and acceptor moieties one can conclude that electron transfer from the excited photosensitizer to anthraquinone is exergonic by roughly 0.4 eV. In contrast, electron transfer from the triarylamine site to the excited Ru(bpy)$_3^{2+}$ center has either essentially no driving force (veratryl), or is endergonic by approximately 0.2 eV (tolyl). On the basis of these considerations one can conclude that the electron transfer sequence is most likely initiated by reduction of anthraquinone to form the oxidized species of the photosensitizer. Subsequently the photosensitizer is re-reduced by the triarylamine to form TAA$^+$. A general energy scheme for the investigated triads is shown in Scheme 4.3.

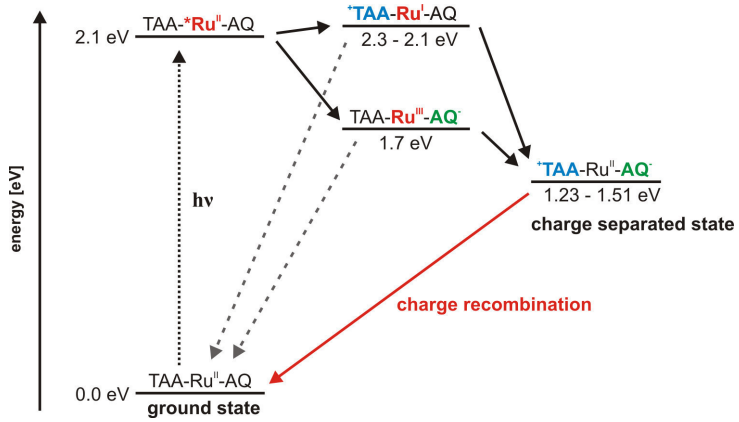

Scheme 4.3 Generalized energy diagram for the triads. The dotted gray arrows indicate undesired recombination processes not occurring from the fully charge-separated state.

In order to identify the photoproducts observed by transient absorption measurements (see below) spectro-electrochemical experiments were performed with all triads. The resulting UV/Vis difference absorption spectra are shown in Figure 4.4 for anisyl-xy_n, in Figure 4.5 for veratryl-xy_n and Figure 4.6 for tolyl-xy_n. All samples contained 0.1 mM complex with 0.1 M KCl as supporting electrolyte in an acetonitrile/water 1:1 (v:v) mixture. All solutions were deoxygenated before each measurement.

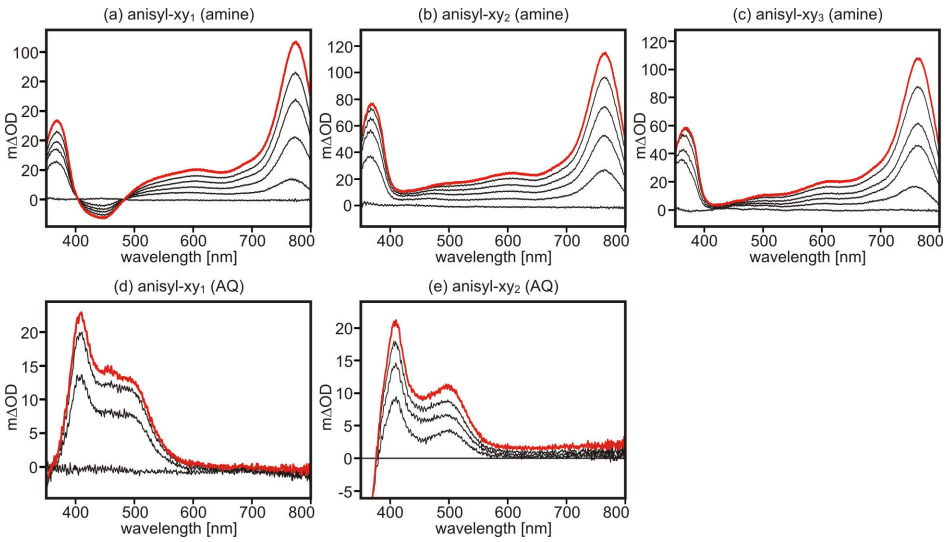

Figure 4.4 Spectro-electrochemical measurements of anisyl-$xy_{1\text{-}3}$. (a-c) difference absorption spectra of the three triads obtained after applying a potential of +0.8 V vs. SCE (TAA oxidation). (d-e) difference absorption spectra of anisyl-$xy_{1\text{-}2}$ obtained after applying a potential of -0.9 V vs. SCE (AQ reduction). All samples contained 0.1 mM of the respective triad with 0.1 M KCl as supporting electrolyte in acetonitrile/water 1:1 (v:v) and were deoxygenated prior to measuring.

The spectro-electrochemical measurements for anisyl-$xy_{1\text{-}3}$ (Figure 4.4) show that oxidation of the TAA moiety at a potential of +0.8 V leads to increased absorption at 770 nm and 370 nm, which has been observed in earlier studies.[81] In addition, the shortest triad shows a bleach in absorption around 440 nm. This loss in absorption probably corresponds to the increased absorbance of this triad in the MLCT-region as seen in Figure 4.2a and does not stem from an oxidation of the $Ru(bpy)_3^{2+}$ moiety. Oxidation of the photosensitizer occurs at higher potentials and additionally would be overlapped by water oxidation. Reduction of the anthraquinone at a potential of -0.9 V to form AQ^- leads to an increased absorbance around 410 nm with an additional absorption band rising around 500 nm. For anisyl-xy_1 this latter band is shaped as a shoulder of the main absorption band at 410 nm. In earlier studies the absorption features of pure anthraquinone were reported to occur around 400 nm accompanied with a more intense absorption around 550 nm in aprotic solvents.[81, 87] The deviation from these observation can be assigned to strong hydrogen-bonding to AQ^- in acetonitrile/water solutions.[83] The measurements for veratryl-xy_n

(Figure 4.5) show that the difference spectra of the TAA^+ moiety obtained at a potential of +0.75 V vs SCE have rising signals around 370 nm and 950 nm. In addition, a broad less intense absorption around 500-550 nm can be detected. For tolyl-xy_n (Figure 4.6) the difference absorption spectra of TAA^+ were obtained at a potential of +1.0 V. The spectra are comprised of two rising signals around 710 nm and 360 nm. The bleach in absorbance at 440 nm as discussed for anisyl-xy_1, is also occurring for the shortest triads veratryl-xy_1 and tolyl-xy_1. The difference absorption spectra of the reduced anthraquinone species in veratryl-$xy_{1\text{-}2}$ and tolyl-$xy_{1\text{-}2}$ are nearly identical to those measured for anisyl-$xy_{1\text{-}2}$ and are therefore not discussed in detail. Spectro-electrochemical measurements of AQ reduction in the longest triads failed for unknown reasons. Nevertheless, the transient absorption measurements (see below) suggest that the reduced anthraquinone species for the longest triads shows very similar characteristics to the one of the xy_1 and xy_2 triads.

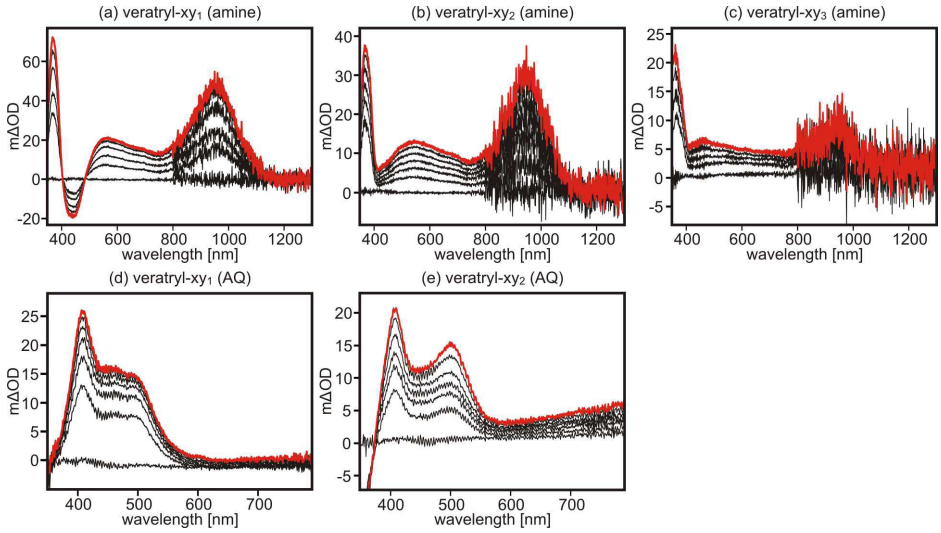

Figure 4.5 Spectro-electrochemical measurements of veratryl-$xy_{1\text{-}3}$. (a-c) difference absorption spectra of the three triads obtained after applying a potential of +0.75 V vs. SCE (TAA oxidation). (d-e) difference absorption spectra of veratryl-$xy_{1\text{-}2}$ obtained after applying a potential of -0.9 V vs. SCE (AQ reduction). All samples contained 0.1 mM of the respective triad with 0.1 M KCl as supporting electrolyte in acetonitrile/water 1:1 (v:v) and were deoxygenated prior to measuring.

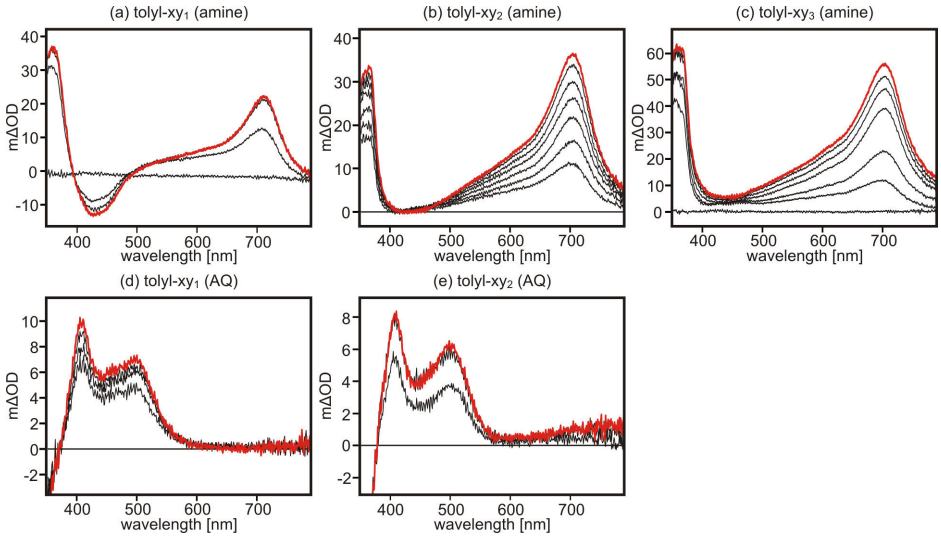

Figure 4.6 Spectro-electrochemical measurements of tolyl-$xy_{1\text{-}3}$. (a-c) difference absorption spectra of the three triads obtained after applying a potential of +1.0 V vs. SCE (TAA oxidation). (d-e) difference absorption spectra of tolyl-$xy_{1\text{-}2}$ obtained after applying a potential of -0.9 V vs. SCE (AQ reduction). All samples contained 0.1 mM of the respective triad with 0.1 M KCl as supporting electrolyte in acetonitrile/water 1:1 (v:v) and were deoxygenated prior to measuring.

4.3. Transient absorption spectroscopy

Transient absorption spectra were recorded in order to identify the individual photoproducts of the triads. The spectra shown in Figure 4.7(a-c) can be interpreted as a superimposition of the spectral signatures for AQ^- and TAA^+ that were obtained from spectro-electrochemical measurements (see Figures 4.4-4.6). As a result, the charge-separated states TAA^+-Ru-AQ^- were observed in all triads. At that point it has to be noted that the formation of the charge-separated state is in kinetic competition with several other processes. As already shown in Scheme 4., the formation of TAA^+-Ru-AQ^- is thermodynamically favored in all cases. However, the electron transfer pathway for charge separation has to compete with (i) the decay of the excited state and (ii) the decay of the intermediate electron transfer products to the ground state.

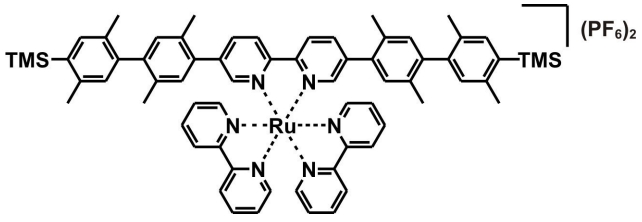

Scheme 4.4 Reference compound TMS-xy_2-Ru-xy_2-TMS.

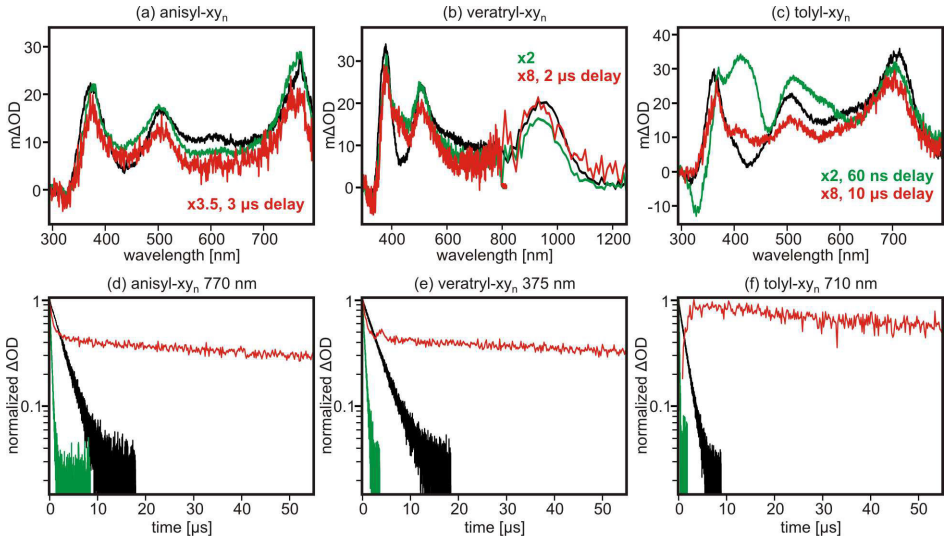

Figure 4.7 Upper row: Transient absorption spectra of 20 µM (a) anisyl-xy$_n$, (b) veratryl-xy$_n$ and (c) tolyl-xy$_n$ in deoxygenated acetonitrile/water 1:1 (v:v). The spectra were recorded within 200 ns directly after excitation at 532 nm with pulses of 10 ns duration, unless noted otherwise. Bottom row: Selected decay kinetics of the transient absorption signals of (d) anisyl-xy$_n$ at 770 nm, (e) veratryl-xy$_n$ at 375 nm and tolyl-xy$_n$ at 710 nm. The extracted lifetimes from the decay curves are listed in Table 4.2. The color code of the individual traces is: xy$_1$ (black traces), xy$_2$ (green traces), xy$_3$ (red traces).

In Figure 4.8 the transient absorption spectra of the xy$_3$ triads, measured within 200 ns directly after excitation, are shown in comparison to the spectra of the excited reference compound TMS-xy$_2$-Ru-xy$_2$-TMS (see Scheme 4.4) which is unable to undergo any intramolecular excited state redox chemistry. From their similarity one can conclude that the transient absorption spectra of the xy$_3$ triads were dominated by the ^{3}MLCT state in this time domain and the spectral signatures of TAA$^+$-Ru-AQ$^-$ can be observed only after the ^{3}MLCT state has decayed. For tolyl-xy$_2$ the situation is somewhat more complicated. The transient absorption spectra show a superimposition of the excited state and the charge-separated state. The spectrum was measured with a delay time of 60 ns due to an additional short lived component. The decay kinetics (see for example Figure A3(d) in the Appendix) are rather complex and were fitted to an A $\rightarrow$ B $\rightarrow$ C reaction sequence with an additional independent decay rate constant. The short time constant (approximately 20 ns) of the A $\rightarrow$ B $\rightarrow$ C reaction sequence in tolyl-xy$_2$ was attributed to an intermediate of the electron transfer sequence leading to the charge-separated state. The second time constant of this reaction sequence can be attributed to the decay of the charge-separated state to the ground state. The independent decay component with a lifetime of several hundred nanoseconds is a contribution of an excited state decay of minor impurities. This conclusion is reached from the observation that the kinetics of tolyl-xy$_2$ at 710 nm (see Figure A3(f) in the appendix) show slightly negative ΔOD values in the time domain

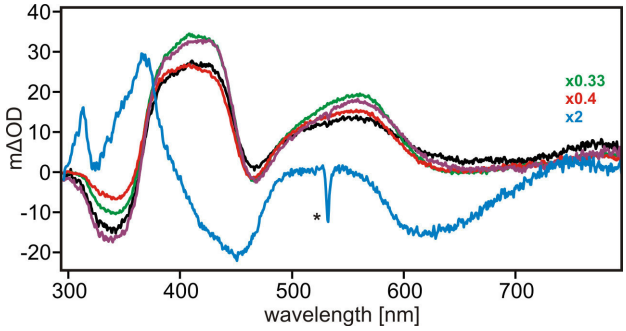

Figure 4.8 Transient absorption spectra of 20 µM solutions of anisyl-xy_3 (black trace), veratryl-xy_3 (red trace), tolyl-xy_3 (green trace), TMS-xy_2-Ru-xy_2-TMS (purple trace) and $[Ru(bpy)_3](PF_6)_2$ (blue trace) in deoxygenated acetonitrile/water 1:1 (v:v). The spectra were recorded within 200 ns directly after excitation at 532 nm with pulses of 10 ns duration. Stray light from the excitation pulse is marked with an asterisk.

between 500 ns and 1000 ns. Since there is no ground state absorption at 710 nm for all triads, emission from a ^{3}MLCT state is the only explanation.

The rate constants for charge recombination measured at the three transient absorption maxima were identical for each individual triad, indicating the charge-separated states recombine to the ground state in one single electron transfer step. Furthermore, kinetic measurements conducted in acetonitrile/D_2O revealed identical charge recombination rates which supports the assumption that protonation of AQ^- does not occur under these conditions. In Figure 4.7(d-f) the decays of the most intense transient absorption signals of the charge-separated states are shown for all triads. The lifetimes (τ_{CR}) for this long-range charge recombination are listed in Table 4.2. The time constants show a rather unusual behavior. For the shortest triads, lifetimes between 1450 ns (tolyl-xy_1) and 3200 ns (veratryl-xy_1) were found. When increasing the spatial separation from 22.0 Å to 30.8 Å for the xy_2 triads, a significant shorting of the lifetimes was observed. The lifetimes of the xy_2 triads are on the order of a few hundred nanoseconds in all three cases. In contrast, further elongation of the bridge to donor-acceptor distances of 39.2 Å leads to lifetimes of 41 µs (tolyl-xy_3), 65 µs (anisyl-xy_3), and 75 µs (veratryl-xy_3). In principle, one would expect the rate constant for electron transfer to decrease with increasing donor-acceptor distance. The steepness of this decrease in electron transfer rate is described by the distance-decay constant β as discussed in Chapter 2. Values for β have been determined to be on the order of 0.52 – 0.77 Å^{-1} for electron transfer along *p*-xylene bridges.[59, 60] Considering these values, one would expect the rate constants for electron transfer to drop by roughly two orders of magnitude when increasing the distance by 8.6 Å from the xy_1 to the xy_2 triads (and from xy_2 to xy_3). In fact, the rate constants for electron transfer increase by a factor between 6.5 (veratryl) and 10 (tolyl) for the xy_1 and xy_2 triads. The lifetimes for charge recombination follow the expected decrease when

going from the xy_2 to the xy_3 triads.

The decays of the transient absorption signals of the charge-separated states of the xy_3 triads are not mono-exponential as shown in Figure 4.7(d-f). In fact, a tri-exponential decay was observed at all three transient absorption signals. The short-lived component of this decay exhibits time constants of 130 ns (veratryl), 210 ns (anisyl), and 850 ns (tolyl). From the transient absorption spectra of the xy_3 triads recorded directly after laser pulse excitation, and in comparison with the reference compound TMS-xy_2-Ru-xy_2-TMS (see Figure 4.8), this short-lived decay component can be unambiguously attributed to the ^{3}MLCT state. Furthermore, the observation of both rise-decay and decay-decay behavior is a consequence of the relative extinction coefficients of the excited and charge-separated state at the individual wavelength.

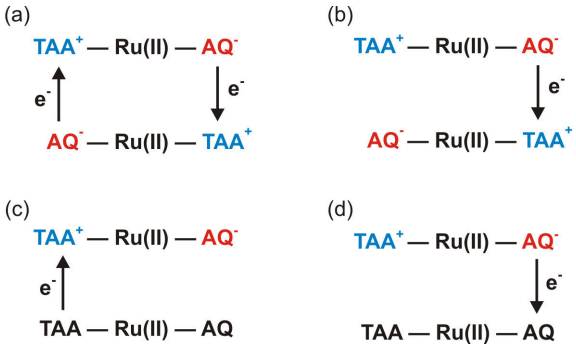

Scheme 4.5 Possible bimolecular electron transfer reactions involving the long-lived charge-separated states of the xy_3 triads. Reaction sequence (a) leads to complete charge recombination between two charge-separated triads. Reaction sequences (b-d) lead to incomplete charge recombination resulting in two triads each bearing either reduced AQ^- or oxidized TAA^+.

After the excited state has vanished in the xy_3 triads, the contribution of the charge-separated state to the transient absorption signal is observed [see Figure 4.7(a-c)]. Taking into account the long lifetimes of the signals of these charge-separated states, bimolecular reactions are supposed to occur quite easily. Scheme 4.5 depicts the bimolecular reactions possibly having an impact on the decay kinetics of the xy_3 triads. It shows that bimolecular electron transfer between AQ^- and TAA^+moieties as well as electron transfer from reduced anthraquinone/oxidized amine to their corresponding neutral species on triads in their electronic ground state (similar to self-exchange reactions) must be considered. In order to identify the contribution of the intramolecular electron transfer to the overall decay kinetics, concentration-dependent measurements were performed. Anisyl-xy_3 was hereby used as an example for this purpose as shown in Figure 4.9. The decay of the signals of the charge-separated state were measured at triad concentrations varying from 20 µM to 50 µM. The obtained decay curves were fitted to a bi-exponential decay, start-

ing after the initially excited state has vanished. The intensity of species A (decaying within ∼500 µs) was correlated to the one of species B (decaying on longer timescales). The ratio between species A and B shows a clear dependency on the triad concentration as shown in Figure 4.9(b). With increasing triad concentrations, species A becomes less prominent which is in line with the assumption of increased bimolecular contributions. A second observation is that the lifetime of species A decreases with increasing concentration. Generally one would expect an intramolecular reaction to be independent of the concentration. However, an increase in triad concentration implies a higher concentration of charge-separated states. As a consequence, the bimolecular reaction of two triads in their charge-separated states to recombine to the ground state as shown in Scheme 4.5(a) becomes more relevant. This results in a shortening of the lifetime for intramolecular electron transfer. With those observations, it is possible to conclude that species A is the intramolecular contribution to the decay of the transient absorption signal, whereas species B can be described by the bimolecular charge recombination reactions of two triads with one of them bearing the oxidized amine and the other triad having a reduced anthraquinone [products of the bimolecular reactions from Scheme 4.5(b-d)].

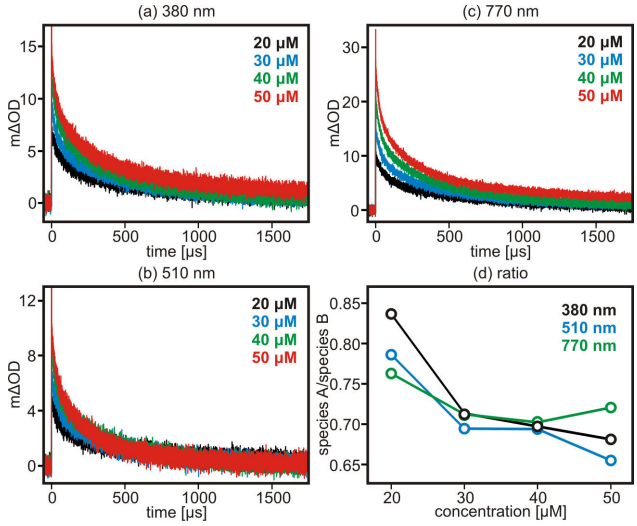

Figure 4.9 Temporal evolution of the transient absorption signals of anisyl-xy$_3$ at (a) 380 nm, (b) 510 nm and (c) 770 nm in deoxygenated acetonitrile/water 1:1 (v:v) after excitation at 532 nm with laser pulses of 10 ns duration. The concentrations of the solutions were: 20 µM (black traces), 30 µM (blue traces), 40 µM (green traces) and 50 µM (red traces). (d) The ratio of the different species A and B (see text) as a function of the triad concentration.

A crude estimation, of the importance of bimolecular reactions, can be made by comparing the average distance between two triads and the maximal diffusion distance in solution. In a 20 µM solution the volume available for each triad can be calculated to $8.3{\cdot}10^7$ Å^3. A perfect distribution of molecules and a space-filling packing of cubes that are centered

by a triad were assumed in the following. In this model, the shortest distance between two neighboring triads can be described by the edge length of such a cube which gives a distance of 436 Å. This value can be compared to the maximum accessible translation distance of molecules in solution, R_t, given by equation 4.2. The diffusion coefficient, D_0, for particles in liquid media is described by the STOKES-EINSTEIN equation (4.2). When combining equations 4.2 and 4.3, a few assumptions have to be made. The STOKES radius of anisyl-xy$_3$ is estimated to be equivalent to $r = (R_{DA} + r_D + r_A)/2 \approx 25$ Å, with r_D and r_A being the hard sphere radii of the donor and the acceptor ($r_D = r_A = 5$ Å). Within the lifetime of the charge-separated state of anisyl-xy$_3$, $t = \tau_{CR} = 65$ µs, the maximum accessible translation distance can be calculated to be 1190 Å. This is roughly three times the average distance between two triads in solution. Although these values can only be handled as crude estimations, they clearly demonstrate that bimolecular reactions definitely can occur under these conditions.

$$R_t = \sqrt{2D_0t} \tag{4.2}$$

$$D_0 = \frac{k_BT}{6\pi\eta r} \tag{4.3}$$

with

t	time
k_B	BOLTZMANN constant
T	temperature (298 K)
η	solvent viscosity ($8.01 \cdot 10^{-4}$ Pa·s for acetonitrile/water 1:1)[88]
r	STOKES radius

4.4. Activation and reorganization energies

With a clear and valid assignment of the lifetimes for charge recombination of the xy$_3$ triads at hand, the origin of the unusual distance-dependence of the rate constant for electron transfer will be explored in detail in this section. In principle, the rate constant for electron transfer, as described by the Marcus equation, is an interplay of three main parameters: the reaction free energy ΔG^0, the reorganization energy λ in a given solvent environment, and the electronic coupling H_{DA} between donor and acceptor. Latter is a function of the properties of the electron transfer medium, represented by the distance decay constant β, and the spatial separation between the donor/acceptor couple. In the triad systems investigated here the reaction free energy for charge recombination ΔG_{CR} is virtually constant for each set of triads, as demonstrated by the cyclic voltammetry

measurements (see Figure 4.3 and Table 4.1). Additionally, the electronic coupling is expected to decrease with increasing distance. The molecular design of the triads ensures that no significantly enhanced π-conjugation occurs upon bridge lengthening which could manifest in increased electronic coupling at longer distances. As a consequence, the origin of the unusual distance-dependence has to be found in the activation free energy and the reorganization energy (see Chapter 2). For the determination of the activation free energies ($\Delta G^{\ddagger}$), the rate constants for charge recombination of all triads were measured at different temperatures ranging from 5 °C to 65 °C. The resulting ARRHENIUS plots are shown in Figure 4.10. From the slope of the linear fits to the individual measurements the activation free energies were extracted. The results are listed in Table 4.2. The actual decay curves at different temperatures are shown in the Appendix (Figures A1-A3). For the shortest triads, the activation free energies range from 26 ± 3 meV (tolyl-xy_1) to 43 ± 2 meV (anisyl-xy_1). The next longer triads all undergo activationless charge recombination. Further increase of the donor-acceptor distance to the xy_3 triads results in $\Delta G^{\ddagger}$ values between 46 ± 5 meV (tolyl-xy_3) and 126 ± 11 meV (veratryl-xy_3). The observation that the xy_2 triads show activationless electron transfer is clearly in line with the fact that these triads exhibit the fastest charge recombination. Using equation 4.4, the reorganization energies can be calculated from the experimental values of ΔG^0 and $\Delta G^{\ddagger}$, and the λ-values are listed in the fourth column of Table 4.2. The quadratic nature of this equation produces two values for λ. Since the xy_2 triads show an activationless behavior, their reorganization energies are defined by $\lambda = -\Delta G^0$. With the assumption that the reorganization energy has to increase with increasing spatial separation between donor and acceptor in a given system[72, 89], the calculated values for λ have to be smaller than $-\Delta G^0$ for the xy_1 triads and bigger for the xy_3 triads. However, this simple selection of proper values for λ has some very important implications. It states that electron transfer in the xy_1 triads is operative in the inverted region of the MARCUS theory ($\lambda < -\Delta G^0$). The next longer triads show activationless ($\lambda = -\Delta G^0$) charge recombination and the xy_3 triads exhibit electron transfer in the normal region ($\lambda > -\Delta G^0$). This observation reflects the unusual distance-dependence of the triads with respect to their charge-separated state lifetimes. With the experimental values for λ and the intercept of the linear fits from the ARRHENIUS plot in Figure 4.10 it is possible to calculate estimates for the electronic coupling H_{AD} with $H_{AD}{}^2 = H_{AD,(0)}{}^2 \cdot \exp(-\beta \cdot r)$ according to equation 4.5. The values are given in the last column of Table 4.2, and they are all on the same order of magnitude, around 0.1 cm^{-1}. This finding of a very weak distance-dependency of the electronic coupling is surprising. Earlier studies on electron transfer along *p*-xylene bridges produced β values between 0.52 and 0.77 $Å^{-1}$.[59, 60] These values were obtained for photoinduced forward electron transfer in the normal region, whereas the triads in

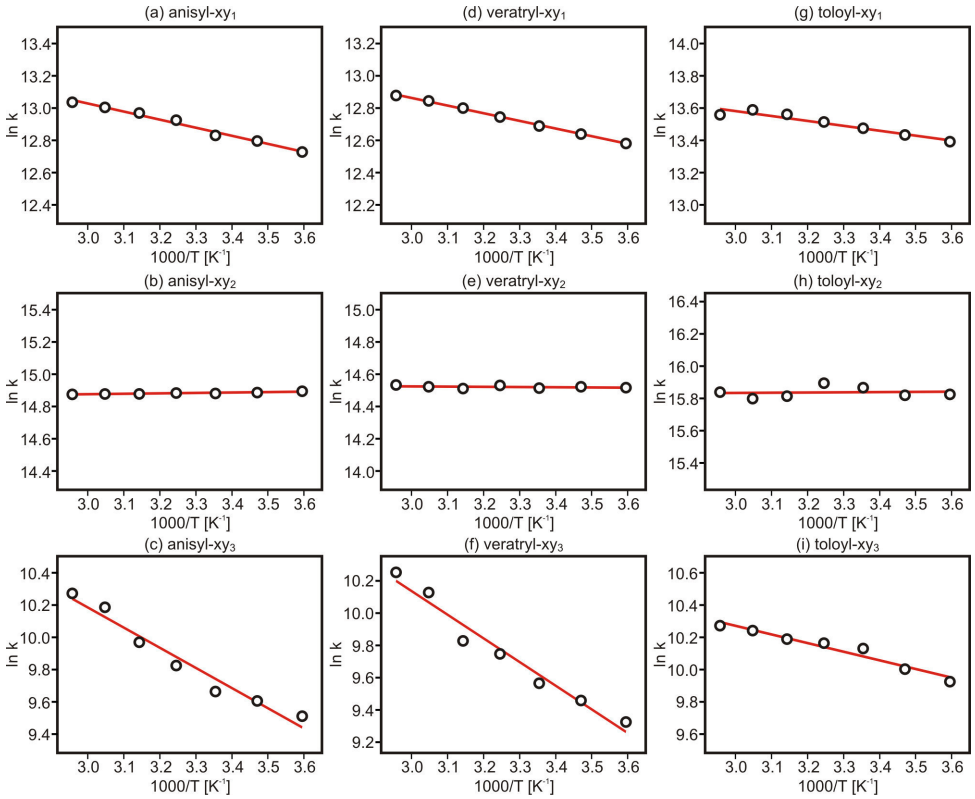

Figure 4.10 ARRHENIUS plots of the rate constants for charge recombination of (a-c) anisyl-xy_n, (d-f) veratryl-xy_n, and (g-i) tolyl-xy_n as a function of temperature in a range between 5 °C and 65 °C . The 20 µM solutions of the triads in acetonitrile/water 1:1 (v:v) were deoxygenated. Excitation occurred at 532 nm. The activation free energies extracted from these plots are listed in Table 4.2.

this work undergo thermal charge recombination. Though it is known in literature that both processes can have fundamentally different distance-dependences, due to different superexchange pathways.[90]

$$\Delta G^{\ddagger} = \frac{(\lambda+\Delta G^0)^2}{4\lambda} \tag{4.4}$$

As already mentioned at the beginning of this chapter, the MARCUS equation predicts that electron transfer rates for systems operating in the inverted region (like the xy_1 triads) should exhibit a rather unique distance-dependence with rate maxima at a certain spatial separation. Early theoretical work on this subject highlighted two opposing contributions to the rate constants of electron transfer: (1) decrease of the electronic coupling between donor and acceptor with increasing distance, associated with slower rate constants, and (2) increasing reorganization energy which leads to an increase of the rate constant up to a distance where $\lambda = -\Delta G^0$.[72, 89, 91] For electron transfer operating in the normal region (small driving forces), the decrease in electronic coupling is the predominant effect leading to the well-known exponential decrease of rate constants with

Table 4.2 Lifetimes for charge recombination τ_{CR}, activation energies $\Delta G^{\ddagger}$, reorganization energies λ and electronic coupling H_{AD} of all triads in acetonitrile/water 1:1 (v:v).

triad	τ_{CR} [ns]	$\Delta G^{\ddagger}$ [meV]	λ [eV][a]	H_{AD} [cm^{-1}]
anisyl-xy$_1$	2800	43 ± 2	0.93 ± 0.35	0.09 ± 0.02
anisyl-xy$_2$[b]	350	-2 ± 1	1.29 ± 0.05	0.11 ± 0.01
anisyl-xy$_3$	65000	108 ± 10	2.21 ± 0.28	0.08 ± 0.02
veratryl-xy$_1$	3200	43 ± 2	0.91 ± 0.34	0.08 ± 0.01
veratryl-xy$_2$[b]	500	-2 ± 8	1.26 ± 0.05	0.10 ± 0.03
veratryl-xy$_3$	75000	126 ± 11	2.31 ± 0.23	0.11 ± 0.03
tolyl-xy$_1$	1450	26 ± 3	1.16 ± 0.38	0.09 ± 0.02
tolyl-xy$_2$[b]	140	1 ± 1	1.46 ± 0.05	0.18 ± 0.02
tolyl-xy$_3$	41000	46 ± 5	2.02 ± 0.29	0.03 ± 0.01

[a] assuming $\Delta\Delta G_{CR} = 0.05$ eV. [b] $\lambda = -\Delta G^0 = -\Delta G_{CR}$ for activationless ET.

increasing distances. The reorganization energy is larger than $-\Delta G^0$ in the normal region. Consequently, when increasing λ by increasing the spatial separation between donor and acceptor it will lead to higher a activation barrier according to equation 4.4 and therefore, to lower rate constants. For electron transfer in the inverted region the situation is somewhat different. The effect of increasing λ now leads to a decrease in the activation energy since $\lambda < -\Delta G^0$ and therefore, facilitates electron transfer. Depending on the individual system (especially when the drop of electronic coupling with increasing separation is rather small), this effect can compensate the decrease of the rate constants caused by the loss of electronic coupling. Any further increase of the electron transfer distance leads to a larger reorganization energy than $-\Delta G^0$, causing the system to be operative in the normal region of the MARCUS equation. Figure 4.11 displays the calculated rate constants for electron transfer in acetonitrile according to the MARCUS equation (4.5). The reorganization energy λ itself is comprised of an inner-sphere reorganization energy, λ_{in}, representing changes in bond lengths and angles upon electron transfer and the reorganization of the solvent, λ_{out}(equation 4.6). The contribution of λ_{in} is mostly independent of the distance between donor and acceptor and is usually much smaller than the solvent reorganization energy. The input values were set as follows and are in a typical range for donor-acceptor assemblies: $H_{AD,(0)} = 200$ cm^{-1}, $\beta = 0.50$ Å^{-1}, $r_A = r_D = 5.0$ Å, $\lambda_{in} = 0.1$ eV.

$$k_{ET} = \frac{2\pi}{h} H_{AD,(0)}^2 \cdot e^{-\beta(R_{DA}-\sigma)} \sqrt{\frac{\pi}{\lambda k_B T}} \cdot e^{\left[-\frac{(\lambda+\Delta G)^2}{4\lambda k_B T}\right]} \tag{4.5}$$

$$\lambda = \lambda_{in} + \lambda_{out} = \lambda_{in} + \frac{e^2}{4\pi\varepsilon_0}\left(\frac{1}{2r_A} + \frac{1}{2r_D} - \frac{1}{R_{DA}}\right) \cdot \left(\frac{1}{D_{op}} - \frac{1}{D_s}\right) \tag{4.6}$$

with	h	PLANCK constant
	σ	sum of the hard sphere radii ($r_A + r_D$)
	k_B	BOLTZMANN constant
	T	temperature (298 K)
	ε_0	vacuum permittivity
	D_{op}	optical dielectric constant of the solvent
	D_s	static dielectric constant of the solvent

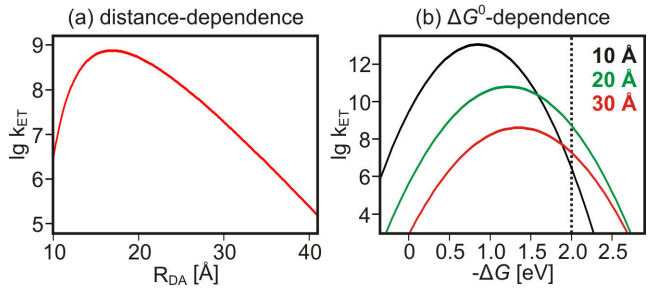

Figure 4.11 (a) Distance-dependence of electron transfer rate constants in the inverted region (ΔG^0 = -2.0 eV) calculated from equations 4.4 and 4.5 using $H_{AD,(0)}$ = 200 cm^{-1}, β = 0.50 Å^{-1}, $r_A = r_D$ = 5.0 Å, λ_{in} = 0.1 eV. (b) Gaussian free energy curves with the same input values for distances r of 10 Å (black trace), 20 Å (green trace) and 30 Å (red trace).

The calculated rate constants in Figure 4.11a for the inverted region (ΔG^0 = -2.0 eV) exhibit a rate maximum which is not at close proximity of the redox centers. This behavior is similar to the observation made for the three sets of triads. In addition, the Gaussian free energy curves (so called MARCUS parabola) for three different donor-acceptor distances are shown in Figure 4.11b. These curves demonstrate that the observed phenomenon of a rate maximum at long distances is predicted only for the inverted region with very large driving forces. Although the experimental data follow exactly the same trend, it was not possible to fit the measured rate constants to the MARCUS equation. The main deviation from the theoretical values stems from the fact that the measured reorganization energies do not fit the two-sphere model in equation 4.5. This model describes the solvent reorganization energy as a function of the size of the redox centers, their spatial separation, and the polarity of the solvent. For acetonitrile/water 1:1 (ε_r = 55.7[85], n = 1.347[92]) and hard-sphere radii of 5 Å, the outer-sphere reorganization energy reaches a maximum value of 1.54 eV at an infinite distance. Assuming an independent λ_{in} of 0.1 eV a maximum total reorganization energy of 1.64 eV is predicted. That value is obviously not in line

with the experimental data showing reorganization energies of more than 2.0 eV for the xy_3 triads. There are several weaknesses of the two-sphere model that might explain this discrepancy. One possible explanation is that the theoretical model does not take into account any coulombic interactions between the solvent and the charged photosensitizer. Considering a twofold positively charged metal center like $Ru(bpy)_3^{2+}$, with two additional counter ions, one might think of the solvent molecules being somewhat shielded from changes in polarity due to electron transfer reactions. If so, this effect would lower the reorganization energy especially for the shortest triads. It would probably have much less effect on the longest ones, because it clearly depends on the distance between the redox centers and the charged photosensitizer. A second, even more important weakness of equation 4.6 is that it treats the solvent environment as chemically inert molecules. In fact, the formation of any bonds between the solvent and the redox centers is neglected. This assumption does not hold true for water. As already demonstrated in the electrochemical measurements, the reduced anthraquinone undergoes hydrogen bonding to surrounding water molecules (see Figures 4.3-4.6). Under these conditions, water can not be treated as an inert solvent which is probably the main reason for the deviation of the experimental values for λ from the two-sphere model. In a previous study the reorganization energy for the proton-coupled electron transfer reaction of a phenolic unit has been determined to be 2.0 eV.[93] However, within the same molecule the reorganization energy for pure electron transfer was found to be only 0.9 eV.[93] Although in the triad systems investigated in this chapter only hydrogen bonding and not proton transfer was observed, this example strongly supports the hypothesis that the two-sphere model for λ only holds true for solvents which do not chemically interact with the redox centers.

In the previous sections of this chapter, the major contribution of the reorganization energy to the effect of rate maxima at large distances has been discussed. The fact that the experimentally obtained values for λ are in contrast to the established two-sphere model was mainly attributed to the formation of hydrogen bonds between bulk water and the anthraquinone anion. This hypothesis still requires further investigation to validate the rather large reorganization energies obtained in acetonitrile/water. For that reason a complete set of data in neat acetonitrile was prepared for anisyl-xy_n and will be discussed in the following section.

4.5. Measurements of anisyl triads in neat acetonitrile

The main objective of this section is to explore whether the effect of a rate maximum at large donor-acceptor distances can be reproduced using non-aqueous solvents such

as neat acetonitrile. This was done with the anisyl-xy_n triads. Experimental data for the reorganization energies associated with charge recombination will be compared to those obtained in acetonitrile/water. This investigation aims towards validation of the hypothesis that hydrogen bonds are the reason for the larger λ values in the xy_3 triads as compared to the theoretical prediction.

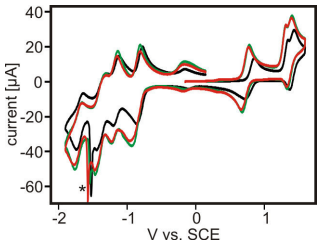

Figure 4.12 Cyclic voltammograms of 1 mM anisyl-xy_1 (black trace), anisyl-xy_2 (green trace) and anisyl-xy_3 (red trace) in acetonitrile with additional 0.1 M $TBAPF_6$ as supporting electrolyte. The scan rate was 0.1 V/s. The asterisk marks the adsorption peaks associated with the second reduction of anthraquinone.

In Figure 4.12 the cyclic voltammograms of the anisyl-xy_n triads in acetonitrile are shown. The oxidation of the triarylamine occurs between 0.79 V and 0.72 V vs. SCE. The reduction of the anthraquinone appears to be between -0.89 V and -0.82 V vs. SCE. As commonly observed for $Ru(bpy)_3^{2+}$, three reversible reduction waves appear between -1.1 V and -1.8 V, accompanied by an oxidation wave at 1.38 V vs. SCE. The second reduction of the anthraquinone moiety overlaps with the bpy reductions, and is associated with an adsorption peak around -1.55 V (marked with an asterisk). Another irreversible wave can be detected at 1.30 V overlapping with the oxidation of the photosensitizer. It can be assigned to the second oxidation of the triarylamine. All relevant potentials are listed in Table 4.3. From the reduction potentials of the donor and the acceptor the driving forces for charge recombination were calculated using equation 4.1. The ΔG_{CR}-values are noted in the last column of Table 4.3. The reaction free energies for charge recombination, ΔG_{CR}, are virtually identical for all three triads. They are roughly 0.3 eV more exergonic than in acetonitrile/water 1:1. This is because neat acetonitrile is less polar, leading to a decreased stabilization of the charged species. In addition, no charge stabilizing hydrogen bonds can be formed, resulting in a charge-separated state which is higher in energy. A detailed discussion of the photoinduced electron transfer steps leading to the charge-separated step was performed in earlier studies in our group for anisyl-xy_1.[79, 94] A reaction sequence of electron transfer from TAA to the excited photosensitizer followed by reduction of anthraquinone was observed. For thermodynamic reasons, this sequence is expected to be applicable for all anisyl-xy_n triads in acetonitrile.

The transient absorption spectra of the anisyl-xy_n triads in acetonitrile are shown in

Table 4.3 Reduction potentials (in Volts vs. SCE) of anisyl-xy$_n$ in acetonitrile and driving forces for charge recombination.

triad	$E(Ru^{II/I})$	$E(AQ^{0/-})$	$E(TAA^{+/0})$	$E(Ru^{III/II})$	R_{DA} [Å]	ΔG_{CR} [eV][a]
anisyl-xy$_1$	-1.16	-0.82	0.79	1.37	22.0	-1.62
anisyl-xy$_2$	-1.18	-0.87	0.73	1.38	30.6	-1.61
anisyl-xy$_3$	-1.19	-0.89	0.72	1.38	39.2	-1.62

[a] calculated using equation 4.1.

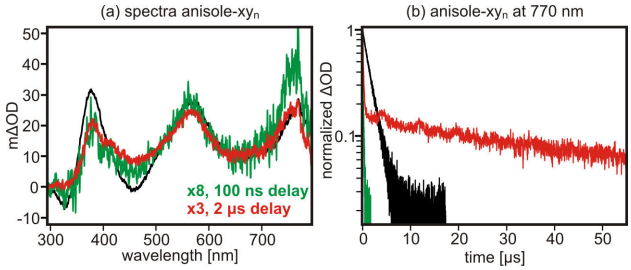

Figure 4.13 (a) Transient absorption spectra of 20 µM anisyl-xy$_n$ in deoxygenated acetonitrile. The spectra were recorded within 200 ns either directly (anisyl-xy$_1$) or with delay times of 100 ns (anisyl-xy$_2$) and 2 µs (anisyl-xy$_3$) after excitation at 532 nm with pulses of 10 ns duration. (b) Decay of the transient absorption signals of the three triads at 770 nm. The color code is: anisyl-xy$_1$ (black traces), anisyl-xy$_2$ (green traces) and anisyl-xy$_3$ (red traces).

Figure 4.13a and they are consistent with spectra reported previously for anisyl-xy$_1$ in non-aqueous solutions.[79, 81] Compared to the spectra obtained in acetonitrile/water 1:1, there is a shift in the transient absorption band of AQ^- to 570 nm due to the absence of hydrogen bonds. The decay kinetics of the charge-separated state were identical at all detection wavelengths, indicating that a single electron transfer step leads to charge recombination. Exemplary decays of the most intense transient absorption signal for the three triads at 770 nm are shown in Figure 4.13b. The lifetimes extracted from these decays are given in Table 4.4. Similar to the measurements in acetonitrile/water, a rate maximum for charge recombination can be observed for anisyl-xy$_2$ with τ_{CR}= 160 ns, whereas lifetimes of 1600 ns for anisyl-xy$_1$ and 27 µs for anisyl-xy$_3$ were obtained. The decays of the transient absorption signals for anisyl-xy$_2$ and anisyl-xy$_3$ are not mono-exponential. For anisyl-xy$_3$ an identical behavior was observed as for the measurements in acetonitrile/water. A short component with a lifetime of 160 ns, exhibiting the same spectral signature as the excited state of TMS-xy$_2$-Ru-xy$_2$-TMS was observed. As a result, on short timescales the ^{3}MLCT state is observed. Additionally, the decay of the actual charge-separated state revealed a contribution with lifetimes of several hundred microseconds corresponding to bimolecular recombination reactions (see Scheme 4.5) . For anisyl-xy$_2$ a bi-exponential decay was detected with lifetimes of 30 ns and 160 ns. The spectra of the faster decaying component could not be resolved because of similar amplitudes and rate constants of the

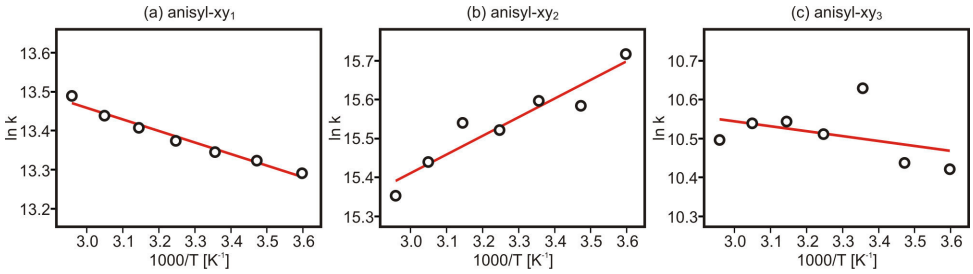

Figure 4.14 ARRHENIUS plots of the rate constants for charge recombination of (a) anisyl-xy_1, (b) anisyl-xy_2, and (c) anisyl-xy_3. The 20 μM solutions of the triads in acetonitrile were deoxygenated. Excitation occurred at 532 nm. The activation free energies extracted from these plots are listed in Table 4.4.

Table 4.4 Lifetimes for charge recombination τ_{CR}, activation free energies $\Delta G^{\ddagger}$and reorganization energies λ for the anisyl-xy_n triads in acetonitrile.

triad	τ_{CR} [ns]	$\Delta G^{\ddagger}$ [meV]	λ [eV][a]
anisyl-xy_1	1600	26 ± 2	1.26 ± 0.47
anisyl-xy_2[b]	160	-41 ± 6	1.61 ± 0.05
anisyl-xy_3[b]	27000	11 ± 11	1.62 ± 0.05

[a] assuming $\Delta\Delta G_{CR} = 0.05$ eV.
[b] $\lambda = -\Delta G^0 = -\Delta G_{CR}$ for activationless ET.

two decays. However, from thermodynamic considerations the short component can be assigned most likely to an intermediate of the electron transfer cascade, bearing a reduced photosensitizer and an oxidized amine. In contrast to anisyl-xy_1, the somewhat more intense TAA^+ signal compared to the AQ^- signal at 570 nm for anisyl-xy_2 is an indication for this assignment.

The activation energies, $\Delta G^{\ddagger}$, were obtained from ARRHENIUS plots (Figure 4.14) in the temperature range between 5 °C and 65 °C, performed in the same manner as for the previous measurements. The actual decays for the triads are shown in Figure A4 in the Appendix. For the shortest triad, an activation free energy of 26 ± 2 meV was extracted from Figure 4.14, whereas the next longer xy_2 triad shows a negative activation energy of -41 ± 6 meV. This phenomenon of a negative activation energy is very likely the result of a conformational equilibrium, decreasing the electronic coupling with increasing temperature. Similar behavior has been observed in other donor-acceptor systems.[95] For anisyl-xy_3, the transient absorption signals are very weak due to charge separation becoming much less competitive with increasing distance with respect to the decay of the ^{3}MLCT state. This results in rather large uncertainties for the individual rate constants for intramolecular charge recombination in anisyl-xy_3 at different temperatures, which manifests in a large scattering of the data points in the respective ARRHENIUS plot.

The reorganization energies λ have been calculated with equation 4.4 using the experi-

mental values of ΔG^0 and $\Delta G^{\ddagger}$. The results are listed in Table 4.4. For anisyl-xy_2 an activationless behavior was assumed. The same was done for anisyl-xy_3 because no clear trend in the ARRHENIUS plot could be observed due to the large scattering of the data points. With the obtained λ values of 1.26 ± 0.47 eV (anisyl-xy_1), 1.61 ± 0.05 eV (anisyl-xy_2), and 1.62 ± 0.05 eV (anisyl-xy_3), a saturation effect for the reorganization energy was found at long distances. Indeed, an upper limit of 1.6 eV for λ is in perfect agreement with the two-sphere electrostatic model (assuming an independent λ_{in} of 0.1 eV) as discussed for the acetonitrile/water measurements. In fact, it demonstrates that this theoretical model is suitable for inert solvents in which only electrostatic contributions to the reorganization energy need to be considered. In contrast, the model fails for systems where bond formation or bond breaking, i.e. proton transfer or hydrogen bonding, plays an important role. Considering these conclusions with respect to the electron transfer rate constants obtained for charge recombination in acetonitrile/water, it is not surprising that a fit of the experimental data to the two-sphere model was unsuccessful.

4.6. Reaction free energy dependence

Aside from the unusual distance-dependence of the three triads discussed in detail in the prior sections, another important conclusion can be extracted from the experimental data. As already mentioned in Chapter 2, the MARUCS equation predicts that in a given system electron transfer rates increase in the normal region ($\lambda > -\Delta G^0$) when increasing the reaction free energy. A further increase of the driving force leads to the opposite effect of decreasing rate constants, the so called inverted MARUCS region ($\lambda < -\Delta G^0$). The molecular design of the three investigated series of triads allows a more detailed investigation of this effect. In this context, especially the shortest xy_1 triads are of interest since their charge recombination reaction take place in the inverted region. The reaction free energies were found to be -1.30 eV (veratryl-xy_1), -1.34 eV (anisyl-xy_1), and -1.51 eV (tolyl-xy_1), respectively (Table 4.1). This clear trend in ΔG_{CR} should manifest in a situation where the triad with the largest driving force, in this case tolyl-xy_1, should exhibit the smallest rate constant. On the other hand, the significantly less exergonic electron transfer of veratryl-xy_1 should occur much faster. However, the opposite was observed. Tolyl-xy_1 is undergoing faster electron transfer than veratryl-xy_1 (see Table 4.2). The same observation was made when comparing the electron transfer rates of anisyl-xy_1 in acetonitrile/water 1:1 (v:v) and in neat acetonitrile. In aqueous solution the reaction free energy is less exergonic by about 0.3 eV, therefore, thermal back-ET is expected to occur faster than in neat acetonitrile. However, the actual lifetimes are 2800 ns in acetonitrile/water and 1600 ns in pure acetonitrile. The reason for this unexpected behavior is

that the statement of decreasing rate constants with increasing reaction free energy in the inverted region is only true if the reorganization energy is kept constant. In practice, this is usually not the case. Altering a system's driving force usually means that either the solvent polarity or the chemical nature of the acceptor or donor is changed. Considering that the reorganization energy mainly depends on the solvent reorganization, the value for λ does not necessarily need to stay constant. For example, when changing the methoxy-substituents on the anisyl-xy$_1$ triad to methyl-substituents (tolyl-xy$_1$) in order to change the reaction free energy, the reorganization energy changes significantly from 0.93 eV to 1.16 eV. This fact demonstrates that ΔG-dependent measurements generally need to be conducted in relation to the individual reorganization energies. When comparing the lifetimes of the xy$_1$ triads with regard to the ratio between driving force and reorganization energy ($-\Delta G^0/\lambda$), the expected behavior for systems operative in the inverted region becomes visible. Comparing the degree of inversion for veratryl-xy$_1$ ($-\Delta G_{CR}/\lambda = 1.43$) and tolyl-xy$_1$ ($-\Delta G_{CR}/\lambda = 1.30$) it becomes obvious that the latter is significantly less inverted and consequently, showing faster rate constants for electron transfer. The same observation can be made for anisyl-xy$_1$ in aqueous solution and in neat acetonitrile. In acetonitrile/water the degree of inversion is found to be 1.44, whereas for neat acetonitrile it is only 1.29, resulting in faster electron transfer in neat acetonitrile.

The observation that the ratio $-\Delta G^0/\lambda$ has to be considered for driving force-dependent investigations is not new. However, this effect is often underestimated. For the set of triads investigated, the importance of this consideration is not negligible. Particularly the observation of this effect for the anisyl-xy$_1$ triad in different solvent systems is important because driving force-dependent measurements are often performed by merely changing the solvent polarity. The present study shows that this is clearly not adequate in all cases.

4.7. Summary

The aim of this study was the investigation of the distance-dependence of long-range electron transfer. Three series of rigid linear triads with well defined donor-acceptor distances between 22.0 Å and 39.2 Å were synthesized and investigated with respect to their electron transfer kinetics. The time-resolved measurements focused on the thermal back-ET of the photochemically formed charge-separated state. The rate constants for this electron transfer revealed an unusual distance-dependence with rate maxima for large spatial separation. This phenomenon was attributed to a change-over from Marcus inverted electron transfer at short distances to electron transfer operating in the normal region at large separation. At intermediate distance an activationless (and consequently very fast) ET was observed, caused by an increase in reorganization energy. This counter-

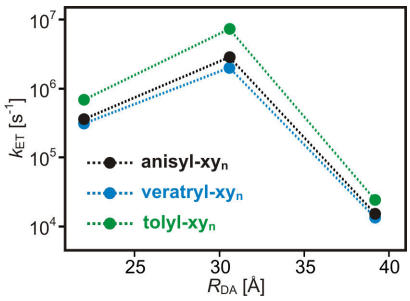

Figure 4.15 Distance dependence of k_{ET} for charge recombination in the three series of triads.

intuitive behavior of increasing rate constants with increasing distance to a maximum value with a subsequent decrease for increased separation as shown in Figure 4.15, though predicted earlier,[72–74] has not yet been observed in experimental studies.

This observation is not only of particular interest for the general understanding of electron transfer, but it is also of fundamental importance for the conversion of solar light to chemical energy. Photoinduced electron transfer from a donor to an acceptor producing a charge-separated state usually occurs in the normal region of the MARCUS theory. Accordingly, for bimolecular reactions these electron transfers occur preferably when both reactants are at close contact. For conversion of solar light into chemical energy, the thermal charge recombination of this initially formed electron-hole pair is an undesired, energy-wasting process. In fact, back electron transfer from the reduced acceptor to the oxidized donor often occurs in the inverted region, presumably with rate maxima at large separations as shown in Scheme 4.1. Usually, after formation of a charge-separated state, the donor and acceptor diffuse away from each other, passing a region where an undesired thermal back-reaction becomes more favorable. This suggests that the quantum yield for the conversion of solar light to chemical energy can be drastically limited due to this effect.

Another important conclusion drawn from the experimental data concerns the importance of considering the reorganization energy for driving force-dependent measurements. It was shown that within the series of the shortest triads, operating in the inverted region, the expected effect of slower rate constants with increasing driving force was not observed. The opposite is the case. Consequently, a satisfying correlation with the expected behavior was only found when the ratio of $-\Delta G^0/\lambda$, characterizing the certain degree of inversion, was considered. This finding, again, demonstrates the importance of the reorganization energy which is commonly underestimated. Especially with respect to driving force-dependent measurements done by altering the solvent polarity, as often found in literature, the importance of considering the reorganization energies becomes evident.

5. Charge Accumulation in a Molecular Pentad

Aside from single-electron transfer, whether proton-coupled or not, recent studies on charge separation turned their focus towards the accumulation of charges.[96] Efficient generation of solar fuels, for example hydrogen formation from protons or CO_2 reduction, requires at least two redox equivalents as discussed in Chapter 2. Several examples have been reported in literature using sacrificial agents[47, 48, 97] or nanoparticles[50, 51, 98] to achieve charge accumulation. Purely molecular systems which do not depend on sacrificial agents are still very rare and exhibit short lifetimes, on the order of a few nanoseconds, for the twofold charge-separated state.[52, 53]Recently, an approach to accumulate two redox equivalents on one donor and one acceptor, respectively, within a molecular assembly was reported by our group.[99] The lack of evidence for twofold charge-separated species in this study reflects the difficulties accompanied with photoinduced build-up of more than one charge on a single small molecule.

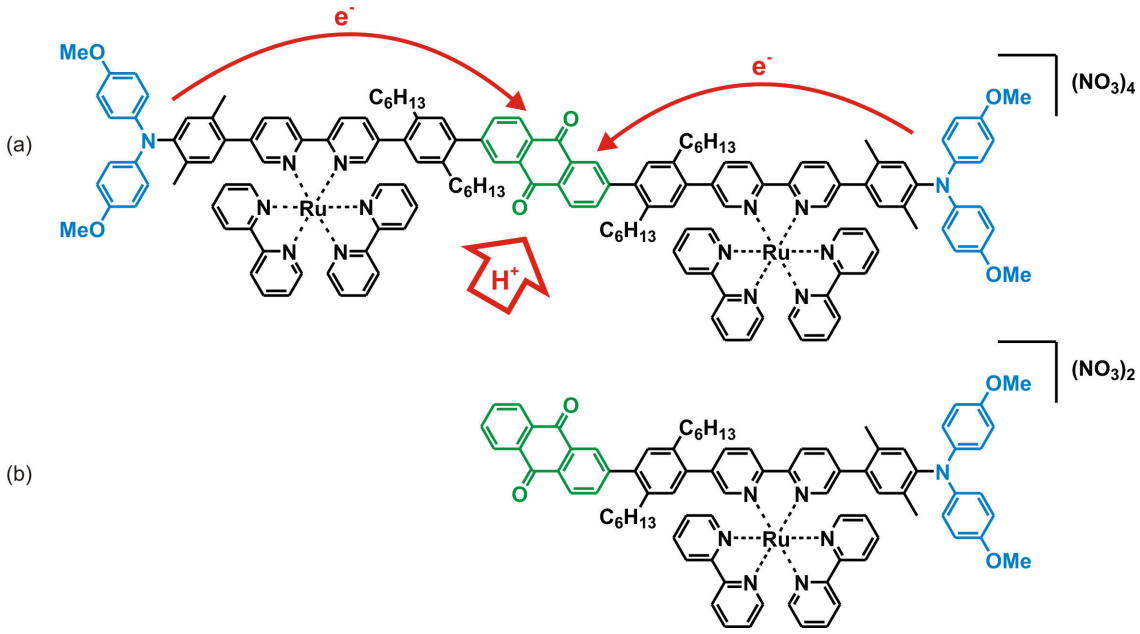

Scheme 5.1 (a) Pentad investigated with respect to its charge accumulation abilities. (b) Reference triad.

In this study a purely molecular system theoretically capable to accumulate two redox equivalents without the need of high-energy sacrificial agents was designed. The principle of a donor-photosensitizer-acceptor assembly, as used for example in the studies in Chapter 4, was extended to the pentad system shown in Scheme 5.1. A detailed description of the synthesis of the molecules used in this study is given in the experimental section in Chapter 7. The pentad is composed of a central two-electron acceptor which is covalently linked to two photosensitizer-donor assemblies. Anthraquinone (AQ), with its well-documented redox-chemistry, served as the central electron accepting site. triarylamines were used as one-electron donors in combination with $Ru(bpy)_3{}^{2+}$ photosensitizers. As bridging units *p*-xylene and *p*-di-*n*-hexylphenylene units were applied. The latter were introduced for solubility reasons. By accumulating two charges on a single small molecule, very high-energy species are generated. This points towards two mayor drawbacks of charge accumulation: (1) high redox potentials that might exceed those of the photosensitizer, and (2) a high tendency for thermal charge recombination. In contrast, protonation in combination with electron transfer results in a neutral species, leading to a situation where a possible second charge would lack any electrostatic repulsions within the molecule. Consequently, storing a second redox equivalent on any moiety is usually much easier when associated with proton transfer. Therefore anthraquinone was chosen as an electron accumulating site.

5.1. Optical absorption

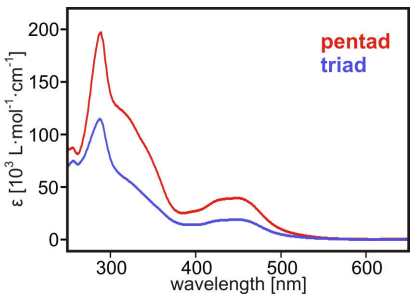

Figure 5.1 UV-Vis absorption spectra of 20 µM solutions of the pentad (red trace) and the reference triad (blue trace) in acetonitrile.

The absorption spectra of 20 µM solutions of the pentad and the reference triad in acetonitrile are shown in Figure 5.1. As expected, both complexes show nearly identical absorption spectra, with the intensity of the absorption bands being twice as high for the pentad compared to the reference triad. In both cases a prominent absorption band around 450 nm was detected which can be assigned to a metal-to-ligand charge transfer

(MLCT) as well as an absorption band around 290 nm arising from $\pi \rightarrow \pi^*$ transitions centered on the bipyridine ligands. A broad absorption band between 300 nm and 400 nm, shaped as a shoulder, can be attributed to transitions originating from anthraquinone as well as from the triarylamines.

5.2. Electrochemistry and reaction free energies

In order to estimate the reaction free energies for the individual charge separation steps, the redox potentials of the relevant moieties were determined by cyclic voltammetry. The measurements were performed in deoxygenated acetonitrile containing 1 mM substrate and 0.1 M $TBAPF_6$ as supporting electrolyte. The measured voltammograms are shown in Figure 5.2 and the extracted potentials are summarized in Table 5.1.

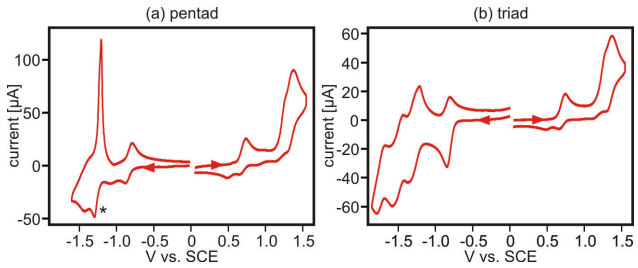

Figure 5.2 Cyclic voltammograms of 1 mM solutions of (a) the pentad and (b) the reference triad in acetonitrile with 0.1 M $TBAPF_6$ as supporting electrolyte and a scan rate of 0.1 V/s. The oxidative and reductive sweeps were measured separately to obtain voltammograms of higher quality. The asterisk marks the adsorption peak associated with the second reduction of anthraquinone.

Table 5.1 Reduction potentials (in Volts vs. SCE) of the relevant species of the pentad and the reference triad in acetonitrile extracted from Figure 5.2.

	pentad	triad
$E(Ru^{III/II})$	1.33	1.33
$E(TAA^{+/0})$	0.69	0.70
$E(AQ^{0/-})$	-0.84	-0.83
$E(AQ^{-/2-})^a$	-1.34	-1.34
$E(Ru^{II/I})$	-1.26	-1.28

[a] in DMF, taken from reference [87].

The voltammograms in Figure 5.2 exhibit nearly identical reduction potentials in the pentad and the reference triad. The voltammograms of the triad are not discussed in more detail. In the pentad, oxidation of the $Ru(bpy)_3^{2+}$ photosensitizer was observed at 1.33 V, bipyridine-centered reduction waves are between -1.25 V and -1.80 V. Although

all three reduction waves were observed for the reference triad, for the pentad only the relevant first reduction wave at -1.26 V was well observable. The oxidation wave of the electron donor moiety, TAA, was detected at a potential of 0.69 V vs. SCE in the pentad. The first reduction of anthraquinone was found to occur at -0.84 V, whereas the second reduction wave overlaps with the bpy reductions resulting in an adsorption peak around -1.3 V (marked with an asterisk in Figure 5.2). Since a proper value for the reduction potential of AQ^{2-} could not be observed, the reported value of -1.34 V vs. SCE in DMF was used for further calculations.[87] With all relevant redox potentials at hand, the energies of the individual species involved during charge accumulation were calculated with equation 5.1. for the pentad in neat acetonitrile.

$$E = e \cdot (\sum E_{ox} - \sum E_{red}) \tag{5.1}$$

$$pK_A(MeCN) = 12.31 + 0.98 \cdot pK_A(DMSO) \tag{5.2}$$

$$\Delta G_{PT} = -e \cdot 0.059V \cdot [pK_A(base) - pK_A(acid)] \tag{5.3}$$

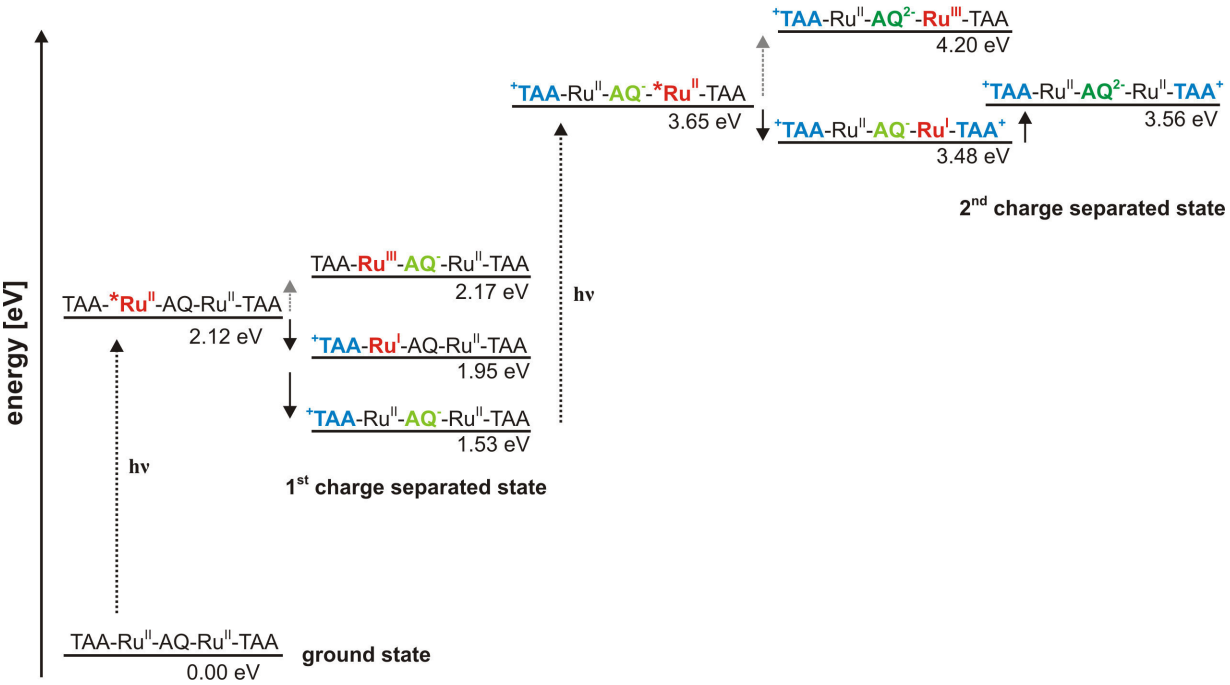

Scheme 5.2 Energy diagram for the formation of the first (CSS1) and second (CSS2) charge-separated state in the pentad in neat acetonitrile based on the redox potentials listed in Table 5.1.

Scheme 5.2 shows the energy level diagram developed for photoinduced charge accumulation in the pentad in neat acetonitrile based on the reduction potentials listed in Table 5.1.

Explicit calculations of the energies of the individual states are given in the Appendix. It has to be noted that these energy estimates, though reported with two digits, are only accurate to ±0.1 eV for electron transfers and to ±0.3 eV for proton transfer steps. After excitation of the pentad (excitation energy: E_{00} = 2.12 eV[86]), the formation of the first charge-separated state (CSS1) at 1.53 eV occurs via oxidation of the triarylamine, followed by electron transfer from the reduced photosensitizer to the anthraquinone site. After absorption of a second photon, electron transfer from the excited CSS1 to the singly reduced anthraquinone is endergonic by 0.55 eV and therefore unlikely. In contrast, oxidation of the second triarylamine is exergonic by 0.17 eV, similar to the formation of CSS1, leading to a state at 3.48 eV comprised of two oxidized amines, AQ^-, and a reduced photosensitizer. From that state, electron transfer from the reduced photosensitizer to the central anthraquinone is slightly endergonic by roughly 0.1 eV. In other words, the formation of CSS2 is not favored from a thermodynamic point of view. However, slightly endergonic reactions might still occur, though a low quantum yield for charge accumulation in neat acetonitrile is to be expected. To compensate for this disadvantage, proton transfer coupled to charge accumulation seems to be a promising possibility. In order to estimate the energies of the relevant states, the pK_A of a given acid and those of the reduced anthraquinone species in acetonitrile need to be considered. However, pK_A values for the anthraquinone species have not been reported in literature, neither for acetonitrile nor DMSO. As an alternative, the pK_A values of *p*-benzoquinone were considered. Its pK_A values in DMSO[100] were used to estimate values in acetonitrile by applying equation 5.2.[101] For all spectroscopic measurements, chloroacetic acid (with a pK_A value of 18.8 in acetonitrile[102]) was used as the proton source. Attempts to determine the pK_A value for neutral TAA failed. UV/Vis titration experiments with much stronger acids like trifluoroacetic acid gave no significant spectral changes. As a result, under the conditions applied for the spectroscopic measurements no protonation of TAA is expected. All relevant acidity constants are listed in Table 5.2. Additionally, the driving forces for the protonation of the individual anthraquinone species, ΔG_{PT} , were calculated using equation 5.3. They are noted in the last column of Table 5.2. The protonation of singly reduced anthraquinone by chloroacetic acid is exergonic by 0.25 eV. The driving force is expected to be -1.15 eV for the first protonation step and -0.75 eV for the second protonation, respectively.

Table 5.2 Acid-base constants, pK_A, for *p*-benzoquinone (BQ) and chloroacetic acid in acetonitrile and driving forces, ΔG_{PT} , for the individual protonation steps of singly and twofold reduced anthraquinone.

compound	pK_A (MeCN)	ΔG_{PT}[eV][a]
chloroacetic acid	18.8[b]	
$BQH^{\cdot}$	23.1[c]	-0.25
BQH^{-}	38.3[c]	-1.15
BQH_2	31.7[c]	-0.75

[a] calculated using equation 5.3. [b] from reference [102].
[c] calculated from reference [100] using equation 5.2

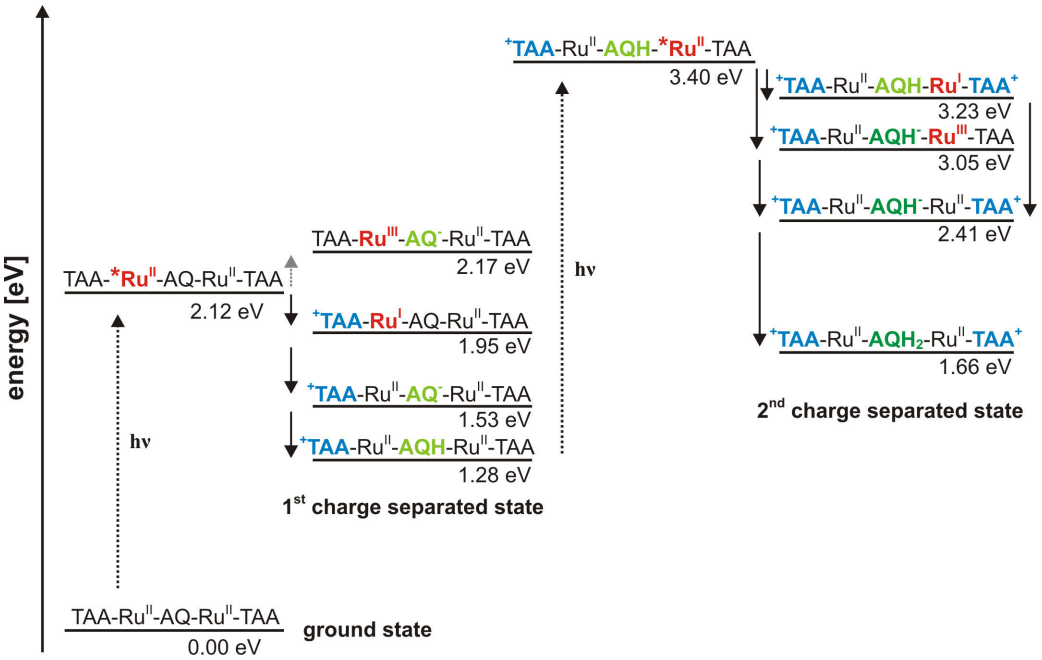

Scheme 5.3 Energy diagram for the formation of the first (CSS1) and second (CSS2) charge-separated state in the pentad in acetonitrile in the presence of chloroacetic acid as a proton donor. The energies were calculated based on the redox potentials listed in Table 5.1 and the estimated values for ΔG_{PT} as listed in Table 5.2.

With the calculated driving forces for the individual protonation steps, the energy scheme for charge accumulation in the pentad was extended, now also taking into account the protonated states (Scheme 5.3). Explicit calculations of the energies of the individual states are given in the Appendix. According to Scheme 5.3, the formation of CSS1 involves protonation of the semiquinone by chloroacetic acid, yielding a charge-separated state which is lower in energy by 0.25 eV than that formed in neat acetonitrile. After a second photon is absorbed, the excited state of CSS1 can now undergo two possible electron transfer pathways: (1) oxidative quenching to form a second TAA^+, and (2) reductive quenching, producing AQH^-. However, the thermodynamic estimations clearly show that formation

of the second charge-separated state (CSS2) is exergonic for both intermediate species. With the uptake of a second proton by the twofold reduced anthraquinone, a final CSS2 at 1.66 eV should be reached. The calculated values for the protonated states, of course, bear a relatively high uncertainty, due to the fact that pK_A values of *p*-benzoquinone were employed. Nevertheless, the comparison with the expected thermodynamics in neat acetonitrile clearly demonstrate that charge accumulation should be achieved more easily with concomitant protonation of anthraquinone. Additionally, thermal back-ET to the ground state coupled to release of the proton(s) might be slowed down drastically. This is due to the bimolecular nature of the proton transfer reaction (even trimolecular for AQH_2) to the conjugate chloroacetic acid. As a consequence, if charge accumulation is observed in the pentad, the lifetime of CSS2 will potentially be much longer compared to the lifetimes that have been reported for other purely molecular systems without sacrificial agents.[52, 53]

5.3. Transient IR spectroscopy in absence of acid

As shown in Scheme 5.2, the final electron transfer step to generate the second charge-separated state is slightly endergonic in pure acetonitrile. Although not favored, this CSS2 might be populated to a certain extent. The probability of a single pentad being excited twice within the same laser pulse is generally rather low. Therefore, it can be expected that mainly the CSS1 will be observed. As a consequence, transient UV/Vis spectroscopy is not suitable to unambiguously observe minor contributions of a CSS2. Even more so when considering that charge recombination of the CSS2 might be faster compared to the CSS1. In contrast ultrafast transient IR spectroscopy could be more suitable to detect a possible AQ^{2-} species unambiguously. The carbonyl functionalities within the anthraquinone give rise to a very specific detection of singly and twofold reduced species, respectively.[103, 104] The relevant IR measurements were conducted by Margherita Orazietti from the group of Prof. Peter Hamm at the university of Zürich.

Having in mind the quadratic power-dependency of a two-photon process such as charge accumulation in the pentad, it is necessary to estimate the excitation probability. For the transient IR experiments 415 nm laser pulses with an energy of 2 µJ and a laser beam diameter of 150 µm FWHM were used. The optical path length was 50 µm. With a pentad concentration of 1 mM and and extinction coefficient of ε_{415} = 32800 M^{-1} cm^{-1} (from Figure 5.1) the excitation probability can be estimated to be 62 %. This is a more than sufficient value for two-photon processes. The transient IR spectra of the pentad and the reference triad in deoxygenated CD_3CN recorded 0.5 ns after excitation with 100 fs pulses are shown in Figure 5.3. Both compounds exhibit a prominent bleach at

1508 cm^{-1} associated with a signal at 1576 cm^{-1} . These spectral features can be attributed to the loss of ground state absorption of the triarylamine and the formation of TAA^+, respectively.[105] Bleaches associated with the depletion of anthraquinone were detected at 1322, 1600 and 1680 cm^{-1}. Recently, spectro-electrochemical IR studies on anthraquinone reported absorption bands at 1487 cm^{-1} and 1403 cm^{-1} for the singly reduced species. [106] These reported values are clearly in line with the observed signals at 1485 cm^{-1} for the pentad and the reference triad, confirming the formation of AQ^-. In other words, the CSS1 was observed for both complexes, as expected from the thermodynamic estimations. However, a signal at 1404 cm^{-1} was only detected for the reference triad. In addition to that, the transient spectrum of the pentad exhibits a signal around 1365 cm^{-1} which is not present in the reference triad as shown in Figure 5.3. The IR spectro-electrochemical studies mentioned earlier report a signal at 1356 cm^{-1} for twofold reduced anthraquinone (AQ^{2-}).[106] These observations suggest that formation of the CSS2 is observed in the pentad. In contrast, in the reference triad the formation of a two-fold reduced anthraquinone is very unlikely from a thermodynamic viewpoint. Furthermore, the photosensitizer in the reference triad would have to absorb a second photon after formation of the CSS1. The complete formation of the CSS1 in a similar triad (anisyl-xy_1 from Chapter 4) was reported to occur within 200 ps.[94] However, with an excitation pulse duration of 100 fs for the transient IR measurements, the absorption of a second photon after formation of the CSS1 is very unlikely. Consequently, only the pentad which bear two photosensitizer moieties can absorb a second photon and form the CSS2 under these conditions.

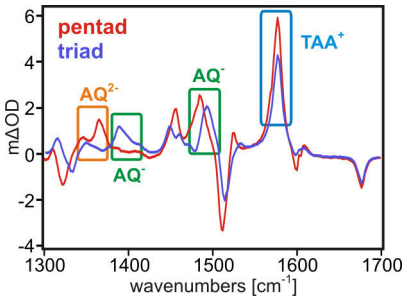

Figure 5.3 Transient IR spectra of the pentad (red trace) and the reference triad (blue trace) in dry deoxygenated CD_3CN (c = 1 mM). The spectra were recorded 0.5 ns after excitation with 415 nm laser pulses. The pulse duration was 100 fs with an energy of 2 μJ and a beam diameter of approximately 150 μm FWHM.

The temporal evolution of the transient IR absorption signals of the pentad are shown in Figure 5.4. From the kinetic data a time constant of 40 ps for the formation of the singly reduced anthraquinone at 1483 cm^{-1} can be extracted. The second charge-separated state (CSS2), indicated by the signal of AQ^{2-} at 1365 cm^{-1}, is formed with a time constant of 62 ps. The signal of TAA^+ at 1575 cm^{-1} exhibits a rather complex rise kinetic, due to a

spectral overlap with the signal for the excited state of the photosensitizer. In accordance with the signal of AQ^{2-}, complete formation of TAA^{+} was observed within 180 ps. The decays of the observed signals on longer timescales are similar and biexponential for all detected wavenumbers. Hereby the time constants of the faster decay were determined to be 851 ns (TAA^{+}), 942 ns (AQ^{-}), and 907 ns (AQ^{2-}) whereas the longer decay components exhibits lifetimes of 12.7 µs (TAA^{+}), 13.9 µs (AQ^{-}), and 13.3 µs (AQ^{2-}), respectively. From transient UV/Vis absorption experiments conducted with a similar triad, the CSS1 is supposed to exhibit lifetimes on the order of 1.6 µs in acetonitrile (see anisyl-xy_1 in Table 4.4). This discrepancy probably stems from the high sample concentrations of 1 mM used for the IR measurements. This can lead to bimolecular charge recombination reactions which would cause a shortening of the lifetime of the charge separated states. Furthermore, bimolecular reactions leading to separated oxidized and reduced species on different pentad molecules (analog to Scheme 4.5) is expected to occur. While the lifetime of the CSS1 is not surprising, the relatively long lifetime of the CSS2 is particularly remarkable when considering a stored energy of 3.56 eV (see Scheme 5.2) and the multitude of possible decay pathways. However, recombination of the CSS1 to the ground state is associated with a reaction free energy of ΔG = -1.53 eV and is supposed to operate in the MARCUS-inverted region (see anisyl-xy_1 from Chapter 4). Recombination of the CSS2 to CSS1 is associated with a reaction free energy of $\Delta G \approx$ -2 eV and therefore might be decelerated by an inverted-driving force effect.

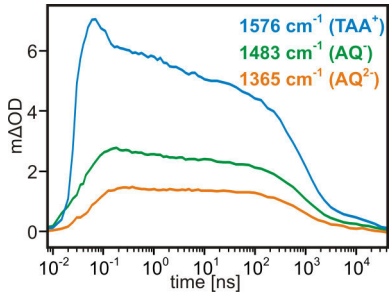

Figure 5.4 Temporal evolution of the transient IR absorption signals of the pentad from Figure 5.3. The detected signals are: 1576 cm^{-1} (pale blue trace, TAA^{+}), 1483 cm^{-1} (green trace, AQ^{-}), and 1365 cm^{-1} (orange trace, AQ^{2-}).

5.4. Transient UV/Vis spectroscopy

The UV/Vis spectral properties of the charge-separated states can be described as a superimposition of the spectral features of TAA^{+} and the different anthraquinone species, respectively. In order to identify the anthraquinone contribution to the overall transient absorption spectrum, the precise spectral signature of TAA^{+} in the pentad is needed.

The signature of TAA^+ can be subtracted from the transient spectra, in order to obtain the corresponding absorption features of the anthraquinone species. For that reason, spectro-electrochemical measurements were performed on the pentad. Figure 5.5 depicts the difference-absorption spectrum after an applied potential of +0.8 V vs. SCE (TAA oxidation) in deoxygenated acetonitrile. The results are similar to what was observed for the anisyl-xy_1 triad in Chapter 4. The spectrum shows two prominent absorptions at 770 nm and 370 nm. Additionally, a bleach in the MLCT region around 450 nm was detected.

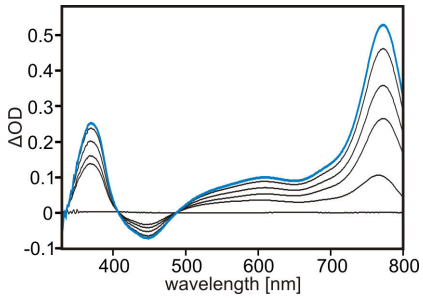

Figure 5.5 Spectro-electrochemical measurements, showing the UV/Vis difference-absorption spectrum of the pentad obtained after applying a potential of +0.8 V vs. SCE (TAA oxidation). The sample contained 0.2 mM of the pentad with 0.1 M $TBAPF_6$ as supporting electrolyte in acetonitrile. The solution was deoxygenated prior to the measurement. The baseline corresponds to no applied potential.

The transient UV/Vis measurements were performed in acetonitrile solution and excitation occurred with 10 ns laser pulses at 532 nm. The energy per laser pulse was approximately 44 mJ with a beam diameter of approximately 0.6 cm. The pentad concentration was 20 µM with an extinction coefficient of $\varepsilon_{532} = 3350\ M^{-1}\ cm^{-1}$ (see Figure 5.1) . With these values in hand, a theoretical excitation probability of 5 can be calculated concluding an excitation probability of 100 %. With regard to the quadratic power-dependency of two-photon processes, this is deeply in the saturation regime. The transient UV/Vis experiments were performed under aerated conditions which usually results in significantly shorter lifetimes for charge-separated states. As a result, the likelihood of bimolecular reactions, like the disproportionation of $AQH^{\cdot}$ to AQH_2 from the CSS1, is significantly decreased. In Figure 5.6(a-b) the transient UV/Vis absorption spectra (black traces) of the pentad are shown in neat acetonitrile and with 0.2 M chloroacetic acid. The spectra were measured directly after laser pulsed excitation and time-integrated over 50 ns (in neat acetonitrile) or 200 ns (with 0.2 M chloroacetic acid), respectively. For the measurements in neat acetonitrile, the same spectral features at 770 nm, 570 nm, and 370 nm were observed as already shown in Chapter 4 for anisyl-xy_1 (see Figure 4.13a). In contrast, for the measurements with 0.2 M chloroacetic acid, the prominent signal at 570 nm is absent. In addition, the band at 370 nm has changed to a broader absorption

band centered at 390 nm. In order to obtain the spectral contribution of the individual reduced anthraquinone species, the difference-absorption spectrum of TAA^+ (see Figure 5.5), shown as pale blue trace in Figure 5.6(a-b), was subtracted from the initial spectra. Hereby, the TAA^+-spectrum was normalized to the absorption maximum at 770 nm. This procedure was applied because all AQ species are supposed to have neglectable absorbance in this region. The resulting spectral signature of the reduced AQ species are shown as green traces in Figure 5.6(a-b). For neat acetonitrile, the resulting spectral features of the reduced anthraquinone species are comprised of two signals at 400 nm and 580 nm. This finding is in line with an assignment as $AQ^{\bullet-}$.[81, 87] Consequently, only the CSS1 is detected in neat acetonitrile. The spectrum lacks the absorption signature of AQ^{2-} at 470 nm,[87] that would indicate formation of the CSS2. Although the transient IR measurements confirmed its formation in pure acetonitrile, the situation in the UV/Vis measurements is somewhat different. For instance, the significantly longer laser pulse of 10 ns in combination with the fast formation of the CSS1 and CSS2 within a few hundred picoseconds give access to additional unproductive electron transfer pathways. As an example, after formation of the first charge-separated state the pentad can absorb a second photon leading to a state at 3.56 eV (see Scheme 5.2). This state can either undergo an additional charge separation or can recombine to the CSS1 or the ground state. As a consequence, these unproductive pathways can severely limit the probability of forming a second charge-separated state. Additionally, a potentially weak signal for AQ^{2-} in the CSS2 might not be detectable, if overlapped by the major spectral contribution of the CSS1. Furthermore, the lifetime of the CSS2 should be significantly shortened when measurements are conducted under aerated conditions, making it possible that this state decays faster than the temporal resolution of the instrument setup.

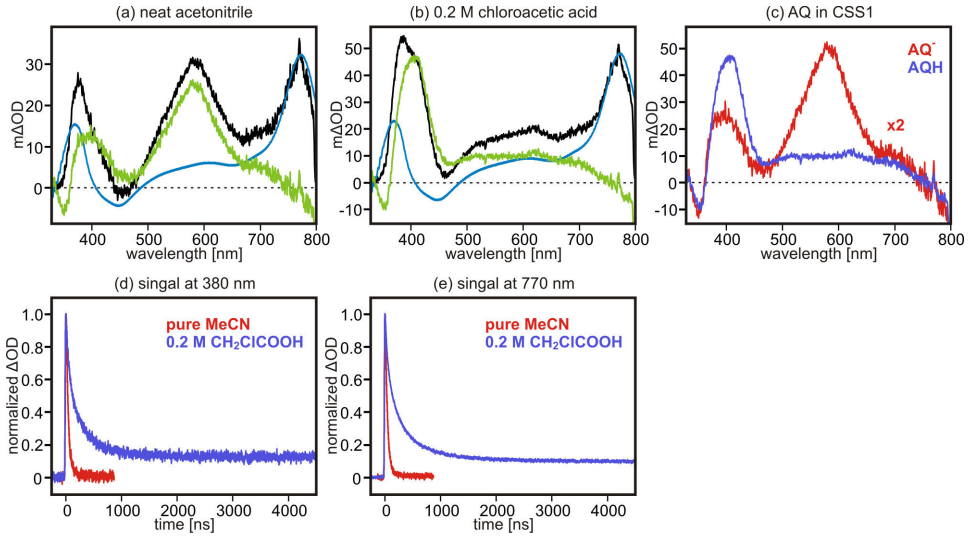

Figure 5.6 UV/Vis transient absorption spectra (black traces) of 20 µM pentad in (a) neat acetonitrile, and (b) with 0.2 M chloroacetic acid. From the initial spectra, the difference-absorption spectrum of TAA^+ (pale blue traces) was subtracted to obtain the contribution of the reduced anthraquinone species (green traces). (c) Comparison of the spectral signatures of reduced AQ from (a-b) in neat acetonitrile (red trace) and with 0.2 M chloroacetic acid (blue trace). (d-e) Temporal evolution of the transient absorption signal at 380 nm(d) and 770 nm (e) of the pentad in neat acetonitrile (red traces) and with 0.2 M chloroacetic acid (blue traces). The measurements were conducted under aerated conditions. Excitation occurred with 10 ns laser pulses at 532 nm with energies of approximately 44 mJ. The transient spectra were recorded directly after the excitation pulse and time-integrated during 50 ns (a) and 200 ns (b), respectively.

The reduced anthraquinone species in the measurements conducted with 0.2 M chloroacetic acid (green trace in Figure 5.6b) exhibits an intense absorption around 405 nm associated with a weak, structureless absorption beginning at 450 nm. The spectral changes, compared to AQ^-, are most likely the result of protonation of the singly reduced anthraquinone, compatible with the pK_A values of the relevant species. Furthermore, pulse radiolysis studies of functionalized anthraquinones report similar absorption signatures for $AQH^\cdot$ with a prominent band around 400 nm and broad, less intense absorption in the red part of the visible spectrum.[107–109] In consequence, the CSS1 with the protonated semiquinone form of AQ is observed immediately after excitation of the pentad in presence of 0.2 M chloroacetic acid. The different spectral signatures of the AQ species of the CSS1, with and without acid, are overlayed in Figure 5.6c. The decay kinetics at 380 nm and 770 nm are depicted in Figure 5.6(d,e). The decays were identical at the two detection wavelengths for the individual measurement conditions. The decay of the CSS1 in neat acetonitrile is mono-exponential with a lifetime of 40 ns under aerated conditions. In contrast, the signal of the CSS1 of the pentad with 0.2 M chloroacetic acid exhibits a tri-exponential decay with lifetimes of 80 ns, 450 ns, and $\geq$ 100 µs. The faster decay

components (80/450 ns) are associated with the biexponential decay of the CSS1. Why exactly this decay is biexponential is not clear at that point. Recombination to the ground state has to be accompanied by the liberation of the semiquinone proton. Therefore, two competing mechanisms of proton-coupled electron transfer might be the reason for the observed biexponential behavior. However, this suggestion remains speculative and is only of minor interest in this study.

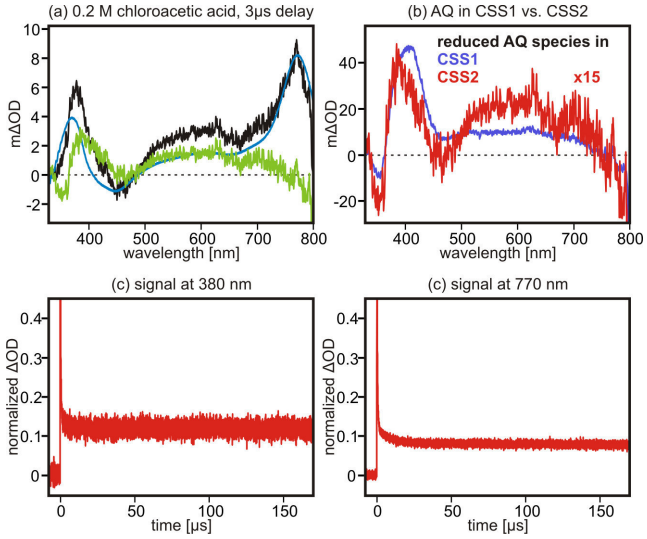

Figure 5.7 (a) UV/Vis transient absorption spectrum (black trace) of the pentad in acetonitrile with 0.2 M chloroacetic acid recorded with a time delay of 3 µs. From the initial spectrum, the difference-absorption spectrum of TAA^+ (pale blue traces) was subtracted to obtain the contribution of the reduced anthraquinone species (green traces). (b) Comparison of the anthraquinone species of the pentad in acetonitrile with additional acid detected directly after excitation (blue trace) and with a time delay of 3 µs (red trace), respectively. (c,d) Temporal evolution of the transient absorption signal at 380 nm (c) and 770 nm (d). The measurements were conducted under aerated conditions and the spectrum was time-integrated during 200 ns. Excitation occurred with 10 ns laser pulses at 532 nm with energies of approximately 44 mJ per pulse.

A more important finding is the fact that after the signal of the CSS1 has vanish, a long-living transient absorption signal remains in the presence of acid ($\tau \geq 100$ µs). The transient absorption spectrum of this long-living signal, measured with a time delay of 3 µs after excitation, is shown in Figure 5.7a (black trace). The spectrum changed such that the prominent absorption band around 400 nm has shifted to 380 nm and is less intense compared to the TAA^+ signal at 770 nm. Additionally, a weak bleach can be observed around 460 nm. Applying the same procedure as described for the spectra without time delay, the contribution of the reduced AQ species to the overall spectrum was obtained (green trace in Figure 5.7a, red trace in Figure 5.7b). The spectral features are comprised of a signal at 385 nm and a less intense absorption band between 500 nm

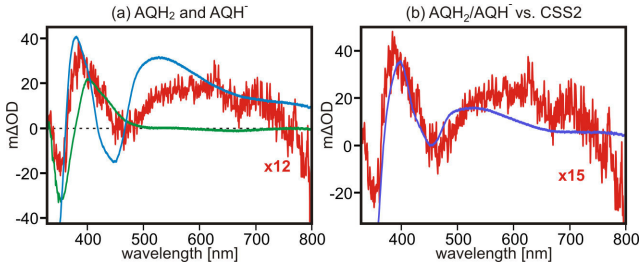

Figure 5.8 (a) Difference-absorption spectra of the pentad in acetonitrile in presence of chloroacetic acid obtained after an applied potential of -1 V vs. SCE. The deoxygenated solution contained 0.2 mM substrate, 4 mM chloroacetic acid, and 0.1 M $TBAPF_6$ as supporting electrolyte. The spectra were recorded at the beginning of the measurement (green trace) and approximately 20 minutes later (pale blue trace). The red traces in (a) and (b) represent the reduced anthraquinone species of the CSS2 extracted from Figure 5.7. (b) Comparison of the AQ species of the CSS2 with a combined difference-absorption spectrum (blue trace), representing a mixture of AQH_2/0.5 AQH^- (see text).

and 700 nm. The comparison of the two reduced anthraquinone species, obtained from the different time intervals, is shown in Figure 5.7b. It is directly observable that the species are not identical. The spectrum of $AQH^{\cdot}$ shows an absorption band at 405 nm with a structureless weak absorption beginning at 450 nm (blue trace in Figure 5.7b). In contrast, the spectrum for the species detected with a time delay of 3 µs (red trace in Figure 5.7b) exhibits an absorption band that is shifted to 385 nm, associated with a broad absorption band between 500 nm and 700 nm. This spectrum can not be assigned to any singly reduced anthraquinone species (AQ^-, $AQH^{\cdot}$, or hydrogen bonded AQ^-, as shown in Chapter 4). Consequently, twofold reduced anthraquinone is the most plausible explanation. According to Scheme 5.3, the CSS2 in presence of chloroacetic acid is expected to involve AQH_2 as the final photoproduct. In order to test this assignment, spectro-electrochemical measurements of the pentad in presence of acid were conducted. The reduction of anthraquinone under acidic conditions has been reported to be an irreversible two-electron process at -0.82 V vs. SCE, associated with the uptake of two protons, yielding AQH_2.[87] The difference-absorption spectrum of a deoxygenated acetonitrile solution containing 0.2 mM pentad, 4 mM chloroacetic acid, and 0.1 M $TBAPF_6$ after applying a potential of -1 V vs. SCE is shown in Figure 5.8a. The green trace is the difference-spectrum recorded at the beginning of the measurement, with a broad signal between 380 nm and 500 nm and a maximum at 400 nm. This signature can be attributed to AQH_2. The pale blue trace represents the spectrum recorded approximately 20 minutes later. It exhibits an intense absorption band at 380 nm with an additional broad absorption beginning at 470 nm. Furthermore, a significant bleach in the MLCT region was detected.

These changes in the difference spectrum with respect to the duration of the electrochemi-

cal reduction, are due to the fact of protons being reduced (see equation 5.4). This results in the observation, that after a certain period of time the initially formed AQH_2 (green trace in Figure 5.8a) is converted to AQH^- (pale blue trace in Figure 5.8a).

$$AQH_2 \rightleftharpoons AQH^- + H^+ \xrightarrow{e^-} AQH^- + \tfrac{1}{2}H_2 \tag{5.4}$$

When comparing the observed AQ species for the CSS2 from the transient UV/Vis absorption measurements (red traces in Figure 5.8) with the spectral signatures for AQH_2 and AQH^- in the pentad, no clear analogy can be observed at first glance. However, the spectrum of the reduced AQ species of the CSS2 extracted from Figure 5.7a exhibits similarities to both difference-absorption spectra in Figure 5.8a, pointing towards a mixture of AQH_2 and AQH^- in the charge-accumulated state. Indeed, a simple linear combination of the spectral signatures for AQH_2 (1 equivalent) and AQH^- (0.5 equivalent) shows a remarkable analogy to the AQ species of the CSS2 (see Figure 5.8b). The conclusion that probably both species, AQH_2 and AQH^-, are observed for the second charge-separated state is somewhat surprising. Considering the pK_A values of the relevant species (although only available for *p*-benzoquinone as an analogue, see above) this observation of a mixed state can not be explained satisfactorily. In general, semiquinones are much more acidic than the twofold reduced species of quinones. As a consequence, when observing $AQH^\cdot$ for the CSS1 in presence of chloroacetic acid, the twofold protonated AQH_2 should exclusively be formed for the second charge-separated state (see Scheme 5.3). Even when measuring the transient absorption spectrum with a time delay of several hundred microseconds, no changes in the absorption features were observed. As a result, the presence of AQH^- in the CSS2 after a time delay of only 3 µs is not originating from a potentially slow protonation step. Although the reason for the presence of two different protonation states in CSS2, as indicated in Figure 5.8, is unknown, the main objective of charge-accumulation in a purely molecular system, without sacrificial agents, was achieved. Furthermore, as shown in Figure 5.7c, only a lower limit of the lifetime ($\tau \geq 100$ µs) of the transient absorption signal for the second charge-separated was determined. In general, thermal charge recombination to the ground state is supposed to be a very complex process for the CSS2. Not only two electrons need to be transferred to the corresponding oxidized donor, but bimolecular proton transfer, to the conjugate base of chloroacetic acid, has to take place. Consequently, when considering AQH_2 as the main photoproduct, four reaction steps need to occur. Furthermore, taking into account the considerations of bimolecular reactions for long-living charge-separated states made in Chapter 4, one might easily think of a situation where oxidized TAA^+ and reduced anthraquinone are no longer located on the same molecule. This careful consideration demonstrates that a proper determination of a rate constant for the intramolecular charge recombination is very tricky in this case.

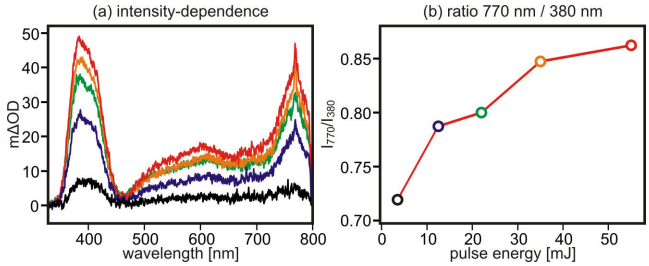

Figure 5.9 (a) Transient UV/Vis absorption spectra of 20 μM solutions of pentad in acetonitrile containing 0.2 M chloroacetic acid. Excitation occurred with 10 ns laser pulser at 532 nm, and the spectra were time-integrated during 200 ns. The pulse energies were: 3.5 mJ (black trace), 12.5 mJ (blue trace), 22 mJ (green trace), 35 mJ (orange trace), 55 mJ (red trace). (b) The ratio of the intensity of the signals at 770 nm and 380 nm (I_{770}/I_{380}) as a function of the excitation energy. The absorption maxima at 770 nm were determined by a Gaussian fit because of the spike in absorbance at that wavelength.

Another issue that needs to be discussed is the possibility that AQH_2 is formed as a result of bimolecular disproportionation ($2\ AQH^{\cdot} \rightarrow AQH_2 + AQ$) of the semiquinone form of the CSS1. In order to validate the assumption that charge accumulation in the transient UV/Vis experiments is a photoinduced process, transient spectra were recorded directly after pulsed excitation as a function of Laser excitation intensity. During the time integration over 200 ns possible bimolecular reactions of two pentads in the CSS1 are supposed to be negligible. Therefore, changes in the transient absorption spectra during this time interval are expected to stem from intramolecular processes. The spectra are shown in Figure 5.9a. They all exhibit the typical absorption features described above for the pentad with 0.2 M chloroacetic acid. However, when comparing the spectra of the pentad detected in presence of acid with and without time delay (Figure 5.6b and 5.7a), the spectral features of the CSS1 exhibit a less intense absorption of the TAA^+ signal 770 nm with respect to the signal at 400 nm. For the CSS2 the opposite situation is the case, due to two oxidized amines being present. Having in mind the expected quadratic power-dependency of two-photon processes, the charge-accumulated state should become more prominent at a high excitation energy, i.e. at a higher photon flux. As a result, the energy-dependent spectra shown in Figure 5.9a detected directly after excitation should reveal an increasing contribution of the second charge-separated state. This increasing contribution is expected to manifest in an increasing intensity of the TAA^+ signal at 770 nm relative to the signal at around 400 nm as a result of the different spectral signatures of the CSS1 and the CSS2. The plot of the ratio of the signal-intensity at 770 nm and 380 nm (I_{770}/I_{380}) as a function of excitation energy is shown in Figure 5.9b. It shows that with increasing amount of excitation energy the relative amount of TAA^+ signal (at 770 nm) increases. This indicates that increasing proportions of the CSS2 state indeed are formed at higher excitation powers. These increased proportions of the CSS2

are very likely a result of intramolecular charge-separation after absorption of a second photon rather than bimolecular reactions of the CSS1.

5.5. Summary

The aim of this study was the investigation of a purely molecular donor-acceptor-donor assembly with regard to its ability to undergo photoinduced charge accumulation. A central design principle for the pentad was its capability of performing charge accumulation without sacrificial agents. By coupling charge-accumulation to proton transfer reactions, the storage of two redox equivalents on the anthraquinone was expected to be facilitated. From transient IR measurements in neat acetonitrile, the formation of twofold reduced anthraquinone was confirmed, despite the fact that the final electron transfer step is associated with a weak driving force. A potential drawback in regard to experiment was the high photon flux of approximately 2200 photons per molecule that was applied in order to obtain an adequate signal-to-noise ratio. In the transient UV/Vis absorption measurements with chloroacetic acid, $AQH^{\cdot}$ is formed in the first charge-separated state (CSS1). After this CSS1 has vanished with a biexponential decay exhibiting lifetimes of 80 ns and 450 ns in aerated solution, a persisting transient absorption signal was observed. The spectral signature of this signal was attributed to the second charge-separated state (CSS2). However, the absorption features of the contribution of the anthraquinone species to the overall spectrum can not be clearly attributed to either AQH^{-} or AQH_2. In fact, a mixture of both species being present in the CSS2 was found to be very likely, based on the comparison with spectro-electrochemical measurements. The observation of both AQH_2 and AQH^{-} in the charge-accumulated state is surprising, because thermodynamic considerations point towards AQH_2 as the final photoproduct. The lifetime of this second charge-separated state was determined to longer than 100 µs. Charge recombination is a complex reaction, requiring two electron transfers and at least one bimolecular proton transfer to occur. This account for the very long lifetime of the CSS2. Additionally, bimolecular self-exchange reactions are supposed to occur quite easily on these timescales, as discussed in detail in Chapter 4 for other systems. This leads to a situation in which the reduced anthraquinone and the oxidized amine are not necessarily located on the same pentad. In principle, this very long-lived charge-separated state, formed without the need of sacrificial agents, is potentially useful for artificial photosynthesis and the formation of solar fuels. Especially when taking into account that anthraquinone is the active catalyst for the industrial production of hydrogen peroxide.

6. Summary and conclusion

The studies presented in this thesis are relevant in the context of artificial photosynthesis. An ideal molecular system would be capable to use light energy to drive efficient splitting of water and subsequently uses the liberated protons and electrons for the formation of hydrogen. The aim of this thesis was the investigation of fundamental aspects of electron transfer reactions initiated by light. This thesis focused on three major topics: (i) mechanistic studies of electron transfer reactions that are coupled to proton transfer, (ii) kinetic investigations of electron transfer reactions over large distances, and (iii) the achievement of charge accumulation in a molecular system without the need of sacrificial agents.

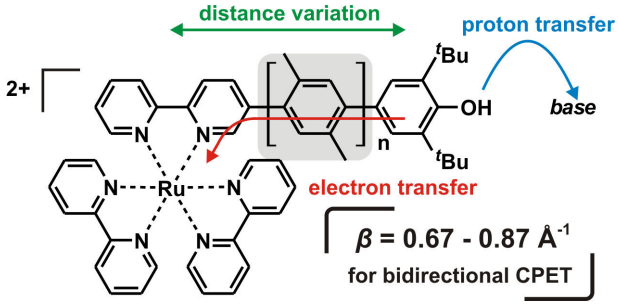

Figure 6.1 Ruthenium(II)-phenol dyads which were investigated with regard to their PCET chemistry as a function of the electron donor-acceptor distance.

In analogy to the $^{+}$P680-Tyr$_{Z}$-His$_{190}$ reaction triple in the photosystem II, two series of dyads were synthesized and investigated with respect to their proton-coupled electron transfer (PCET) chemistry. The reaction mechanisms were studied as a function of spatial separation between electron donor and acceptor. The respective dyads were comprised of either a ruthenium(II) or rhenium(I) photosensitizer which is covalently attached to a phenol, acting as combined electron and proton donor. The donor-acceptor distance was adjusted by introducing varying numbers (n = 0 - 3) of *p*-xylene spacer molecules. Figure 6.1 exemplary shows the ruthenium(II)-phenol dyads. Interestingly, for the shortest dyads, with the phenol being directly attached to the photosensitizer, photoacid behavior was observed rather than proton-coupled electron transfer (*J. Am. Chem. Soc.* **2012**, *134*, 12844; *J. Phys. Chem A* **2013**, *117*, 5726). In contrast, with increased spatial separation (n $\geq$ 1) PCET was found to be operative. Proton-coupled electron transfer in the

ruthenium(II) dyads was assigned to be a CPET, whereas it is a stepwise ET-PT mechanism for the rhenium(I) dyads. This observation demonstrates that for short distances (and therefore a strong electronic interaction between donor and acceptor) photoacid behavior needs to be considered as an alternative reaction pathway to PCET. Besides this mechanistic change-over at short distances, the first distance-decay constants (β) for bidirectional concerted proton-coupled electron transfer (CPET) were determined. These β-values were found to be 0.67 ± 0.23 $Å^{-1}$ and 0.87 ± 0.09 $Å^{-1}$ for CPET originating from the excited and oxidized photosensitizer, respectively (*Chem. Eur. J.* **2014**, *20*, 4098; *J. Phys. Chem. B* **2014**, *119*, 2263). Similar values of β along *p*-xylene bridges have already been reported for pure electron transfer.[59, 60] This observation points towards the conclusion that the overall electronic coupling matrix element for these CPET reactions is dominated by the distance-dependence of the electron transfer step. Consequently, long electron transfer distances do not hamper a concerted transfer of a proton into different directions, as might have been expected due the electrostatic attraction between these particles.

Mechanistic investigations of the PCET chemistry of thiophenols have been performed. Thiols and thiyl radicals are known to play an important role in many biochemical processes. However, detailed mechanistic studies concerning the PCET reactivity of thiophenols are comparably scarce.[67, 68] For that reason, the photoinduced oxidation of thiophenols with varying substituents was investigated in bimolecular reactions with photoexcited $Ru(bpz)_3^{2+}$ (bpz = 2,2'-bipyrazine). $Ru(bpz)_3^{2+}$ acted as a combined electron and proton acceptor. Dependent on the substituents of the thiophenols, all three possible mechanisms for PCET were observed *(J. Phys. Chem. Lett.* **2013**, *4*, 2535). This demonstrates that the whole mechanistic diversity, intensively studied on phenols, is also applicable for the PCET chemistry of thiophenols.

In a second project, the kinetics of thermal charge recombination were investigated in three sets of linear triads. These triads were comprised of a ruthenium(II) photosensitizer, a triarylamine (TAA) electron donor, and anthraquinone (AQ) as an electron acceptor as shown in Figure 6.2. The spatial separation between the donor and acceptor was adjusted by the introduction of 1 - 3 *p*-xylene spacer molecules on each side. This results in electron transfer distances for charge recombination ranging from 22.0 Å to 39.2 Å. Additionally, the substituents on the triarylamine donor were varied for driving force-dependent investigations.

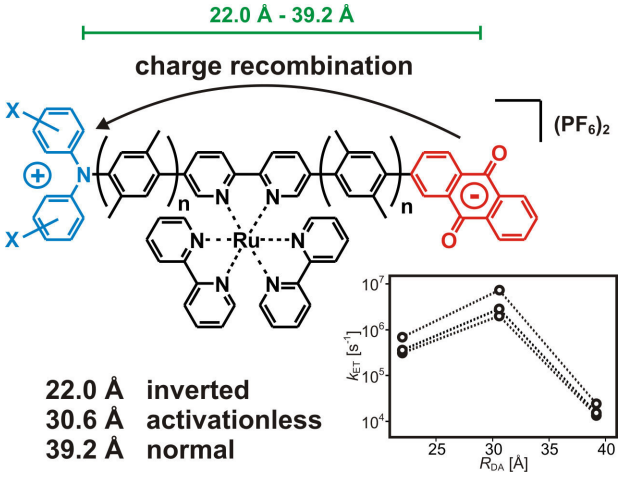

Figure 6.2 Linear triads investigated with regard to their thermal charge recombination kinetics as a function of the donor-acceptor distance.

The kinetics for the thermal charge recombination as a function of spatial separation between donor and acceptor revealed a maximum in rate constants for large distances. Such counter-intuitive behavior was first postulated by SUTIN and coworkers in the 1980s, in accordance with the Marcus theory.[72] They calculated the rate constants for a highly exergonic system (which is operative in the MARCUS inverted region) as a function of donor-acceptor distance. As a result, they were able to demonstrate by theory that such a system should exhibit increasing rate constants until a certain critical distance at which the rate maximizes. A further increase of the donor-acceptor distance should then lead to an exponential decrease in rate constants, as regularly observed for electron transfer (ET) reactions in the MARCUS normal region. SUTIN and coworkers attributed this behavior to an opposing interplay between an increasing outer-sphere reorganization energy and a decreasing electronic coupling by increasing the donor-acceptor distance. To the best of our knowledge the study presented in this thesis provides the first unambiguous experimental evidence for this unusual behavior of electron transfer rates. In the shortest triads, the lifetimes of the charge-separated states were on the order of a few microseconds. In contrast, the systems of intermediate length exhibited lifetimes of only several hundred nanoseconds. Thus, the factor of ET rate acceleration ranges from 6 to 10. A further increase of spatial separation between TAA and AQ yielded lifetimes between 41 µs and 75 µs. In addition to the rate constants, the activation barriers and reorganization energies for all triads were determined. These studies lead to the conclusion that the shortest triads undergo thermal back electron transfer in the MARCUS inverted region. In contrast, the intermediate triads recombine in an activationless manner, whereas the longest systems operate in the normal region. This change-over can be clearly attributed to a significant increase in the outer-sphere reorganization energy with increasing distance. These results are not only of academic interest. In fact, this observation is of vital importance for

bimolecular photoinduced electron transfer reactions. The charge separation process of such systems is usually associated with small reaction free energies, i.e. electron transfer occurs in the normal region. On the other hand, (undesired) thermal charge recombination processes often take place in the inverted region. For the forward reaction the donor and acceptor need to be in close contact to each other for an efficient electron transfer process to occur. However, after formation of the charge-separated state the photoproducts must diffuse away from each other. When doing so, the reaction couple passes a region where the undesired back electron transfer is activationless and therefore can become faster than at close contact. This can seriously limit the quantum efficiency of the conversion of light into chemical energy. In this context, long-living charge-separated states are pivotal for efficient charge accumulation and catalytic turnovers. Therefore, the spatial separation between donor and acceptor needs to be thoroughly adjusted, particularly in molecular systems designed for artificial photosynthesis.

Another important observation from these kinetic measurements concerns the importance of considering the reorganization energy for driving force-dependent measurements. The three shortest triads, bearing different substituents on the triarylamine donors, are undergoing charge recombination in the inverted region. However, the expected effect of slower rate constants with increasing driving force was not observed. In fact, the opposite holds true, i.e. an increase of the rate constants at higher driving forces. A meaningful correlation with the expected behavior was found when the ratio of $-\Delta G/\lambda$ was considered. This observation, although not new, underscores the significance of the reorganization energy when performing driving-force dependency studies. In particular, for driving force-dependent measurements conducted by merely altering the solvent polarity, changes of the reorganization can not be neglected.

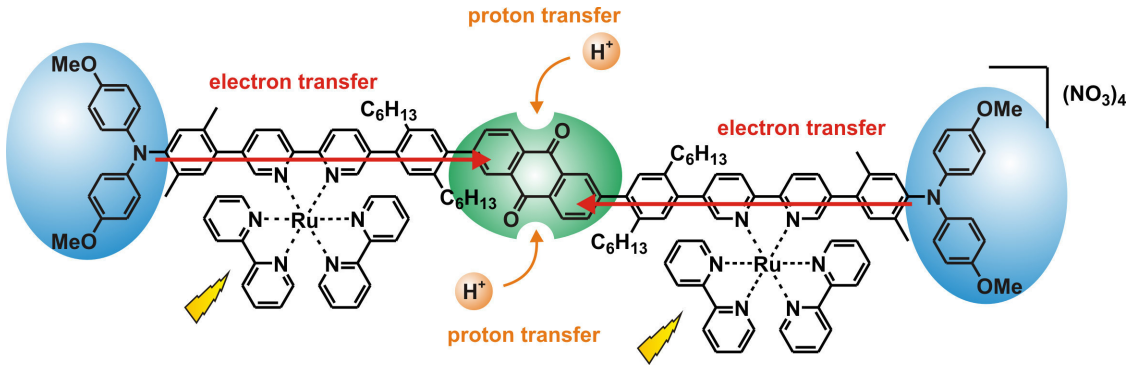

Figure 6.3 Molecular pentad studied with respect to its ability to perform photoinduced charge accumulation on the central anthraquinone.

The aim of the third project of this thesis was the synthesis of a purely molecular binuclear donor-acceptor-donor assembly as shown in Figure 6.3. This compound based on

the triads which are mentioned above and was extended to a molecular pentad. A central anthraquinone acting as a potential two-electron and two-proton acceptor was employed. Two end-on triarylamines were introduced as one-electron donors in combination with two ruthenium(II) photosensitizers. This pentad was investigated with regard to its capability of photoinduced charge-accumulation. An important design principle for the pentad was its ability to perform charge accumulation without sacrificial electron donors. By coupling the photoinduced charge-accumulation process to proton transfer reactions, the storage of two redox equivalents on an anthraquinone unit was expected to be facilitated. Using transient IR spectroscopy the formation of twofold reduced anthraquinone in neat acetonitrile was confirmed upon excitation with visible light. A lifetime of at least 60 ns was extracted for the second charge-separated state from these measurements in absence of acid. A potential drawback, with regard to this observation, is the high photon flux of approximately 2200 photons per molecule that was applied in order to obtain an adequate signal-to-noise ratio. Additionally, the last electron transfer step to form AQ^{2-} exhibits only weak driving forces in neat acetonitrile. In transient UV/Vis absorption experiments performed in presence of chloroacetic acid, the first charge-separated state (CSS1) is associated with the formation of $AQH^{\cdot}$. Once this CSS1 has decayed after a few hundred nanoseconds, a persisting transient absorption signal was detected. The spectral signature of this signal is compatible with the second charge-separated state (CSS2). The absorption features of the contribution of the reduced anthraquinone species to the overall spectrum of the CSS2 was attributed to a mixture of AQH_2 and AQH^-. This observation is somewhat surprising, since thermodynamic considerations clearly point towards AQH_2 as the final most stable photoproduct. Interestingly, the transient absorption signal for the charge-accumulated state exhibits a lifetime of at least 100 µs.

The pentad presented here fulfills the requirements for potential applications in the field of artificial photosynthesis. Upon excitation with visible light, formation of a long-lived charge-accumulated state was achieved without the use of sacrificial agents. Long-lived charge-separated states, generated without high-energy sacrificial agents, are potentially useful for artificial photosynthesis and the formation of solar fuels. In this context, the observed photoproducts in this study, AQH_2 and AQH^-, are equal to a formal storage of a hydride or hydrogen, respectively. Taking into account that anthrahydroquinone is used in industrial processes for the production of hydrogen peroxide, the results of this study might become even more relevant.

7. Experimental section

7.1. Analytical methods

The analytical methods given below were employed for the studies described in Chapter 4 and Chapter 5. The methods applied for the studies from Chapter 3 are described separately in each publication.

general methods

All commercially available chemicals used for synthesis were purchased from common suppliers (Sigma-Aldrich, ABCR, Fluorochem, Acros, Alfa Aesar) and were used without further purification. Dry diethyl ether, THF and dichloromethane were obtained from a solvent purification system of Innovative Technology. Dry toluene was purchased from Sigma-Aldrich (crown cap, over molecular sieve). Acetonitrile for spectroscopic measurements was bought from Sigma-Aldrich (anhydrous, crown cap) or from Macron (HPLC grade). Deuterated solvents for NMR spectroscopy were purchased from Cambridge Isotope Laboratories. Thin layer chromatography was performed on silica plates from Merck (60 F254). Column chromatography was performed on silica gel (40-63 μm, silicycle) or on C18-reversed phase silica gel (90 Å pore size, Sigma-Aldrich). All quoted temperatures in the synthetic protocols are oil bath temperatures.

NMR spectroscopy

^{1}H NMR spectra were recorded on a 400 MHz Bruker Avance III instrument. All chemical shifts (δ) are given in ppm and were referenced to the proton residue signal of the deuterated solvents. Coupling constants are listed in Hz and the multiplicity is stated as follows: singlet (s), broad singlet (s_{br}), doublet (d), doublet of doublet (dd), doublet of doublet of doublet (ddd), triplet (t), doublet of triplet (dt), triplet of doublet (td), quartet (q), multiplet (m).

Mass spectrometry

ESI mass spectra were measured on a Bruker Esquire 3000plus Ion-trap ESI-MS. High resolution mass spectra were recorded on a Bruker maXis 4G QTOF ESI spectrometer.

Elemental analysis

Elemental analyses were performed by Ms. Sylvie Mittelheisser (Department of Chemistry at the University of Basel) with a Vario Micro Cube from Elementar.

UV-Vis spectroscopy

All UV-Vis spectra were recorded on a Cary 5000 UV-Vis-NIR spectrophotometer.

Cyclic voltammetry

Cyclic voltammograms and chronoamperometric experiments for spectro-electrochemical measurements were performed with a VersaStat3-200 potentiostat from Princeton Applied Research. Measurements were performed in dry, deoxygenated acetonitrile or acetonitrile/water mixtures with either tetrabutylammonium hexafluorophosphate ($TBAPF_6$) or KCl as supporting electrolyte. The setup for cyclic voltammetry was comprised of a glassy carbon disc serving as working electrode, a silver wire as counter electrode and an SCE reference electrode. For spectro-electrochemical experiments a quartz cuvette equipped with a platinum grid as working electrode, a platinum counter electrode and a SCE reference electrode was used.

Transient UV/Vis absorption spectroscopy

Transient absorption measurements were performed with a LP920-KS spectrometer from Edinburgh Instruments, equipped with an R928 photomultiplier or an NIR 301/2 (InGaAs) detector (900-1700 nm, 100 ns response time) or an iCCD camera from Andor. A frequency-doubled Quantel Brilliant b laser was used as excitation source. The duration of the laser excitation pulse was approximately 10 ns. Quartz cuvettes from Starna were used for all optical measurement. For deoxygenated measurements, Schlenk-cuvettes were used, and the solutions were subjected to four freeze-pump-thaw cycles.

Transient IR spectroscopy

The system for UV-pump-IR-probe spectroscopy consisted of two synchronized commercially available Ti:sapphire-oscillator/regenerative amplifier femtosecond laser systems operating at 843 nm and 800 nm (Spectra Physics; duration ∼100 fs; repetition rate 1 kHz; energy ∼600 µJ/pulse). The setup allows to cover a time range from 2 ps to 42 µs. Laser system 1 was frequency-doubled with a barium borate (BBO) crystal. The obtained 420 nm pulses were subsequently focused into the sample cell (50 µm thick) with a spot size of ∼200 µm diameter. Laser system 2 pumped a white-light-seeded two-stage BBO optical parametric amplifier (OPA), the signal and idler pulses of which were difference-frequency mixed in a AgGaS2 crystal. They were separated into two parts to achieve broad-band probe and reference pulses. These IR-probe pulses were focused into the sample cell in spatial overlap with the 420 nm pump pulse. The reference and probe pulses were dispersed in a monochromator (SPEX Triax Series) and imaged onto a 2 × 64 pixel MCT (Mercury Cadmium Telluride) detector array (InfraRed Associates Inc.), revealing a spectral resolution of 3.5 cm^{-1}. To ensure efficient exchange of the excited volume, the sample was pumped rapidly by a tubing pump (Ismatec BVP equipped with EasyLoad II pump-head, flow ∼5.0 mL/min). The concentration of the samples in CD_3CN is 1 mM, and the solution was purged with argon continuously.

This paragraph was kindly provided by Margherita Orazietti (group of Prof. Dr. Peter Hamm, University of Zurich).

7.2. Synthesis of anisyl-xy$_n$, veratryl-xy$_n$ and tolyl-xy$_n$

The triad anisyl-xy$_1$ was available in our lab from previous studies.[81] The synthetic route to obtain the ligands **32**-**39** for the other triads is shown in Schemes 7.1, 7.2 and 7.3.

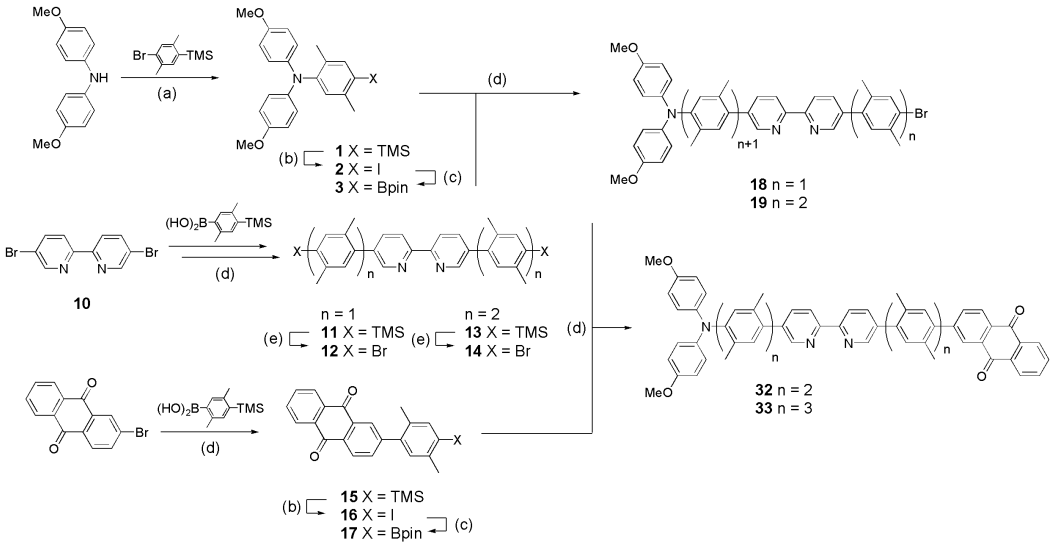

Scheme 7.1 Reaction scheme for the synthesis of the donor-acceptor ligands **32** and **33** for anisyl-xy$_2$ and anisyl-xy$_3$. (a) Pd(dba)$_2$, (HP^{t}Bu$_3$)BF$_4$, KO^{t}Bu in toluene; (b) ICl in CH_2Cl_2; (c) (Bpin)$_2$, KOAc, Pd(PPh$_3$)$_2$Cl$_2$ in DMSO; (d) Pd(PPh$_3$)$_4$, Na_2CO_3 in THF/water; (e) Br_2, NaOAc in THF.

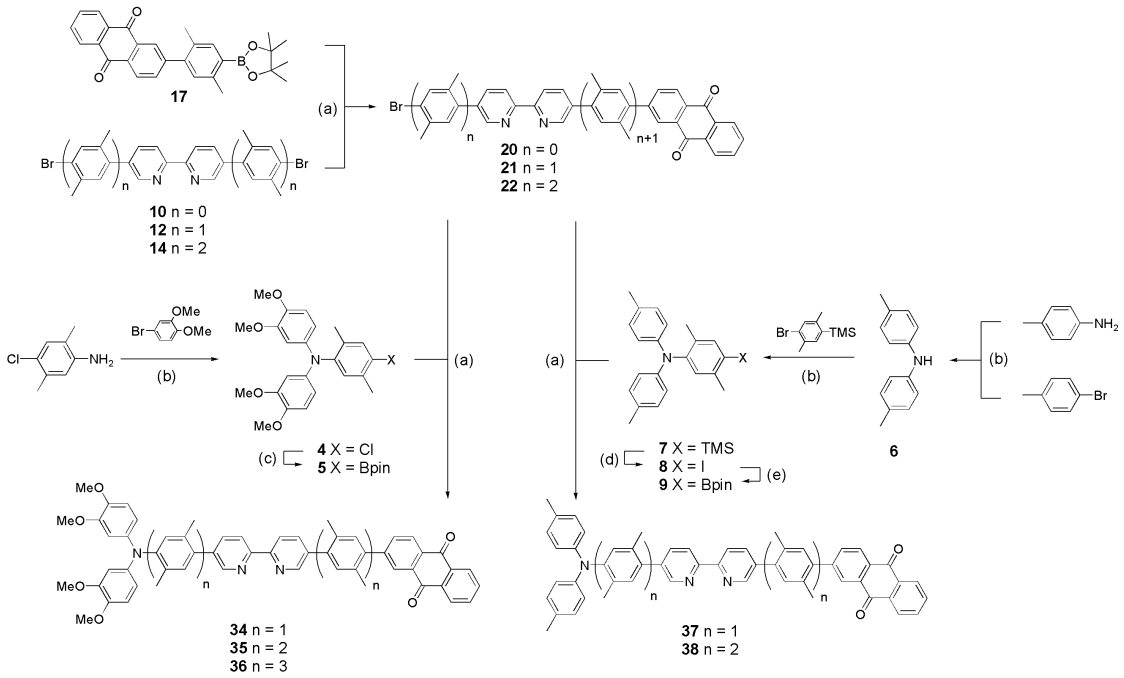

Scheme 7.2 Reaction scheme for the synthesis of the donor-acceptor ligands **34-38** for veratryl-$xy_{1\text{-}3}$ and tolyl-$xy_{1\text{-}2}$. (a) $Pd(PPh_3)_4$, Na_2CO_3 in THF/water; (b) $Pd(dba)_2$, KO^tBu, $(HP^tBu3)BF_4$ in toluene; (c) $(Bpin)_2$, $Pd(dba)_2$, PCy_3, KOAc in 1,4-dioxane; (d) ICl in CH_2Cl_2; (e) $(Bpin)_2$, KOAc, $Pd(PPh_3)_2Cl_2$ in DMSO.

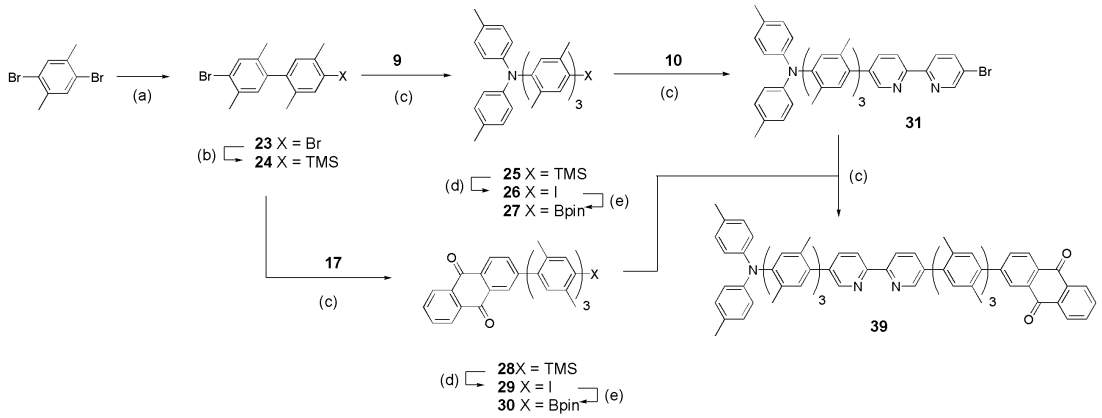

Scheme 7.3 Reaction scheme for the synthesis of the donor-acceptor ligand **39** for tolyl-xy_3. (a) *n*-BuLi, CuCN, duroquinone in THF at -78°C; (b) *n*-BuLi, TMSCl in THF at -78°C; (c) $Pd(PPh_3)_4$, Na_2CO_3 in THF/water; (d) ICl in CH_2Cl_2; (e) $(Bpin)_2$, KOAc, $Pd(PPh_3)_2Cl_2$ in DMSO.

Synthetic protocols

1: Bis(*p*-anisyl)amine (1.15 g, 5.00 mmol), 2-bromo-5-trimethylsilyl-*p*-xylene[110] (1.41 g, 5.50 mmol), $Pd(dba)_2$ (144 mg, 0.25 mmol), $HP^tBu_3BF_4$ (73 mg, 0.25 mmol) and KO^tBu (1.68 g, 15.0 mmol) in dry toluene (25 mL) were degassed prior to stirring at 90 °C over

night. Water (100 mL) was added and the mixture was extracted with dichloromethane. The combined organic layers were dried over Na_2SO_4, filtered and the solvent was removed in vacuo. The crude product was purified by column chromatography on silica using pentane/diethyl ether 5:1 (v:v) as an eluent to yield **1** as a white solid (1.67 g, 4.12 mmol, 82%). ^{1}H-NMR (400 MHz, $CDCl_3$): δ (ppm) = 7.22 (s, 1 H), 6.88 – 6.84 (m, 4 H), 6.80 (s, 1 H), 6.78 – 6.74 (m, 4 H), 3.77 (s, 6 H), 2.31 (s, 3 H), 1.95 (s, 3 H), 0.32 (s, 9 H).

2: A solution of **1** (1.67 g, 4.12 mmol) in dry dichloromethane (30 mL) was cooled to -78 °C prior to addition of a solution of iodine monochloride (1.34 g, 8.24 mmol) in dry dichloromethane (10 mL). The resulting mixture was stirred for 10 minutes and a saturated aqueous solution of $Na_2S_2O_3$ was added. The layers were separated and the aqueous layer was extracted with dichloromethane. The combined organic layers were dried over Na_2SO_4, filtered, and the solvent was removed in vacuo. The crude product was purified by column chromatography on silica using pentane/diethyl ether 5:1 (v:v) as an eluent to yield **2** as a white solid (1.87 g, 4.07 mmol, 99%). ^{1}H-NMR (400 MHz, CD_2Cl_2): δ (ppm) = 7.64 (s, 1 H), 6.90 (s, 1 H), 6.85 – 6.79 (m, 4 H), 6.78 – 6.73 (m, 4 H), 3.75 (s, 6 H), 2.28 (s, 3 H), 1.91 (s, 3 H).

3: A mixture of **2** (1.87 g, 4.07 mmol), bis(pinacol)diboron (1.55 g, 6.11 mmol), KOAc (1.60 g, 16.3 mmol) and $Pd(PPh_3)_2Cl_2$ (143 mg, 0.2 mmol) in DMSO (20 mL) was degassed and stirred at 90 °C over night. After cooling to room temperature, the reaction mixture was treated with water (60 mL) and saturated aqueous NH_4Cl-solution (20 mL), and the aqueous phase was extracted with diethyl ether. The combined organic layers were dried over Na_2SO_4, filtered, and the solvent was removed in vacuo. The crude product was purified by column chromatography on silica using pentane/diethyl ether 9:1 (v:v) as an eluent to yield **3** as a white solid (1.72 g, 3.74 mmol, 92%). ^{1}H-NMR (400 MHz, CD_2Cl_2): δ (ppm) = 7.54 (s, 1 H), 6.84 -6.79 (m, 4 H), 6.79 (s, 1 H), 6.77 -6.73 (m, 4 H), 3.75 (s, 6 H), 2.37 (s, 3 H), 1.92 (s, 3 H), 1.32 (s, 12 H).

4: 4-Chloro-2,5-dimethylaniline (1.56 g, 10.0 mmol), 4-bromo-veratryl (4.77 g, 22.0 mmol), $Pd(dba)_2$ (288 mg, 0.50 mmol), $HP^tBu_3BF_4$ (145 mg, 0.50 mmol) and KO^tBu (3.37 g, 30.0 mmol) in dry toluene (30 mL) were degassed prior to stirring at 90 °C over night. Water (150 mL) was added and the mixture was extracted with dichloromethane. The combined organic layers were dried over Na_2SO_4, filtered, and the solvent was removed in vacuo. The crude product was purified by column chromatography on silica using pentane/diethyl ether 1:1 (v:v) as an eluent to yield **4** as a beige solid (2.84 g, 6.64 mmol, 66%). 1H-NMR (400 MHz, acetone-d_6): δ (ppm) = 7.24 (s, 1 H), 6.99 (s, 1 H), 6.82 (d,

J = 8.6 Hz, 2 H), 6.61 (d, J = 2.5 Hz, 2 H), 6.34 (dd, J = 8.6, 2.5 Hz, 2 H), 3.76 (s, 6 H), 3.65 (s, 6 H), 2.24 (s, 3 H), 1.98 (s, 3 H).

5: A mixture of **4** (856 mg, 2.00 mmol), bis(pinacol)diboron (609 mg, 2.40 mmol), KOAc (393 mg, 4.00 mmol), Pcy_3 (67 mg, 0.24 mmol) and $Pd(dba)_2$ (58 mg, 0.10 mmol) in 1,4-dioxane (15 mL) was degassed and stirred at 80 °C for 24 h. After cooling to room temperature the reaction mixture was treated with water (60 mL) and saturated aqueous NH_4Cl-solution (20 mL), and the aqueous phase was extracted with dichloromethane. The combined organic layers were dried over Na_2SO_4, filtered, and the solvent was removed in vacuo. The crude product was purified by column chromatography on silica using pentane/diethyl ether 1:1 (v:v) as an eluent to yield a white solid (1.00 g). NMR-analysis confirmed that the obtained product consisted of a 3:1 mixture of **5** (≈800 mg, 1.50 mmol, 75%) and de-chlorinated starting material. A purification from the side product failed, and therefore the mixture was used for further coupling reactions. ^{1}H-NMR (**9**, 400 MHz, acetone-d_6): δ (ppm) = 7.56 (s, 1 H), 6.83 – 6.80 (m, 3 H), 6.61 (d, J = 2.6 Hz, 2 H), 6.35 (dd, J = 8.6, 2.6 Hz, 2 H), 3.76 (s, 6 H), 3.65 (s, 6 H), 2.38 (s, 3 H), 1.95 (s, 3 H), 1.34 (s, 12 H).

6: A mixture of 4-methylaniline (1.07 g, 10.0 mmol), 4-bromo-toluene (1.88 g, 11.0 mmol), $Pd(dba)_2$ (288 mg, 0.50 mmol), $HP^tBu_3BF_4$ (145 mg, 0.50 mmol) and KO^tBu (3.37 g, 30.0 mmol) in dry toluene (30 mL) was degassed prior to stirring at 90 °C over night. Water (100 mL) was added and the mixture was acidified with delute HCl followed by extraction with dichloromethane. The combined organic layers were dried over Na_2SO_4, filtered, and the solvent was removed in vacuo. The crude product was purified by column chromatography on silica using pentane/diethyl ether 5:1 (v:v) as an eluent to yield **6** as a beige solid (1.64 g, 8.33 mmol, 83%). ^{1}H-NMR (400 MHz, CD_2Cl_2): δ (ppm) = 7.08 – 7.03 (m, 4 H), 6.95 – 6.91 (m, 4 H), 5.60 (s_{br}, 1 H), 2.27 (s, 6 H).

7: A mixture of **6** (1.64 g, 8.33 mmol), 2-bromo-5-trimethylsilyl-*p*-xylene[110] (2.36 g, 9.16 mmol), $Pd(dba)_2$ (239 mg, $4.16 \cdot 10^{-4}$ mol), $HP^tBu_3BF_4$ (121 mg, $4.16 \cdot 10^{-4}$ mol) and KO^tBu (2.80 g, 25.0 mmol) in dry toluene (30 mL) were degassed prior to stirring at 90 °C over night. Water (100 mL) was added and the mixture was extracted with dichloromethane. The combined organic layers were dried over Na_2SO_4, filtered, and the solvent was removed in vacuo. The crude product was purified by column chromatography on silica using pentane/diethyl ether 10:1 (v:v) as an eluent to yield **7** as a white solid (2.34 g, 6.28 mmol, 75%). ^{1}H-NMR (400 MHz, acetone-d_6): δ (ppm) = 7.32 (s, 1 H), 7.06 – 7.01 (m, 4 H), 6.84 (s, 1 H), 6.80 – 6.76 (m, 4 H), 2.34 (s, 3 H), 2.25 (s, 6 H), 1.95 (s, 3 H), 0.32 (s, 9 H).

8: A solution of **7** (2.34 g, 6.28 mmol) in dry dichloromethane (30 mL) was cooled to -78 °C prior to addition of a solution of iodine monochloride (2.04 g, 12.6 mmol) in dry dichloromethane (10 mL). The resulting mixture was stirred for 10 minutes and a saturated aqueous solution of $Na_2S_2O_3$ was added. The layers were separated and the aqueous layer was extracted with dichloromethane. The combined organic layers were dried over Na_2SO_4, filtered, and the solvent was removed in vacuo. The crude product was purified by column chromatography on silica using pentane/diethyl ether 5:1 (v:v) as an eluent to yield **8** as a white solid (2.54 g, 5.94 mmol, 95%). ^{1}H-NMR (400 MHz, acetone-d_6): δ (ppm) = 7.72 (s, 1 H), 7.07 – 7.02 (m, 4 H), 6.99 (s, 1 H), 6.81 – 6.77 (m, 4 H), 2.30 (s, 3 H), 2.25 (s, 6 H), 1.93 (s, 3 H).

9: A mixture of **8** (2.56 g, 6.00 mmol), bis(pinacol)diboron (2.28 g, 9.00 mmol), KOAc (2.36 g, 24.0 mmol) and $Pd(PPh_3)_2Cl_2$ (211 mg, 0.30 mmol) in DMSO (30 mL) was degassed and stirred at 90 °C over night. After cooling to room temperature the reaction mixture was treated with water (100 mL) and saturated aqueous NH_4Cl-solution (20 mL), and the aqueous phase was extracted with dichloromethane. The combined organic layers were dried over Na_2SO_4, filtered, and the solvent was removed in vacuo. The crude product was purified by column chromatography on silica using pentane/diethyl ether 10:1 (v:v) as an eluent to yield **9** as a white solid (1.84 g, 4.30 mmol, 72%). ^{1}H-NMR (400 MHz, acetone-d_6): δ (ppm) = 7.59 (s, 1 H), 7.06 – 7.02 (m, 4 H), 6.83 (s, 1 H), 6.81 – 6.77 (m, 4 H), 2.39 (s, 3 H), 2.26 (s, 6 H), 1.93 (s, 3 H), 1.35 (s, 12 H).

11: A biphasic mixture of 5,5'-dibromo-2,2'-bipyridine[111] (**10**, 1.90 g, 6.05 mmol), 2,5-dimethyl-4-trimethylsilyl-1-phenylboronic acid[110] (3.22 g, 14.5 mmol), Na_2CO_3 (3.85 g, 36.3 mmol) and $Pd(PPh_3)_4$ (699 mg, 0.61 mmol) in THF (40 mL) and water (15 ml) was degassed prior to heating to reflux over night. After cooling to room temperature, the reaction mixture was extracted with dichloromethane. The combined organic layers were dried over Na_2SO_4, filtered, and the solvent was removed in vacuo. The crude product was dissolved in a minimum amount of dichloromethane and poured into pentane. The precipitate was filtered and dried, yielding **11** as an off-white solid (2.33 g, 4.58 mmol, 76%). ^{1}H-NMR (400 MHz, CD_2Cl_2): δ (ppm) = 8.65 (dd, J = 2.3, 0.9 Hz, 2 H), 8.52 (d, J = 8.1 Hz, 2 H), 7.82 (dd, J = 8.1, 2.3 Hz, 2 H), 7.40 (s, 2 H), 7.11 (s, 2 H), 2.48 (s, 6 H), 2.31 (s, 6 H), 0.37 (s, 18 H).

12: To a suspension of **11** (2.42 g, 4.63 mmol) and NaOAc (760 mg, 9.26 mmol) in dry

THF (50 mL) was added bromine (0.95 mL, 18.5 mmol). The reaction mixture was stirred for 4 h at room temperature under exclusion of light. Subsequently, triethylamine (5.13 mL, 37.0 mmol) and a saturated aqueous solution of $Na_2S_2O_3$ were added. The mixture was extracted with dichloromethane. The combined organic layers were dried over Na_2SO_4, filtered, and the solvent was removed in vacuo. The crude product was dissolved in a minimum amount of dichloromethane and poured into pentane. The precipitate was filtered and dried, yielding **12** as a beige solid (2.42 g, 4.63 mmol, ∼100%). ^{1}H-NMR (400 MHz,CD_2Cl_2): δ (ppm) = 8.63 (dd, J = 2.3, 0.9 Hz, 2 H), 8.52 (dd, J = 8.2, 0.9 Hz, 2 H), 7.80 (dd, J = 8.2, 2.3 Hz, 2 H), 7.52 (s, 2 H), 7.18 (s, 2 H), 2.42 (s, 6 H), 2.28 (s, 6 H).

13: A biphasic mixture of **12** (1.57 g, 3.00 mmol), 2,5-dimethyl-4-trimethylsilyl-phenylboronic acid[110] (1.60 g, 7.20 mmol), Na_2CO_3 (1.90 g, 18.0 mmol) and $Pd(PPh_3)_4$ (347 mg, 0.30 mmol) in THF (40 mL) and water (15 ml) was degassed prior to heating to reflux for 3 days. After cooling to room temperature, the reaction mixture was extracted with dichloromethane. The combined organic layers were dried over Na_2SO_4, filtered, and the solvent was removed in vacuo. The crude product was suspended in diethyl ether (30 mL) and sonicated. The solid was filtered off and subjected to column chromatography (SiO_2) using dichloromethane as an eluent. **13** was obtained as a beige solid (1.99 g, 2.78 mmol, 92%). ^{1}H-NMR (400 MHz, CD_2Cl_2): δ (ppm) = 8.73 (dd, J = 2.3, 0.9 Hz, 2H), 8.55 (dd, J = 8.1, 0.8 Hz, 2 H), 7.89 (dd, J = 8.1, 2.3 Hz, 2 H), 7.37 (s, 2 H), 7.22 (s, 2 H), 7.05 (s, 2 H), 6.94 (s, 2 H), 2.45 (s, 6H), 2.33 (s, 6 H), 2.09 (s, 12 H), 0.37 (S, 18 H).

14: To a suspension of **13** (1.95 g, 2.72 mmol) and NaOAc (446 mg, 5.44 mmol) in dry THF (30 mL) was added bromine (0.56 mL, 10.9 mmol). The reaction mixture was stirred for 4 h at room temperature under exclusion of light. Subsequently triethylamine (3.02 mL, 21.8 mmol) and a saturated aqueous solution of $Na_2S_2O_3$ were added. The mixture was extracted with dichloromethane. The combined organic layers were dried over Na_2SO_4, filtered, and the solvent was removed in vacuo. The crude product was dissolved in hot diethyl ether (25 mL) and pentane (40 mL) was added. The mixture was kept in the refrigerator over night, and subsequently the precipitate was filtered and dried, yielding **14** as a beige solid (1.52 g, 2.08 mmol, 77%). ^{1}H-NMR (400 MHz, CD_2Cl_2): δ (ppm) = 8.72 (dd, J = 2.3, 0.9 Hz, 2 H), 8.55 (dd, J = 8.2, 0.9 Hz, 2H), 7.88 (dd, J = 8.1, 2.3 Hz, 2 H), 7.48 (s, 2 H), 7.22 (s, 2 H), 7.04 (s, 2 H), 7.03 (s, 2 H), 2.39 (s, 6 H), 2.33 (S, 6 H), 2.08 (s, 6 H), 2.07 (s, 6 H).

15: A biphasic mixture of 2-bromoanthraquinone (4.31 g, 15.0 mmol), 2,5-dimethyl-4-trimethylsilyl-1-phenylboronic acid[110] (4.00 g, 18.0 mmol), Na_2CO_3 (4.77 g, 45.0 mmol)

and $Pd(PPh_3)_4$ (867 mg, 0.75 mmol) in THF (60 mL) and water (15 ml) was degassed prior to heating to reflux over night. After cooling to room temperature, the reaction mixture was extracted with dichloromethane. The combined organic layers were dried over Na_2SO_4, filtered, and the solvent was removed in vacuo. The crude product was purified by column chromatography on silica using pentane/dichloromethane 2:1 (v:v) as an eluent to yield **15** as a yellow solid (5.66 g, 14.7 mmol, 98%). ^{1}H-NMR (400 MHz, $CDCl_3$): δ (ppm) = 8.38 – 8.29 (m, 4 H), 7.85 – 7.75 (m, 3 H), 7.40 (s, 1 H), 7.11 (s, 1 H), 2.48 (s, 3 H), 2.30 (s, 3 H), 0.37 (s, 9 H).

16: To a solution of **15** (5.66 g, 14.7 mmol) in dry dichloromethane (60 mL) was added a solution of iodine monochloride (3.58 g, 22.1 mmol) in dry dichloromethane (10 mL) and the reaction mixture was stirred for 1 h at room temperature. A saturated aqueous solution of $Na_2S_2O_3$ was added, the layers were separated. The aqueous phase was extracted with dichloromethane. The combined organic layers were dried over Na_2SO_4, filtered, and the solvent was removed in vacuo. The crude product was purified by column chromatography on silica using pentane/dichloromethane 1:1 (v:v) as an eluent to yield **16** as a yellow solid (5.23 g, 11.9 mmol, 81%). ^{1}H-NMR (400 MHz, $CDCl_3$): δ (ppm) = 8.38 – 8.30 (m, 3 H), 8.25 (d, J = 1.8 Hz, 1H), 7.85 - 7.80 (m, 2 H), 7.78 (s, 1 H), 7.73 (dd, J = 7.9, 1.8 Hz, 1H), 7.14 (s, 1H), 2.45 (s, 3 H), 2.23 (s, 3H).

17: A mixture of **16** (2.19 g, 5.00 mmol), bis(pinacol)diboron (1.90 g, 7.50 mmol), KOAc (1.960 g, 20.0 mmol) and $Pd(PPh_3)_2Cl_2$ (175 mg, 0.25 mmol) in DMSO (30 mL) was degassed and stirred at 90 °C over night. After cooling to room temperature, the reaction mixture was treated with water (100 mL) and saturated aqueous NH_4Cl-solution (20 mL), and the aqueous phase was extracted with diethyl ether. The combined organic layers were dried over Na_2SO_4, filtered, and the solvent was removed in vacuo. The crude product was purified by column chromatography on silica using pentane/diethyl ether 4:1 (v:v) as an eluent to yield **17** as a yellow solid (1.99 g, 4.55 mmol, 91%). ^{1}H-NMR (400 MHz, $CDCl_3$): δ (ppm) = 8.38 – 8.31 (m, 3 H), 8.28 (d, J = 1.8 Hz, 1 H), 7.85 - 7.79 (m, 2 H), 7.76 (dd, J = 8.0, 1.8 Hz, 1 H), 7.72 (s, 1 H), 7.11 (s, 1 H), 2.56 (s, 3 H), 2.28 (s, 3 H), 1.37 (s, 12 H).

18: A biphasic mixture of **12** (522 mg, 1.00 mmol), **3** (306 mg, $6.67 \cdot 10^{-4}$ mol), Na_2CO_3 (212 mg, 2.00 mmol) and $Pd(PPh_3)_4$ (39 mg, $3.34 \cdot 10^{-5}$ mol) in THF (20 mL) and water (4 ml) was degassed prior to heating to reflux over night. After cooling to room temperature, the reaction mixture was extracted with dichloromethane. The combined organic layers were dried over Na_2SO_4, filtered, and the solvent was removed in vacuo. The crude product was purified by column chromatography on silica using pentane/diethyl

ether 5:1 (v:v) with 2% triethylamine as an eluent to yield **18** as a white solid (264 mg, $3.41 \cdot 10^{-4}$ mol, 51%). ^{1}H-NMR (400 MHz, CD_2Cl_2): δ (ppm) = 8.73 (dd, J = 2.3, 0.8 Hz, 1 H), 8.64 (dd, J = 2.3, 0.8 Hz, 1 H), 8.55 (t, J = 0.8 Hz, 1 H), 8.53 (t, J = 0.8 Hz, 1 H), 7.89 (dd, J = 8.1, 2.3 Hz, 1 H), 7.81 (dd, J = 8.2, 2.3 Hz, 1 H), 7.52 (s, 1 H), 7.22 (s, 1 H), 7.20 (s, 1 H), 7.11 (s, 1 H), 6.98 (s, 1 H), 6.97 (s, 1 H), 6.82 – 6.77 (m, 4 H), 3.77 (s, 6 H), 2.42 (s, 3 H), 2.34 (s, 3 H), 2.29 (s, 3 H), 2.14 (s, 3 H), 2.01 (s, 6 H).

19: A biphasic mixture of **14** (731 mg, 1.00 mmol), **3** (306 mg, $6.67 \cdot 10^{-4}$ mol), Na_2CO_3 (212 mg, 2.00 mmol) and $Pd(PPh_3)_4$ (39 mg, $3.34 \cdot 10^{-5}$ mol) in THF (25 mL) and water (5 ml) was degassed prior to heating to reflux over night. After cooling to room temperature, the reaction mixture was extracted with dichloromethane. The combined organic layers were dried over Na_2SO_4, filtered, and the solvent was removed in vacuo. The crude product was purified by column chromatography on silica using a gradient of pentane/diethyl ether starting from 5:1 (v:v) to 2:1 (v:v) each with 2% triethylamine as an eluent, yielding **19** as a white solid (251 mg, $2.55 \cdot 10^{-4}$ mol, 38%). ^{1}H-NMR (400 MHz, CD_2Cl_2): δ (ppm) = 8.74 (ddd, J = 8.7, 2.3, 0.9 Hz, 2 H), 8.57 (dd, J = 8.1, 0.9 Hz, 2 H), 7.90 (td, J = 8.4, 2.3 Hz, 2 H), 7.48 (s, 1 H), 7.25 (s, 1 H), 7.23 (s, 1 H), 7.15 (s_{br}, 1 H), 7.09 – 7.00 (m, 5 H), 6.97 (s, 1 H), 6.94 – 6.89 (m, 4 H), 6.82 -6.78 (m, 4 H), 3.77 (s, 6 H), 2.40 (s, 3 H), 2.36 (s, 3 H), 2.34 (s, 3 H), 2.17 – 2.07 (m, 15 H), 2.04 – 2.00 (m, 6 H).

20: A biphasic mixture of 5,5'-dibromo-2,2'-bipyridine[111] (**10**, 1.18 g, 3.75 mmol), **17** (1.10 g, 2.50 mmol), Na_2CO_3 (795 mg, 7.50 mmol) and $Pd(PPh_3)_4$ (144 mg, $1.25 \cdot 10^{-4}$ mol) in THF (40 mL) and water (10 ml) was degassed prior to heating to reflux over night. After cooling to room temperature, the reaction mixture was extracted with dichloromethane. The combined organic layers were dried over Na_2SO_4, filtered, and the solvent was removed in vacuo. The crude product was purified by recrystallization from toluene (150 mL). The precipitate was filtered, washed with diethyl ether, and dried in vacuo to yield **20** as a yellow solid (1.16 g, 2.12 mmol, 85%). ^{1}H-NMR (400 MHz, CD_2Cl_2): δ (ppm) = 8.75 (dd, J = 2.4, 0.7 Hz, 1 H), 8.70 (dd, J = 2.3, 0.9 Hz, 1 H), 8.49 (dd, J = 8.1, 0.9 Hz, 1 H), 8.41 (d, J = 8.4 Hz, 1 H), 8.38 (d, J = 8.0 Hz, 1 H), 8.35 – 8.31 (m, 3 H), 7.99 (dd, J = 8.5, 2.4 Hz, 1 H), 7.89 – 7.83 (m, 4 H), 7.29 (s, 1 H), 7.27 (s, 1 H), 2.36 (s, 3 H), 2.35 (s, 3 H).

21: A biphasic mixture of **12** (1.57 g, 3.00 mmol), **17** (1.10 g, 2.50 mmol), Na_2CO_3 (795 mg, 7.50 mmol) and $Pd(PPh_3)_4$ (144 mg, $1.25 \cdot 10^{-4}$ mol) in THF (40 mL) and water (10 ml) was degassed prior to heating to reflux over night. After cooling to room temperature, the reaction mixture was filtered and the solid was washed with water and diethyl ether.

Drying in vacuo yielded **21** as a pale yellow solid (1.06 g, 1.41 mmol, 56%). ^{1}H-NMR (400 MHz, CD_2Cl_2): δ (ppm) = 8.67 (dd, J = 6.8, 2.3 Hz, 1 H), 8.57 (d, J = 2.3 Hz, 1 H), 8.50 (d, J = 8.2 Hz, 1 H), 8.47 (d, J = 8.0 Hz, 1 H), 8.32 – 8.23 (m, 4 H), 7.86 – 7.71 (m, 5 H), 7.45 (s, 1 H), 7.21 – 7.17 (m, 2 H), 7.12 (s, 1 H), 7.05 (s, 1 H), 7.04 (s, 1 H), 2.35 (s, 3 H), 2.30 – 2.27 (m, 3 H), 2.26 (s, 3 H), 2.21 (s, 3 H), 2.09 (s, 3 H), 2.08 (s, 3 H). MS (ESI): m/z = 753/755 $[C_{48}H_{37}BrN_2O_2+H]^+$.

22: A biphasic mixture of **14** (1.40 g, 1.92 mmol), **17** (701 mg, 1.60 mmol), Na_2CO_3 (509 mg, 4.80 mmol) and $Pd(PPh_3)_4$ (92 mg, $8.0 \cdot 10^{-5}$ mol) in THF (40 mL) and water (10 ml) was degassed prior to heating to reflux for 3 days. After cooling to room temperature, the reaction mixture was filtered and the solid was washed with water and diethyl ether. Drying in vacuo yielded **22** as a beige solid (1.19 g, 1.24 mmol, 78%). ^{1}H-NMR (400 MHz, CD_2Cl_2): δ (ppm) = 8.78 – 8.71 (m, 2 H), 8.57 (d, J = 8.0 Hz, 2 H), 8.40 – 8.31 (m, 4 H), 7.95 – 7.83 (m, 5 H), 7.48 (s, 1 H), 7.27 (s, 2 H), 7.23 (s, 1 H), 7.17 (s, 1 H), 7.15 (s, 1 H), 7.08 (s, 2 H), 7.04 (s, 1 H), 7.03 (s, 1 H), 2.40 (s, 3 H), 2.37 (s, 3 H), 2.34 (s, 6 H), 2.18 (s, 3 H), 2.17 (s, 3 H), 2.14 (s, 6 H), 2.08 (s, 6 H). MS (ESI): m/z = 961/963 $[C_{64}H_{53}BrN_2O_2+H]^+$.

23: This compound was prepared following the procedure for similar homo-coupling reactions.[112] To a solution of 1,4-dibromo-*p*-xylene (5.28 g, 20.0 mmol) in dry THF (150 mL) at -78°C was added *n*-BuLi (2.5 M in hexane, 8.80 mL, 22.0 mmol) drop-wise over a period of approximately 20 minutes. The mixture was stirred at -78°C for 1.5 h prior to addition of CuCN (896 mg, 10.0 mmol). The reaction was allowed to warm to room temperature until all CuCN was dissolved. To the clear solution was added duroquinone (4.93 g, 30.0 mmol) causing an instant color change to deep-blue. The reaction was stirred further for 3 h at room temperature before aqueous HCl (2 M, 100 mL) was added. The mixture was extracted with diethyl ether. The combined organic layers were dried over Na_2SO_4, filtered, and the solvent was removed in vacuo. The crude product was purified by column chromatography on silica using pentane as an eluent to yield **23** as a colorless viscous oil (3.35 g, 9.11 mmol, 91%). ^{1}H-NMR (400 MHz, $CDCl_3$): δ (ppm) = 7.43 (s, 2 H), 6.92 (s, 2 H), 2.36 (s, 6 H), 1.98 (s, 6 H).

24: To a solution of **23** (3.35 g, 9.11 mmol) in dry THF (100 mL) at -78°C was added *n*-BuLi (2.5 M in hexane, 3.83 mL, 9.57 mmol) drop-wise over a period of approximately 15 minutes. The mixture was stirred at -78°C for 1 h prior to addition of TMSCl (1.27 mL, 10.0 mmol). The reaction was allowed to warm to room temperature and was stirred over night. Subsequently, water (100 mL) was added and the mixture was extracted with

diethyl ether. The combined organic layers were dried over Na_2SO_4, filtered, and the solvent was removed in vacuo. The crude product was purified by column chromatography on silica using pentane as an eluent to yield **24** as a colorless viscous oil (2.56 g, 7.09 mmol, 78%). ^{1}H-NMR (400 MHz, $CDCl_3$): δ (ppm) = 7.43 (s, 1 H), 7.31 (s, 1 H), 6.97 (s, 1 H), 6.85 (s, 1 H), 2.42 (s, 3 H), 2.36 (s, 3 H), 2.02 (s, 3 H), 2.01 (s, 3 H), 0.35 (s, 9 H).

25: A biphasic mixture of **9** (1.28 g, 3.00 mmol), **24** (904 mg, 2.50 mmol), Na_2CO_3 (795 mg, 7.50 mmol) and $Pd(PPh_3)_4$ (144 mg, $1.25 \cdot 10^{-4}$ mol) in THF (20 mL) and water (5 ml) was degassed prior to heating to reflux over night. After cooling to room temperature, the reaction mixture was extracted with dichloromethane. The combined organic layers were dried over Na_2SO_4, filtered, and the solvent was removed in vacuo. The crude product was purified by column chromatography on silica using pentane/dichloromethane 5:1 (v:v) as an eluent, yielding **25** as a white solid (1.06 g, 1.82 mmol, 73%). ^{1}H-NMR (400 MHz, CD_2Cl_2): δ (ppm) = 7.35 (s, 1 H), 7.05 – 7.00 (m, 6 H), 6.99 – 6.94 (m, 3 H), 6.90 – 6.85 (m, 4 H), 2.44 (s, 3 H), 2.28 (s, 6 H), 2.09 – 2.03 (m, 9 H), 2.00 (s_{br}, 6 H), 0.36 (s, 9 H).

26: A solution of **25** (1.06 g, 1.82 mmol) in dry dichloromethane (30 mL) was cooled to 0 °C prior to addition of a solution of iodine monochloride (591 mg, 3.64 mmol) in dry dichloromethane (10 mL). The resulting mixture was stirred for 30 minutes at 0 °C and an saturated aqueous solution of $Na_2S_2O_3$ was added. The layers were separated, and the aqueous layer was extracted with dichloromethane. The combined organic layers were dried over Na_2SO_4, filtered, and the solvent was removed in vacuo. The crude product was purified by column chromatography on silica using pentane/dichloromethane 5:1 (v:v) as an eluent, yielding **26** as a white solid (1.08 g, 1.70 mmol, 93%). ^{1}H-NMR (400 MHz, CD_2Cl_2): δ (ppm) = 7.75 (s, 1 H), 7.06 – 7.00 (m, 6 H), 7.00 – 6.94 (m, 3 H), 6.90 – 6.85 (m, 4 H), 2.42 (s, 3 H), 2.28 (s, 6 H), 2.09 – 1.97 (m, 15 H).

27: A mixture of **26** (1.08 g, 1.70 mmol), bis(pinacol)diboron (648 mg, 2.55 mmol), KOAc (667 mg, 6.80 mmol) and $Pd(PPh_3)_2Cl_2$ (60 mg, $8.50 \cdot 10^{-5}$ mol) in DMSO (25 mL) was degassed and reacted at 90 °C over night. After cooling to room temperature, the reaction mixture was treated with water (100 mL) and saturated aqueous NH_4Cl-solution (20 mL), and the aqueous phase was extracted with dichloromethane. The combined organic layers were dried over Na_2SO_4, filtered, and the solvent was removed in vacuo. The crude product was purified by column chromatography on silica using pentane/dichloromethane 5:1 (v:v) as an eluent to yield **27** as a white solid (710 mg, 1.12 mmol, 66%). ^{1}H-NMR (400 MHz, CD_2Cl_2): δ (ppm) = 7.64 (s, 1 H), 7.06 – 7.00 (m, 6 H), 6.99 – 6.95 (m, 3 H), 6.90 – 6.86 (m, 4 H), 2.51 (s, 3 H), 2.28 (s, 6 H), 2.09 – 2.05 (m, 6 H), 2.02 (s, 3 H), 2.01

– 1.99 (m, 6 H), 1.36 (s, 12 H).

28: A biphasic mixture of **17** (789 mg, 1.80 mmol), **24** (542 mg, 1.50 mmol), Na_2CO_3 (477 mg, 4.50 mmol) and $Pd(PPh_3)_4$ (87 mg, $7.50 \cdot 10^{-5}$ mol) in THF (20 mL) and water (5 ml) was degassed prior to heating to reflux over night. After cooling to room temperature, the reaction mixture was extracted with dichloromethane. The combined organic layers were dried over Na_2SO_4, filtered, and the solvent was removed in vacuo. The crude product was purified by column chromatography on silica using pentane/dichloromethane 1:1 (v:v) as an eluent, yielding **28** as a yellow solid (803 mg, 1.37 mmol, 91%). ^{1}H-NMR (400 MHz, $CDCl_3$): δ (ppm) = 8.39 (d, J = 8.0 Hz, 1 H), 8.38 – 8.34 (m, 3 H), 7.86 (dd, J = 8.0, 1.8 Hz, 1 H), 7.85 – 7.81 (m, 2 H), 7.35 (s, 1 H), 7.22 (s, 1 H), 7.15 (s, 1 H), 7.05 – 7.01 (m, 2 H), 6.99 (s, 1 H), 2.46 (s, 3 H), 2.33 (s, 3 H), 2.17 – 2.14 (m, 3 H), 2.12 – 2.06 (m, 9 H), 0.37 (s, 9 H).

29: To a solution of **28** (813 mg, 1.37 mmol) in dry dichloromethane (40 mL) was added a solution of iodine monochloride (334 mg, 2.05 mmol) in dry dichloromethane (10 mL). The resulting mixture was stirred for 1 h, and then a saturated aqueous solution of $Na_2S_2O_3$ was added. The layers were separated, and the aqueous layer was extracted with dichloromethane. The combined organic phases were dried over Na_2SO_4, filtered, and the solvent was removed in vacuo. The crude product was purified by short column chromatography on silica using dichloromethane as an eluent, yielding **29** as a pale-yellow solid (758 mg, 1.17 mmol, 85%). ^{1}H-NMR (400 MHz, $CDCl_3$): δ (ppm) = 8.39 (d, J = 8.0 Hz, 1 H), 8.38 – 8.34 (m, 3 H), 7.87 – 7.81 (m, 3 H), 7.75 (s, 1 H), 7.22 (s, 1 H), 7.13 (d, J = 3.3 Hz, 1 H), 7.06 (d, J = 3.0 Hz, 1 H), 7.04 (d, J = 5.4 Hz, 1 H), 6.98 (d, J = 5.3 Hz, 1 H), 2.43 (s, 3 H), 2.33 (s, 3 H), 2.15 – 2.13 (m, 3 H), 2.10 (s, 3 H), 2.07 – 2.04 (m, 6 H).

30: A mixture of **29** (758 mg, 1.17 mmol), bis(pinacol)diboron (446 mg, 1.75 mmol), KOAc (459 mg, 4.68 mmol) and $Pd(PPh_3)_2Cl_2$ (41 mg, $5.85 \cdot 10^{-5}$ mol) in DMSO (20 mL) was degassed and stirred at 90 °C over night. After cooling to room temperature, the reaction mixture was treated with water (80 mL) and saturated aqueous NH_4Cl-solution (20 mL), and the aqueous phase was extracted with dichloromethane. The combined organic phases were dried over Na_2SO_4, filtered, and the solvent was removed in vacuo. The crude product was purified by column chromatography on silica using a gradient starting from pentane/dichloromethane 1:1 (v:v) to neat dichloromethane as an eluent, yielding **30** as a yellow solid (536 mg, $8.29 \cdot 10^{-4}$ mol, 71%). ^{1}H-NMR (400 MHz, CD_2Cl_2): δ (ppm) = 8.39 (d, J = 8.0 Hz, 1 H), 8.38 – 8.34 (m, 3 H), 7.86 (dd, J = 8.0, 1.9 Hz, 1 H), 7.85 – 7.81 (m, 2 H), 7.69 (s, 1 H), 7.22 (s, 1 H), 7.15 (s, 1 H), 7.04 – 6.98 (m, 3 H), 2.55 (s, 3

H), 2.33 (s, 3 H), 2.16 – 2.13 (m, 3 H), 2.12 – 2.09 (m, 6 H), 2.05 (s, 3 H).

31: A biphasic mixture of 5,5'-dibromo-2,2'-bipyridine[111] (**10**, 527 mg, 1.68 mmol), **27** (710 mg, 1.12 mmol), Na_2CO_3 (356 mg, 3.36 mmol) and $Pd(PPh_3)_4$ (65 mg, $5.60 \cdot 10^{-5}$ mol) in THF (20 mL) and water (5 ml) was degassed prior to heating to reflux over night. After cooling to room temperature, the reaction mixture was extracted with dichloromethane. The combined organic layers were dried over Na_2SO_4, filtered, and the solvent was removed in vacuo. The crude product was purified by column chromatography on C-18 reversed phase silica using as eluent a gradient starting from acetonitrile to acetone to dichloromethane, yielding **28** as a white solid (372 mg, $5.00 \cdot 10^{-4}$ mol, 45%). ^{1}H-NMR (400 MHz,CD_2Cl_2): δ (ppm) = 8.75 (dd, J = 2.4, 0.7 Hz, 1 H), 8.71 (dd, J = 2.3, 0.9 Hz, 1 H), 8.48 (dd, J = 8.2, 0.9 Hz, 1 H), 8.42 (dd, J = 8.5, 0.8 Hz, 1 H), 7.99 (dd, J = 8.5, 2.4 Hz, 1 H), 7.88 (dd, J = 8.2, 2.3 Hz, 1 H), 7.22 (s, 1 H), 7.13 (d, J = 4.2 Hz, 1 H), 7.08 – 7.01 (m, 7 H), 6.99 (s, 1 H), 6.91 – 6.86 (m, 4 H), 2.33 (s, 3 H), 2.29 (s, 6 H), 2.16 – 2.09 (m, 9 H), 2.04 – 1.99 (m, 6 H).

32: A mixture of **18** (264 mg, $3.41 \cdot 10^{-4}$ mol), **17** (179 mg, $4.09 \cdot 10^{-4}$ mol), Na_2CO_3 (108 mg, 1.02 mmol) and $Pd(PPh_3)_4$ (20 mg, $1.71 \cdot 10^{-5}$ mol) in THF (6 mL) and water (1.5 mL) was degassed prior to heating to reflux over night. After cooling to room temperature, the reaction mixture was extracted with dichloromethane. The combined organic layers were dried over Na_2SO_4, filtered, and the solvent was removed in vacuo. The crude product was purified by column chromatography on silica using pentane/diethyl ether 1:1 (v:v) with 2% triethylamine as an eluent to yield **32** as a pale brown solid (270 mg, $2.68 \cdot 10^{-4}$ mol, 79%). ^{1}H-NMR (400 MHz, ,CD_2Cl_2): δ (ppm) = 8.75 (dd, J = 2.2, 0.9 Hz, 1 H), 8.74 (dd, J = 2.3, 0.9 Hz, 1 H), 8.58 (dd, J = 2.1, 0.9 Hz, 1 H), 8.56 (dd, J = 2.1, 0.9 Hz, 1 H), 8.38 (d, J = 8.0 Hz, 1 H), 8.36 – 8.32 (m, 3 H), 7.93 – 7.83 (m, 5 H), 7.27 (s, 2 H), 7.24 (s, 1 H), 7.13 (s, 2 H), 7.12 (s, 1 H), 6.99 (s, 1 H), 6.97 (s,1 H), 6.94 – 6.89 (m, 4 H), 6.83 – 6.77 (m, 4 H), 3.77 (s, 6 H), 2.37 (s, 3 H), 2.36 (s, 3 H), 2.34 (s, 3 H), 2.17 (s, 6 H), 2.15 (s, 3 H), 2.02 (s, 6 H).

33: A mixture of **19** (251 mg, $2.55 \cdot 10^{-4}$ mol), **17** (134 mg, $3.06 \cdot 10^{-4}$ mol), Na_2CO_3 (81 mg, $7.66 \cdot 10^{-4}$ mol) and $Pd(PPh_3)_4$ (15 mg, $1.28 \cdot 10^{-5}$ mol) in THF (6 mL) and water (1.5 mL) was degassed prior to heating to reflux over night. After cooling to room temperature, the reaction mixture was extracted with dichloromethane. The combined organic layers were dried over Na_2SO_4, filtered, and the solvent was removed in vacuo. The crude product was purified by column chromatography on silica using pentane/diethyl ether 1:1 (v:v) with 2% triethylamine as an eluent to yield **33** as a yellow-brown solid (155 mg, $1.28 \cdot 10^{-4}$

mol, 50%). ^{1}H-NMR (400 MHz, CD_2Cl_2): δ (ppm) = 8.77 – 8.75 (m, 2 H), 8.60 – 8.56 (m, 2 H), 8.38 (d, J = 8.0 Hz, 1 H), 8.37 – 8.32 (m, 3 H), 7.94 – 7.83 (m, 5 H), 7.27 (s, 2 H), 7.26 (s, 1 H), 7.17 (s, 1 H), 7.16 (s, 1 H), 7.14 (s, 1 H), 7.08 (s, 2 H), 7.07 (s, 1 H), 7.05 (s, 1 H), 7.02 (s_{br}, 1 H), 6.97 (s, 1 H), 6.94 – 6.89 (m, 4 H), 6.82 – 6.78 (m, 4 H), 3.77 (s, 6 H), 2.38 (s, 3 H), 2.37 (s, 3 H), 2.35 (s, 3 H), 2.19 – 2.10 (m, 21 H), 2.04 – 2.00 (m, 6 H).

34: A biphasic mixture of **20** (382 mg, $7.00 \cdot 10^{-4}$ mol), **5** (crude: 559 mg; containing 436 mg, $8.40 \cdot 10^{-4}$ mol of pure **5**), Na_2CO_3 (223 mg, 2.10 mmol) and $Pd(PPh_3)_4$ (41 mg, $3.50 \cdot 10^{-5}$ mol) in THF (15 mL) and water (4 ml) was degassed prior to heating to reflux over night. After cooling to room temperature, the reaction mixture was extracted with dichloromethane. The combined organic layers were dried over Na_2SO_4, filtered, and the solvent was removed in vacuo. The crude product was purified by column chromatography on silica using a gradient starting from pentane/diethyl ether 1:1 (v:v) to neat diethyl ether with 2% methanol as an eluent, yielding **34** as a yellow-brown solid (515 mg, $6.00 \cdot 10^{-4}$ mol, 86%). ^{1}H-NMR (400 MHz, CD_2Cl_2): δ (ppm) = 8.72 (ddd, J = 7.4, 2.3, 0.8 Hz, 2 H), 8.55 (td, J = 8.0, 0.9 Hz, 2 H), 8.38 (d, J = 8.0 Hz, 1 H), 8.36 – 8.31 (m, 3 H), 7.91 – 7.83 (m, 5 H), 7.30 (s, 2 H), 7.17 (s, 1 H), 7.01 (s, 1 H), 6.76 (d, J = 8.7 Hz, 2 H), 6.64 (d, J = 2.6 Hz, 2 H), 6.44 (dd, J = 8.6, 2.5 Hz, 2 H), 3.80 (s, 6 H), 3.71 (s, 6 H), 2.38 (s, 3 H), 2.36 (s, 3 H), 2.25 (s, 3 H), 2.05 (s, 3 H). MS (ESI): m/z = 858 $[C_{56}H_{47}N_3O_6+H]^+$.

35: A biphasic mixture of **21** (377 mg, $5.00 \cdot 10^{-4}$ mol), **5** (crude: 416 mg; containing 312 mg, $6.00 \cdot 10^{-4}$ mol of pure **5**), Na_2CO_3 (159 mg, 1.50 mmol) and $Pd(PPh_3)_4$ (29 mg, $2.50 \cdot 10^{-5}$ mol) in THF (15 mL) and water (4 ml) was degassed prior to heating to reflux for 2 days. After cooling to room temperature, the reaction mixture was extracted with dichloromethane. The combined organic layers were dried over Na_2SO_4, filtered, and the solvent was removed in vacuo. The crude product was purified by column chromatography on silica using a gradient starting from pentane/diethyl ether 1:1 (v:v) to neat diethyl ether with 2% methanol as an eluent to yield **35** as a yellow-brown solid (515 mg, $6.00 \cdot 10^{-4}$ mol, 86%). ^{1}H-NMR (400 MHz, CD_2Cl_2): δ (ppm) = 8.75 (ddd, J = 4.1, 2.3, 0.9 Hz, 2 H), 8.57 (ddd, J = 8.1, 1.5, 0.8 Hz, 2 H), 8.38 (d, J = 8.0, 1 H), 8.36 – 8.32 (m, 3 H), 7.93 – 7.84 (m, 5 H), 7.24 (s, 2 H), 7.24 (s, 1 H), 7.13 (s, 3 H), 6.99 (s, 2 H), 6.76 (d, J = 8.7 Hz, 2 H), 6.63 (d, J = 2.6 Hz, 2 H), 6.46 (dd, J = 8.6, 2.6 Hz, 2 H), 3.80 (s, 6 H), 3.70 (s, 6 H), 2.37 (s, 3 H), 2.36 (s, 3 H), 2.34 (s, 3 H), 2.17 (s, 6 H), 2.13 (s, 3 H), 2.04 (s, 3 H), 2.03 (s, 3 H). MS (ESI): m/z = 1066 $[C_{72}H_{63}N_3O_6+H]^+$.

36: A mixture of **22** (481 mg, $5.00 \cdot 10^{-4}$ mol), **5** (crude: 416 mg; containing 312 mg, $6.00 \cdot 10^{-4}$ mol of pure **5**), Cs_2CO_3 (489 mg, 1.50 mmol) and $Pd(PPh_3)_4$ (29 mg, $2.50 \cdot 10^{-5}$

mol) in DMF (50 ml) was degassed prior to stirring at 100 °C for 3 days. After cooling to room temperature, water (200 mL) was added and the precipitate was filtered, washed with water, and dried. The crude product was purified by column chromatography on silica using dichloromethane with 1.5% methanol and 1.5% triethylamine as an eluent. A second purification by column chromatography was necessary in this case using diethyl ether with 2% triethylamine as an eluent, yielding **36** as a beige solid (137 mg, $1.07 \cdot 10^{-4}$ mol, 21%). ^{1}H-NMR (400 MHz, CD_2Cl_2): δ (ppm) = 8.77 – 8.75 (m, 2 H), 8.58 (d, J = 8.2 Hz, 2 H), 8.38 (d, J = 8.0 Hz, 1 H), 8.36 – 8.32 (m, 3 H), 7.94 – 7.84 (m, 5 H), 7.27 (s, 2 H), 7.26 (s, 1 H), 7.18 – 7.14 (m, 3 H), 7.08 (s, 3 H), 7.06 - 7.01 (m, 2 H), 6.99 (s, 1 H), 6.76 (d, J = 8.7 Hz, 2 H), 6.64 (d, J = 2.6 Hz, 2 H), 6.46 (dd, J = 8.6, 2.6 Hz, 2 H), 3.80 (s, 6 H), 3.70 (s, 6 H), 2.38 (s, 3 H), 2.37 (s, 3 H), 2.35 (s, 3 H), 2.19 – 2.11 (m, 18 H), 2.10 (s, 3 H), 2.06 – 2.01 (m, 6 H). MS (ESI): m/z = 1275 $[C_{88}H_{79}N_3O_6+H]^+$.

37: A biphasic mixture of **20** (382 mg, $7.00 \cdot 10^{-4}$ mol), **9** (359 mg, $8.40 \cdot 10^{-4}$ mol), Na_2CO_3 (223 mg, 2.10 mmol) and $Pd(PPh_3)_4$ (41 mg, $3.50 \cdot 10^{-5}$ mol) in THF (15 mL) and water (5 ml) was degassed prior to heating to reflux over night. After cooling to room temperature, the reaction mixture was extracted with dichloromethane. The combined organic layers were dried over Na_2SO_4, filtered, and the solvent was removed in vacuo. The crude product was purified by column chromatography on silica using a gradient starting from pentane/dichloromethane 2:1 (v:v) to neat dichloromethane with additional 2% triethylamine as an eluent to yield **37** as an orange solid (389 mg, $5.08 \cdot 10^{-4}$ mol, 73%). ^{1}H-NMR (400 MHz, CD_2Cl_2): δ (ppm) = 8.72 (dd, J = 8.3, 2.3 Hz, 2 H), 8.55 (t, J = 8.0 Hz, 2 H), 8.38 (d, J = 8.0 Hz, 1 H), 8.36 – 8.31 (m, 3 H), 7.91 – 7.83 (m, 5 H), 7.30 (s, 2 H), 7.19 (s, 1 H), 7.07 – 7.02 (m, 5 H), 6.90 – 6.86 (m, 4 H), 2.38 (s, 3 H), 2.36 (s, 3 H), 2.29 (s, 6 H), 2.25 (s, 3 H), 2.03 (s, 3 H).

38: A biphasic mixture of **21** (339 mg, $4.50 \cdot 10^{-4}$ mol), **9** (231 mg, $5.40 \cdot 10^{-4}$ mol), Na_2CO_3 (143 mg, 1.35 mmol) and $Pd(PPh_3)_4$ (26 mg, $2.25 \cdot 10^{-5}$ mol) in THF (12 mL) and water (3 ml) was degassed prior to heating to reflux for 2 days. After cooling to room temperature, the reaction mixture was extracted with dichloromethane. The combined organic layers were dried over Na_2SO_4, filtered, and the solvent was removed in vacuo. The crude product was purified by column chromatography on silica using dichloromethane with 2% methanol as an eluent, yielding **38** as an orange solid (329 mg, $3.37 \cdot 10^{-4}$ mol, 75%). ^{1}H-NMR (400 MHz, CD_2Cl_2): δ (ppm) = 8.77 – 8.74 (m, 2 H), 8.60 – 8.55 (m, 2 H), 8.38 (d, J = 8.0 Hz, 1 H), 8.36 – 8.32 (m, 3 H), 7.94 – 7.84 (m, 5 H), 7.27 (s, 2 H), 7.24 (s, 1 H), 7.13 (s, 3 H), 7.06 – 7.02 (m, 4 H), 7.01 (s, 2 H), 6.90 – 6.86 (m, 4 H), 2.37, (s, 3 H), 2.36 (s, 3 H), 2.34 (s, 3 H), 2.29 (s, 6 H), 2.17 (s, 6 H), 2.15 (s, 3 H), 2.03 (s, 3 H), 2.01 (s, 3 H).

39: A biphasic mixture of **31** (372 mg, $5.00 \cdot 10^{-4}$ mol), **30** (388 mg, $6.00 \cdot 10^{-4}$ mol), Na_2CO_3 (159 mg, 1.50 mmol) and $Pd(PPh_3)_4$ (29 mg, $2.50 \cdot 10^{-5}$ mol) in THF (16 mL) and water (4 ml) was degassed prior to heating to reflux over night. After cooling to room temperature, the reaction mixture was extracted with dichloromethane. The combined organic layers were dried over Na_2SO_4, filtered, and the solvent was removed in vacuo. The crude product was purified by column chromatography on silica using a gradient starting from pentane/diethyl ether 5:1 (v:v) with 1% methanol and 1% triethylamine to pentane/dichloromethane 1:1 (v:v) with 2% methanol as an eluent. In order to remove further impurities, the product was dissolved in a minimum amount of dichloromethane and given into methanol. The precipitate was dried in vacuo, yielding **39** as an pale pink solid (438 mg, $37.0 \cdot 10^{-4}$ mol, 74%). ^{1}H-NMR (400 MHz, CD_2Cl_2): δ (ppm) = 8.76 (s_{br}, 2 H), 8.58 (d, J = 8.1 Hz, 2 H), 8.38 (d, J = 8.0 Hz, 1 H), 8.37 - 8.32 (m, 3 H), 7.95 – 7.83 (m, 5 H), 7.29 – 7.24 (m, 3 H), 7.19 – 7.13 (m, 3 H), 7.11 – 7.02 (m, 9 H), 7.00 (s, 1 H), 6.92 – 6.87 (m, 4 H), 2.38 (s, 3 H), 2.37 (s, 3 H), 2.35 (s, 3 H), 2.29 (s, 6 H), 2.20 – 2.11 (m, 21 H), 2.05 – 2.01 (m, 6 H). MS (ESI): m/z = 1183 $[C_{86}H_{75}N_3O_2+H]^+$.

anisyl-xy$_2$: A solution of **32** (270 mg, $2.68 \cdot 10^{-4}$ mol) and $[Ru(bpy)_2Cl_2]$[113] (130 mg, $2.68 \cdot 10^{-4}$ mol) in ethanol (12 mL) and chloroform (4 mL) was heated to reflux under a N_2-atmosphere for 2 days. The solvent was evaporated and the residue was dissolved in dichloromethane and water. KPF_6 was added and the aqueous phase was extracted with dichloromethane. The combined organic layers were washed with water. The solvent was evaporated and the residue was dissolved in a minimal amount of acetone, and then added drop-wise to diethyl ether. The precipitate was filtered and washed thoroughly with diethyl ether and water. The product was collected by rinsing the frit with acetone and evaporation of the solvent, yielding **anisyl-xy$_2$** as a red solid (383 mg, $2.68 \cdot 10^{-4}$ mol, 83%). ^{1}H-NMR (400 MHz, acetone-d_6): δ (ppm) = 9.00 (dd, J = 8.4, 2.6 Hz, 2 H), 8.91 – 8.86 (m, 4 H), 8.38 (d, J = 8.0 Hz, 1 H), 8.37 – 8.31 (m, 6 H), 8.31 – 8.20 (m, 5 H), 8.20 – 8.16 (m, 2 H), 8.10 – 8.06 (m, 2 H), 8.01 – 7.95 (m, 3 H), 7.68 (dd, J = 7.6, 5.8 Hz, 2 H), 7.63 - 7.57 (m, 2 H), 7.32 (s, 1 H), 7.20 (s_{br}, 1 H), 7.16 (s_{br}, 1 H), 7.08 (s, 1 H), 7.06 (s, 1 H), 7.03 (s, 1 H), 6.96 (s, 1 H), 6.91 (s, 1 H), 6.89 – 6.83 (m, 8 H), 3.77 (s, 6 H), 2.34 (s, 3 H), 2.11 – 2.04 (m, 15 H), 2.00 (s, 3 H), 1.93 (s, 3 H). MS (ESI): m/z = 709.7464 (calc. 709.7469). Anal. calc. for $C_{90}H_{75}F_{12}N_7O_4P_2Ru \cdot 1.5CH_3C(O)CH_3 \cdot H_2O$ (%): C, 62.55; H, 4.69; N, 5.49. Found: C, 62.84; H, 5.03; N, 5.79.

anisyl-xy$_3$: A solution of **33** (155 mg, $1.27 \cdot 10_{-4}$ mol) and $[Ru(bpy)_2Cl_2]$[113] (62 mg, $1.27 \cdot 10^{-4}$ mol) in ethanol (9 mL) and chloroform (3 mL) was heated to reflux under a

N_2-atmosphere for 3 days. The solvent was evaporated and the residue was dissolved in dichloromethane and water. KPF_6 was added and the aqueous phase was extracted with dichloromethane. The combined organic layers were washed with water. The solvent was evaporated and the residue was dissolved in a minimal amount of acetone, and then added drop-wise to diethyl ether. The precipitate was filtered and washed thoroughly with diethyl ether and water. The product was collected by rinsing the frit with acetone and evaporation of the solvent, yielding **anisyl-xy$_3$** as a red solid (127 mg, $6.62 \cdot 10^{-5}$ mol, 52%). ^{1}H-NMR (400 MHz, acetone-d_6): δ (ppm) = 9.01 (d, J = 8.4, 2 H), 8.90 (d, J = 8.5 Hz, 4 H), 8.39 (d, J = 8.0 Hz, 1 H), 8.38 – 8.17 (m, 13 H), 8.11 – 8.07 (m, 2 H), 8.03 – 7.96 (m, 3 H), 7.71 – 7.66 (m, 2 H), 7.64 - 7.58 (m, 2 H), 7.34 (s, 1 H), 7.21 – 7.17 (m, 2 H), 7.15 (s, 1 H), 7.11 (s, 1 H), 7.07 (s, 1 H), 7.05 (s, 2 H), 7.00 (s, 2 H), 6.99 (s, 1 H), 6.96 (s, 1 H), 6.92 – 6.83 (m, 8 H), 3.77 (s, 6 H), 2.37 (s, 3 H), 2.18 – 1.98 (m, 33 H). MS (ESI): m/z = 813.8092 (calc. 813.8085). Anal. calc. for $C_{106}H_{91}F_{12}N_7O_4P_2Ru \cdot 2H_2O$ (%): C, 65.16; H, 4.90; N, 5.02. Found: C, 65.49; H, 5.23; N, 5.31.

veratryl-xy$_1$: A solution of **34** (257 mg, $3.00 \cdot 10^{-4}$ mol) and $[Ru(bpy)_2Cl_2]$[113] (145 mg, $3.00 \cdot 10^{-4}$ mol) in ethanol (18 mL) and chloroform (6 mL) was heated to reflux under a N_2-atmosphere over night. The solvent was evaporated and the residue was purified by column chromatography on silica using a gradient of (1) acetone, (2) acetone/water 9:1 (v:v) and (3) acetone/water 9:1 with 1% saturated aqueous KNO_3 solution as an eluent. The product containing solutions were collected and KPF_6 was added. Acetone was completely evaporated and the aqueous phase was extracted with dichloromethane. The combined organic layers were washed with water, the solvent was evaporated, and the product was dried in vacuo, yielding **veratryl-xy$_1$** as a red solid (281 mg, $1.80 \cdot 10^{-4}$ mol, 60%). ^{1}H-NMR (400 MHz, acetone-d_6): δ (ppm) = 9.00 – 8.94 (m, 2 H), 8.89 – 8.84 (m, 4 H), 8.37 – 8.15 (m, 14 H), 8.07 (dd, J = 2.0, 0.7 Hz, 1 H), 8.01 – 7.96 (m, 3 H), 7.92 (dd, J = 8.0, 1.9 Hz, 1 H), 7.66 (ddt, J = 7.3, 5.7, 1.4 Hz, 2 H), 7.59 (ddt, J = 7.4, 5.6, 1.5 Hz, 2 H), 7.27 (s, 1 H), 7.23 (s, 1 H), 7.11 (s, 1 H), 6.90 (s, 1 H), 6.83 (d, J = 8.7 Hz, 2 H), 6.58 (d, J = 2.5 Hz, 2 H), 6.34 (dd, J = 8.6, 2.6 Hz, 2 H), 3.77 (s, 6 H), 3.65 (s, 6 H), 2.29 (s, 3 H), 2.10 (s, 3 H), 1.97 (s, 3 H), 1.94 (s, 3 H). MS (ESI): m/z = 635.6951 (calc. 635.6946). Anal. calc. for $C_{76}H_{63}F_{12}N_7O_6P_2Ru \cdot H_2O$ (%): C, 57.80; H, 4.15; N, 6.21. Found: C, 57.71; H, 4.25; N, 6.37.

veratryl-xy$_2$: A solution of **35** (257 mg, $2.41 \cdot 10^{-4}$ mol) and $[Ru(bpy)_2Cl_2]$[113] (117 mg, $2.41 \cdot 10^{-4}$ mol) in ethanol (15 mL) and chloroform (5 mL) was heated to reflux under a N_2-atmosphere for 2 days. The solvent was evaporated and the residue was purified by column chromatography on silica using a gradient of (1) acetone, (2) acetone/water 9:1

(v:v) and (3) acetone/water 9:1 with 1% saturated aqueous KNO_3 solution as an eluent. The product containing solutions were collected and KPF_6 was added. Acetone was completely evaporated and the aqueous phase was extracted with dichloromethane. The combined organic layers were washed with water, the solvent was evaporated, and the product was dried in vacuo, yielding **veratryl-xy$_2$** as a red solid (199 mg, $1.12 \cdot 10^{-4}$ mol, 47%). ^{1}H-NMR (400 MHz, acetone-d$_6$): δ (ppm) = 9.00 (dd, J = 8.4, 2.5 Hz, 2 H), 8.92 – 8.86 (m, 4 H), 8.38 (d, J = 8.0 Hz, 1 H), 8.37 – 8.32 (m, 6 H), 8.31 – 8.21 (m, 5 H), 8.20 – 8.17 (m, 2 H), 8.08 (dt, J = 8.5, 2.1 Hz, 2 H), 8.01 – 7.96 (m, 3 H), 7.71 – 7.66 (m, 2 H), 7.64 – 7.58 (m, 2 H), 7.32 (s, 1 H), 7.20 (d, J = 2.4 Hz, 1 H), 7.16 (d, J = 2.6 Hz, 1 H), 7.07 (s, 1 H), 7.05 (s, 1 H), 7.04 (s, 1 H), 7.00 (s, 1 H), 6.91 (s, 1 H), 6.84 (d, J = 8.7 Hz, 2 H), 6.65 (d, J = 2.6 Hz, 2 H), 6.41 (dd, J = 8.6, 2.6 Hz, 2 H), 3.78 (s, 6 H), 3.67 (s, 6 H), 2.34 (s, 3 H), 2.09 (s, 9 H), 2.08 – 2.04 (m, 6 H), 2.02 (s, 3 H), 1.94 (s, 3 H). MS (ESI): m/z = 739.7582 (calc. 739.7575). Anal. calc. for $C_{92}H_{79}F_{12}N_7O_6P_2Ru \cdot 2H_2O$ (%): C, 61.20; H, 4.63; N, 5.43. Found: C, 61.13; H, 4.57; N, 5.63.

veratryl-xy$_3$: A solution of **36** (137 mg, $1.07 \cdot 10^{-4}$ mol) and $[Ru(bpy)_2Cl_2]$[113] (52 mg, $1.07 \cdot 10^{-4}$ mol) in ethanol (18 mL) and chloroform (6 mL) was heated to reflux under a N_2-atmosphere for 3 days. The solvent was evaporated and the residue was purified by column chromatography on silica using a gradient of (1) acetone, (2) acetone/water 9:1 (v:v) and (3) acetone/water 9:1 with 1% saturated aqueous KNO_3 solution as an eluent. The product containing solutions were collected and KPF_6 was added. Acetone was completely evaporated, and the aqueous phase was extracted with dichloromethane. The combined organic layers were washed with water, the solvent was evaporated, and the product was dried in vacuo, yielding **veratryl-xy$_3$** as a red solid (61 mg, $3.08 \cdot 10^{-5}$ mol, 29%). ^{1}H-NMR (400 MHz, acetone-d$_6$): δ (ppm) = 9.01 (d, J = 8.5 Hz, 2 H), 8.90 (d, J = 8.2 Hz, 4 H), 8.39 (d, J = 8.0 Hz, 1 H), 8.38 – 8.32 (m, 6 H), 8.31 – 8.21 (m, 5 H), 8.19 (d, J = 5.7 Hz, 2 H), 8.11 – 8.07 (m, 2 H), 8.01 (dd, J = 8.1, 2.0 Hz, 1 H), 8.00 – 7.96 (m, 2 H), 7.72 – 7.66 (m, 2 H), 7.64 – 7.58 (m, 2 H), 7.34 (s, 1 H), 7.21 – 7.17 (m, 2 H), 7.15 (s, 1 H9, 7.11 (s, 1 H), 7.09 – 7.04 (m, 3 H), 7.03 (s, 1 H), 7.01 (s, 1 H), 7.00 (s, 1 H), 6.96 (s, 1 H), 6.85 (d, J = 8.7 Hz, 2 H), 6.67 (d, J = 2.6 Hz, 2 H), 6.43 (dd, J = 8.6, 2.6 Hz, 2 H), 3.78 (s, 6 H), 3.68 (s, 6 H), 2.37 (s, 3 H), 2.16 (d, J = 3.5 Hz, 3 H), 2.12 (s, 3 H), 2.11 – 2.04 (m, 24 H), 2.00 (d, J = 4.4 Hz, 3 H). MS (ESI): m/z = 843.8204 (calc. 843.8191). Anal. calc. for $C_{108}H_{95}F_{12}N_7O_6P_2Ru \cdot H_2O \cdot 2CH_3C(O)CH_3$ (%): C, 64.83; H, 5.20; N, 4.64. Found: C, 64.90; H, 5.54; N, 4.75.

tolyl-xy$_1$: A solution of **37** (192 mg, $2.50 \cdot 10^{-4}$ mol) and $[Ru(bpy)_2Cl_2]$[113] (121 mg, $2.50 \cdot 10^{-4}$ mol) in ethanol (12 mL) and chloroform (4 mL) was heated to reflux under a

N_2-atmosphere over night. The solvent was evaporated and the residue was purified by column chromatography on silica using a gradient of (1) acetone, (2) acetone/water 9:1 (v:v) and (3) acetone/water 9:1 with 1% saturated aqueous KNO_3 solution as an eluent. The product containing solutions were collected and KPF_6 was added. Acetone was completely evaporated and the aqueous phase was extracted with dichloromethane. The combined organic layers were washed with water, the solvent was evaporated, and the product was dried in vacuo, yielding **tolyl-xy$_1$** as a red solid (149 mg, $1.01 \cdot 10^{-4}$ mol, 41%). ^{1}H-NMR (400 MHz, acetone-d_6): δ (ppm) = 8.98 (dd, J = 10.1, 8.4 Hz, 2 H), 8.89 – 8.83 (m, 4 H), 8.36 (d, J = 8.0 Hz, 1 H), 8.35 – 8.30 (m, 5 H), 8.30 – 8.18 (m, 5 H), 8.18 – 8.15 (m, 3 H), 8.07 (s_{br}, 2 H), 8.00 – 7.96 (m, 2 H), 7.92 (dd, J = 8.0, 1.8 Hz, 1 H), 7.69 – 7.64 (m, 2 H), 7.61 – 7.56 (m, 2 H), 7.27 (s, 1 H), 7.23 (s, 1 H), 7.14 (s, 1 H), 7.08 – 7.04 (m, 4 H), 6.91 (s, 1 H), 6.79 – 6.74 (m, 4 H), 2.29 (s, 3 H), 2.27 (s, 6 H), 2.10 (s, 3 H), 1.95 (s, 6 H). MS (ESI): m/z = 589.6891 (calc. 589.6891). Anal. calc. for $C_{74}H_{59}F_{12}N_7O_2P_2Ru \cdot 2CH_3C(O)CH_3 \cdot 3.5H_2O$ (%): C, 58.29; H, 4.77; N, 5.95. Found: C, 58.24; H, 4.98; N, 5.99.

tolyl-xy$_2$: A solution of **38** (195 mg, $2.00 \cdot 10^{-4}$ mol) and $[Ru(bpy)_2Cl_2]$[113] (97 mg, $2.00 \cdot 10^{-4}$ mol) in ethanol (12 mL) and chloroform (4 mL) was heated to reflux under a N_2-atmosphere over night. The solvent was evaporated and the residue was purified by column chromatography on silica using a gradient of (1) acetone, (2) acetone/water 9:1 (v:v) and (3) acetone/water 9:1 with 1% saturated aqueous KNO_3 solution as an eluent. The product containing solutions were collected and KPF_6 was added. Acetone was completely evaporated and the aqueous phase was extracted with dichloromethane. The combined organic layers were washed with water, the solvent was evaporated, and the product was dried in vacuo, yielding **tolyl-xy$_2$** as a red solid (111 mg, $6.61 \cdot 10^{-5}$ mol, 33%). ^{1}H-NMR (400 MHz, acetone-d_6): δ (ppm) = 9.01 (dd, J = 8.5, 2.5 Hz, 2 H), 8.92 – 8.86 (m, 4 H), 8.38 (d, J = 8.0 Hz, 1 H), 8.37 – 8.32 (m, 6 H), 8.31 – 8.21 (m, 5 H), 8.20 – 8.17 (m, 2 H), 8.10 – 8.06 (m, 2 H), 8.01 – 7.95 (m, 3 H), 7.71 – 7.65 (m, 2 H), 7.64 – 7.58 (m, 2 H), 7.32 (s, 1 H), 7.21 – 7.15 (m, 2 H), 7.10 – 7.03 (m, 7 H), 7.00 (s, 1 H), 6.93 (s, 1 H), 6.87 – 6.82 (m, 4 H), 2.34 (s, 3 H), 2.27 (s, 6 H), 2.09 (s, 9 H), 2.07 – 2.04 (m, 6 H), 2.00 (s, 3 H), 1.95 (s, 3 H). MS (ESI): m/z = 693.7527 (calc. 693.7520). Anal. calc. for $C_{90}H_{75}F_{12}N_7O_2P_2Ru \cdot CH_3C(O)CH_3 \cdot 2H_2O$ (%): C, 63.05; H, 4.84; N, 5.53. Found: C, 63.20; H, 5.09; N, 5.65.

tolyl-xy$_3$: A solution of **39** (438 mg, $3.70 \cdot 10^{-4}$ mol) and $[Ru(bpy)_2Cl_2]$[113] (179 mg, $3.70 \cdot 10^{-4}$ mol) in ethanol (21 mL) and chloroform (7 mL) was heated to reflux under a N_2-atmosphere for 2 days. The solvent was evaporated and the residue was purified by

column chromatography on silica using a gradient of (1) acetone, (2) acetone/water 9:1 (v:v) and (3) acetone/water 9:1 with 1% saturated aqueous KNO_3 solution as an eluent. The product containing solutions were collected and KPF_6 was added. Acetone was completely evaporated and the aqueous phase was extracted with dichloromethane. The combined organic layers were washed with water, the solvent was evaporated, and the product was dried in vacuo, yielding **tolyl-xy$_3$** as a red solid (157 mg, $8.32 \cdot 10^{-5}$ mol, 22%). ^{1}H-NMR (400 MHz, acetone-d_6): δ (ppm) = 9.02 (d, J = 8.5 Hz, 2 H), 8.90 (d, J = 8.2 Hz, 4 H), 8.40 (d, J = 8.0 Hz, 1 H), 8.38 – 8.33 (m, 6 H), 8.32 – 8.22 (m, 5 H), 8.21 – 8.18 (m, 2 H), 8.11 – 8.08 (m, 2 H), 8.03 – 7.97 (m, 3 H), 7.72 – 7.67 (m, 2 H), 7.64 – 7.59 (m, 2 H), 7.34 (s, 1 H), 7.21 – 7.17 (m, 2 H), 7.15 (s, 1 H), 7.11 (s, 1 H), 7.10 – 7.05 (m, 7 H), 7.03 (s, 1 H), 7.02 (s, 1 H), 7.00 (s, 1 H), 6.97 (s, 1 H), 6.89 – 6.84 (m, 4 H), 2.37 (s, 3 H), 2.28 (s, 6 H), 2.16 (*d*, J = 3.5 Hz, 3 H), 2.12 (s, 3 H), 2.11 – 2.04 (m, 21 H), 2.03 (s, 3 H), 2.01 (d, J = 4.3 Hz, 3 H). MS (ESI): m/z = 797.8154 (calc. 797.8136). Anal. calc. for $C_{106}H_{91}F_{12}N_7O_2P_2Ru \cdot 1.5CH_3C(O)CH_3$ (%): C, 67.27; H, 5.11; N, 4.97. Found: C, 67.08; H, 5.39; N, 5.14.

TMS-xy$_2$-Ru-xy$_2$-TMS: A solution of **13** (143 mg, $2.00 \cdot 10^{-4}$ mol) and $[Ru(bpy)_2Cl_2]$[113] (97 mg, $2.00 \cdot 10^{-4}$ mol) in ethanol (21 mL) and chloroform (7 mL) was heated to reflux under a N_2-atmosphere over night. The solvent was evaporated and the crude product was purified by column chromatography on silica using a gradient of (1) acetone, (2) acetone/water 9:1 (v:v) and (3) acetone/water 9:1 (v:v) with 1% saturated aqueous KNO_3-solution as an eluent. To the combined fractions KPF_6 was added, and acetone was completely evaporated. Subsequently the aqueous phase was extracted with dichloromethane and the combined organic layers were washed with water. The solvent was evaporated and the product was dried in vacuo. **TMS-xy$_2$-Ru-xy$_2$-TMS** was obtained as a red solid (249 mg, $1.75 \cdot 10^{-4}$ mol, 88%). ^{1}H-NMR (400 MHz, acetone-d_6): δ (ppm) = 8.98 (d, J = 8.4 Hz, 2 H), 8.87 (d, J = 8.3 Hz, 4 H), 8.35 – 8.20 (m, 8 H), 8.17 (d, J = 5.3 Hz, 2 H), 8.07 – 8.05 (m, 2 H), 7.69 – 7.64 (m, 2 H), 7.61 – 7.57 (m, 2 H), 7.37 (s, 2 H), 7.15 (s_{br}, 2 H), 6.96 (s_{br}, 2 H), 6.83 (s, 2 H), 2.43 (s, 6 H), 2.06 (s, 3 H), 2.02 (s, 3 H), 2.01 (s, 6 H), 1.99 (s, 6 H), 0.35 (s, 18 H). MS (ESI): m/z = 565.2213 (calc. 565.2204). Anal. calc. for $C_{68}H_{72}F_{12}N_6P_2RuSi_2 \cdot 0.5H_2O \cdot 0.75\ CH_3C(O)CH_3$ (%): C, 57.28; H, 5.30; N, 5.71. Found: C, 57.26; H, 5.67; N, 6.03.

7.3. Synthesis of the pentad and the reference triad

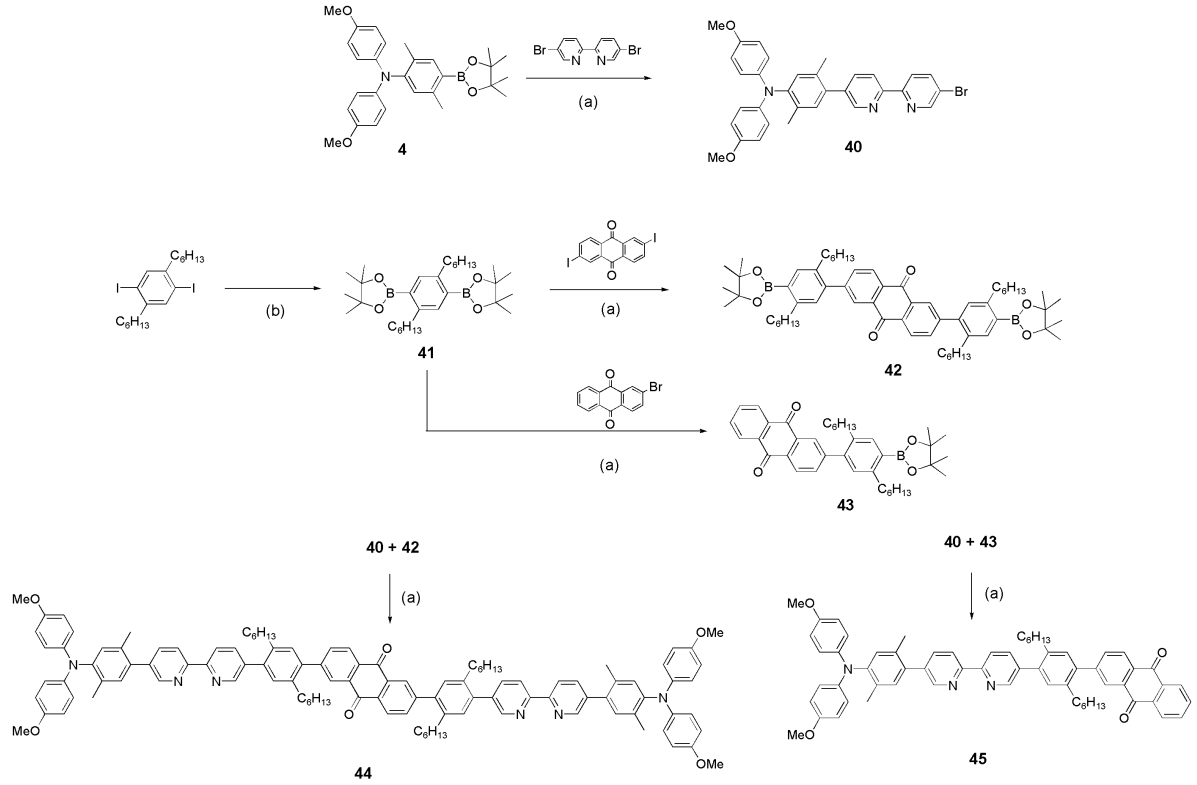

Scheme 7.4 Reaction scheme for the synthesis of the donor-acceptor ligands **44** and **45** for the pentad and triad from Chapter 5. (a) $Pd(PPh_3)_4$, Na_2CO_3 in THF/water; (b) $(Bpin)_2$, KOAc, $Pd(PPh_3)_2Cl_2$ in DMSO.

Synthetic protocols

40: 5,5'-Dibromo-2,2'-bipyridine[111] (1.01 g, 3.23 mmol), **4** (0.99 g, 2.15 mmol), Na_2CO_3 (684 mg, 6.45 mmol) and $Pd(PPh_3)_4$ (124 mg, 0.11 mmol) were suspended in THF (25 mL) and water (5 mL). The biphasic mixture was degassed prior to heating to reflux overnight. Subsequently the phases were separated and the aqueous layer was extracted with dichloromethane. The combined organic layers were dried over Na_2SO_4 and the solvent was removed in vacuo. The crude product was purified by column chromatography on silica using a gradient of pentane/dichloromethane mixtures from 4:1 to 2:1 (v:v) each with 2% methanol. **40** was obtained as a bright yellow solid (590 mg, 1.04 mmol, 48 %). ^{1}H-NMR (400 MHz, $CDCl_3$): δ (ppm) = 8.75 (d, J = 2.3 Hz, 1 H), 8.69 (d, J = 1.8 Hz, 1 H), 8.46 – 8.37 (m, 2 H), 7.97 (dd, J = 8.5 Hz, 2.3 Hz, 1 H), 7.85 (d, J = 8.0 Hz, 1 H), 7.07 (s, 1 H), 6.98 (s, 1 H), 6.95 – 6.89 (m, 4 H), 6.83 – 6.77 (m, 4 H), 3.79 (s, 6 H), 2.21 (s, 3 H), 2.01 (s, 3 H).

41: 1,4-Di-*n*-hexyl-2,5-diiodobenze[114] (1, 7.47 g, 15.0 mmol), bis(pinacol)diboron (9.52 g, 37.5 mmol), KOAc (11.78 g, 120 mmol) and $Pd(PPh_3)_2Cl_2$ (1.05 g, 1.50 mmol) were stirred in DMSO (100 mL) under a nitrogen atmosphere at 90 °C over night. Water (300 mL) and saturated aqueous NH_4Cl-solution (100 mL) were added, and the resulting mixture was extracted with diethyl ether. The combined organic layers were dried over Na_2SO_4, filtered, and the solvent was removed in vacuo. The crude product was purified by repeated column chromatography on silica using pentane/diethyl ether 20:1 (v:v) as an eluent. **41** was obtained as a white solid (5.74 g, 11.5 mmol, 77%). ^{1}H-NMR (400 MHz, $CDCl_3$): δ (ppm) = 7.52 (s, 2 H), 2.83 – 2.78 (m, 4 H), 1.55 – 1.47 (m, 4 H), 1.40 – 1.25 (m, 12 H), 1.33 (s, 24 H), 0.90 - 0.86 (m, 6 H).

42: 2,6-Diiodo-9,10-anthraquinone[115] (753 mg, 1.64 mg), **41** (3.26 g, 6.55 mmol) Na_2CO_3 (1.04 g, 9.82 mmol) and $Pd(PPh_3)_4$ (189 mg, $1.64 \cdot 10^{-4}$ mol) were dissolved in a mixture of toluene (40 mL), ethanol (10 ml) and water (10 mL). The biphasic mixture was degassed prior to stirring at 90°C for three days. The reaction mixture was neutralized with saturated aqueous NH_4Cl-solution, and then extracted with dichloromethane. The combined organic layers were dried over Na_2SO_4, filtered, and the solvent was removed in vacuo. The crude product was purified by repeated column chromatography on silica using pentane/diethyl ether 10:1 (v:v) as an eluent. **42** was obtained as a yellow solid (541 mg, $5.70 \cdot 10^{-4}$ mol, 35%). ^{1}H-NMR (400 MHz, $CDCl_3$): δ (ppm) = 8.37 (d, J = 8.0 Hz, 2 H), 8.31 (d, J = 1.7 Hz, 2 H), 7.76 (dd, J = 8.0 Hz, 1.7 Hz, 2 H), 7.73 (s, 2 H), 7.07 (s, 2 H), 2.92 – 2.87 (m, 4 H), 2.61 – 2.56 (m, 4 H), 1.63 – 1.54 (m, 4 H), 1.50 -1.42 (m, 4 H), 1.39 (s, 24 H), 1.36 -1.25 (m, 12 H), 1.22 -1.10 (m, 12 H), 0.92 – 0.86 (m, 6 H), 0.82 -0.75 (m, 6 H).

43: 2-Bromo-9,10-anthraquinone (287 mg, 1.00 mmol), **41** (1.00 g, 2.00 mmol), Na_2CO_3 (318 mg, 3.00 mmol) and $Pd(PPh_3)_4$ (58 mg, $5.0 \cdot 10^{-5}$ mol) were dissolved in THF (20 mL) and water (5 mL). The reaction mixture was degassed prior to heating to reflux for two days. Subsequently saturated aqueous NH_4Cl-solution (10 mL) was added, and the mixture was extracted with diethyl ether. The organic layers were dried over Na2SO4, filtered, and the solvent was removed in vacuo. The crude product was purified by repeated column chromatography on silica using pentane/ether 10:1 (v:v) as an eluent. **43** was obtained as a yellow solid (261 mg, $4.51 \cdot 10^{-4}$ mol, 45 %). ^{1}H-NMR (400 MHz, $CDCl_3$): δ (ppm) =8.39 – 8.30 (m, 3 H), 8.28 (d, J = 1.8 Hz, 1 H), 7.85 – 7.78 (m, 2 H), 7.75 (dd, J = 8.0 Hz, 1.8 Hz, 1 H), 7.73 (s, 1 H), 7.06 (s, 1 H), 2.93 – 2.85 (m, 2 H), 2.61 – 2.53 (m, 2 H), 1.65 – 1.43 (m, 4 H), 1.38 (s, 12 H), 1.36 – 1.26 (m, 8 H), 1.19 – 1.11 (m, 4 H), 0.93 -0.85 (m, 3 H), 0.80 – 0.74 (m, 3 H).

44: **42** (244 mg, $2.57 \cdot 10^{-4}$ mol), **40** (350 mg, $6.18 \cdot 10^{-4}$ mol), Na_2CO_3 (164 mg, 1.54 mmol) and $Pd(PPh_3)_4$ (30 mg, $2.57 \cdot 10^{-5}$ mol) dissolved in THF (20 mL) and water (4 mL). The reaction mixture was degassed prior to heating to reflux for two days. Subsequently the mixture was extracted with dichloromethane. The combined organic layers were dried over Na_2SO_4, filtered, and the solvent was removed in vacuo. The crude product was purified by column chromatography on silica using a gradient of pentane/diethyl ether mixtures from 5:1 to 1:1 (v:v) with each 2% methanol as an eluent. The ligand **44** was obtained as a dark-yellow solid (364 mg, $2.18 \cdot 10^{-4}$ mol, 85 %). ^{1}H-NMR (400 MHz, $CDCl_3$): δ (ppm) = 8.77 (s_{br}, 4 H), 8.59 (s_{br}, 4 H), 8.44 (d, J = 8.0 Hz, 2 H), 8.39 (d, J = 1.8 Hz, 2 H), 7.92 (s_{br}, 4 H), 7.84 (dd, J = 8.0 Hz, 1.8 Hz, 2 H), 7.25 (s, 2 H), 7.24 (s, 2 H), 7.14 (s, 2 H), 7.00 (s, 2 H), 6.96 -6.90 (m, 8 H), 6.84 – 6.78 (m, 8 H), 3.80 (s, 12 H), 2.69 – 2.61 (m, 8 H), 2.24 (s, 6 H), 2.03 (s, 6 H), 1.58 – 1.48 (m, 8 H), 1.29 – 1.13 (m, 24 H), 0.85 – 0.77 (m, 12 H).

45: **40** (91 mg, 1.60·10-4 mol), **43** (110 mg, $1.90 \cdot 10^{-4}$ mol), Na_2CO_3 (51 mg, $4.80 \cdot 10^{-4}$ mol) and $Pd(PPh_3)_4$ (9.2 mg, $8.0 \cdot 10^{-6}$ mol) were dissolved in THF (8 mL) and water (2 mL). The reaction mixture was degassed prior to heating to reflux overnight. The mixture was extracted with diethyl ether. The combined organic layers were dried over Na_2SO_4, filtered, and the solvents were removed in vacuo. The crude product was purified by column chromatography on silica using pentane/diethyl ether 2:1 (v:v) with 2% MeOH as an eluent. The ligand **45** was obtained as a dark-yellow solid (97 mg, $1.03 \cdot 10^{-4}$ mol, 64 %). ^{1}H-NMR (400 MHz, $CDCl_3$): δ (ppm) = 8.75 (d, J = 1.7 Hz, 2 H), 8.62 – 8.49 (m, 2 H), 8.41 (d, J = 8.0 Hz, 1 H), 8.39 – 8.34 (m, 3 H), 7.93 – 7.86 (m, 2 H), 7.86 – 7.80 (m, 3 H), 7.23 (s, 2 H), 7.13 (s, 1 H), 7.00 (s, 1 H), 6.96 – 6.90 (m, 4 H), 6.84 – 6.77 (m, 4 H), 3.80 (s, 6 H), 2.67 – 2.60 (m, 4 H), 2.24 (s, 3 H), 2.03 (s, 3 H), 1.56 – 1.46 (m, 4 H), 1.35 – 1.11 (m, 12 H), 0.84 – 0.75 (m, 6 H).

pentad: The Ligand **44** (364 mg, $2.18 \cdot 10^{-4}$ mol) and $[Ru(bpy)_2Cl_2]$[113] (232 mg, $4.80 \cdot 10^{-4}$ mol) were dissolved in ethanol (21 mL) and chloroform (7 mL). The reaction mixture was heated to reflux under a nitrogen atmosphere overnight. The solvent was removed in vacuo and the crude product purified by column chromatography on silica with first acetone until all purple precursor was removed from the column. Afterwards the complex was eluted with a mixture of acetone/water 9:1 (v:v) with additional 1% saturated KNO_3-solution. Subsequently, all acetone was removed under reduced pressure, the red solid was filtered off, and washed thoroughly with water and diethyl ether. The product was collected by rinsing the frit with acetonitrile. Removal of the solvent in vacuo yielded the **pentad** as a red crystalline solid (355 mg, $1.29 \cdot 10^{-4}$ mol, 59 %). ^{1}H-NMR (400 MHz, CD_3OD): δ (ppm) = 8.86 – 8.72 (m, 12 H), 8.40 (d, J = 8.0 Hz, 2 H), 8.23 – 8.10 (m ,14

H), 8.08 (d, J = 5.6 Hz, 4 H), 7.93 (d, J = 5.6 Hz, 2 H), 7.89 (d, J = 5.6 Hz, 2 H), 7.83 (dd, J = 8.0 Hz, 1.8 Hz, 2 H), 7.75 (d, J = 1.8 Hz, 2 H), 7.72 (d, J = 1.8 Hz, 2 H), 7.63 - 7.56 (m, 4 H), 7.52 – 7.46 (m, 4 H), 7.23 (s, 2 H), 7.18 (s, 2 H), 7.08 (s, 2 H), 6.84 – 6.75 (m, 18 H), 3.76 (s, 12 H), 2.65 – 2.58 (m, 4 H), 2.44 – 2.35 (m, 2 H), 2.25 2.17 (m, 2 H), 1.94 (s, 6 H), 1.82 (s, 6 H), 1.47 – 1.27 (m, 8 H), 1.21 – 1.06 (m, 18 H), 1.01 – 0.88 (m, 6 H), 0.80 (t, J = 7.3 Hz, 6 H), 0.74 (t, 6 H, J = 6.9 Hz). MS (ESI): m/z = 624.5015 (calc. 624.4993). Anal. calc. for $C_{154}H_{150}N_{18}O_{18}Ru_2 \cdot 5\ H_2O$ (%): C, 65.29; H, 5.69; N, 8.90. Found: C, 65.01; H, 5.64; N, 9.01.

triad: Ligand **45** (97 mg, $1.03 \cdot 10^{-4}$ mol) and $[Ru(bpy)_2Cl_2]$[113] (50 mg, $1.03 \cdot 10^{-4}$ mol) in ethanol (12 mL) and chloroform (4 mL) were heated to reflux under a nitrogen atmosphere overnight. The solvent was removed in vacuo and the crude product purified by column chromatography on silica with first acetone until all purple precursor was removed from the column. Afterwards the complex was eluted with a mixture of acetone/water 9:1 (v:v) with additional 1% saturated KNO_3-solution. Subsequently, all acetone was removed under reduced pressure, the red solid was filtered off, and washed thoroughly with water and diethyl ether. The product was collected by rinsing the frit with acetonitrile. Removal of the solvent in vacuo yielded the title compound as a red crystalline solid (105 mg, $7.12 \cdot 10^{-5}$ mol, 69 %). ^{1}H-NMR (400 MHz, CD_3OD): δ (ppm) = 8.86 – 8.71 (m, 6 H), 8.37 (d, J = 8.0 Hz, 1 H), 8.35 – 8.29 (m, 2 H), 8.23 – 8.15 (m, 5 H), 8.15 – 8.09 (m, 2 H), 8.07 (d, J = 6.0 Hz, 2 H), 7.94 – 7.87 (m, 4 H), 7.80 (dd, J = 8.0 Hz, 1.8 Hz, 1 H), 7.75 (d, J = 1.8 Hz, 1 H), 7.72 (d, J = 1.8 Hz, 1 H), 7.63 -7.56 (m, 2 H), 7.52 – 7.46 (m, 2 H), 7.20 (s, 1 H), 7.16 (s, 1 H), 7.07 (s, 1 H), 6.85 – 6.75 (m, 9 H), 3.76 (s, 6 H), 2.63 – 2.56 (m, 2 H), 2.44 – 2.34 (m, 1 H), 2.25 – 2.17 (m, 1 H), 1.94 (s, 3 H), 1.82 (s, 3 H), 1.47 – 1.26 (m, 4 H), 1.21 – 1.06 (m, 8 H), 1.02 – 0.87 (m, 4 H), 0.80 (t, J = 7.3 Hz, 3 H), 0.73 (t, J = 6.9 Hz, 3 H). MS (ESI): m/z = 675.7631 (calc. 675.7613). Anal. calc. for $C_{84}H_{79}N_9O_{10}Ru \cdot 2\ H_2O \cdot 0.5\ CH_3CN$ (%): C, 66.63; H, 5.56; N, 8.68. Found: C, 66.54; H, 5.81; N, 8.67.

8. Appendix

Decay data used for the Arrhenius plots in Chapter 4

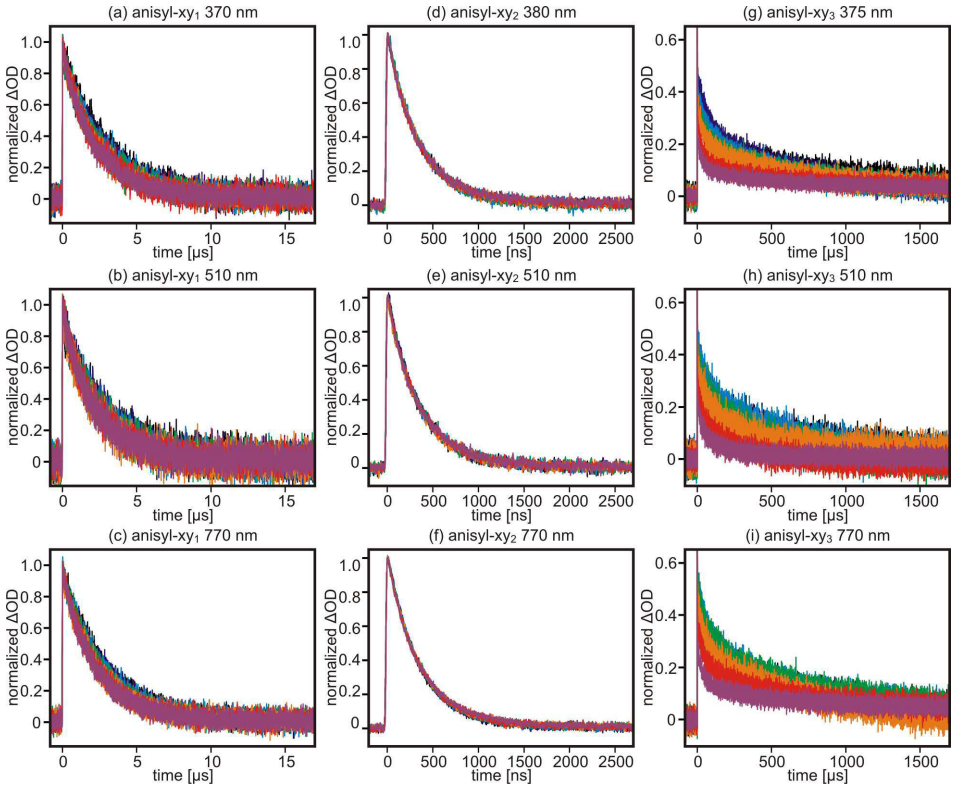

Figure A1 Temporal evolution of the transient absorption signals of 20 µM solutions of (a-c) anisyl-xy_1, (d-f) anisyl-xy_2 and (g-i) anisyl-xy_3 in deoxygenated acetonitrile/water 1:1 (v:v) at 370 nm, 510 nm and 770 nm. The temperature was varied between 5 °C and 65 °C. The color code of the individual traces is: 5 °C (black), 15 °C (dark blue), 25 °C (light blue), 35 °C (green), 45 °C (orange), 55 °C (red), 65 °C (purple).

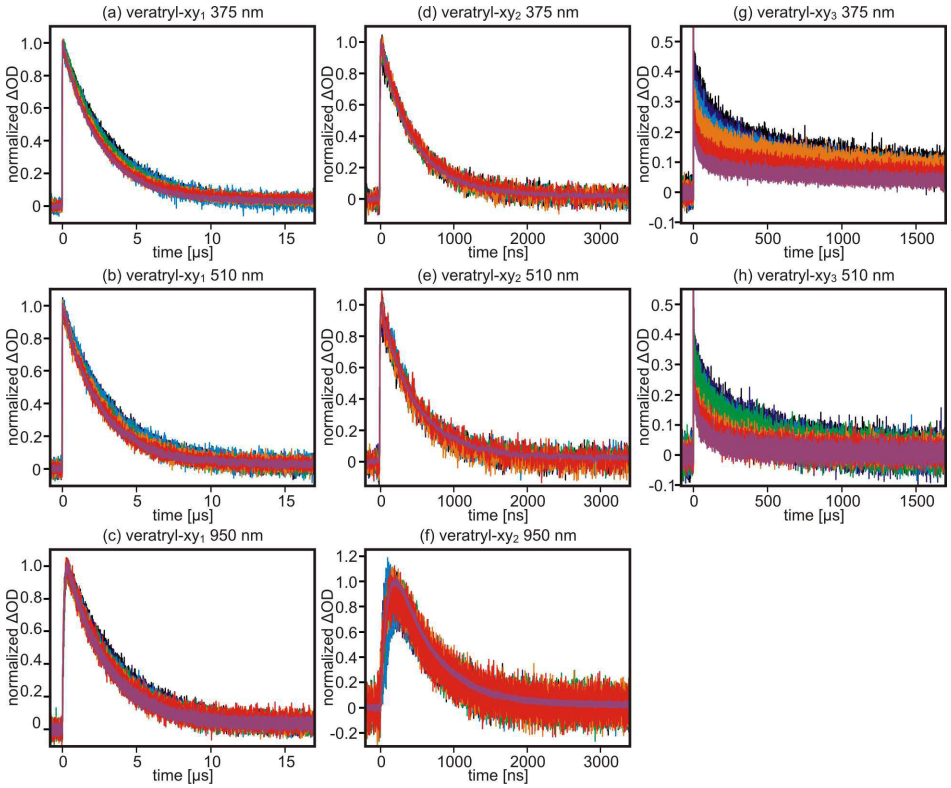

Figure A2 Temporal evolution of the transient absorption signals of 20 µM solutions of (a-c) veratryl-xy_1, (d-f) veratryl-xy_2 and (g-h) veratryl-xy_3 in deoxygenated acetonitrile/water 1:1 (v:v) at 375 nm, 510 nm and 950 nm. The temperature was varied between 5 °C and 65 °C. The color code of the individual traces is: 5 °C (black), 15 °C (dark blue), 25 °C (light blue), 35 °C (green), 45 °C (orange), 55 °C (red), 65 °C (purple). Measurements of veratryl-xy_3 at 950 nm were omitted due to poor signal-to-noise ratio. The rise of the signals at 950 nm corresponds to the response time of the NIR detector (100 ns).

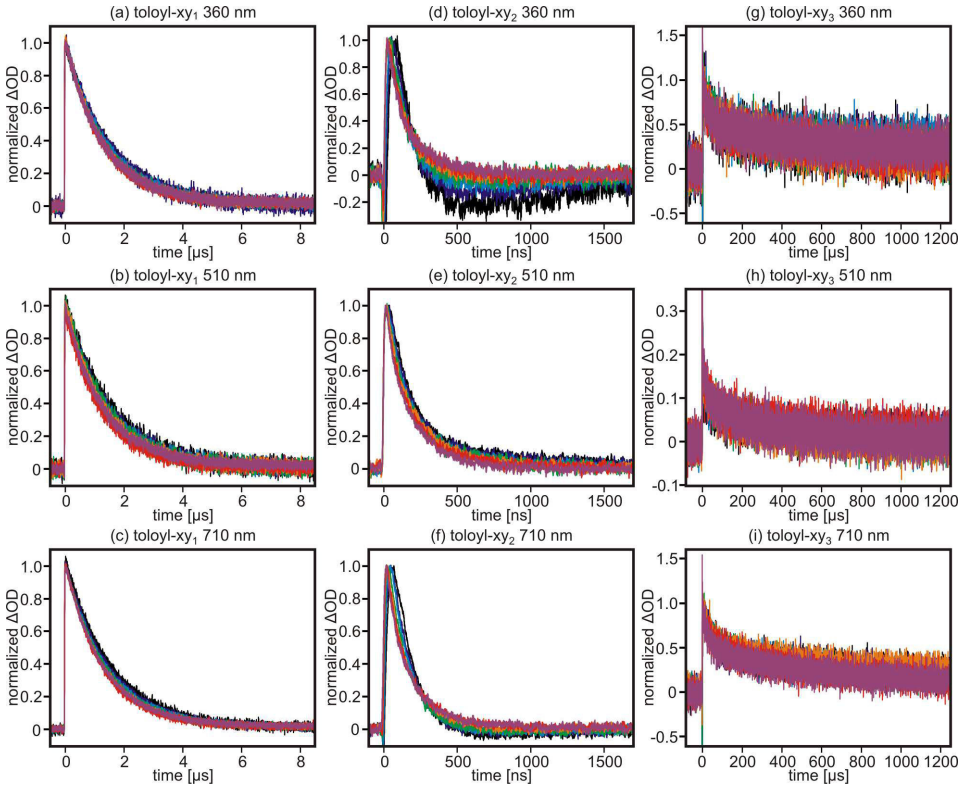

Figure A3 Temporal evolution of the transient absorption signals of 20 µM solutions of (a-c) tolyl-xy_1, (d-f) tolyl-xy_2 and (g-i) tolyl-xy_3 in deoxygenated acetonitrile/water 1:1 (v:v) at 360 nm, 510 nm and 710 nm. The temperature was varied between 5 °C and 65 °C. The color code of the individual traces is: 5 °C (black), 15 °C (dark blue), 25 °C (light blue), 35 °C (green), 45 °C (orange), 55 °C (red), 65 °C (purple). For tolyl-xy_2 the decay signals were fitted to process A→B→C reaction kinetics with the rate constant for charge recombination represented by B→C. An additional, independent rate constant due to an excited state decay of minor impurities had to be included.

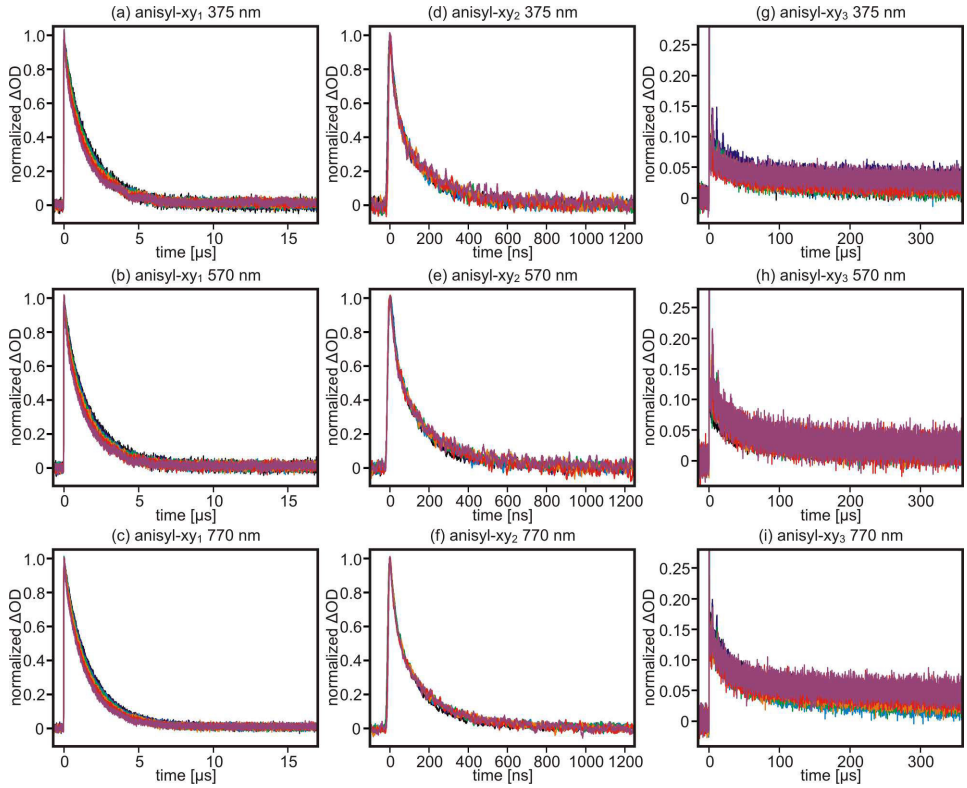

Figure A4 Temporal evolution of the transient absorption signals of 20 µM solutions of (a-c) anisyl-xy_1, (d-f) anisyl-xy_2 and (g-i) anisyl-xy_3 in deoxygenated acetonitrile at 375 nm, 570 nm and 770 nm. The temperature was varied between 5 °C and 65 °C. The color code of the individual traces is: 5 °C (black), 15 °C (dark blue), 25 °C (light blue), 35 °C (green), 45 °C (orange), 55 °C (red), 65 °C (purple).

Energy estimates for the individual states of the pentad from Chapter 5 in neat acetonitrile

- TAA-Ru^{II}-AQ-Ru^{II}-TAA. This state is the ground state and its energy is set to **0.00 eV**.
- TAA-$^{*}\mathbf{Ru^{II}}$-AQ-Ru^{II}-TAA. This state corresponds to the ^{3}MLCT state of $Ru(bpy)_3^{2+}$ with an energy of **2.12 eV**.[86]
- TAA-$\mathbf{Ru^{III}}$-$\mathbf{AQ^{-}}$-Ru^{II}-TAA. E = e·[$E(Ru^{III/II})$ - $E(AQ^{0/-})$] = e·(1.33 V + 0.84 V) = **2.17 eV**.
- $\mathbf{TAA^{+}}$-$\mathbf{Ru^{I}}$-AQ-Ru^{II}-TAA. E = e·[$E(TAA^{+/0})$ - $E(Ru^{II/I})$] = e·(0.69 V + 1.26 V) = **1.95 eV**.
- $\mathbf{TAA^{+}}$-Ru^{II}-$\mathbf{AQ^{-}}$-Ru^{II}-TAA. This is the first charge-separated state (CSS1). E = e·[$E(TAA^{+/0})$ - $E(AQ^{0/-})$] = e·(0.69 V + 0.84 V) = **1.53 eV**.

- **TAA^{+}**-Ru^{II}-**AQ^{-}**-***Ru^{II}**-TAA. The energy of this state was calculated relative to the CSS1 by adding the ^{3}MLCT energy of Ru(bpy)$_3^{2+}$. E = E(CSS1) + 2.12 eV = **3.65 eV**.
- **TAA^{+}**-Ru^{II}-**AQ^{2-}**-**Ru^{III}**-TAA. E = e·[E(TAA$^{+/0}$) + E(Ru$^{III/II}$) - E(AQ$^{0/-}$) - E(AQ$^{-/2-}$)] = e·(0.69 V + 1.33 V + 0.84 V + 1.34 V) = **4.20 eV**.
- **TAA^{+}**-Ru^{II}-**AQ^{-}**-Ru^{I}-**TAA^{+}**. E = e·[2·E(TAA$^{+/0}$) - E(AQ$^{0/-}$) - E(Ru$^{II/I}$)] = e·(2·0.69 V + 0.84 V + 1.26 V) = **3.48 eV**.
- **TAA^{+}**-Ru^{II}-**AQ^{2-}**-Ru^{II}-**TAA^{+}**. This is the second charge-separated state (CSS2). E = e·[2·E(TAA$^{+/0}$) - E(AQ$^{0/-}$) - E(AQ$^{-/2-}$)] = e·(2·0.69 V + 0.84 V + 1.34 V) = **3.56 eV**.

Energy estimates for the individual states of the pentad from Chapter 5 in acetonitrile in presence of chloroacetic acid

- TAA-Ru^{II}-AQ-Ru^{II}-TAA. This state is the ground state and its energy is set to **0.00 eV**.
- TAA-***Ru^{II}**-AQ-Ru^{II}-TAA. This state corresponds to the ^{3}MLCT state of Ru(bpy)$_3^{2+}$ with an energy of **2.12 eV**.[86]
- TAA-**Ru^{III}**-**AQ^{-}**-Ru^{II}-TAA. E = e·[E(Ru$^{III/II}$) - E(AQ$^{0/-}$)] = e·(1.33 V + 0.84 V) = **2.17 eV**.
- **TAA^{+}**-**Ru^{I}**-AQ-Ru^{II}-TAA. E = e·[E(TAA$^{+/0}$) - E(Ru$^{II/I}$)] = e·(0.69 V + 1.26 V) = **1.95 eV**.
- **TAA^{+}**-Ru^{II}-**AQ^{-}**-Ru^{II}-TAA. E = e·[E(TAA$^{+/0}$) - E(AQ$^{0/-}$)] = e·(0.69 V + 0.84 V) = **1.53 eV**.
- **TAA^{+}**-Ru^{II}-**AQH**-Ru^{II}-TAA. This is the first charge-separated state (CSS1). E = e·[E(TAA$^{+/0}$) - E(AQ$^{0/-}$)] - 0.059 eV·[pK_A(BQH·) - pK_A(CH$_2$ClCOOH)] = e·(0.69 V + 0.84 V) - 0.059 eV·(23.1 - 18.8) = **1.28 eV**.
- **TAA^{+}**-Ru^{II}-**AQH**-***Ru^{II}**-TAA. The energy of this state was calculated relative to the CSS1 by adding the ^{3}MLCT energy of Ru(bpy)$_3^{2+}$. E = E(CSS1) + 2.12 eV = **3.40 eV**.
- **TAA^{+}**-Ru^{II}-**AQH**-**Ru^{I}**-**TAA^{+}**. E = e·[2·E(TAA$^{+/0}$) - E(AQ$^{0/-}$) - E(Ru$^{II/I}$)] - 0.059 eV·[pK_A(BQH·) - pK_A(CH$_2$ClCOOH)] = e·(2·0.69 V + 0.84 V + 1.26 V) - 0.059 eV·(23.1 - 18.8) = **3.23 eV**.

- **TAA^{+}**-Ru^{II}-**AQH^{-}**-**Ru^{III}**-TAA. E = e·[E(TAA$^{+/0}$) + E(Ru$^{III/II}$) - E(AQ$^{0/-}$) - E(AQ$^{-/2-}$)] - 0.059 eV·[pK_A(BQH^{-}) - pK_A($CH_2ClCOOH$)] = e·(0.69 V + 1.33 V + 0.84 V + 1.34 V) - 0.059 eV·(38.3 - 18.8) = **3.05 eV**.
- **TAA^{+}**-Ru^{II}-**AQH^{-}**-Ru^{II}-**TAA^{+}**. E = e·[2·E(TAA$^{+/0}$) - E(AQ$^{0/-}$) - E(AQ$^{-/2-}$)] - 0.059 eV·[pK_A(BQH^{-}) - pK_A($CH_2ClCOOH$)] = e·(2·0.69 V + 0.84 V + 1.34 V) - 0.059 eV·(38.3 - 18.8) = **2.41 eV**.
- **TAA^{+}**-Ru^{II}-**AQH$_2$**-Ru^{II}-**TAA^{+}**. This is the second charge-separated state (CSS2). E = e·[2·E(TAA$^{+/0}$) - E(AQ$^{0/-}$) - E(AQ$^{-/2-}$)] - 0.059 eV·[pK_A(BQH^{-}) - pK_A($CH_2ClCOOH$)] - 0.059 eV·[pK_A(BQH$_2$) - pK_A($CH_2ClCOOH$)] = e·(2·0.69 V + 0.84 V + 1.34 V) - 0.059 eV·(38.3 - 18.8) - 0.059 eV·(31.7 - 18.8) = **1.66 eV**.

Bibliography

[1] Gust, D.; Moore, T. A.; Moore, A. L. *Acc. Chem. Res.* **2009**, *42*, 1890–1898.

[2] BP Statistical Review of World Energy 2015.

[3] Ciamician, G. *Science* **1912**, *36*, 385–94.

[4] Schlapbach, L.; Zuttel, A. *Nature* **2001**, *414*, 353–358.

[5] van Troostwijk, A. P.; Deiman, J. R. *Obs. Phys.* **1789**, *35*, 369.

[6] de Levie, R. *J. Electroanal. Chem.* **1999**, *476*, 92–93.

[7] Dau, H.; Limberg, C.; Reier, T.; Risch, M.; Roggan, S.; Strasser, P. *ChemCatChem* **2010**, *2*, 724–761.

[8] Barber, J. *Chem. Soc. Rev.* **2009**, *38*, 185–196.

[9] Barber, J. *Q. Rev. Biophys.* **2003**, *36*, 71–89.

[10] Tommos, C.; Babcock, G. T. *Acc. Chem. Res.* **1998**, *31*, 18–25.

[11] Dempsey, J. L.; Winkler, J. R.; Gray, H. B. *Chem. Rev.* **2010**, *110*, 7024–7039.

[12] Holzwarth, A. R.; Müller, M. G.; Reus, M.; Nowaczyk, M.; Sander, J.; Rögner, M. *Proc. Natl. Acad. Sci. U.S.A.* **2006**, *103*, 6895–6900.

[13] Weinberg, D. R.; Gagliardi, C. J.; Hull, J. F.; Murphy, C. F.; Kent, C. A.; Westlake, B. C.; Paul, A.; Ess, D. H.; McCafferty, D. G.; Meyer, T. J. *Chem. Rev.* **2012**, *112*, 4016–4093.

[14] Ferreira, K. N.; Iverson, T. M.; Maghlaoui, K.; Barber, J.; Iwata, S. *Science* **2004**, *303*, 1831–1838.

[15] Umena, Y.; Kawakami, K.; Shen, J. R.; Kamiya, N. *Nature* **2011**, *473*, 55–60.

[16] Dau, H.; Haumann, M. *Coord. Chem. Rev.* **2008**, *252*, 273–295.

[17] Atkins, P. W. *Physical Chemistry*, 8th ed.; Oxford University Press, 2006.

[18] Haga, M. A.; Dodsworth, E. S.; Eryavec, G.; Seymour, P.; Lever, A. B. P. *Inorg. Chem.* **1985**, *24*, 1901–1906.

[19] Gade, L. H. *Koordinationschemie*, 1st ed.; Viley-VCH: Weinheim, 1998.

[20] Damrauer, N. H.; Cerullo, G.; Yeh, A.; Boussie, T. R.; Shank, C. V.; McCusker, J. K. *Science* **1997**, *275*, 54–57.

[21] Marcus, R. A. *J. Chem. Phys.* **1956**, *24*, 966–978.

[22] Marcus, R. A. *J. Chem. Phys.* **1956**, *24*, 979–989.

[23] Marcus, R. A. *J. Chem. Phys.* **1957**, *26*, 867–871.

[24] Marcus, R. A. *J. Chem. Phys.* **1957**, *26*, 872–877.

[25] Eyring, H. *J. Chem. Phys.* **1935**, *3*, 107–115.

[26] Miller, J. R.; Calcaterra, L. T.; Closs, G. L. *J. Am. Chem. Soc.* **1984**, *106*, 3047–3049.

[27] Miller, J. R.; Beitz, J. V.; Huddleston, R. K. *J. Am. Chem. Soc.* **1984**, *106*, 5057–5068.

[28] Closs, G. L.; Calcaterra, L. T.; Green, N. J.; Penfield, K. W.; Miller, J. R. *J. Phys. Chem.* **1986**, *90*, 3673–3683.

[29] Closs, G. L.; Miller, J. R. *Science* **1988**, *240*, 440–447.

[30] Creutz, C.; Taube, H. *J. Am. Chem. Soc.* **1969**, *91*, 3988–3989.

[31] Wenger, O. S. *Acc. Chem. Res.* **2011**, *44*, 25–35.

[32] Edwards, P. P.; Gray, H. B.; Lodge, M. T. J.; Williams, R. J. P. *Angew. Chem. Int. Ed.* **2008**, *47*, 6758–6765.

[33] Mayer, J. M. *Annu. Rev. Phys. Chem.* **2004**, *55*, 363–390.

[34] Meyer, T. J.; Huynh, M. H. V.; Thorp, H. H. *Angew. Chem. Int. Ed.* **2007**, *46*, 5284–5304.

[35] Huynh, M. H. V.; Meyer, T. J. *Chem. Rev.* **2007**, *107*, 5004–5064.

[36] Costentin, C.; Robert, M.; Savéant, J.-M. *Acc. Chem. Res.* **2010**, *43*, 1019–1029.

[37] Reece, S. Y.; Nocera, D. G. *Annu. Rev. Biochem.* **2009**, *78*, 673–699.

[38] Hodgkiss, J. M.; Damrauer, N. H.; Presse, S.; Rosenthal, J.; Nocera, D. G. *J. Phys. Chem. B* **2006**, *110*, 18853–18858.

[39] Kuss-Petermann, M.; Wenger, O. S. *J. Phys. Chem. A* **2013**, *117*, 5726–5733.

[40] Irebo, T.; Zhang, M.-T.; Markle, T. F.; Scott, A. M.; Hammarström, L. *J. Am. Chem. Soc.* **2012**, *134*, 16247–16254.

[41] Pizano, A. A.; Yang, J. L.; Nocera, D. G. *Chem. Sci.* **2012**, *3*, 2457–2461.

[42] Zhang, M.-T.; Irebo, T.; Johansson, O.; Hammarström, L. *J. Am. Chem. Soc.* **2011**, *133*, 13224–13227.

[43] Markle, T. F.; Rhile, I. J.; Mayer, J. M. *J. Am. Chem. Soc.* **2011**, *133*, 17341–17352.

[44] Costentin, C.; Robert, M.; Savéant, J. M.; Tard, C. *Phys. Chem. Chem. Phys.* **2011**, *13*, 5353–5358.

[45] Irebo, T.; Reece, S. Y.; Sjödin, M.; Nocera, D. G.; Hammarström, L. *J. Am. Chem. Soc.* **2007**, *129*, 15462–15464.

[46] Kalyanasundaram, K.; Grätzel, M. *Angew. Chem. Int. Ed.* **1979**, *18*, 701–702.

[47] Konduri, R.; Ye, H. W.; MacDonnell, F. M.; Serroni, S.; Campagna, S.; Rajeshwar, K. *Angew. Chem. Int. Ed.* **2002**, *41*, 3185–3187.

[48] Konduri, R.; de Tacconi, N. R.; Rajeshwar, K.; MacDonnell, F. M. *J. Am. Chem. Soc.* **2004**, *126*, 11621–11629.

[49] Chiorboli, C.; Fracasso, S.; Scandola, F.; Campagna, S.; Serroni, S.; Konduri, R.; MacDonnell, F. M. *Chem. Commun.* **2003**, 1658–1659.

[50] Karlsson, S.; Boixel, J.; Pellegrin, Y.; Blart, E.; Becker, H.-C.; Odobel, F.; Hammarström, L. *J. Am. Chem. Soc.* **2010**, *132*, 17977–17979.

[51] Karlsson, S.; Boixel, J.; Pellegrin, Y.; Blart, E.; Becker, H.-C.; Odobel, F.; Hammarström, L. *Faraday Discuss.* **2012**, *155*, 233–252.

[52] Oneil, M. P.; Niemczyk, M. P.; Svec, W. A.; Gosztola, D.; Gaines, G. L.; Wasielewski, M. R. *Science* **1992**, *257*, 63–65.

[53] Imahori, H.; Hasegawa, M.; Taniguchi, S.; Aoki, M.; Okada, T.; Sakata, Y. *Chem. Lett.* **1998**, 721–722.

[54] Naqvi, K. R.; Staerk, H.; Gillbro, T. *Chem. Phys. Lett.* **1977**, *49*, 160–164.

[55] Knight, T. E.; McCusker, J. K. *J. Am. Chem. Soc.* **2010**, *132*, 2208–2221.

[56] Guo, D.; Knight, T. E.; McCusker, J. K. *Science* **2011**, *334*, 1684–1687.

[57] Hammes-Schiffer, S.; Stuchebrukhov, A. A. *Chem. Rev.* **2010**, *110*, 6939–6960.

[58] Hammarström, L.; Styring, S. *Energy Environ. Sci.* **2011**, *4*, 2379–2388.

[59] Hanss, D.; Wenger, O. S. *Inorg. Chem.* **2008**, *47*, 9081–9084.

[60] Hanss, D.; Wenger, O. S. *Inorg. Chem.* **2009**, *48*, 671–680.

[61] Concepcion, J. J.; Brennaman, M. K.; Deyton, J. R.; Lebedeva, N. V.; Forbes, M. D. E.; Papanikolas, J. M.; Meyer, T. J. *J. Am. Chem. Soc.* **2007**, *129*, 6968–6969.

[62] Lebedeva, N. V.; Schmidt, R. D.; Concepcion, J. J.; Brennaman, M. K.; Stanton, I. N.; Therien, M. J.; Meyer, T. J.; Forbes, M. D. E. *J. Phys. Chem. A* **2011**, *115*, 3346–3356.

[63] Cape, J. L.; Bowman, M. K.; Kramer, D. M. *J. Am. Chem. Soc.* **2005**, *127*, 4208–4215.

[64] Bronner, C.; Wenger, O. S. *J. Phys. Chem. Lett.* **2012**, *3*, 70–74.

[65] Bronner, C.; Wenger, O. S. *Inorg. Chem.* **2012**, *51*, 8275–8283.

[66] Nomrowski, J.; Wenger, O. S. *Inorg. Chem.* **2015**, *54*, 3680–3687.

[67] Alam, M. M.; Sato, M.; Watanabe, A.; Akasaka, T.; Ito, O. *J. Phys. Chem. A* **1998**, *102*, 7447–7451.

[68] Nauser, T.; Koppenol, W. H.; Schöneich, C. *J. Phys. Chem. B* **2012**, *116*, 5329–5341.

[69] Kuss-Petermann, M. *Synthese und Charakterisierung neuer Donor-Akzeptor-Verbindungen zum protonengekoppelten Elektronentransfer*; Diploma Thesis, Universität Göttingen, 2011.

[70] Moser, C. C.; Keske, J. M.; Warncke, K.; Farid, R. S.; Dutton, P. L. *Nature* **1992**, *355*, 796–802.

[71] Cordes, M.; Giese, B. *Chem. Soc. Rev.* **2009**, *38*, 892–901.

[72] Brunschwig, B. S.; Ehrenson, S.; Sutin, N. *J. Am. Chem. Soc.* **1984**, *106*, 6858–6859.

[73] Murata, S.; Tachiya, M. *J. Phys. Chem.* **1996**, *100*, 4064–4070.

[74] Tachiya, M.; Murata, S. *J. Phys. Chem.* **1992**, *96*, 8441–8444.

[75] Weiss, E. A.; Ahrens, M. J.; Sinks, L. E.; Gusev, A. V.; Ratner, M. A.; Wasielewski, M. R. *J. Am. Chem. Soc.* **2004**, *126*, 5577–5584.

[76] Stangel, C.; Schubert, C.; Kuhri, S.; Rotas, G.; Margraf, J. T.; Regulska, E.; Clark, T.; Torres, T.; Tagmatarchis, N.; Coutsolelos, A. G.; Guldi, D. M. *Nanoscale* **2015**, *7*, 2597–2608.

[77] Rau, H.; Frank, R.; Greiner, G. *J. Phys. Chem.* **1986**, *90*, 2476–2481.

[78] Hankache, J.; Wenger, O. S. *Phys. Chem. Chem. Phys.* **2012**, *14*, 2685–2692.

[79] Hankache, J.; Niemi, M.; Lemmetyinen, H.; Wenger, O. S. *J. Phys. Chem. A* **2012**, *116*, 8159–8168.

[80] Hankache, J.; Wenger, O. S. *Chem. Eur. J.* **2012**, *18*, 6443–6447.

[81] Hankache, J.; Wenger, O. S. *Chem. Commun.* **2011**, *47*, 10145–10147.

[82] Rao, P. S.; Hayon, E. *J. Phys. Chem.* **1973**, *77*, 2274–2276.

[83] Quan, M.; Sanchez, D.; Wasylkiw, M. F.; Smith, D. K. *J. Am. Chem. Soc.* **2007**, *129*, 12847–12856.

[84] Weller, A. *Z. Phys. Chem.* **1982**, *133*, 93–98.

[85] Gagliardi, L. G.; Castells, C. B.; Rafols, C.; Roses, M.; Bosch, E. *J. Chem. Eng. Data* **2007**, *52*, 1103–1107.

[86] Roundhill, D. M. *Photochemistry and Photophysics of Metal Complexes*; Plenum Press: New York, 1994.

[87] Babaei, A.; Connor, P. A.; McQuillan, A. J.; Umapathy, S. *J. Chem. Ed.* **1997**, *74*, 1200–1204.

[88] Cunningham, G. P.; Vidulich, G. A.; Kay, R. L. *J. Chem. Eng. Data* **1967**, *12*, 336–337.

[89] Isied, S. S.; Vassilian, A.; Wishart, J. F.; Creutz, C.; Schwarz, H. A.; Sutin, N. *J. Am. Chem. Soc.* **1988**, *110*, 635–637.

[90] Albinsson, B.; Eng, M. P.; Pettersson, K.; Winters, M. U. *Phys. Chem. Chem. Phys.* **2007**, *9*, 5847–5864.

[91] Yonemoto, E. H.; Saupe, G. B.; Schmehl, R. H.; Hubig, S. M.; Riley, R. L.; Iverson, B. L.; Mallouk, T. E. *J. Am. Chem. Soc.* **1994**, *116*, 4786–4795.

[92] Bertie, J. E.; Lan, Z. D. *J. Phys. Chem. B* **1997**, *101*, 4111–4119.

[93] Sjödin, M.; Styring, S.; Åkermark, B.; Sun, L. C.; Hammarström, L. *J. Am. Chem. Soc.* **2000**, *122*, 3932–3936.

[94] Hankache, J.; Niemi, M.; Lemmetyinen, H.; Wenger, O. S. *Inorg. Chem.* **2012**, *51*, 6333–6344.

[95] Weiss, E. A.; Tauber, M. J.; Kelley, R. F.; Ahrens, M. J.; Ratner, M. A.; Wasielewski, M. R. *J. Am. Chem. Soc.* **2005**, *127*, 11842–11850.

[96] Bonn, A. G.; Wenger, O. S. *Chimia* **2015**, *69*, 17–21.

[97] Wouters, K. L.; de Tacconi, N. R.; Konduri, R.; Lezna, R. O.; MacDonnell, F. M. *Photosynth. Res.* **2006**, *87*, 41–55.

[98] Song, W.; Ito, A.; Binstead, R. A.; Hanson, K.; Luo, H.; Brennaman, M. K.; Concepcion, J. J.; Meyer, T. J. *J. Am. Chem. Soc.* **2013**, *135*, 11587–11594.

[99] Bonn, A. G.; Neuburger, M.; Wenger, O. S. *Inorg. Chem.* **2014**, *53*, 11075–11085.

[100] Warren, J. J.; Tronic, T. A.; Mayer, J. M. *Chem. Rev.* **2010**, *110*, 6961–7001.

[101] Kütt, A.; Leito, I.; Kaljurand, I.; Soovali, L.; Vlasov, V. M.; Yagupolskii, L. M.; Koppel, I. A. *J. Org. Chem.* **2006**, *71*, 2829–2838.

[102] Muckerman, J. T.; Skone, J. H.; Ning, M.; Wasada-Tsutsui, Y. *Biochim. Biophys. Acta* **2013**, *1827*, 882–891.

[103] Jin, B. K.; Li, L.; Huang, J. L.; Zhang, S. Y.; Tian, Y. P.; Yang, J. X. *Anal. Chem.* **2009**, *81*, 4476–4481.

[104] Jin, B. K.; Huang, J. L.; Zhao, A. K.; Zhang, S. Y.; Tian, Y. P.; Yang, J. X. *J. Electroanal. Chem.* **2010**, *650*, 116–126.

[105] Ritschl, F. *Spectrochim. Acta A* **1967**, *23*, 655–675.

[106] Cheng, W. X.; Jin, B. K.; Huang, P.; Cheng, L. J.; Zhang, S. Y.; Tian, Y. P. *J. Phys. Chem. C* **2013**, *117*, 3940–3948.

[107] Pal, H.; Mukherjee, T.; Mittal, J. P. *J. Chem. Soc. Faraday Trans.* **1994**, *90*, 711–716.

[108] Rath, M. C.; Pal, H.; Mukherjee, T. *Radiat. Phys. Chem.* **1996**, *47*, 221–227.

[109] Das, S.; Bhattacharya, A.; Mandal, P. C.; Rath, M. C.; Mukherjee, T. *Radiat. Phys. Chem.* **2002**, *65*, 93–100.

[110] Freys, J. C.; Wenger, O. S. *Eur. J. Inorg. Chem.* **2010**, 5509–5516.

[111] Bai, X. L.; Liu, X. D.; Wang, M.; Kang, C. Q.; Gao, L. X. *Synthesis* **2005**, *3*, 458–464.

[112] Miyake, Y.; Wu, M.; Rahman, M. J.; Iyoda, M. *Chem. Commun.* **2005**, 411–413.

[113] Sullivan, B. P.; Salmon, D. J.; Meyer, T. J. *Inorg. Chem.* **1978**, *17*, 3334–3341.

[114] Mössinger, D.; Jester, S.-S.; Sigmund, E.; Müller, U.; Höger, S. *Macromolecules* **2009**, *42*, 7974–7978.

[115] Li, Z.; Siklos, M.; Pucher, N.; Cicha, K.; Ajami, A.; Husinsky, W.; Rosspeintner, A.; Vauthey, E.; Gescheidt, G.; Stampfl, J.; Liska, R. *J. Polym. Sci. A* **2011**, *49*, 3688–3699.

A. Curriculum Vitae

Personal Details

Name	Martin Kuß-Petermann
Date of birth	27.06.1985
Place of birth	Hoyerswerda, Saxony, Germany

Education

2013 - 2015	University of Basel (CH) PhD thesis: "*Photoinduced Formation and Decay of Charge-Separated States*" Supervisor: Prof. Dr. Oliver S. Wenger
2011 - 2013	Georg-August-University Göttingen (D) Started PhD thesis under supervision of Prof. Dr. Oliver S. Wenger
2004 - 2011	Georg-August University Göttingen (D); chemistry studies Degree: diploma Diploma thesis: "*Synthese und Charakterisierung neuer Donor-Akzeptor-Verbindungen zum protonengekoppelten Elektronentransfer*" Supervisor: Prof. Dr. Oliver S. Wenger
2003	Lessing Academic High School Hoyerswerda (D) A-level: Chemistry, Mathematics, German, History

Conferences

Talks

8^{th} Coordination Chemistry Meeting
"Proton-coupled electron transfer (PCET) over long distances"

02/2012 Dortmund, Germany

Joint workshop of IRTG 1422 and FOR1405
"Proton-coupled electron transfer (PCET) over long distances"
04/2012 Hofgeismar, Germany

23rd Lecture Conference of the division of photochemistry of GDCh.
"*Influence of donor-acceptor-distance on photoinduced PCET*"
10/2012 Potsdam, Germany

Posters

Joint workshop of IRTG 1422 and Emerging Field Initiative, University of Erlangen
"*Distance-Dependent Changeover from Photoacid Behavior to Proton-Coupled Electron Transfer*"
05/2013 Homberg, Germany

25th IUPAC Symposium on Photochemistry
"Dyads Mimicking the Proton-Coupled Electron Transfer Chemistry in Photosystem II"
07/2014 Bordeaux, France

21st International Symposium on the Photochemistry and Photophysics of Coordination Compounds
"*Photoinduced Charge Accumulation in a Molecular Pentad*"
07/2015 Krakow, Poland

B. Publications

Kuss-Petermann, M.; Wolf, H.; Stalke, D.; Wenger, O. S.
"*Influence of Donor-Acceptor Distance Variation on Photoinduced Electron and Proton Transfer in Rhenium(I)-Phenol Dyads*"
J. Am. Chem. Soc. **2012**, *134*, 12844.

Hoenes, R.; Kuss-Petermann, M.; Wenger, O. S.
"*Photochemistry between a ruthenium(II) pyridylimidazole complex and benzoquinone: simple electron transfer versus proton-coupled electron transfer*"
Photochem. Photobiol. Sci. **2013**, *12*, 254.

Kuss-Petermann, M.; Wenger, O. S.
"*Photoacid Behavior versus Proton-Coupled Electron Transfer in Phenol-Ru(bpy)$_3^{2+}$ Dyads*"
J. Phys. Chem. A **2013**, *117*, 5726.

Kuss-Petermann, M.; Wenger, O. S.
"*Mechanistic Diversity in Proton-Coupled Electron Transfer between Thiophenols and Photoexcited [Ru(2,2′-Bipyrazine)$_3$]$^{2+}$*"
J. Phys. Chem. Lett. **2013**, *4*, 2535.

Chen, J.; Kuss-Petermann, M., Wenger, O. S.
"*Distance Dependence of Bidirectional Concerted Proton–Electron Transfer in Phenol-Ru(2,2'-bipyridine)$_3^{2+}$ Dyads*"
Chem. Eur. J. **2014**, *20*, 4098.

Chen, J.; Kuss-Petermann, M., Wenger, O. S.
"*Dependence of Reaction Rates for Bidirectional PCET on the Electron Donor-Electron Acceptor Distance in Phenol-Ru(2,2'-Bipyridine)$_3^{2+}$ Dyads*"
J. Phys. Chem. B **2014**, *119*, 2263.

Kuss-Petermann, M.; Wenger, O. S.

"*Reaction Rate Maxima at Large Distances between Reactants*"
Chimia, submitted.

Kuss-Petermann, M.; Wenger, O. S.
"*Electron Transfer Rate Maxima at Large Donor-Acceptor Distances*"
submitted.

Kuss-Petermann, M.; Wenger, O. S.
"*Increasing Electron Transfer Rates with Increasing Donor-Acceptor Distance*"
in preparation

Kuss-Petermann, M; Orazietti, M.; Hamm, P.; Wenger, O. S.
"Photoinduced Charge Accumulation in a molecular Pentad"
in preparation.